

Experimental Investigation of Magnetohydrodynamic Flow For An Intense Proton Target

A Dissertation Presented

by

Hee Jin Park

to

The Graduate School

in Partial Fulfillment of the

Requirements

for the Degree of

Doctor of Philosophy

in

Mechanical Engineering

Stony Brook University

May 2009

16

Stony Brook University

17

The Graduate School

18

Hee Jin Park

19

We, the dissertation committee for the above candidate for the

20

Doctor of Philosophy degree,

21

hereby recommend acceptance of this dissertation.

22

Harold G. Kirk, Dissertation Co-Advisor,
Physicist, Department of Physics, Brookhaven National Laboratory

23

Foluso Ladeinde, Dissertation Co-Advisor,
Professor, Department of Mechanical Engineering

24

Lili Zheng, Chairperson of Defense,
Professor, Department of Mechanical Engineering

25

Kirk T. McDonald , Outside Member,
Professor, Physics Department, Princeton University

26

James Glimm, Outside Member,
Professor, Department of Applied Math. & Stat., Stonybrook University

27

This dissertation is accepted by the Graduate School.

28

Lawrence Martin
Dean of the Graduate School

29 Abstract of the Dissertation
30 **Experimental Investigation of Magnetohydrodynamic**
31 **Flow For An Intense Proton Target**
32 by
33 **Hee Jin Park**
34 **Doctor of Philosophy**
35 in
36 **Mechanical Engineering**
37 **Stony Brook University**
38 **2009**

39 Efficient production of pions can be achieved by colliding an intense proton
40 beam with a high-Z target. The experiments of Hg jet on the interaction of
41 an intense proton beam in magnetic field has been carried out for the thesis
42 work. The primary diagnostics in this work employed the technique of back-
43 illuminated laser shadow photography to freeze the transient events. The
44 images are recorded by several high speed cameras. The performance of the
45 optical diagnostic system is presented.

46 Flowing mercury in a magnetic field causes induced currents, which pro-
47 duce distortions of the mercury jet. The effect of Lorentz force is investigated
48 theoretically in a stability analysis of the conducting flow in the presence of a
49 magnetic field. The effects of Lorentz force on the vortices are also investigated

50 qualitatively. The role of joule damping as a loss on a time scale of magnetic
51 damping term in global kinetic energy is discussed.

52 Quantitative and qualitative data analysis using image processing based
53 on probability approach is described. The experimental measurement of the
54 various dynamic behaviors of Hg jet in magnetic field through image process-
55 ing is presented. In experiment, it is observed that the imposition of magnetic
56 field tends to suppress the fluctuating motion in Hg jet and correspondingly
57 the jet surface is more stabilized, where the Re is large enough and the Re_m is
58 0.26. Finally, the disruption of Hg jet with the proton beam and the magnetic
59 field effect to its suppression are presented. The collected images of beam-jet
60 interaction shows the response of Hg jet due to the proton beam induced en-
61 ergy deposition. The filament velocity induced by the energy deposition and
62 the time response of the velocity in magnetic field is presented, where joule
63 damping effect is explained. The experimental results investigated the the
64 performance and feasibility of utilizing liquid jet as a target for future accel-
65 erator. The experimental key components were designed and constructed at
66 Princeton University, ORNL, MIT Plasma Science and Fusion Center, CERN,
67 and BNL respectively.

69 Table of Contents

70	List of Figures	xvi
71	List of Tables	xvii
72	Acknowledgements	xviii
73	Nomenclature	xxii
74	1 Introduction	4
75	1.1 Neutrino Factory For High Power Neutrino Beam	4
76	1.1.1 The concept of neutrino factory	4
77	1.1.2 Neutrino physics	6
78	1.2 A High Power Target For Neutrino Factory	7
79	1.2.1 Material consideration for a high power target	7
80	1.2.2 Moving metallic target for pion production	8
81	1.2.3 Free mercury jet flow in magnetic field for a high power target	9
82	1.2.4 Impact of the MHD mercury jet experiment for an intense proton target	11
83	1.3 Mercury Target Issues	12
84	1.3.1 Mercury jet disruption by energy deposition from an intense proton beam	12
85	1.3.2 Magnetohydrodynamic issues in mercury jet target . .	13

86	1.3.3	Overview of experimental investigation of MHD flow and discussion	14
87	2	Magnetohydrodynamics of Conducting Flow in Magnetic Field	21
88	2.1	Governing Equations for MHD Flow	23
89	2.1.1	Electromagnetic equations	23
90	2.1.1.1	<i>electromagnetic relation in a linear material</i> .	24
91	2.1.1.2	<i>Maxwell's equations</i>	25
92	2.1.2	The Navier Stokes and magnetic induction equations in a conducting liquid flow	2
93	2.1.2.1	<i>magnetic Reynolds number</i>	29
94	2.1.2.2	<i>frozen-in theorem in magnetic induction equation</i>	31
95	2.1.2.3	<i>the diffusion limit in induction equation</i> . . .	32
96	2.2	The Energy Equation in MHD	32
97	2.2.1	Energetics and effects of Lorentz force	33
98	2.2.2	Proton beam induced energy deposition and equation of state	35
99	2.2.3	Magnetic damping with joule dissipation	37
100	2.3	Vorticity Equations in MHD flow	39
101	2.3.1	Governing equations for vorticity	40
102	2.3.2	Vorticity suppression	41
103	2.3.2.1	<i>spanwise magnetic field effect to vorticity suppression</i>	42
104	2.3.2.2	<i>longitudinal and transverse magnetic field effect to vorticity suppression</i>	
105	2.4	One Dimensional Pipe Flow in Transverse Magnetic Field . . .	45
106	2.4.1	Non-dimensional form of the governing equations using cylindrical coordinates	46
107	2.4.1.1	<i>boundary conditions in pipe flow</i>	46
108	2.4.2	Exact solutions of pipe flow in magnetic field	47
109	2.5	Stability of Conducting Flow in a Magnetic Field	48
110	2.5.1	Propagation of waves at an interface separating two flows in magnetic field	49

111	2.5.2	Magnetic pressure and tension	51
112	3	Experimental Method for Investigation of Magnetohydrodynamic Mercury Jet Flo	
113	3.1	Optical Diagnostics as a Principal Diagnostics of High Power Target Experiment	57
114	3.1.1	Working principle of shadowgraph for optical diagnostics	57
115	3.1.2	Development of optical diagnostic system	59
116	3.1.2.1	<i>the optical imaging system and Viewports design</i>	60
117	3.1.2.2	<i>the consideration for focusing and tilting alignment of optics</i>	64
118	3.1.2.3	<i>high speed cameras and light sources</i>	65
119	3.1.2.4	<i>radiation-hardness</i>	68
120	3.1.2.5	<i>scintillating fiber channel</i>	69
121	3.1.3	Schematic of electronic trigger and high speed camera control	70
122	3.2	Windows Consideration as Viewports for Observation	72
123	3.2.1	Fiducial mark on windows	72
124	3.2.2	Impact resistance test	73
125	3.2.3	Pressure leaking test of sapphire windows	73
126	3.3	Integrated Experimental Setup for High Power Target	74
127	3.3.1	Mercury loop system in solenoid magnet	74
128	3.3.1.1	<i>the considerations in nozzle design</i>	75
129	3.3.2	Water jet observation for nozzle performance test	76
130	4	Experimental Investigation of Mercury Jet Flow in Magnetic Fields	89
131	4.1	Image Analysis for Data Reduction	90
132	4.1.1	Image acquisition	90
133	4.1.2	Image processing	91
134	4.1.3	Study on the scaling length and the location of center of window	94

135	4.2	Motion of Mercury Jet and Stability in Magnetic Field	95
136	4.2.1	Jet deflection and surface flattening	95
137	4.2.2	Trajectory of mercury jet projectile in magnetic field	102
138	4.3	Dynamics of Liquid Jet Flow From Nozzle	104
139	4.3.1	Jet equations for analysis	104
140	4.3.2	Pressure loss and magnetic effect to the Hg delivery pipe	106
141	4.3.2.1	<i>pressure loss in pipe flow</i>	108
142	4.3.2.2	<i>the measurement of wall tap pressure</i>	113
143	5	Interaction of an Intense Proton Beam with Hg Jet in Magnetic Field	134
144	5.1	High Energy Proton Beam Structure	134
145	5.1.1	Proton synchrotron machine	134
146	5.1.2	Proton beam pulse length	136
147	5.1.3	Proton beam envelope by optics and camera screen	137
148	5.2	MARS Simulation for Energy Deposition to Mercury Jet by Proton Beam	138
149	5.2.1	Physics model	138
150	5.2.2	Mercury jet modeling in MARS code	139
151	5.2.3	Energy deposition to mercury jet	140
152	5.2.3.1	<i>energy deposition in magnetic field</i>	140
153	5.2.3.2	<i>geometric distribution of energy deposition in elliptic Hg jet cross section</i>	
154	5.2.3.3	<i>proton beam spot size to the energy deposition</i>	142
155	5.3	Observation of Interaction and Hg Jet Response to The Energy Deposition by Proton Beam	
156	5.3.1	Hg jet pressurization by energy deposition of proton beam	144
157	5.3.2	Observation of proton beam interaction and jet breakup	145
158	5.3.2.1	<i>energy deposition calculation with low intensity of proton beam and its ob</i>	
159	5.3.2.2	<i>energy deposition calculation with high intensity of proton beam and its ob</i>	

160	5.3.3	Hg jet disruption and magnetic suppression of the disruption	147
161	5.3.3.1	<i>characteristics of beam structure in disruption length, harmonic 8 and 16</i>	
162	5.3.3.2	<i>disruption length with 14 GeV proton beam</i>	149
163	5.3.3.3	<i>disruption length with 24 GeV proton beam</i>	150
164	5.3.3.4	<i>validation of measurements of Viewport 3 through comparison with Viewport 4</i>	
165	6	Mercury Jet Surface Development in Magnetic Field	181
166	6.1	Filament Model on Jet Surface	181
167	6.1.1	Geometry of viewing mercury filaments	181
168	6.1.2	Distribution of filaments on jet surface	183
169	6.1.3	Approximation of filaments velocity	184
170	6.1.3.1	<i>first order approximation</i>	184
171	6.2	Observation of Filaments Development on Mercury Jet Surface	185
172	6.2.1	Image calibration	185
173	6.2.1.1	<i>image calibration with proton beam arrival signal</i>	185
174	6.2.1.2	<i>time delay structure of proton beam to light source triggering</i>	186
175	6.2.2	Parameter optimization with uncertainty	187
176	6.2.2.1	<i>linear curve fit for estimation of model</i>	187
177	6.2.2.2	<i>Levenberg-Marquardt minimization</i>	190
178	6.2.3	Filaments distribution and uncertainty of measurement	192
179	6.2.3.1	<i>onset of filamentation on jet surface</i>	192
180	6.2.3.2	<i>measurement of traveled distance of filament</i>	192
181	6.2.4	Linear regression with the first order polynomial	194
182	6.2.4.1	<i>curve fit function</i>	194
183	6.2.4.2	<i>parameter estimation using multiple data points</i>	195
184	6.2.4.3	<i>filaments velocity distribution on jet surface</i>	195

185	6.3	Velocity of Filaments on Mercury Jet Surface	197
186	6.3.1	Magnetic dissipation of energy	197
187	6.3.2	Time response of filaments in magnetic field	197
188	6.3.2.1	<i>averaged time response of filament in magnetic field</i>	197
189	6.3.2.2	<i>instantaneous time response of filament in magnetic field</i>	198
190	6.3.3	Beam induced filaments velocity in magnetic field . . .	199
191	6.3.3.1	<i>filaments velocity with 14 GeV beam in magnetic field</i>	199
192	6.3.3.2	<i>filaments velocity with 24 GeV beam in magnetic field</i>	199
193	7	Conclusions	215
194		Bibliography	222
195	A	Tabular Data for Chapter 3, Chapter 5, and Chapter 6	229
196	A.1	Specifications of Optics	229
197	A.2	Characteristic Response of 25 W Laser	231
198	A.3	Mercury Properties	232
199	A.4	Measurement of Events with Pump Probe Condition	233
200	A.5	Beam Program List and Disruption Length Measurements . .	234
201	B	Image Data for Chapter 6	245
202	B.1	Images for filament velocity measurement at Viewport 2 . . .	245
203	C	Mathematical Derivation for Chapter 2	262
204	C.1	The governing equations for MHD in cylindrical coordinates .	262
205	C.2	Derivation of Rayleigh's instability at an interface separating two flows in magnetic field	262
206	C.2.1	<i>kinematic boundary condition at interface</i>	264
207	C.2.2	<i>hydrodynamic stability in magnetic field</i>	265

208	C.2.3 <i>dynamic boundary condition at interface</i>	266
-----	--	-----

List of Figures

210	1.1	Pion yield versus atomic mass number of the target at three proton beam energies, Osaki	
211	1.2	Pion yield from Hg targets versus tilt angle between the target/beam axis and the solenoid	
212	1.3	Geometry of key elements of target system and Viewports, showing the overlap between t	
213	1.4	Schematics of the relative overlap between proton beam axis, Hg jet axis , and solenoid m	
214	2.1	Wave-shaped interface separating two different fluids traveling at different average speeds	
215	2.2	Axes and electrodes of circular duct.	54
216	2.3	Energy decay in magnetic field. a.)Normalized energy decay. b.)Dissipation of normalized	
217	3.1	Displacement of light beam for shadowgraph.	78
218	3.2	Design of optical layout and installation of 4 Viewports of primary containment vessel. a.	
219	3.3	Photograph of optical head assembly and its illumination of laser. a.) Front view of optic	
220	3.4	Polished fiber end, 50X and 800X magnifications, respectively	81
221	3.5	Schematic of synchronized signal of high speed camera and laser pulse.	82
222	3.6	The triggering time for high speed camera upon beam arrival.	83
223	3.7	Schematic of electrical triggering and high speed camera control in tunnel for experiment.	
224	3.8	Top fiducial on the front window and bottom fiducial on the rear window. a.) Photo of fi	
225	3.9	Photographs of the entire MERIT experiment. a.) Sectional side view of mercury loop sy	
226	4.1	Image data conversion for image analysis. a.) Collected image data. b.) 2 bit scaled imag	

227	4.2	Sensitivity of threshold in a 2 bit scaled image conversion.	118
228	4.3	Jet height determination from image analysis. a.) Histogram of number of events in the jet	
229	4.4	Mercury jet flows as observed from the 3 Viewports. The jet flows from left to right on each	
230	4.5	Same as Fig. 4.4 but with a jet velocity of 20 m/s. a.) B=0T. b.) B=0T. c.) B=0T. d.) B=5T.	
231	4.6	Calculated solenoid magnetic induction field map. a.) Radial field map. b.) Axial field map.	
232	4.7	Hg jet height measurement in magnetic fields. a.) Histogram fitting of number of events.	
233	4.8	Comparison of Hg jet deflection ratio at 15 T to that at 10 T. a.) Numerical calculation of	
234	4.9	Intermittency of Hg jet at Viewport 2. The jet velocity is 15 m/s. a.) B=0T. b.) B=5T.	
235	4.9	Intermittency of Hg jet at Viewport 2. The jet velocity is 20 m/s. e.) B=0T. f.) B=5T. g.)	
236	4.10	Surface fluctuations in a magnetic field.	127
237	4.11	Trajectory of beam axis and Hg jet axis projectile with respect to magnetic axis in magnetic	
238	4.12	Hg jet angle at the center of magnetic axis (Viewport 2) as a function of magnetic field.12	
239	4.13	Boundary layer induced by a jet emerging from a nozzle.	130
240	4.14	Stream velocity and boundary layer thickness for various values of density ratio.131	
241	4.15	Pipe inlet pressure for driving Hg jet. a.) Static pressure. b.) Dynamic pressure. 132	
242	4.16	Longitudinal Hg jet flow velocity in magnetic field. a.) Velocity at each Viewport depending	
243	5.1	Infrastructures for experiment at CERN. a.) Proton synchrotron and TT2 tunnel for experiment	
244	5.2	Installation of integrated experimental components in tunnel TT2/TT2A for high power t	
245	5.3	Schematics of beam to jet interaction in magnetic field and the location of each Viewport	
246	5.4	1σ proton beam size at the center of magnet by optics (Efthymiopoulos, 2008).158	
247	5.5	1σ proton beam size by camera screen (Skoro, 2008). a.) 14 GeV beam. b.) 24 GeV beam	
248	5.6	Beam size measured by phosphor screen monitor as a function of time interval between be	
249	5.7	Modeling in MARS code for energy deposition calculation (Striganov, 2009). a.) Sectional	
250	5.8	Influence of magnetic field to the energy deposition distribution to Hg jet considering exp	
251	5.9	Radial energy deposition distribution along jet axis interacting with 24 GeV proton beam	

252	5.10 Radial energy deposition distribution along jet axis interacting with 14 GeV proton beam
253	5.11 Energy deposition distribution per proton according to the variation of beam spot size along
254	5.12 Peak energy deposition per proton and total energy deposition per proton according to the
255	5.13 Peak energy deposition and total energy deposition in total number of protons. a.) Peak
256	5.14 Photographs of the Hg jet interaction with 16 TP, 14 GeV proton beam at 5 T. Captured
257	5.14 Photographs of the Hg jet interaction with 16 TP, 14 GeV proton beam at 5 T. Captured
258	5.14 Photographs of the Hg jet interaction with 16 TP, 14 GeV proton beam at 5 T. Captured
259	5.15 Qualitative comparison of the jet response incident by interaction of low intensity (3 Tp)
260	5.16 Qualitative comparison of the jet response incident by interaction of high intensity (10 Tp)
261	5.17 Standard deviation of disruption length as a function of disruption length and the function
262	5.18 Proton beam pulse structure of harmonic 8 and harmonic 16 in 14 GeV and 6 TP. 174
263	5.19 Disruption length of Hg jet depending on the beam pulse structure as a function of 14 GeV
264	5.20 Disruption length of Hg jet as a function of 14 GeV beam intensity and magnetic field. H
265	5.21 Disruption length of Hg jet and its estimation as a function of 24 GeV beam intensity and
266	5.22 Validation of disruption measurement for the evaluation of evolution of disruption length
267	5.23 Disruption length distribution measurement in a same condition. Pump probe conditions
268	5.24 Disruption of mercury jet in magnetic fields as a function of total energy deposition and i
269	6.1 Schematic geometry of viewing mercury filaments. 202
270	6.2 Time structures between light source enabling and proton beam arrival. 203
271	6.3 Photographs of filament evolution on the Hg jet surface as a function of time at 25 μ s fra
272	6.4 Location on the Hg jet surface for velocity measurement of 14 points of filament. The sho
273	6.5 Illustration of curve fit for parameters estimation. a.) Multiple data points. b.) 3 data po
274	6.6 Approximation of velocity and onset time of filaments shown in Fig. 6.3. The beam is 10
275	6.7 Time response of instantaneous filament velocity at jet surface in Fig. 6.3 as a function of
276	6.8 Time response of averaged filament velocity as a function of magnetic field. a.) 14 GeV, 2

277	6.9 Time response of instantaneous filament velocity as a function of magnetic field. a.) 14 GeV
278	6.10 Filament velocity as a function of 14 GeV beam intensity and magnetic field. a.) Apparent
279	6.11 Filament velocity as a function of 24 GeV beam intensity and magnetic field. a.) Apparent
280	6.12 Filament velocity distribution measurement in a same condition. Pump probe conditions
281	6.13 Filament velocity in magnetic fields ejected from jet surface as a function of peak energy
282	A.1 Measurement of characteristic response of 25 laser used for high speed camera at Viewport
283	B.1 Photo of continuous 15 frames of captured image. The timing for the 1 st image is given in
284	B.2 Location on the Hg jet surface for velocity measurement of filaments. The numbers above
285	B.3 Photo of continuous 15 frames of captured image. The timing for the 1 st image is given in
286	B.4 Location on the Hg jet surface for velocity measurement of filaments. The numbers above
287	B.5 Photo of continuous 15 frames of captured image. The timing for the 1 st image is given in
288	B.6 Location on the Hg jet surface for velocity measurement of filaments. The numbers above
289	B.7 Photo of continuous 15 frames of captured image. The timing for the 1 st image is given in
290	B.8 Location on the Hg jet surface for velocity measurement of filaments. The numbers above
291	B.9 Photo of continuous 15 frames of captured image. The timing for the 1 st image is given in
292	B.10 Location on the Hg jet surface for velocity measurement of filaments. The numbers above
293	B.11 Photo of continuous 15 frames of captured image. The timing for the 1 st image is given in
294	B.12 Location on the Hg jet surface for velocity measurement of filaments. The numbers above
295	B.13 Photo of continuous 15 frames of captured image. The timing for the 1 st image is given in
296	B.14 Location on the Hg jet surface for velocity measurement of filaments. The numbers above
297	B.15 Photo of continuous 15 frames of captured image. The timing for the 1 st image is given in
298	B.16 Location on the Hg jet surface for velocity measurement of filaments. The numbers above

299

List of Tables

300	3.1	Specifications of high speed cameras.	87
301	3.2	Effects of irradiation up to an equivalent radiation dose of 1 Mrad on the reflectance and	
302	4.1	Error estimation of fiducial length at each viewport.	115
303	4.2	Pressure head losses by geometry in pipe for mercury loop. . .	115
304	4.3	Parameterized coefficients, its error, and statistics summary of fit function in figures.	116
305	5.1	Measurement of vertical distances of center of jet from magnetic axis and jet size for mod	
306	5.2	Parameterized coefficients, its error, and statistics summary of fit function in figures.	154
307	6.1	Parameterized coefficients, its error, and statistics summary of fit function in figures.	201
308	A.1	Specifications of optical components in optical diagnostics. . .	229
309	A.2	Properties of mercury.	232
310	A.3	Measurement of disruption and filament velocity in pump probe condition with 8 and 16	
311	A.4	Measured disruption length and beam shot program.	234
312	B.1	Properties of shots used for filaments velocity analysis.	245

ACKNOWLEDGEMENTS

The author greatly appreciates the indispensable guide and constant encouragements from Dr. Harold Kirk at Brookhaven National Laboratory and Prof. Foluso Ladeinde, who served as the author's dissertation advisor.

The author would like to express a special appreciation to Prof. Kirk McDonald at Princeton University and Dr. Thomas Tsang at Brookhaven National Laboratory for their contribution to the procedures used in this work.

The author would also like to thank Prof. Lili Zheng for agreeing to be the Chair of his dissertation committee, Prof. James Glimm, for agreeing to serve on the dissertation committee, Prof. Roman Samulyak, for valuable suggestions on the analysis of the experimental results.

This work was supported in part by the United States Department of Energy Contract No. DE-AC02-98CH10886. The experiment was carried out at CERN (European Organization for Nuclear Research) in Geneva, Switzerland and the analysis performed at Brookhaven National Laboratory. The text of this dissertation in part is a reprint of the materials as it appears in Review of Scientific Instruments **79**, 045111(2008). The co-authors listed in the publication directed and supervised the research that forms the basis for this dissertation.

Nomenclature

B	Magnetic induction field, T (Wb/m^2)
H	Magnetic field, A/m
E	Electric field, N/C (V/m); Global kinetic energy, J
J	Current density, A/m^2
V	Electric potential, V
D	Electric displacement field, C/m^2 ; Energy dissipation, J/s
P	Polarization density, C/m^2 ; Probability; Particle momentum, $J \cdot s/m$
M	Magnetization density, $J/(T \cdot m^3)$
J	Jacobian matrix
T	Temperature, $^{\circ}C$ (K); Time, s
B_o	Applied magnetic field, T (Wb/m^2)
v	Directional fluid velocity, m/s ; Mean velocity, m/s
U	Mean velocity in the x coordinate direction, m/s
e	Specific internal energy, J/kg
x, y, z	Cartesian coordinates, m
μ	Magnetic permeability, H/m (N/A^2)
ε	Electrical permittivity, F/m ($C^2/(N \cdot m^2)$)
χ_e	Electrical susceptibility
χ_m	Magnetic susceptibility
ε_o	Electrical permittivity of free space, F/m ($C^2/(N \cdot m^2)$)
μ_o	Magnetic permeability of free space, H/m (N/A^2)
t	Time, s
ε	Amplitude of a sinusoidal wave, m

α_v	Volume coefficient of thermal expansion, K^{-1}
c_p, c_v	Specific heat capacity, $J/(g\ K)$
λ	Wavelength of a sinusoidal wave, m
c	Wave velocity, m/s
p	Pressure, N/m^2
ρ	Density, kg/m^3
g	Gravity, m/s^2
M	Mass, kg ; Molar mass, g/mol
ζ	Intermittency factor
Γ	Surface tension, N/m
γ	Ratio of specific heats, c_p/c_v
η	Absolute viscosity, $kg/(m\ s)$
ν	Kinematic viscosity, η/ρ , m^2/s
σ	Electrical conductivity, S/m ; Standard deviation
κ	Compressibility, m^2/N
L	Characteristic length; Pipe length, m
τ	Joule damping term
I_T	Initial intensity of light, cd
I_o	Intensity of light, cd
ω	Vorticity, s^{-1}
ψ	Stream function, m^2/s
ϕ	Velocity potential, m^2/s
ϕ_E	Electric potential, V
E_{dep}	Energy deposition, J/g
f	Focal length, m ; Force, N ; Friction factor

τ	Wall shear stress, N/m^2
ξ	free surface perturbation, m
h	Head loss, m
K	Loss coefficient; Bulk modulus, N/m^2
A	Cross sectional area, m^2
e	Surface roughness, m ; Error, %
a	Radius of circular pipe, Radius of jet, m
c	Local speed of sound, m/s
d	Diameter of circular pipe, Diameter of nozzle, m
D	Diameter of jet, m
R	Gas constant, $J/(K \text{ mol})$; Radius of curvature of the centerline of the elbow, m
G	Pressure ratio
C	Contraction coefficient; Discharge coefficient; Constant
Q	Flow rate, m^3/s
r	Residual; Radial coordinates
β	Ratio of diameter
Re_m	Magnetic Reynolds number
Re	Reynolds number
Fr	Froude number
Al	Alfvén Number
Ha	Hartmann number
We	Weber number
N	Stuart number; Number of events; Augmented Jacobian matrix
$\nabla \cdot$	Divergence operator
$\nabla \times$	Curl operator

\times	Cross product operator
\cdot	Inner product operator; Multiplication

Superscripts

$'$	Differentiation with respect to variable; Perturbation; Fluctuation
\cdot	Differentiation with respect to time

Subscripts

x, y, z	Component values over the cartesian coordinates
o	Component mean value, Initial value at the nozzle
R	Reference location
a	Air
l	Liquid
T	Transpose of matrix

Nomenclature

B	Magnetic induction field
H	Magnetic field
E	Electric field; Global kinetic energy
J	Current density
V	Electric potential
D	Electric displacement field; Energy dissipation
P	Polarization density
M	Magnetization density; Molar mass
T	Temperature
R	Gas constant
B_o	Applied magnetic field
v	Directional fluid velocity; Mean velocity
U	Mean velocity in the x coordinate direction
e	Specific internal energy
x, y, z	Cartesian coordinates
μ	Magnetic permeability
ε	Electrical permittivity
χ_e	Electrical susceptibility
χ_m	Magnetic susceptibility
ε_o	Permeability of free space
μ_o	Permittivity of free space
t	Time
ϵ	Amplitude of a sinusoidal wave; Emittance
β	Amplitude function
α_v	Volume coefficient of thermal expansion
κ	Electrical conductivity
c_p, c_v	Specific heat capacity
β	Amplitude function
λ	Wavelength of a sinusoidal wave
c	Wave velocity
p	Pressure
ρ	Density
g	Gravity
ζ	Intermittency factor
Γ	Surface tension
γ	Ratio of specific heats

η	Absolute viscosity
ν	Kinematic viscosity
σ	Electrical conductivity; Standard deviation; Gaussian beam profile
L	Characteristic length; Luminosity; Pipe length
τ	Joule damping term
I_T	Initial intensity of light
I_o	Intensity of light
ω	Vorticity
ψ	Jet growth rate with respect to time
f	Focal length; Force; Friction factor
τ	Wall shear stress
ξ	free surface perturbation
h	Head loss
K	Loss coefficient
A	Cross sectional area
e	Surface roughness; Error
a	Radius of circular pipe
d	Diameter of circular pipe
R	Radius of curvature of the centerline of the elbow
G	Pressure ratio
C	Contraction coefficient; Discharge coefficient
Q	Flow rate
β	Ratio of diameter
Re_m	Magnetic Reynolds number
Re	Reynolds number
Fr	Froude number
Al	Alfven Number
Ha	Hartmann number
We	Weber number
N	Stuart number; Number of events
$\nabla \cdot$	Divergence operator
$\nabla \times$	Curl operator
\times	Cross product operator
\cdot	Inner product operator

Superscripts

'	Differentiation with respect to variable; Perturbation; Fluctuation
---	---

\cdot Differentiation with respect to time

Subscripts

x, y, z Component values over the cartesian coordinates

o Component mean value

R Reference location

Chapter 1

Introduction

Accelerator-based sources of exceptionally intense, tightly focused beams of x rays and ultraviolet radiation make possible both basic and applied research in fields from physics to biology to technology that are not possible with more conventional equipment. The development of a high-intensity source of muons can be useful for the production of high-energy neutrino, thereby opening the door for a broad range of important new physics experiments such as neutrino oscillation. The concept is to use a high-intensity proton beam incident on a mercury jet to produce pions which decay to give the muons. These muons is magnetically captured, accelerated, and then inserted into a storage ring.

1.1 Neutrino Factory For High Power Neutrino Beam

1.1.1 The concept of neutrino factory

Accelerators are used to accelerate primary particle beams such as protons and electrons. The required statistics in the collision processes demand a very

high flux of primary particles. On interaction of the primary particles with a target, it is possible to produce secondary beams of elementary particles like pions, neutrons, and gammas. Primary protons pass through a linear accelerator and further through a synchrotron, bunch compressors, and accumulators to achieve a beam with a certain energy, intensity and beam structure. This beam is directed toward a target. On interaction with the target, secondary particles of different kinds are produced. A neutrino factory is the ultimate tool for producing a high-intensity neutrino beam to study neutrino oscillations. The neutrino factory is based on a new concept of an accelerator that produces a high-intensity, high-energy beam of muon and electron neutrinos. It will allow an investigation of a new domain in neutrino physics such as

- High intensity. Its flux is 10^3 times greater than conventional neutrino beams.
- High energy. It features a very high beam energy of 20 to 50 GeV.
- In a neutrino factory, the muon sign can be selected. Thus, it is possible to deliver particles and anti-particles.

The basic concept of the Neutrino Factory is the production of muon neutrinos and anti-electron neutrinos from the decay of muons that are circulating in a storage ring. An intense proton beam is delivered to a target, where pions are produced. These pions are collected in a solenoidal magnetic field, which can capture both charged states of pions. The pions decay into muons in a decay channel. The muon beam has both a large energy spread and transverse

emittance. The energy spread is reduced using a phase rotation, while emittance is improved by ionization cooling. The cooled beam is accelerated (in a linac followed by two recirculating linacs) to energies of 20 to 50 GeV and injected into a storage ring.

1.1.2 Neutrino physics

Muons are a promising source of neutrinos. They have a short lifetime of $2.2\mu s$. Muons cannot be produced directly, so pions have to be produced first. The first stage of a neutrino factory is thus a high-power proton driver that deliver protons onto a target, where pions are produced. These pions have to be collected and transported. After about 20m, most of the pions decay into muons. A neutrino beam can be produced from the decay of high-energy muons:

- Pions from $Proton + Material \longrightarrow \pi^\pm + X$

- Muons from $\pi^\pm \longrightarrow \mu^\pm \nu_\mu (\bar{\nu}_\mu)$

- Neutrinos from $\mu^\pm \longrightarrow e^\pm \bar{\nu}_\mu \nu_e (\nu_\mu \bar{\nu}_e)$

At this stage, the muon beam has a low phase space density and resembles more a cloud than a beam. The next step is to create a usable muon beam. Phase rotation as well as ionization cooling is applied to reduce the energy spread and the emittance of the muon beam. Once the beam is cooled, it can be accelerated to a final energy of 20 to 50 GeV. In the final stage of a

neutrino factory, the accelerated muons are injected into a storage ring with long straight sections.

1.2 A High Power Target For Neutrino Factory

1.2.1 Material consideration for a high power target

The intensity of the muon beam is directly proportional to the power of the proton beam which initiates the process. Considering that a high intensity proton beam is required in order to generate the required muons, the choice of the target material becomes a particularly important issue. Modeling studies (Osaki, Palmer, Zisman, Gallardo, 2001) point to high-Z materials being more efficient at producing pions of both signs, whereas low-Z materials are better at preventing the absorption of the produced pions. The pion yield per proton increases with the atomic number of the target, as shown in Fig. 1.1 from a MARS calculation. A high-Z material is desirable because the pion production cross-section increases with increasing Z. However, the intense proton beam would melt a target made of a solid high-Z material. A target system using a flowing stream of mercury could recycle the spent target. Several types of target material have been proposed including copper, graphite, and mercury.

Since these targets are envisaged as being stationary, one must consider the problem of removing the energy deposited by the beam without interfering with the production of the particles.

1.2.2 Moving metallic target for pion production

While schemes for moving solid targets can be envisaged (Thieberger, Kirk, Weggel, McDonald, 2003), a flowing liquid target is simpler, and mercury as a high Z material presents itself as the liquid metal. The liquid target should be in the form of a free jet, rather than being confined in containment, since the beam-induced cavitation of the liquid metal can be destructive to solid walls in the immediate vicinity of the interaction region. Another issue associated with the proton beam is the effect of the energy that it deposits in the target. The temperature of the target rises almost instantaneously after the beam pulse, resulting in large internal stresses that might crack a solid target or disperse a liquid target (Kirk *et al*, 2001). In the case of a liquid jet target, the dispersal of the jet by the beam should not be destructive to the surrounding target system components and should not adversely affect pion production during subsequent beam pulses, either on the microsecond scale, if several micro-pulses are extracted from a proton synchrotron, or on the scale of the macro-pulse period. The operation of a liquid metal jet inside a strong magnetic field raises several magnetohydrodynamic issues such as possible deformation of the jet's shape and trajectory, as well as the effect of the magnetic field on the beam-induced dispersal of the jet.

1.2.3 Free mercury jet flow in magnetic field for a high power target

The free mercury jet in magnetic field is proposed for a high power target to overcome the issues described in the above chapter. The concept is to use a high intensity proton beam incident on a Hg jet to produce pions which decay to give the muons (Gabriel *et al*, 2001). The key elements of the target system are an intense proton source, mercury jet, and capture of the generated pions in a high field solenoidal magnet (McDonald, 2001). The schematics of the key elements of the target system is described in Fig. 1.3.

Previous studies (Osaki, Palmer, Zisman, Gallaro, 2001) indicated that pion yield is maximized with a mercury target in the form of a 1 cm diameter at the interacting center, tilted by about 150 milliradian with respect to the magnetic axis. The target is tilted with respect to the axis of the capture solenoid, thus permitting the pions, whose trajectories are spirals, to leave the side of the target with a minimal probability for re-entering the target volume. The pion yield per proton increases with the atomic number of the target, as shown in Fig. 1.1 from a MARS calculation. For 24 GeV protons, a high-Z target is superior in yield. As the pions emerge from the target at large angles to the beam, and follow helical paths that may intersect the target at more than one point, it is advantageous for the target to be in the form of a narrow rod, tilted at a small angle to the magnetic axis. As shown in Fig. 1.2, suitable parameters for a mercury target are a tilt angle of 150 mrad and a target radius of 5 mm.

Based on the previous studies described in the above, the experimental setup parameters are determined. The layout of experimental setup is briefly described in the below and will be more discussed in chapter 3. Fig. 1.4 shows the detailed schematic of the overlap between key components of the experiment. The trajectory of the mercury jet overlaps with the proton beam over 30 cm. The velocity of the jet is 15 m/s. The facility is a closed piping loop, constructed primarily of 316 stainless steel, and designed to circulate liquid mercury. The parameters of the proton beam and solenoid system are determined by the required conditions of particle production rates (Alessi *et al*, 1998). Basic system parameters consist of a proton energy 24 GeV, number of protons in one bunch $\approx 3 \times 10^{13}$. Only 10 % of the beam power is absorbed inside the target. The solenoid length is 100 cm, inside radius is 7.5 cm, and a maximum magnetic field is 15 T. The solenoid magnet is titled at 67 milliradian angle with respect to the beam. The beam arrives at an angle 34 milliradian with respect to the jet which has a radius ≈ 0.5 cm, as schematically shown in Fig. 1.4. The 24 GeV proton beam is directed on to the solenoid at 67 milliradian off the solenoid axis, so that most high momentum particles do not travel straight down the beam line (Gallardo *et al*, 2001). If there are no magnetic and gravitational effects on the mercury jet trajectory, the beam should enter at the bottom surface of Hg jet at Viewport 1, which is located at approximately 30 cm from the nozzle and the beam should exit on the top surface of Hg jet at Viewport 3, which is located at approximately 60 cm from the nozzle. The required jet velocity is determined by two conditions: 1),

the need to replenish the target before the arrival of subsequent proton beam pulse, and 2), it should be high enough to overcome the deceleration force induced by Lorentz force (Hassanein, Kinkashbaev, 2001).

Initial tests involving the interaction of proton beams on mercury targets were performed at the Brookhaven Alternating Gradient Synchrotron (AGS) (Kirk *et al.*, 2001), and continued at the CERN ISOLDE facility (Lettry *et al.*, 2003). The BNL test featured a 24 GeV proton beam interacting with a free mercury jet with a nozzle diameter of 1 cm and a velocity of 2.5 m/s. The delivered proton bunch was focused to <1 mm radius, resulting in a peak energy deposition of 80 J/g, delivering 24 GeV proton beam at 15 Hz (Tsoupas *et al.*, 2003). These initial tests did not have a magnetic field on the target. A parallel effort was undertaken to study the effects of high velocity mercury jets in the presence of high-magnetic fields, but with no proton beam.

1.2.4 Impact of the MHD mercury jet experiment for an intense proton target

The previous experiments did not perform the mercury jet in a high magnetic field interacting with an intense proton beam. In this work, we integrated the mercury jet, solenoid magnet, and intense proton beam all together. The performance and feasibility of utilizing liquid metal jet as a target for an intense proton beam is explored experimentally, which is the explicit objective of the experiment. The liquid jet target concept is recyclability otherwise the target would be destroyed. Therefore, the power of the target has to be eval-

uated in terms of the replacing capability and validated experimentally. In order to validate the performance of the target, the MHD jet behavior in a strong magnetic field has to be investigated. The response of the mercury jet due to the energy deposition by interacting with an intense proton beam has to be studied and the magnetic field effect to the disruption of mercury jet has to be studied, as well. The experimental results reveals that the effect of the Lorentz force to the jet stabilization as well as the deflection of jet. The experimental results will provide feasibility of utilizing liquid metal jet as a target for an intense proton beam. Also, the results will validate the phenomenology of conduction flow in magnetic field based on the MHD theory.

1.3 Mercury Target Issues

1.3.1 Mercury jet disruption by energy deposition from an intense proton beam

The production of large fluxes of particles using high energy, high intensity proton pulses impinging on solid or liquid targets presents unique problems which have not yet been entirely solved. The large amount of power deposition required in the material coupled with the short pulse duration produce large, almost instantaneous local heating. The resulting sudden thermal expansion can result in damage causing stresses in solids and in the violent disruption of liquid jets. The volume expansion initiates vibrations in the material. The amplitude of these vibrations is such that stresses that exceed the strength of the material can be generated, causing mechanical failure (Thieberger *et al*,

2003).

The interaction of the proton beam with the mercury target leads to very high heating rates in the target. When proton beam energy reaches approximately 100 kJ/pulse range, the heat from the beam could melt or crack a high-Z target.

1.3.2 Magnetohydrodynamic issues in mercury jet target

Liquid metal jets are proposed as potential target candidates because the heat energy can be removed along with the moving liquid. There are three important problems that are associated with the use of liquid metal targets in these environments. First, as the liquid jet penetrates the magnetic field, perturbations in jet motion and deceleration may occur because of the large field gradients at the entrance and exit of the solenoid. Second, during the intense pulse of energy deposition in a short time, the resultant stress could break up the target. Third, the liquid jet can develop instabilities in the strong inhomogeneous magnetic field and after beam interaction, because of the jet break up induced by the energy deposition of beam. These instabilities can change the jet shape into one that is significantly less efficient for pion production (Hassanein, Kinkashbaev, 2001).

Mercury flow in a magnetic field experiences induced currents, which cause the jet to produce transverse forces normal to jet axis direction resulting deflection normal to jet axis (Gallardo *et al*, 2001). In addition, axial currents

are induced if the jet axis does not coincide with the magnetic field axis. These axial currents produce elliptical distortions of the mercury jet. Faraday's law can be used to obtain the azimuthal current density from changing the axial field in the local coordinate system of the Hg jet. The transverse component of the magnetic field normal to the jet axis also varies along the trajectory of the mercury jet. The axial current density can be related to the changing transverse component of the magnetic field normal to the jet axis. These axial currents produce a magnetic force. This force will be balanced by a restoring force from the surface tension of the mercury, and with the condition that the mercury is an incompressible liquid, will produce an elliptic deformation of the mercury jet.

1.3.3 Overview of experimental investigation of MHD flow and discussion

A proof-of-principle experiment at the CERN Proton Synchrotron that combined a free mercury jet target with a 15T solenoid magnet and a 24 GeV primary proton beam was performed. The experiment validates the target concept for producing an intense secondary source of muons by showing the jet repetition rate to replace the disrupted target by the energy deposition from an intense proton beam. The PS runs in a harmonic-16 mode and can fill up to 2×10^{12} protons/bunch. The spot RMS size in experiment is approximately 1.5 mm. This allows up to 30×10^{12} protons per pulse on the mercury target, generating a peak energy deposition of 180 J/g. For this experiment, a high

magnetic field pulsed solenoid with a bore of 15 cm is designed. This magnet is capable of delivering a pulsed peak field of 15 T. which is cooled to 80 K by liquid nitrogen to reduce the resistance of its copper coils. The Hg jet delivery system generates a mercury jet from 1 cm diameter nozzle with velocities up to 15 m/s. The primary diagnostic of the beam-jet interaction is optical. A set of four view-ports along the interaction region is connected by imaging fiber-optic bundles to four high speed cameras.

Each pulse of the proton beam delivered to this system constitutes a separate experiment. About 360 beam pulses are utilized in a beam-on-demand mode at CERN. These pulses span a range of intensities and time intervals between the multiple extracted bunches per pulse. The magnet operates over a range of field strengths of 0 – 15 T.

In chapter 2, the full MHD governing equation using Maxwell's equations are presented. Various modeling of conducting flow in a magnetic field are formed, where the contribution of Lorentz force to the hydrodynamic equations is presented and discussed. The formulated and reviewed theory is introduced to explain and support the MHD experimental results.

In chapter 3, the detailed layout of experimental setup and its installation are presented. The design of each key components for the experiment such as nozzle, solenoid magnet and mercury loop system is presented. As a primary diagnostics, the scientific development of optical diagnostics employing the high speed cameras and infrared lasers to freeze the transient motion of mercury jet is presented and the performance of the scientific instrument as

well as the methodology to capture images are discussed in detail.

In chapter 4, 5, and 6, MHD behaviors of the mercury jet in a magnetic field are discussed based on the observation from the experiments. Also, the characteristics of the mercury jet in a magnetic field interacting with an intense proton beam are presented. The key results to validate the feasibility of the High-Z liquid target is addressed based on the experimental measurements and the beam pulse structures.

To conclude the study, the concluding remark are presented and the discussion based on the MHD theory and the experimental results is summarized in chapter 7. The discrepancy and/or consistency between expecting results from MHD theory and the experimental results are discussed and explained to leave a room for a future study.

This program explores the full variety of beam/target conditions anticipated in the design of Neutrino Factories driven by proton synchrotron of 4 MW beam power.

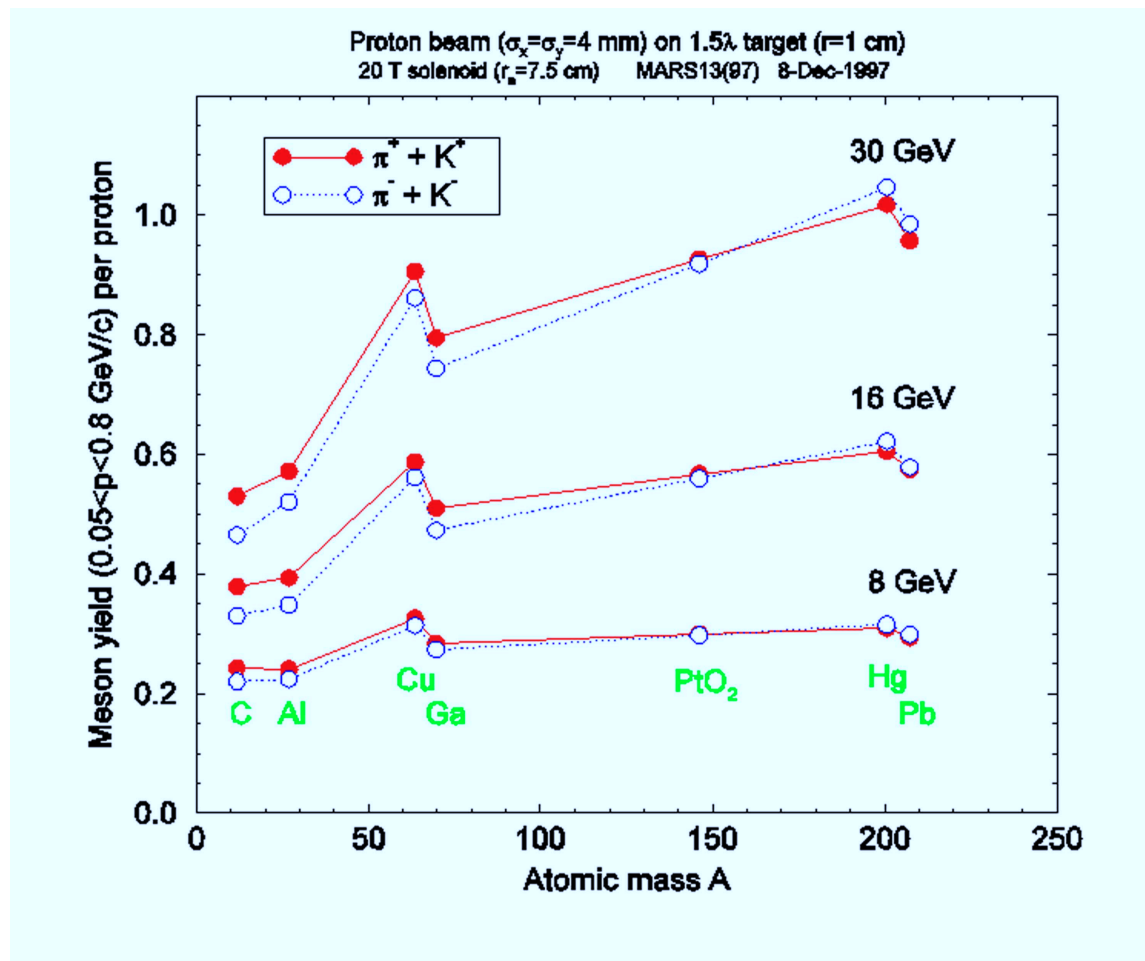


Figure 1.1: Pion yield versus atomic mass number of the target at three proton beam energies, Osaki (2001) and Mokhov (2000).

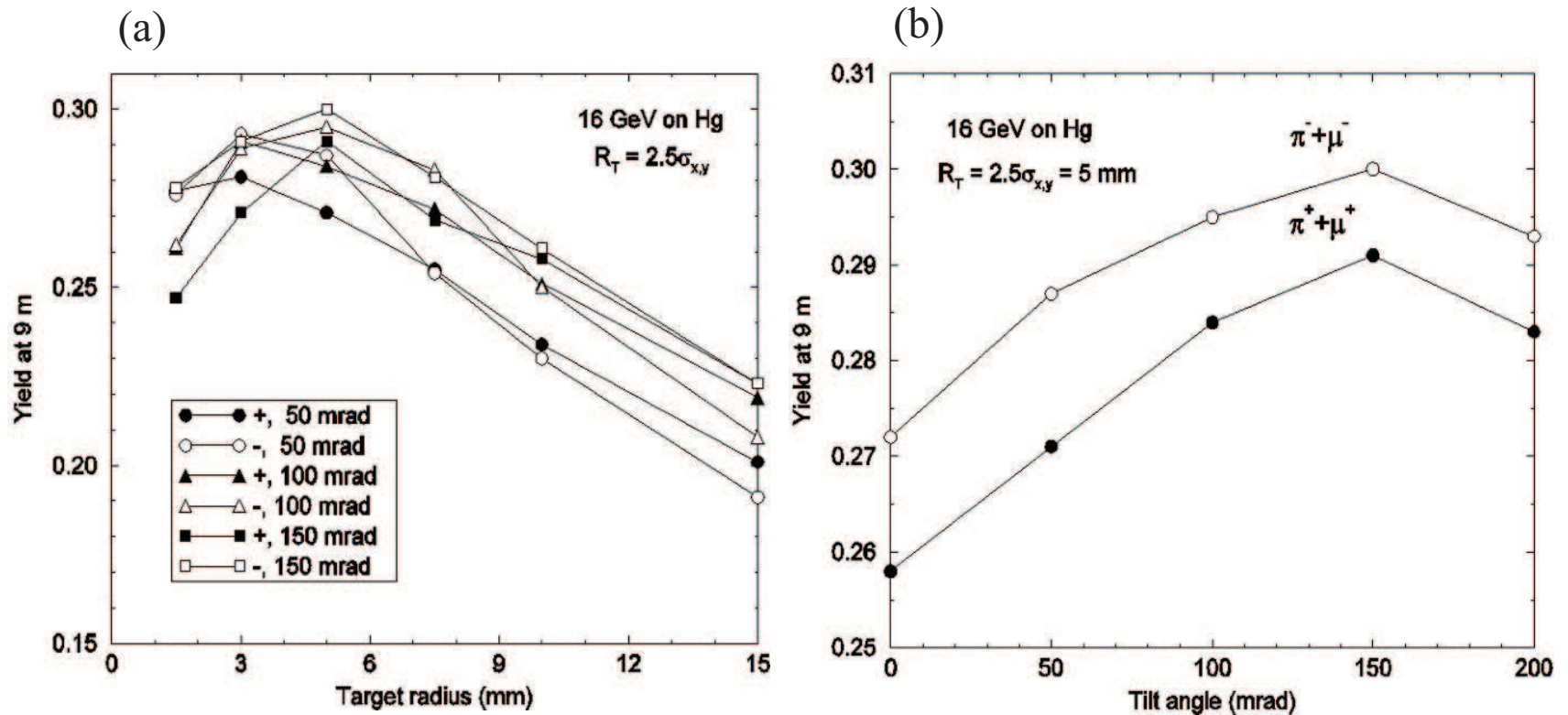


Figure 1.2: Pion yield from Hg targets versus tilt angle between the target/beam axis and the solenoid axis and versus the radius of the target, Osaki (2001) and Mokhov (2000). a.) Pion yield versus tilt angle. b.) Pion yield versus target radius.

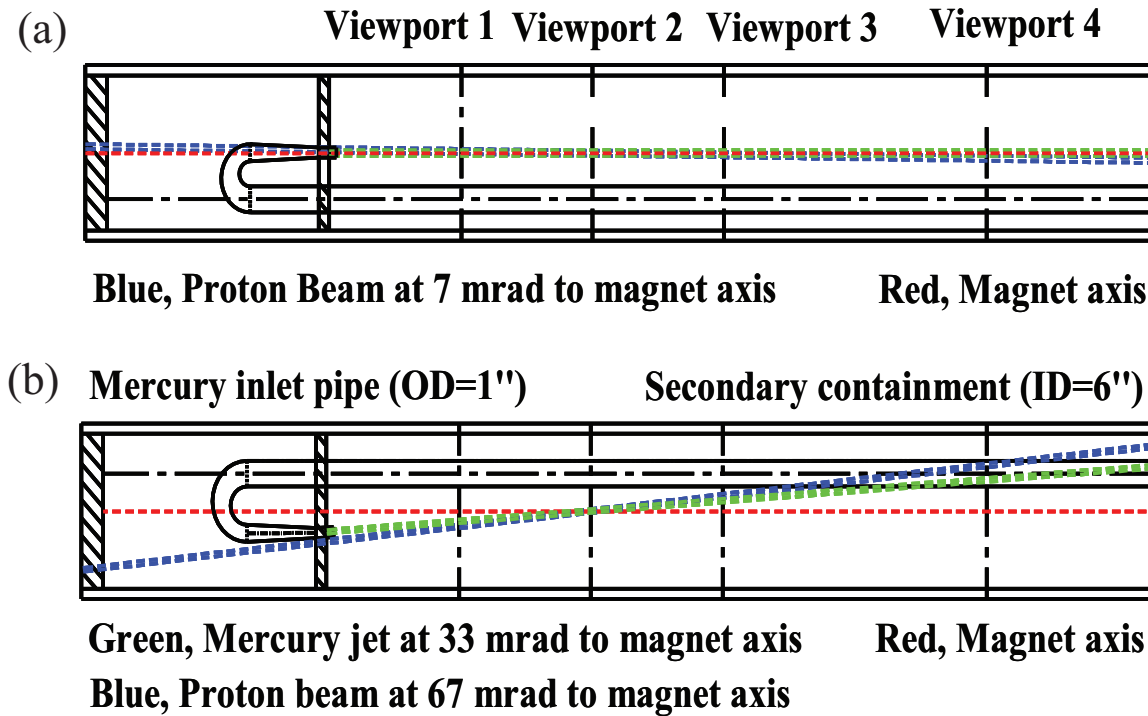


Figure 1.3: Geometry of key elements of target system and Viewports, showing the overlap between the mercury jet, magnetic axis, and the proton beam. a.) Top view. b.) Side view.

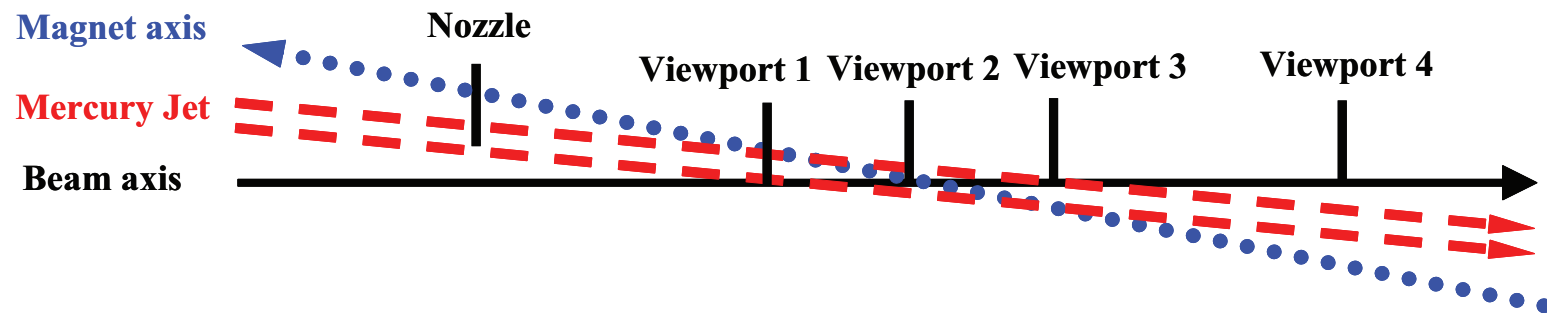


Figure 1.4: Schematics of the relative overlap between proton beam axis, Hg jet axis , and solenoid magnet axis.

Chapter 2

Magnetohydrodynamics of Conducting Flow in Magnetic Field

In this chapter, the issues of electrically conducting fluid in a pipe and jet flow in a magnetic field are presented. The governing equations for magnetohydrodynamics, based on electrodynamic relations of Maxwell's equation and hydrodynamic Navier-Stokes equation, are given and the effects of Lorentz force induced by magnetic field are discussed. The review of previous work provides a basis for these studies. Hartmann (1937) considered the flow between two parallel, infinite, non-conducting walls, with magnetic field applied normal to the walls. An exact solution was obtained for this case by Hartmann (1937). Shercliff (1953) solved the more general problem of three dimensional flow in a rectangular duct. Exact solutions demonstrated the fact that for large Hartmann number, the velocity distribution consists of a uniform core with a boundary layer near the walls. This result enabled the solution of the corresponding problem for a circular pipe in an approximate manner for large

Hartmann numbers, assuming walls of zero conductivities (Shercliff, 1956).
 Chang and Lundgren (1961) considered the effects of wall conductivity for the
 same problem. Gold (1962) considered a steady one-dimensional flow of an
 incompressible, viscous, electrically conducting fluid through a circular pipe
 in the presence of a uniform transverse field. A no-slip condition on the veloc-
 ity is assumed at the electrically non-conducting wall because if the walls are
 conducting, there is a electromagnetic force on the wall and a corresponding
 force on the fluid. The flow is along the z -axis, which coincides with the axis
 of the cylinder, and the uniform applied magnetic field is along the x -axis,
 which is normal to the flow direction. The solution is exact and valid for all
 values of the Hartmann number. The conducting liquid jet inside a strong
 magnetic field raises several magnetohydrodynamic(MHD) issues, such as the
 possible deformation of the jet's shape and trajectory, as well as the effect of
 the magnetic field on the beam-induced dispersal of the jet. The electrically
 conducting flow moving in a magnetic field experiences induced currents (Gal-
 lardo, 2002). These induced currents cause the jet to experience anisotropic
 pressure distribution with respect to the major and minor axis of jet cross
 section normal to the jet flowing axis while the jet penetrates the nonuniform
 magnetic field (Gallardo, 2002). In addition, axial currents are induced if the
 jet axis does not coincide with the magnetic field axis. These currents in turn
 produce transverse elliptical distortions of the mercury jet. Finally, the liquid
 jet can develop surface instabilities such as surface wavelength growing and jet
 breakup during both liquid motion in a inhomogeneous magnetic field and af-

ter the interaction of intense proton beam, because of the Rayleigh instabilities in a magnetic field and the sudden energy deposition leading to jet breakup. These instabilities can change the jet shape into a significantly less efficient target for pion production. The analytical approach to describe the behaviors of MHD conducting flow in a magnetic field is provided in this chapter.

2.1 Governing Equations for MHD Flow

2.1.1 Electromagnetic equations

In this section, we describe the electromagnetic relations that have been used in the derivation of the MHD governing equations. The following properties are defined as follows:

- polarization density \mathbf{P} : the vector field that expresses the density of permanent or induced electric dipole moments in a dielectric material. It is defined as the dipole moment per unit volume.
- magnetization density \mathbf{M} : the magnetic dipole moment per unit volume.
- electrical susceptibility χ_e : a measure of how easily a dielectric material polarizes in response to an electric field. This determines the electric permittivity of the material. It is defined as the constant of proportionality when relating an electric field \mathbf{E} to the induced dielectric polarization density \mathbf{P} .
- magnetic susceptibility χ_m : the degree of magnetization of a material in response to an applied magnetic field.

- 667 • electric displacement field \mathbf{D} : It accounts for the effects of bound charges
668 within materials. It is the macroscopic field average of electric fields from
669 charged particles that make up otherwise electrically neutral material.
670 It can be considered the field after taking into account the response of a
671 medium to an external field such as reorientation of electric dipoles.
- 672 • magnetic field strength \mathbf{H} : A vector field that permeates space and which
673 can exert a magnetic force on moving electric charge and on magnetic
674 dipoles such as permanent magnets.
- 675 • electric field \mathbf{E} : the electric force per unit charge. The direction of the
676 field is taken to be the direction of the force it would exert on a positive
677 test charge.

678 2.1.1.1 *electromagnetic relation in a linear material*

679 In a linear material, the polarization density \mathbf{P} and magnetization density
680 \mathbf{M} are given by

$$682 \qquad \qquad \qquad \mathbf{P} = \chi_e \varepsilon_o \mathbf{E} \ , \qquad \qquad \qquad (2.1)$$

$$683 \qquad \qquad \qquad \mathbf{M} = \chi_m \mathbf{H} \ , \qquad \qquad \qquad (2.2)$$

685 where χ_e is the electrical susceptibility and χ_m is the magnetic suscepti-
686 bility of the material. Electric displacement field, \mathbf{D} , and magnetic induction

field, \mathbf{B} , are related to electric field, \mathbf{E} , and magnetic field \mathbf{H} by

$$\mathbf{D} = \varepsilon_o \mathbf{E} + \mathbf{P} = \varepsilon \mathbf{E} , \quad (2.3)$$

$$\mathbf{B} = \mu_o (\mathbf{H} + \mathbf{M}) = \mu \mathbf{H} , \quad (2.4)$$

where ε is the electrical permittivity and μ is the magnetic permeability of the material.

2.1.1.2 *Maxwell's equations*

The solenoidal condition for the magnetic induction, indicating that there are no magnetic monopoles, is given by

$$\nabla \cdot \mathbf{B} = 0 , \quad (2.5)$$

That is there are no sources and sinks for magnetic field lines.

Faraday's law of magnetic induction is given by

$$\nabla \times \mathbf{E} = -\partial \mathbf{B} / \partial t \quad (2.6)$$

showing that a spatially varying electric field can induce a magnetic field.

Charge conservation gives

$$\nabla \cdot \mathbf{E} = \rho^* / \varepsilon_o , \quad (2.7)$$

where $\rho^* = \varepsilon_o (n^+ - n^-)$ is the charge density, n^+ is the number of ions, and n^- is the number of electrons.

709 Ampère's law is given by

710

711
$$\nabla \times \mathbf{B} = \mu \mathbf{j} + \mu \varepsilon \partial \mathbf{E} / \partial t , \quad (2.8)$$

712 where the last term on the right hand side is the displacement current.

713 Introducing the fundamental units of mass M, length L, velocity v , and time

714 t , we consider the dimensions of the displacement current in Eqn. (2.8). The

715 dimensions of the magnetic field B, electric field E, and the speed of light c

716 itself respectively are considered for simplicity.

717 $\nabla \times \mathbf{E} \sim \frac{E}{L}, \frac{\partial \mathbf{B}}{\partial t} \sim \frac{B}{t}$ gives $E = vB$. From the speed of light, $c = \frac{1}{\sqrt{\mu \varepsilon}}$,

718 $\mu \varepsilon \partial \mathbf{E} / \partial t = \frac{1}{c^2} \partial \mathbf{E} / \partial t \sim \frac{1}{c^2} \frac{E}{t} = \frac{v}{c^2} \frac{B}{t} = \frac{B}{L} \frac{v^2}{c^2}.$

719 Therefore, The displacement current in Ampère's law can be neglected if

720 the flow velocity is much less than the speed of light.

721 By assuming the flow obeys charge neutrality, $n^+ - n^- \ll n$, where n is

722 the total number density, the charge density in Eqn. (2.7) can be neglected.

723 Finally, Ohm's law without Hall effect is given by

724

725
$$\mathbf{j} = \sigma (\mathbf{E} + \mathbf{v} \times \mathbf{B}) . \quad (2.9)$$

726 This is the generalization of the relation between voltage and current in a

727 moving conductor. It provides the link between the electromagnetic equations

728 and the fluid equations.

729 The electric charge is conserved, which is given by Kirchhoff's law:

730

731
$$\nabla \cdot \mathbf{j} = 0. \quad (2.10)$$

2.1.2 The Navier Stokes and magnetic induction equations in a conducting liquid flow

The motion of an electrically conducting fluid in the presence of magnetic field obeys the equations of magnetohydrodynamics. The fluid is treated as a continuum and the classical results of fluid dynamics and electro-dynamics are combined in the derivation of the equations. The first equation is from mass conservation:

$$\rho \frac{\partial \rho}{\partial t} + \nabla \cdot (\rho \mathbf{v}) = 0 . \quad (2.11)$$

Next, Newton's second law of motion gives

$$\rho \frac{D\mathbf{v}}{Dt} = -\nabla p + \mathbf{F} , \quad (2.12)$$

where the external force \mathbf{F} consists of several terms, such as the Lorentz force, given by $\mathbf{j} \times \mathbf{B}$, the gravitational force $\rho \mathbf{g}$, and the viscous force. The viscous term is given by a kinematic viscosity of the form $\rho \nu \nabla^2 \mathbf{v}$ for an incompressible flow. Thus, Eqns. (2.12) become

$$\rho \frac{\partial \mathbf{v}}{\partial t} + \rho (\mathbf{v} \cdot \nabla) \mathbf{v} = -\nabla p + \rho \mathbf{g} + \eta \nabla^2 \mathbf{v} + \mathbf{j} \times \mathbf{B} . \quad (2.13)$$

Note that the Lorentz force couples the fluid equations to the electromagnetic equations. Eqn. (2.13) can be reduced to a dimensionless form.

$$\frac{\partial \mathbf{v}}{\partial t} + \mathbf{v} \cdot \nabla \mathbf{v} = -\nabla p + \frac{\mathbf{g}}{\text{Fr}^2} + \frac{1}{\text{Re}} \nabla^2 \mathbf{v} + \text{Al}(\mathbf{j} \times \mathbf{B}) , \quad (2.14)$$

754 where $Fr = v/\sqrt{gL}$, $Re = \rho vL/\eta$, $Re_m = \mu\sigma vL$, and $Al = B_o^2/\mu\rho v^2$ denote
 755 the Froude, Reynolds, magnetic Reynolds, and Alfvén numbers, respectively.
 756 The Hartmann number gives the ratio of magnetic forces to viscous forces.
 757 Thus, this number is the important parameter in cases where the inertial effects
 758 are small. On the other hand, the Stuart number gives the ratio of magnetic
 759 forces to inertial forces, Thus, this number is the important parameter where
 760 dealing with inviscid or turbulence. The Hartmann number Ha and Stuart
 761 number N are related through $Ha^2 = ReRe_mAl$ and $N = Re_mAl$. Note that
 762 the ratio of Hartmann number and Reynolds number represents a mixture
 763 parameters and involving viscous, magnetic, and inertial forces and can be
 764 thought of the square root of the product of the viscous and magnetic forces
 765 divided by the inertial forces.

766 We consider components of the magnetic induction field B_x, B_y, B_z . Note
 767 that the longitudinal magnetic field along the jet axis x and the transverse mag-
 768 netic field normal to the jet axis are given by $B_x = B_X\cos\theta - B_Y\sin\theta$, $B_y =$
 769 $-B_X\sin\theta + B_Y\cos\theta$ respectively, where B_X is axial magnetic field and B_Y
 770 is radial magnetic field. Also note that the (x, y, z) coordinate system is re-
 771 lated with the dynamics of jet dynamics and the (X, Y, Z) coordinate system
 772 is related with the magnetic field direction in solenoid. The nondimension-
 773 alized momentum equations in the (x, y, z) coordinate system in Fig. 2.1 is

represented as Eqn. (2.15) using Ohm's equation.

$$\begin{aligned}
\frac{\partial v_x}{\partial t} + v_x \cdot \nabla v_x &= -\nabla p + \frac{1}{\text{Re}} \nabla^2 v_x - \frac{\text{Ha}_y^2}{\text{Re}} v_x + \frac{\text{Ha}_x \text{Ha}_y}{\text{Re}} v_y, \\
\frac{\partial v_y}{\partial t} + v_y \cdot \nabla v_y &= -\nabla p + \frac{1}{\text{Re}} \nabla^2 v_y - \frac{\text{Ha}_x^2}{\text{Re}} v_y + \frac{\text{Ha}_x \text{Ha}_y}{\text{Re}} v_x, \\
\frac{\partial v_z}{\partial t} + v_z \cdot \nabla v_z &= -\nabla p + \frac{1}{\text{Re}} \nabla^2 v_z - \frac{\text{Ha}_x^2}{\text{Re}} v_z - \frac{\text{Ha}_y^2}{\text{Re}} v_z.
\end{aligned} \tag{2.15}$$

In MHD, to eliminate the electric field \mathbf{E} and the electric current density \mathbf{j} , we use the Ampere's law and Ohm's law. Then, the Faraday's law gives the magnetic induction equation:

$$\frac{\partial \mathbf{B}}{\partial t} = \nabla \times (\mathbf{v} \times \mathbf{B}) - \frac{1}{\mu\sigma} \nabla \times \nabla \times \mathbf{B} = \nabla \times (\mathbf{v} \times \mathbf{B}) + \frac{1}{\mu\sigma} \nabla^2 \mathbf{B} \tag{2.16}$$

2.1.2.1 *magnetic Reynolds number*

In Eqn. (2.16), the dimension of the term on the left hand side is $\frac{B}{t}$ and the second term on the right hand side is $\frac{B}{\sigma\mu L^2}$. Therefore, $\sigma\mu \sim \frac{t}{L^2}$. The magnetic induction equation can be reduced to a dimensionless form.

$$\frac{\partial \mathbf{B}}{\partial t} = \nabla \times (\mathbf{v} \times \mathbf{B}) + \sigma\mu Lv \nabla^2 \mathbf{B}, \tag{2.17}$$

where the quantity $\sigma\mu Lv$ is a dimensionless number, Re_m , called the magnetic Reynolds number. Re_m is a measure of the size of the advection term, $\nabla \times (\mathbf{v} \times \mathbf{B})$, relative to the diffusion term, $\sigma\mu Lv \nabla^2 \mathbf{B}$. Reynolds number Re measures the extent to which a convective process prevails over a diffusive

one. In viscous flow, the viscosity causes vorticity to diffuse in the face of convection and the Reynolds number measures the power of convection over diffusion of vorticity. In MHD, the conductivity causes convection to overcome diffusion of the magnetic field to a degree measured by the magnetic Reynolds number Re_m . If Re_m is large, convection dominates over diffusion and magnetic boundary layer near the fields are to be expected. The magnetic Prandtl number measures the ratio of viscous diffusivity and magnetic diffusivity and is defined as Re_m/Re . When it is small, magnetic fields diffuse much more rapidly than vorticity and magnetic boundary layers are much thicker than viscous layers. This makes for simplifications such as the neglect of viscosity in the magnetic boundary layer.

In any region of length scale δ where convection and diffusion are equally important, δ must be of order $1/\mu\sigma v$. Only within limited regions where B changes significantly in a distance δ can the gradients be high enough for diffusion and dissipation to matter. The characteristic time in the flow is the transit time L/v , during which a field disturbance diffuses a distance of order $(L/\mu\sigma v)^{1/2}$. This is much less than L if $Re_m \gg 1$, in which case diffusion is negligible. It will diffuse a distance of order $(t/\mu\sigma)^{1/2}$, which is negligible in comparison with the length scale L if $L^2\mu\sigma/t \gg 1$. This is the required criterion for the perfect conductivity approximation to be valid. At the other extreme case where diffusion is dominant is that the medium diffuses to the form it would be in stationary fluid, where no induced magnetic field would occur. The ratio of the induced magnetic field and the imposed magnetic field

is of order $\mu\sigma vL$, which is Re_m . The low Re_m approximation is to ignore the induced field, to replace \mathbf{B} by the known field \mathbf{B}_o in all MHD equations.

2.1.2.2 *frozen-in theorem in magnetic induction equation*

If $\text{Re}_m \gg 1$, the induction equation Eqn. (2.16) is approximated by

$$\frac{\partial \mathbf{B}}{\partial t} = \nabla \times (\mathbf{v} \times \mathbf{B}) \quad (2.18)$$

The timescale with changes due to the fluid motion from Eqn. (2.18) is given by $t_{motion} \sim \frac{L}{v}$. In the case $t_{motion} \ll t_{diffusion}$, which corresponds to $\text{Re}_m \gg 1$, the diffusion term is negligible. According to the frozen-flux theorem of Alfvén, in a perfectly conducting fluid, where $\text{Re}_m \rightarrow \infty$, the magnetic field lines move with the fluid: the field lines are ‘frozen’ into the fluid. This theorem states that motions along the field lines do not change the field but motions transverse to the field carry the field with them. If the area of the flux tube is small, the field strength will be approximately constant across the area of the tube. Thus, the $|\mathbf{B}| \times \text{cross sectional area}$ is constant so that the field strength becomes stronger if the cross sectional area is reduced by the fluid motion. The vorticity flux through any loop moving with the fluid is constant and the particles which initially lied on a vorticity line continue to do so. All the fluid particles which initially lie on a magnetic field line continue to do so in a perfect conductor.

2.1.2.3 the diffusion limit in induction equation

If $\text{Re}_m \ll 1$, the induction equation Eqn. (2.16) is approximated by

$$\frac{\partial \mathbf{B}}{\partial t} = \frac{1}{\mu\sigma} \nabla^2 \mathbf{B} \quad (2.19)$$

The timescale with changes due to field diffusion from Eqn. (2.19) is given by $t_{diffusion} \approx \sigma\mu L^2$. The diffusion equation indicates that any irregularities in an initial magnetic field will diffuse away and be smoothed out. The field will tend to be a simpler uniform field. This process of smoothing out will occur on the given diffusion timescale.

2.2 The Energy Equation in MHD

In general, the energy equation can be written in the form

$$\frac{\rho^\gamma}{\gamma - 1} \frac{D}{Dt} \left(\frac{p}{\rho^\gamma} \right) = -\mathbf{D} , \quad (2.20)$$

where \mathbf{D} is the total energy loss function, γ is the ratio of specific heats, c_p/c_v . The energy loss function consists of thermal conduction, radiation, and heating. The heating consists of several terms, such as small scale magnetic wave heating, ohmic heating, and viscous heating. However, such losses (gains) can be neglected if the medium is either isentropic or adiabatic. There are cases where no energy is added to the flow and no energy losses occur. The adiabatic

term can be represented as follows, using Eqn. (2.11):

$$\rho^\gamma \frac{D}{Dt} \left(\frac{p}{\rho^\gamma} \right) = \frac{\partial p}{\partial t} + \mathbf{v} \cdot \nabla p + \gamma p \nabla \cdot \mathbf{v} = -(\gamma - 1) \mathbf{D}. \quad (2.21)$$

To close the system of equations, an equation of state is needed, which is taken as ideal gas law:

$$p = \frac{\rho}{M} RT, \quad (2.22)$$

where M is molar mass and R is the gas constant ($8.3 \text{ J} \cdot \text{mol}^{-1} \text{K}^{-1}$).

2.2.1 Energetics and effects of Lorentz force

The energy equation that contains all the various types of energy, including kinetic energy, gravitational energy, the internal energy, and the magnetic energy is obtained using the MHD governing equations. The gravitational potential Φ is defined by $-\nabla\Phi = \mathbf{g}$. The kinetic energy is obtained by multiplying Eqn. (2.11) by $v^2/2$ and dotting Eqn. (2.12) with \mathbf{v} . The energy equation can then be written as

$$\frac{\partial}{\partial t} \left(\frac{1}{2} \rho v^2 \right) + \nabla \cdot \left(\frac{1}{2} \rho v^2 \mathbf{v} \right) = -\mathbf{v} \cdot \nabla p + \mathbf{v} \cdot (\mathbf{j} \times \mathbf{B}) - \mathbf{v} \cdot \rho \nabla \Phi + \mathbf{v} \cdot \eta \nabla^2 \mathbf{v}. \quad (2.23)$$

The gravitational term can be expressed as follows using Eqn. (2.11) and the fact that $\partial\Phi/\partial t = 0$.

$$\mathbf{v} \cdot \rho \nabla \Phi = \nabla \cdot (\rho \Phi \mathbf{v}) + \frac{\partial}{\partial t} (\rho \Phi). \quad (2.24)$$

Eqn. (2.24) gives the flux of the gravitational potential energy and the rate of change of gravitational potential energy in time. The Lorentz force term can be expressed as follows using Eqn. (2.9):

$$\mathbf{v} \cdot (\mathbf{j} \times \mathbf{B}) = -\mathbf{j} \cdot (\mathbf{v} \times \mathbf{B}) = -\frac{j^2}{\sigma} + \mathbf{j} \cdot \mathbf{E} . \quad (2.25)$$

Eqn. (2.25) is rearranged using Eqn. (2.6):

$$\mathbf{v} \cdot (\mathbf{j} \times \mathbf{B}) = -\frac{j^2}{\sigma} - \nabla \cdot \left(\frac{\mathbf{E} \times \mathbf{B}}{\mu} \right) - \frac{\partial}{\partial t} \left(\frac{B^2}{2\mu} \right) . \quad (2.26)$$

The pressure gradient term gives

$$-\mathbf{v} \cdot \nabla p = -\nabla \cdot (p\mathbf{v}) + p\nabla \cdot \mathbf{v} . \quad (2.27)$$

Eqn. (2.27) can also be expressed as follows using Eqn. (2.21):

$$p\nabla \cdot \mathbf{v} = -\frac{\partial}{\partial t} \left(\frac{p}{\gamma - 1} \right) - \nabla \cdot \left(\frac{p}{\gamma - 1} \mathbf{v} \right) - \mathbf{D} . \quad (2.28)$$

Substituting the foregoing relations, the full energy equation can be expressed as

$$\frac{\partial}{\partial t} \left[\frac{1}{2} \rho v^2 + \rho \Phi + \frac{p}{\gamma - 1} + \frac{B^2}{2\mu} \right] + \nabla \cdot \left\{ \left[\frac{1}{2} \rho v^2 + \rho \Phi + \gamma \frac{p}{\gamma - 1} \right] \mathbf{v} + \frac{\mathbf{E} \times \mathbf{B}}{\mu} \right\} = -\frac{j^2}{\sigma} - \mathbf{D} . \quad (2.29)$$

2.2.2 Proton beam induced energy deposition and equation of state

Due to the sudden energy deposition by proton beam, it is worthy to consider the components of added energy and the state of energy from compressible density variation as well as ionization to the right hand side of full energy equation Eqn. (2.29). The instantaneous beam energy deposition is

$$E_{beam}(r) = E_{beam}(r) \cdot \delta(t - t_{beam}), \quad (2.30)$$

where

$$E_{beam}(r) = E_o \exp\left[-\frac{r}{a}\right] \quad (2.31)$$

and

$$E_o = \frac{E_{beam}}{\pi r_{beam}^2}. \quad (2.32)$$

$E_{beam}(r)$ is radial energy density distribution of the beam and the proton beam energy is assumed to be deposited as a δ function at time $t = t_{beam}$. E_{beam} is the peak energy deposition corresponding to the beam spot radius r_b . The equation of state (EOS) is considered as the sum of compression, ion thermal, and electron thermal terms. The EOS can be expressed for simplification. The compressible pressure P_c and energy E_c are

$$P_c = P_{co} \left[\left(\frac{\rho}{\rho_o} \right)^\gamma - 1 \right], \quad (2.33)$$

915

916

$$E_c = E_{co}[(\frac{\rho}{\rho_o})^{\gamma-1} - 1]\frac{\rho}{\rho_o} + P_{co}(1 - \frac{\rho}{\rho_o}), \quad (2.34)$$

917

where

918

919

$$P_{co} = \frac{\rho c^2}{\gamma} \quad , \quad E_{co} = \frac{P_{co}}{\gamma - 1}. \quad (2.35)$$

920

Ion and electron thermal pressure and energy are

921

922

$$E_I = 3nk(T - T_o) \quad , \quad P_I = G_I E_I \quad , \quad (2.36)$$

923

924

$$E_e = \frac{1}{2}\beta(T - T_o)^2 \quad , \quad \beta = \beta_o(\frac{\rho_o}{\rho})^{2/3} \quad , \quad P_e = G_e E_e, \quad (2.37)$$

925

where $n = \frac{\rho}{M}$ and k is Boltzmann's constant. Thus, the total energy and

926

pressure are

927

928

$$E = E_c + E_I + E_e \quad , \quad P = P_c + P_I + P_e \quad , \quad (2.38)$$

929

where subscripts c, I, and e correspond to compression, ion thermal, and

930

electron thermal components, respectively. G_I and G_e are the Gruneisen coef-

931

ficients for the ion and electron. c is the speed of sound in the material. Initial

932

mercury pressure P is 0 at $T = T_o = T_{melting}$ and normal density $\rho = \rho_o$.

933

At higher temperatures, the mercury can be ionized and the resulting energy

934

and pressure by free-electron component is added to the EOS. Accordingly,

935

the solid state partition of the electron thermal energy and pressure decreases

936

$(1 - f_z)$ times, where f_z is the ionization fraction.

2.2.3 Magnetic damping with joule dissipation

It is known that a static magnetic field can suppress motion of an electrically conducting liquid. If a conducting liquid moves through an imposed static magnetic field, electric currents are generated. These, in turn, lead to ohmic heating such as Joule dissipation. As the thermal energy of the fluid rises, there is a corresponding drop in its kinetic energy, and so the fluid decelerates. This is to suppress the motion of liquid jets. In many applications, it is believed that the imposition of a static magnetic field is used as one means of suppressing unwanted motion. Considering the uniform perpendicularly imposed magnetic field to the flow direction for simplicity, the damping effect of Lorentz force can be quantified. If the magnetic field is uniform, the Faraday' law requires that $\nabla \times \mathbf{E} = 0$. Using Ohm's law and the fact that the current density is solenoidal, the current relationship is given by

$$\nabla \cdot \mathbf{J} = 0 \quad , \quad \nabla \times \mathbf{J} = \sigma \mathbf{B} \cdot \nabla \mathbf{v} . \quad (2.39)$$

Thus, \mathbf{J} is zero if \mathbf{v} is independent of the magnetic field direction. By doing cross product of \mathbf{J} and \mathbf{B} and using the vector identity, Lorentz force per unit mass is given by

$$\mathbf{F} = -\frac{\mathbf{v}}{\tau} + \frac{\sigma(\mathbf{B} \times \nabla \phi_E)}{\rho} , \quad (2.40)$$

where $\tau = \rho/\sigma B^2$ is Joule damping term and ϕ_E is electrical potential, which is given by the divergence of Ohm's law: $\phi_E = \nabla^{-2}(B \cdot \omega)$. The Lorentz

force then simplifies to $-\mathbf{v}/\tau$ when the magnetic field and the vorticity field are mutually perpendicular. Thus, the perpendicular \mathbf{v} to magnetic field declines on a time scale of τ , which clearly explains the mechanism of magnetic damping. The ratio of the damping time τ to the characteristic time L/v gives the interaction parameter $N = \sigma B^2 L / \rho v$, which is also used for the indication of the ratio of the magnetic and inertial forces.

To investigate the role of Joule dissipation, consider the fully derived energy equation in inviscid flow.

$$\frac{dE}{dt} = -\frac{1}{\sigma\rho} \int \mathbf{J}^2 dV = -\mathbf{D} , \quad (2.41)$$

where \mathbf{D} is joule dissipation and E is global kinetic energy.

\mathbf{J}^2 from Eqn. (2.39) was estimated (Davidson, 1999) and is given.

$$\frac{dE}{dt} \sim -\left(\frac{L_{min}}{L_{\parallel}}\right)^2 \frac{E}{\tau} , \quad (2.42)$$

from which

$$E \sim E_o \exp \left(-\tau^{-1} \int_0^t (L_{min}/L_{\parallel})^2 dt \right) , \quad (2.43)$$

where L_{\parallel} is the characteristic length for the flow, parallel to the magnetic field. Fig. 2.3 (a) shows the decay of energy depending on the Joule damping term with various magnetic field. The energy is dissipated as a result of energy decay by Joule dissipation. So, the time constant required for energy dissipation is getting smaller as the magnetic field strength increases. As a result, the magnetic field affect to the integration of energy, which is shown in

Fig. 2.3 (b). It indicates that the flow decays on a time scale of τ provided that L_{min} and L_{\parallel} are of the same order. However, the Lorentz force can not create or destroy linear (angular) momentum despite the Joule dissipation. This indicates that the flow can not be decayed on a time scale of τ and the Eqn. (2.42) and (2.43) infer that L_{min}/L_{\parallel} must increase with time. Therefore, it is expected that these flow will experience anisotropy, with L_{\parallel} increasing as the flow evolves.

2.3 Vorticity Equations in MHD flow

The possibility of using an electromagnetic field for vortices control in conducting fluids needs to be investigated. Electromagnetic force can influence the stability of a flow, thus prevents its transition to turbulence by suppressing disturbances or changing mean velocity profiles. A significant drag reduction is possible when the surface boundary condition is modified to suppress the vortices. Transverse magnetic field does not reduce drag because the magnetic field increases the skin friction drag by directly altering the mean flow, so called Hartmann flow, even though turbulent fluctuations are significantly reduced. The longitudinal magnetic field does not directly interact with the mean flow although it can reduce turbulent fluctuations. Thus it is possible that the longitudinal magnetic field can result in drag reduction.

1000 2.3.1 Governing equations for vorticity

1001 It is useful to transform the governing equations in terms of vorticity trans-
 1002 port. The equation for the vorticity ω of an incompressible conducting fluid
 1003 in MHD is

1004

$$\begin{aligned} & \frac{\partial \omega}{\partial t} + (\mathbf{v} \cdot \nabla) \omega - (\omega \cdot \nabla) \mathbf{v} \\ & = \nu \nabla^2 \omega + \frac{1}{\rho} \nabla \times (\mathbf{j} \times \mathbf{B}) \\ & = \nu \nabla^2 \omega + \frac{1}{\rho} \{(\mathbf{B} \cdot \nabla) \mathbf{j} - (\mathbf{j} \cdot \nabla) \mathbf{B}\} . \end{aligned} \quad (2.44)$$

1005

1006 The term $(\omega \cdot \nabla) \mathbf{v}$ in Eqn. (2.44) expresses the effect of stretching and
 1007 turning vorticity lines. From the Faraday's law and $\partial \mathbf{B} / \partial t = 0$, the electric
 1008 field in terms of an electric potential, ϕ_E , is

1009

$$1010 \quad \mathbf{E} = -\nabla \phi_E . \quad (2.45)$$

1011 From the Ohm's law, Kirchhoff's law, and Eqn. (2.45), the electromagnetic
 1012 equation can be simplified as Eqn. (2.47) using nondimensionalized Ohm's law
 1013 Eqn. (2.46).

1014

$$1015 \quad \mathbf{j} = \text{Re}_m (-\nabla \phi_E + \mathbf{v} \times \mathbf{B}) . \quad (2.46)$$

1016

$$1017 \quad \nabla^2 \phi_E = \nabla \cdot (\mathbf{v} \times \mathbf{B}) . \quad (2.47)$$

1018 The important parameter in vortices dynamics is the Stuart number N
 1019 ($= Re_m Al = \sigma \mathbf{B}^2 L / \rho v$), which is the ratio of the electromagnetic force to the
 1020 inertial force. Therefore, one can fix the Reynolds number and change the
 1021 Stuart number to see the effect of magnetic field over the vortices strength.
 1022 The Hartmann numbers, $Ha = \sqrt{ReN}$, can be determined correspondingly.
 1023 The Stuart number gives the ratio of Ha to Re . Thus, the Stuart number will
 1024 indicate the stabilizing effect of magnetic field to the unique characteristic of
 1025 transition to turbulence.

1026 **2.3.2 Vorticity suppression**

1027 The vorticity is suppressed by the magnetic field, transverse to the vortic-
 1028 ity. The result is altered if the conductivity σ is nonuniform and varies with
 1029 coordinates, in which case vorticity will be created. When a conducting liquid
 1030 flows along a pipe with an axial magnetic field, there will be no magnetic effect
 1031 if the motion is laminar, though the vorticity is perpendicular to the magnetic
 1032 field, but if the flow is turbulent, adding the field damps the turbulence and
 1033 reduces the Reynolds stresses and the frictional drag. Adding the field also
 1034 raises the critical Reynolds number for instability of flow (Shercliff, 1965).

1035 **2.3.2.1 *spanwise magnetic field effect to vorticity suppression***

1036 For a spanwise magnetic field, $\mathbf{B} = (0, 0, B_z)$, the corresponding Lorentz
 1037 force, $\mathbf{f} = (f_x, f_y, f_z)$ can be represented as follows.

1038

$$\begin{aligned} f_x &= N\left(-\frac{\partial\phi_E}{\partial y}B_z - B_z^2v_x\right) , \\ f_y &= N\left(\frac{\partial\phi_E}{\partial x}B_z - B_z^2v_y\right) , \\ f_z &= 0 . \end{aligned} \tag{2.48}$$

1039

1040 Introducing the stream function ψ ,

1041

$$\frac{\partial^2\psi}{\partial x^2} + \frac{\partial^2\psi}{\partial y^2} = -\omega_z , \tag{2.49}$$

1042

1043 where the spanwise vortex $\omega_z = \partial v_y/\partial x - \partial v_x/\partial y$. The Ohm's law Eqn. (2.47)

1044 yields

1045

$$\frac{\partial^2\phi_E}{\partial x^2} + \frac{\partial^2\phi_E}{\partial y^2} = \omega_z , \tag{2.50}$$

1046

1047 where unity quantity of B_z is assumed.

1048 From Eqn. (2.47) and (2.50), $\phi_E = \psi + \text{const.}$ Correspondingly this
 1049 relation yields $\mathbf{f} = 0$. Therefore, the spanwise vortex flow is not affected by
 1050 the spanwise magnetic field (Lim, 1998). However, it can reduce turbulent
 1051 fluctuations without directly interacting with the mean flow.

2.3.2.2 *longitudinal and transverse magnetic field effect to vorticity suppression*

For longitudinal and transverse magnetic field $\mathbf{B} = (B_x, B_y, 0)$ in a two dimensional flow, Eqn. (2.47) yields $\nabla^2 \phi_E^2 = 0$ assuming that there is no velocity (v_z) onto the normal to the flow direction. The corresponding forces can be represented as follows:

$$\begin{aligned} f_x &= N(B_y \frac{\partial \phi_E}{\partial z} - B_y^2 v_x + B_x B_y v_y) , \\ f_y &= N(-B_x \frac{\partial \phi_E}{\partial z} - B_x^2 v_y + B_x B_y v_x) , \\ f_z &= N(-B_y \frac{\partial \phi_E}{\partial x} + B_x \frac{\partial \phi_E}{\partial y} - B_x^2 v_z - B_y^2 v_z) . \end{aligned} \quad (2.51)$$

The effect of the longitudinal and transverse magnetic field on the strength of spanwise vortices can be shown from the vorticity equation where additional vortices term $\omega_{Lorentz} = \nabla \times \mathbf{f}$ caused by the Lorentz force has been added.

$$\begin{aligned} \frac{\partial \omega_z}{\partial t} + (\mathbf{v} \cdot \nabla) \omega_z &= (\omega_z \cdot \nabla) \mathbf{v} + \frac{1}{\text{Re}} \nabla^2 \omega_z + N \left(-B_x \frac{\partial^2 \phi_E}{\partial x \partial z} \right. \\ &\quad \left. - B_y \frac{\partial^2 \phi_E}{\partial y \partial z} + B_x B_y \left(\frac{\partial v_x}{\partial x} - \frac{\partial v_y}{\partial y} \right) - B_x^2 \frac{\partial v_y}{\partial x} + B_y^2 \frac{\partial v_x}{\partial y} \right) . \end{aligned} \quad (2.52)$$

If we consider the longitudinal magnetic field $\mathbf{B} = (B_x, 0, 0)$ and the transverse magnetic field $\mathbf{B} = (0, B_y, 0)$ independently, the corresponding force can

1067 be shown in Eqn. (2.53), Eqn. (2.54) respectively.

1068

$$\begin{aligned}
 f_x &= 0 , \\
 f_y &= N(-B_x \frac{\partial \phi_E}{\partial z} - B_x^2 v_y) , \\
 f_z &= N(B_x \frac{\partial \phi_E}{\partial y} - B_x^2 v_z) .
 \end{aligned} \tag{2.53}$$

1069

1070

$$\begin{aligned}
 f_x &= N(B_y \frac{\partial \phi_E}{\partial z} - B_y^2 v_y) , \\
 f_y &= 0 , \\
 f_z &= N(-B_y \frac{\partial \phi_E}{\partial x} - B_y^2 v_z) .
 \end{aligned} \tag{2.54}$$

1071

1072 Eqns. (2.53) and (2.54) clearly show that the Lorentz force retards the
 1073 local velocity. The vorticity equation is shown as Eqn. (2.55), Eqn. (2.56).

1074

$$\frac{\partial \omega_z}{\partial t} + (\mathbf{v} \cdot \nabla) \omega_z = (\omega_z \cdot \nabla) \mathbf{v} + \frac{1}{\text{Re}} \nabla^2 \omega_z + N(-B_x \frac{\partial^2 \phi_E}{\partial x \partial z} - B_x^2 \frac{\partial v_y}{\partial x}) . \tag{2.55}$$

1076

$$\frac{\partial \omega_z}{\partial t} + (\mathbf{v} \cdot \nabla) \omega_z = (\omega_z \cdot \nabla) \mathbf{v} + \frac{1}{\text{Re}} \nabla^2 \omega_z + N(-B_y \frac{\partial^2 \phi_E}{\partial y \partial z} + B_y^2 \frac{\partial v_x}{\partial y}) . \tag{2.56}$$

1077

1078 The Lorentz force is negatively correlated with the spanwise vorticity.
 1079 Therefore, the Lorentz force induced by the longitudinal and transverse mag-
 1080 netic field reduces the strength of the spanwise vorticity effectively.

2.4 One Dimensional Pipe Flow in Transverse Magnetic Field

In one-dimensional problem, the governing equations and the boundary conditions are assumed that there is only one component of the velocity, v_z , and only one component of the induced magnetic field, \mathbf{B}_z , along with the applied field \mathbf{B}_o , so that the total velocity and magnetic fields are given by

$$\begin{aligned} v_r = v_\theta = 0, \quad v_z = v_z(r, \theta), \quad B_r = B_o \cos \theta, \\ B_\theta = -B_o \sin \theta, \quad B_z = B_z(r, \theta). \end{aligned} \quad (2.57)$$

Substituting these expressions into Eqn. (2.13) using cylindrical coordinates, we obtain

$$p(r, \theta, z) = -(1/2\mu)B_z^2 + O_1 z + O_2, \quad \partial p / \partial z = O_1 = \text{constant}, \quad (2.58)$$

$$O_1 = \eta \left[\frac{\partial^2 v_z}{\partial r^2} + \left(\frac{1}{r}\right) \frac{\partial v_z}{\partial r} + \left(\frac{1}{r^2}\right) \frac{\partial^2 v_z}{\partial \theta^2} \right] + \left(\frac{1}{r}\right) B_\theta \frac{\partial B_z}{\partial \theta} + B_r \frac{\partial B_z}{\partial r}, \quad (2.59)$$

where O_2 is a constant.

Eqn. (2.5), Eqn. (2.11), Equation (2.57) are identically satisfied and Eqns. (2.16) become

$$\frac{1}{\mu\sigma} \left[\frac{\partial}{\partial r} \left(r \frac{\partial B_z}{\partial r} \right) + \left(\frac{1}{r}\right) \frac{\partial^2 B_z}{\partial \theta^2} \right] + \left[B_r \frac{\partial}{\partial r} (r v_z) + \frac{\partial}{\partial \theta} (v_z B_\theta) \right] = 0. \quad (2.60)$$

2.4.1 Non-dimensional form of the governing equations using cylindrical coordinates

The modified non-dimensional form of Navier-Stokes equations and the magnetic induction equations using cylindrical coordinates is expressed as follows:

$$\nabla^2 v_z - \left(\frac{\text{Ha}^2}{\text{Re}_m}\right) \left[\left(\frac{\sin \theta}{r}\right) \frac{\partial B_z}{\partial \theta} - \cos \theta \frac{\partial B_z}{\partial r} \right] = O , \quad (2.61)$$

$$\nabla^2 B_z - \text{Re}_m \left[\left(\frac{\sin \theta}{r}\right) \frac{\partial v_z}{\partial \theta} - \cos \theta \frac{\partial v_z}{\partial r} \right] = 0 , \quad (2.62)$$

where $\nabla^2 \equiv \frac{\partial^2}{\partial r^2} + \left(\frac{1}{r}\right) \frac{\partial}{\partial r} + \left(\frac{1}{r^2}\right) \frac{\partial^2}{\partial \theta^2}$, $\text{Ha} = B_o a (\sigma/\eta)^{1/2}$, $\text{Re}_m = \sigma \mu v a$, and $O = O_1 a^2 / \eta$.

Eqn. (2.61) and (2.62) apply to any general incompressible, steady magnetohydrodynamic duct flow. The restriction as to geometry and the conditions at the wall enters through the boundary conditions.

2.4.1.1 boundary conditions in pipe flow

No fluid slip at the wall is given by

$$v_z(a, \theta) = 0 , \quad (2.63)$$

where a is the radius of the cylinder, while the assumption of non-conducting walls implies that (Shercliff, 1953)

$$B_z(a, \theta) = 0 . \quad (2.64)$$

1121 We can also obtain the current density \mathbf{j} and the electric field \mathbf{E} from
 1122 Ampere's and Ohm's laws:

1123

$$1124 \quad j_r = \left(\frac{1}{r}\right) \frac{\partial B_z}{\partial \theta}, \quad j_\theta = -\frac{\partial B_z}{\partial r}, \quad j_z = 0, \quad (2.65)$$

1125

$$1126 \quad E_r = (1/\sigma)j_r + v_z B_\theta, \quad E_\theta = (1/\sigma)j_\theta - v_z B_r, \quad j_z = 0. \quad (2.66)$$

1127 2.4.2 Exact solutions of pipe flow in magnetic field

1128 Shercliff (1953) uncoupled the Eqn. (2.61) and (2.62) by a linear transfor-
 1129 mation. The boundary conditions could also be reduced by the transformation.
 1130 The velocity and magnetic field distribution are obtained from the uncoupled
 1131 equations (Gold, 1962):

1132

$$1133 \quad v_z = \frac{-Kv}{4\alpha} \left[e^{-\alpha \frac{r}{a} \cos \theta} \sum_{n=0}^{\infty} \epsilon_n \frac{I'_n(\alpha)}{I_n(\alpha)} I_n\left(\alpha \frac{r}{a}\right) \cos n\theta \right. \\ \left. + e^{\alpha \frac{r}{a} \cos \theta} \sum_{n=0}^{\infty} (-1)^n \epsilon_n \frac{I'_n(\alpha)}{I_n(\alpha)} I_n\left(\alpha \frac{r}{a}\right) \cos n\theta \right], \quad (2.67)$$

1134

$$1135 \quad B_z = \frac{-\text{Re}_m K B_o}{8\alpha^2} \left[e^{-\alpha \frac{r}{a} \cos \theta} \sum_{n=0}^{\infty} \epsilon_n \frac{I'_n(\alpha)}{I_n(\alpha)} I_n\left(\alpha \frac{r}{a}\right) \cos n\theta \right. \\ \left. - e^{\alpha \frac{r}{a} \cos \theta} \sum_{n=0}^{\infty} (-1)^n \epsilon_n \frac{I'_n(\alpha)}{I_n(\alpha)} I_n\left(\alpha \frac{r}{a}\right) \cos n\theta - 2 \frac{r}{a} \cos \theta \right], \quad (2.68)$$

1136 where $\alpha = \frac{1}{2}\text{Ha}$, I_n is the modified Bessel function of order n , $\epsilon_n = 1$ for
1137 $n=0$, and $\epsilon_n = 2$ for $n>0$. Equation (2.65) and (2.66) are used to obtain the
1138 electric field \mathbf{E} :

1139

$$1140 \quad E_r = \left(\frac{a\mu v}{\text{Re}_m r} \right) \frac{\partial B_z}{\partial \theta} - v_z B_o \sin \theta . \quad (2.69)$$

1141 I_n identities are given by

1142

$$1143 \quad I_n(\alpha) = I_{-n}(\alpha) , I_n(-\alpha) = (-1)^n I_n(\alpha) , I_n(\alpha)' = \frac{1}{2}(I_{n+1}(\alpha) + I_{n-1}(\alpha)) , \quad (2.70)$$

1144 and

1145

$$1146 \quad I_n(x) = \frac{1}{\pi} \int_0^\pi e^{x \cos \theta} \cos n\theta d\theta - \frac{1}{\pi} \int_0^\infty e^{-x \cosh u - nu} du . \quad (2.71)$$

1147 **2.5 Stability of Conducting Flow in a Mag-** 1148 **netic Field**

1149 The problem of the flow of liquid metal jets in magnetic field arises in
1150 certain applications of magnetohydrodynamics. The stability of the flow of a
1151 conducting film in the presence of two components of the magnetic field (in
1152 the direction of the flow and normal to the surface) was investigated by B.A.
1153 Kolovadin (1965) using the approximation of small Reynolds numbers: The
1154 ratio of transverse magnetic field to longitudinal magnetic field changes due
1155 to the finite inclination of jet axis to the magnetic field axis. The magnitude
1156 of the inclination angle affects the stability of the liquid jets.

1157 Theses instabilities can change the jet shape into one that makes the jet
 1158 a significantly less efficient target for particle production. As described in
 1159 Chapter 1, the particle production depends on several parameters such as jet
 1160 size and jet angle. Thus, the unstable behaviors of jet in a magnetic field yields
 1161 less or unexpected production of particle. In addition, the larger inclination
 1162 of jet axis makes the jet size become bigger than the nominal jet size due to
 1163 the increased magnetic field. Thus, the mercury jet interacting with beam
 1164 will have different energy deposition leading to different particle production.
 1165 Therefore, the stable motion of mercury jet is required for stable particle
 1166 production and it then needs to be investigated.

1167 **2.5.1 Propagation of waves at an interface separating** 1168 **two flows in magnetic field**

1169 To investigate the surface wave motion of free jet in magnetic field, we
 1170 followed the procedure of a direct extension of Currie (1993) to the case with
 1171 a magnetic field. The detailed procedures and derivations are described in
 1172 Appendix C.2.

1173 We consider the (x, y, z) coordinate system in Fig. 2.1. The magnetic field
 1174 along and normal to the Hg jet axis can be derived from the solenoid mag-
 1175 netic field map. From trigonometry, the longitudinal magnetic field along the
 1176 jet axis and the transverse magnetic field normal to the jet axis are given by
 1177 $B_x = B_X \cos\theta - B_Y \sin\theta$, $B_y = -B_X \sin\theta + B_Y \cos\theta$, respectively, where B_X is
 1178 the axial component of the magnetic field and B_Y is the radial component.

To investigate the effect of sinusoidal wave perturbation at the interface, the equation of the interface is chosen to be $\xi(x, t) = \epsilon e^{i(2\pi/\lambda)(x-ct)} + a$, where ϵ is the wave amplitude, λ is the wavelength, and c is the wave propagation speed. Small perturbations from the basic flow in the form $v_{xi} = U_i + v'_{xi}$, $v_{yi} = v'_{yi}$, $p_i = P_i + p'_i$, $v'_{xi} = \frac{\partial \phi_i}{\partial x}$, $v'_{yi} = \frac{\partial \phi_i}{\partial y}$ are assumed, where ϕ_i is the velocity potential for the perturbation to the uniform wavy flows at the interface. Substituting the perturbed expressions into the equations of motion, neglecting second order terms in the perturbed quantities, and making use of the fact that U, P satisfy the flow equations and the current density in Lorentz force term can be represented using Ohm's law, we have the linearized equations governing the motion of disturbance, which yields the Rayleigh's stability equation of conducting flow in a magnetic field by replacing the perturbed quantities with the equation of motion. The Rayleigh's equation must be solved subject to the boundary conditions. The dynamic boundary condition at interface yields the effect of a magnetic field and the conditions of interfacing flows such as flow velocity and density to the wave velocity and wave number. Without a magnetic field, the quantity c has an imaginary part that results in the interfacial wave growing exponentially with time. Thus, the interface at the shear layer is unstable. However, the magnetic effects to the wave propagation velocity to reduce the wave amplitude and correspondingly the wavelength increases due to the magnetic field.

Several investigations have suggested that magnetic field suppresses turbulent fluctuations in conducting liquid by stabilizing the flow (Shercliff 1956,

Gold 1962, Kozyrev 1981, Bernshtam 1982) and the stabilizing action of the longitudinal component of a magnetic field is considerably weaker than that of the transverse component, where stabilization is judged by an increase in the characteristic wavelength of the flow and Re_{cr} .

2.5.2 Magnetic pressure and tension

Once the jet surface is stabilized and flattened by a magnetic field, the magnetic pressure caused by the Lorentz force is contributing to the hydrodynamic pressure. It gives rise to deflect the jet in directions perpendicular to the magnetic field. Considering that the continuity condition has to be satisfied, the Lorentz force makes the jet shape change elliptically. Therefore, the contributions of each magnetic pressure components to the isotropic hydrodynamic pressure needs to be investigated.

Lorentz force is $\mathbf{F} = \mathbf{J} \times \mathbf{B} = \frac{1}{\mu}(\nabla \times \mathbf{B}) \times \mathbf{B} = \frac{1}{\mu}(\mathbf{B} \cdot \nabla)\mathbf{B} - \frac{1}{2\mu}\nabla B^2$. Suppose the Maxwell stress tensor $T_{ij} = \frac{1}{\mu}(B_{ij} - \frac{1}{2}\delta_{ij}B^2)$, which represents the deviatoric stress tensor of magnetic field. The divergence of the Maxwell stress tensor is represented as follows, which gives the same expression with Lorenz force.

$$\begin{aligned} \nabla \cdot T &= \frac{1}{\mu} \begin{bmatrix} \frac{\partial}{\partial x} & \frac{\partial}{\partial y} & \frac{\partial}{\partial z} \end{bmatrix} \begin{bmatrix} \frac{B_x^2 - B_y^2 - B_z^2}{2} & B_x B_y & B_x B_z \\ B_y B_x & \frac{B_y^2 - B_x^2 - B_z^2}{2} & B_y B_z \\ B_z B_x & B_z B_y & \frac{B_z^2 - B_x^2 - B_y^2}{2} \end{bmatrix} \\ &= \frac{1}{\mu}((\mathbf{B} \cdot \nabla)\mathbf{B} + (\nabla \cdot \mathbf{B})\mathbf{B} - \nabla(\frac{B^2}{2})) \end{aligned} \quad (2.72)$$

1221 T has units of pressure. The shear is given by the off-diagonal elements
 1222 of T and the diagonal elements of T correspond to the pressure acting on a
 1223 differential area element. Total force on a volume is represented as follow.

1224

$$1225 \quad F = \int \int \int_V \nabla \cdot T dV = \oint_S T \cdot dS \quad (2.73)$$

1226 The conservation of momentum in inviscid flow is represented as follow.

1227

$$\begin{aligned} & \frac{d}{dt} \int \int \int_V \rho \mathbf{v} dV + \oint_S \rho \mathbf{v} (\mathbf{v} \cdot \hat{n}) dS \\ 1228 \quad & = - \oint_S p \hat{n} dS + \int \int \int_V \rho \mathbf{g} dV + \int \int \int_V \nabla \cdot T dV \end{aligned} \quad (2.74)$$

1229

$$1230 \quad \frac{d\mathbf{v}}{dt} + (\mathbf{v} \cdot \nabla) \mathbf{v} = -\frac{1}{\rho} \nabla p + \mathbf{g} + \frac{1}{\rho} \nabla \cdot T = -\frac{1}{\rho} \nabla \mathbb{P} + \mathbf{g} \quad (2.75)$$

1231 ,where

$$1232 \quad \mathbb{P} = \begin{bmatrix} p - \frac{B_x^2 - B_y^2 - B_z^2}{2\mu} & -B_x B_y & -B_x B_z \\ -B_y B_x & p - \frac{B_y^2 - B_x^2 - B_z^2}{2\mu} & -B_y B_z \\ -B_z B_x & -B_z B_y & p - \frac{B_z^2 - B_x^2 - B_y^2}{2\mu} \end{bmatrix} \quad (2.76)$$

1233 Note that the magnetic field increases the pressure by an amount $\mathbf{B}^2/2\mu$,
 1234 in directions perpendicular to the magnetic field and decreases the pressure
 1235 by the same amount in the parallel direction. Thus, the magnetic field gives
 1236 rise to a magnetic pressure $\mathbf{B}^2/2\mu$, acting perpendicular to field lines, and a
 1237 magnetic tension $\mathbf{B}^2/2\mu$, acting along field lines.

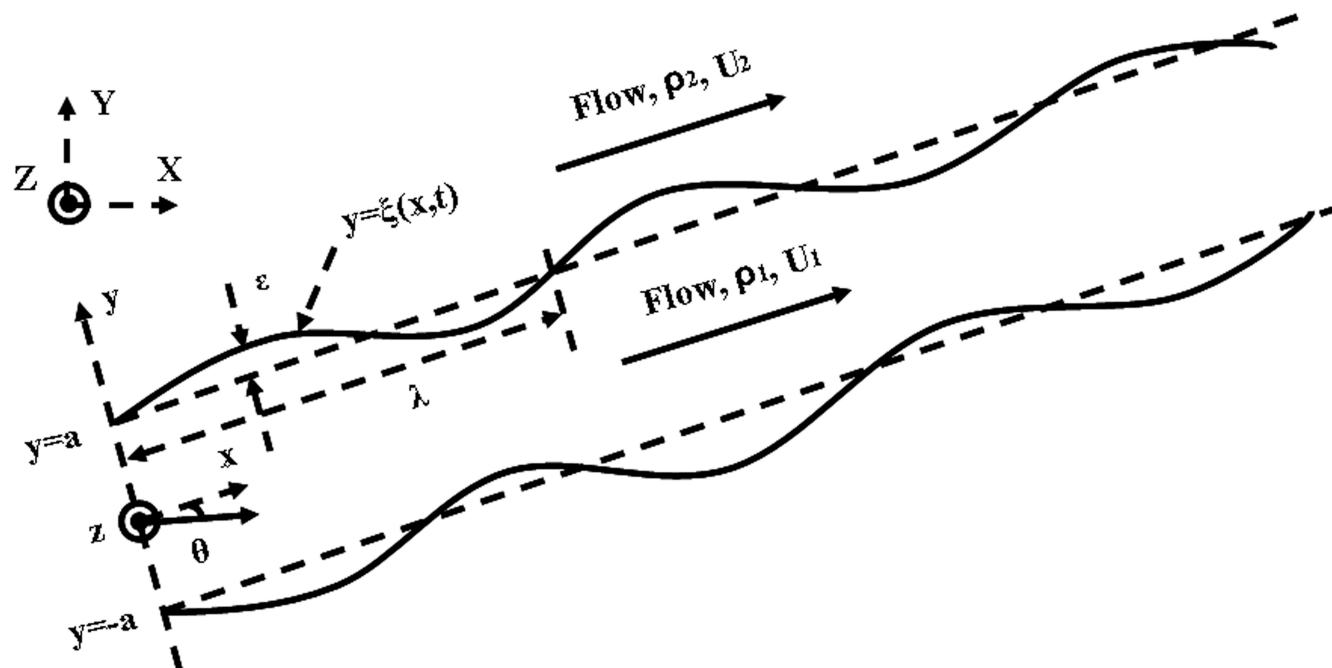


Figure 2.1: Wave-shaped interface separating two different fluids traveling at different average speeds.

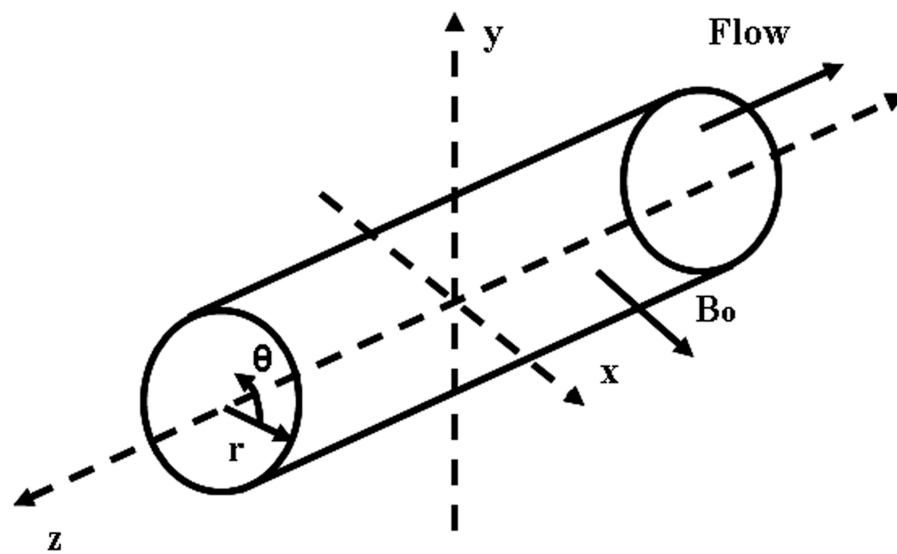


Figure 2.2: Axes and electrodes of circular duct.

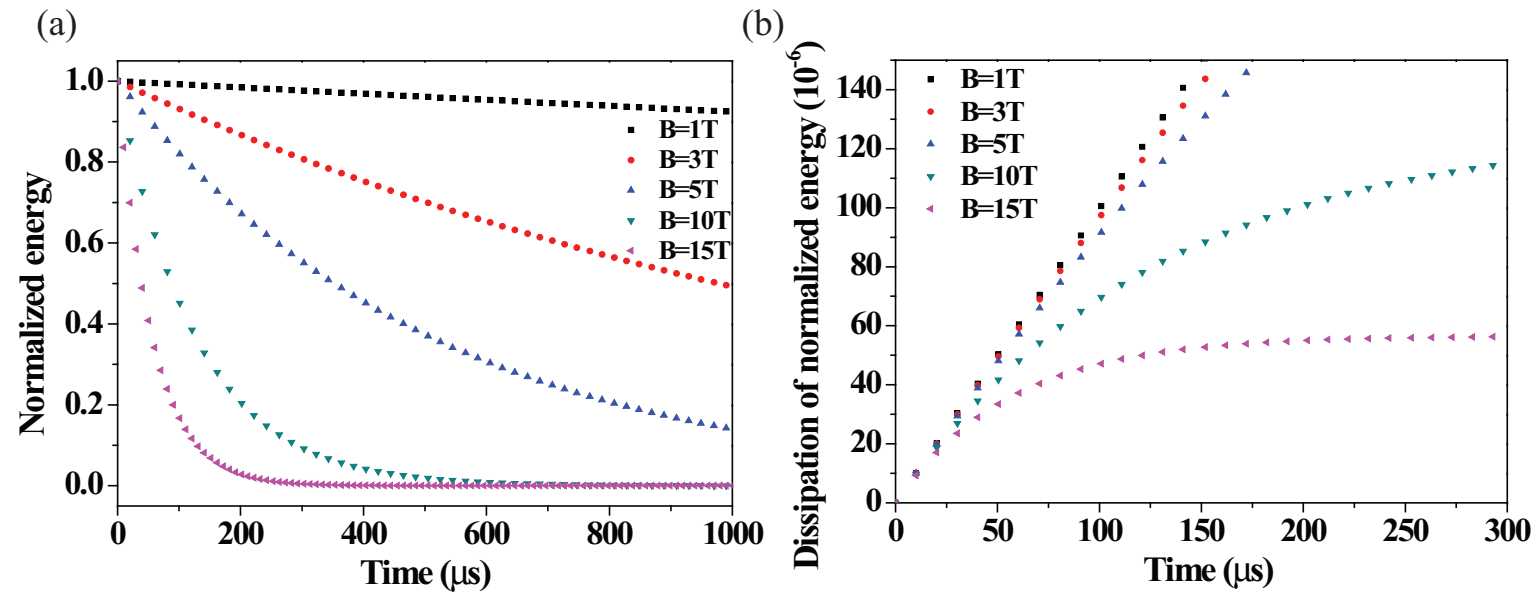


Figure 2.3: Energy decay in magnetic field. a.) Normalized energy decay. b.) Dissipation of normalized energy.

Chapter 3

Experimental Method for Investigation of Magnetohydrodynamic Mercury Jet Flow

The optical method is considered to investigate MHD processes. Optical methods have considerable advantages over other measurement techniques: they do not introduce any perturbations into the medium being investigated, they possess high sensitivity and accuracy, their response is practically instantaneous, which enables them to be used to investigate turbulent flows and transition states, since they provide the possibility of visually following the phenomenon being investigated, and they enable one to obtain the physical characteristics for the whole space being investigated at the same instant of time. Unlike other probeless methods, optical methods possess high spatial resolution. All these features enable optical methods to be widely employed in MHD experiments and underlie the need to search for new ways of using modern optical methods which have not yet been employed.

Direct visualization techniques for hydrodynamic examination have often been employed to investigate the dynamics of MHD flows. In this method, one measures the time taken for the particles to traverse a given path. Because no quantitative results can be deduced from direct visualization methods and difficulties often arise when investigating thin boundary layers in liquids, attention has turned to the use of optical techniques for the investigations of fluid dynamics and MHD (Fedin, 1973).

It should be noted that visualization is usually employed for qualitative investigations, but this method can also be used to measure the average flow velocity and a change in the velocity profile. To do this one measures merely the time taken for the particles to traverse a given path or the path traversed in a given time.

3.1 Optical Diagnostics as a Principal Diagnostics of High Power Target Experiment

3.1.1 Working principle of shadowgraph for optical diagnostics

Optical measurements have many advantages over other techniques. The major one is the absence of an instrument probe that could influence the flow field. The light beam can also be considered as essentially inertialess, so that very rapid transient effects can be studied.

Shadowgraph is often employed in studying shock and flame phenomena,

in which very large density gradients are present. It integrates the quantity measured over the length of the light beam. For this reason they are well suited to measurements in two dimensional fields, where there is no index of refraction or density variation in the field along the light beam.

In a shadowgraph system the linear displacement of the perturbed light is measured. Consider the illumination at the exit of the test section. Figure 3.1 shows the displacement of a light beam for shadowgraph. If the illumination is uniform entering the test section, it should still be closely uniform there. The beam is deflected by an angle α , which is a function of y . The illumination within the region defined by Δy at this position is within the region defined by Δy_{sc} at the screen. If the initial intensity of light is I_T , then at screen,

$$I_o = \frac{\Delta y}{\Delta y_{sc}} I_T . \quad (3.1)$$

If Z_{sc} is the distance to the screen, then the contrast is

$$\frac{\Delta I}{I_T} = \frac{I_o - I_T}{I_T} = \frac{\Delta y}{\Delta y_{sc}} - 1 \simeq -z_{sc} \frac{\partial \alpha}{\partial y} , \quad (3.2)$$

$$\frac{\Delta I}{I_T} = -\frac{z_{sc}}{n_a} \int \frac{\partial^2 n}{\partial y^2} dz = -\frac{z_{sc}}{n_a} \int \frac{\partial^2 \rho}{\partial y^2} \cdot \frac{\partial n}{\partial \rho} dz , \quad (3.3)$$

where n is the index of refraction of a homogeneous transparent medium and $n_a \simeq 1$ for the ambient air.

For gas, Eqn. (3.4) could be substituted into Eqn. (3.3). Eqn. (3.3) is

integrated twice to determine the density distribution. (Goldstein, 1991)

$$\frac{\partial^2 n}{\partial y^2} = C \left[-\frac{\rho}{T} \frac{\partial^2 T}{\partial y^2} + \frac{2\rho}{T^2} \left(\frac{\partial T}{\partial y} \right)^2 \right], \quad (3.4)$$

where the constant C, called the Gladstone-Dale constant, is a function of the particular gas and T is temperature of medium on Kelvin scale.

Shadowgraph is used principally for qualitative descriptions of a density field. Because it yields information on the first and second derivatives of density, its application can be found in systems with steep gradients of density and temperature, such as flame fronts and shock waves.

Optical techniques are non-invasive and do not cause any perturbation of the subject being investigated. Furthermore, their sensitivity increases with photon intensity and the resolution of the subject can reach the diffraction-limited resolution. The optical response of fluid dynamics and MHD are practically instantaneous, enabling the optical technique to study details of turbulent flows and transition states. Coupled to a state-of-the art high-speed camera and the long interaction path length of a light beam with a field of view adjustable to arbitrary dimensions, the optical technique enables one to obtain the physical characteristics for the entire subject being investigated in a short period of time.

3.1.2 Development of optical diagnostic system

An optical diagnostic system is designed and constructed for imaging a free mercury jet interacting with a high intensity proton beam in a pulsed high-

field solenoid magnet. The optical imaging system employs a back-illuminated, laser shadow photography technique. Object illumination and image capture are transmitted through radiation-hard multi-mode optical fibers and flexible coherent imaging fibers. A retro-reflected illumination design allows the entire passive imaging system to fit inside the bore of the solenoid magnet. A sequence of synchronized short laser light pulses are used to freeze the transient events and the images are recorded by several high speed charge coupled devices.

3.1.2.1 *the optical imaging system and Viewports design*

Laser back-illuminated shadow photography technique is employed in experiment to capture the dynamics of the interaction of the proton beam with a moving free mercury jet. The design of the optical imaging system is based on a few essential criteria which are described below. The entire optical imaging head has to fit inside a small portion of a 1 meter long, 150 mm diameter bore magnet. Fig. 3.2(a), Fig. 3.2(b), and Fig. 3.2(c) show the conceptual back illuminated optics design, the installation of 4 Viewports on the primary containment vessel, and the schematic layout of optical components, respectively.

Note that all optics placed inside the interaction beam tunnel are required to be radiation-hard because of high radiation levels in the beam tunnel and the activation of the mercury after proton beam interactions. In our setup, all cameras, lasers, and all other associated electronics are placed in an adjacent beam tunnel controlled locally by several desktop computers. Remote control of the entire system is achieved through designated control desktops located

in the control room via MS Window XP remote desktop connections from the ethernet network (see Fig. 3.7).

A Viewport is located at the beam interaction center and two additional Viewports are located at ± 152.4 mm up/down stream locations. Viewport 4 is positioned at $+457.2$ mm and is designed to capture the residual dynamics of the proton interaction. Because of limited space inside the magnet bore, object illumination and image capture are transmitted through multi-mode optical fibers and coherent imaging fibers, respectively, all positioned on one side exterior to the primary containment vessel. Fig. 3.3 shows the fabricated and assembled optical head containing the integration of ball lens, imaging lens, illumination fiber, and imaging fiber.

The arrangement resembles a compact endoscope design but with a different illumination scheme. Illumination light pulses are coupled into a 15 meter long multi-mode fiber (ThorLabs BFL22-200). It has a numerical aperture of 0.22, 25° cone angle, with a core diameter of $200\text{ }\mu\text{m}$ that matches that of the fiber-coupled lasers. To provide a ~ 55 mm illumination area at the center of the primary containment vessel over a limited short working distance of < 100 mm, the illumination cone angle has to be opened up to a 43° full cone angle. This is achieved by placing a tiny ~ 0.5 mm diameter sapphire ball lens (Edmund Optics M46-117) at the tip of the illumination fiber and secured by a thin stainless steel plate. At the heart of the illumination arrangement is a 76 mm diameter Au-coated concave spherical retro-reflector that has a short radius of curvature of 124 mm (Rainbow Research Optics). When the much

diverged illumination fiber is placed at the radius of curvature and shined
 onto the optical axis of the reflector, a retro-reflected beam returns back to
 the illumination fiber providing the back-illumination scheme. Again, because
 of the tight environment inside the primary, a Au-coated 90° prism mirror
 turns the optical path from longitudinal to transverse onto the center of the
 primary. Two anti-reflection coated sapphire windows (Swiss Jewel Company)
 are mounted on the primary with airtight seals tested up to 1.4 bar pressure.
 The diameter and the thickness of the window is 100 mm and 6 mm respec-
 tively, sufficiently large enough for the observation of a 1 cm diameter jet and
 mechanically strong enough to withstand the momentum of a direct impact
 from mercury jet with a mean velocity of 20 m/s (Simos, 2005).
 Based on this optical arrangement, a mercury jet in front of the reflector nat-
 urally makes a shadow on the retro-reflected beam. The shadow is collected
 by a 1 mm diameter AR-coated cylindrical grin objective lens (GrinTech, GT-
 IFRL-100-inf-50-CC) which has an optical path length of 2.43 mm. The grin
 lens is coupled onto a coherent image fiber. This flexible coherent imaging fiber
 is the key optical element of the imaging system. It is a 10 meter long Sum-
 itomo IGN-08/30 fiber with 30,000 picture elements (pixels). Each individual
 fiber has a core diameter of $\sim 4 \mu\text{m}$ with a total fiber diameter of merely 0.96
 mm including coating. It has a bending radius of 40 mm, sufficiently small to
 allow curving and arching inside the primary containment vessel. All imaging
 fiber ends are hand polished in-house to optical finished quality to allow high
 quality images with maximum light intensity transmission. Fig. 3.4 shows

the final finished end of an imaging fiber after polishing with $0.3\ \mu\text{m}$ lapping film (ThorLabs, LFG03P). The surface quality and the flatness of the imaging fibers are inspected under a microscope. The imaging fibers are jacketed in-house with reinforced furcation tubing (ThorLab FT030-BK). One end of the imaging fiber is finished with an SMA 905 fiber-optics connector to facilitate coupling to a CCD camera. The other ends of the illumination and imaging fibers are positioned next to each other with $\sim 2\ \text{mm}$ separation inserted inside a specially fabricated plastic ferrule. The integrated optical head is shown in Fig. 3.3, where a red laser diode is used to illuminate the optical head. The integrated all-in-one ferrule (ball lens, illumination fiber, objective lens, and imaging fiber bundle) is placed at the radius of curvature as well as on the optical axis of the reflector so that it allows both the illumination and the imaging collection to work on one side of the primary. The liquid mercury target is enclosed in a stainless steel primary containment vessel which is placed in the primary beam tunnel (TT2A). A total of four optical imaging heads for each Viewport are mounted on the exterior of the primary, designated as channels 1 to 4. All fibers are routed through a $\sim 150\ \text{mm}$ diameter, 2 meter long concrete passage to an adjacent beam tunnel (TT2), where radiation is much reduced. All electronics control for the optical diagnostic as well as all other electronics control for the solenoid magnet operation and hydraulic power unit used to generate the mercury jet are also placed in the adjacent tunnel. The exit end of each imaging fiber is coupled to an SMA fiber adaptor (ThorLabs SM1SMA) mounted on an x-y translator (ThorLab LM1XY). Four

1413 40× infinitely corrected microscope objective (Newport M-40x) relay the ~
 1414 0.96 mm image outputs of each imaging fiber onto each corresponding CCD
 1415 with appropriate lens tubes to fully expand the images onto a typical 10 × 10
 1416 mm CCD array. A non-rotating adjustable lens tube zoom housing (ThorLabs
 1417 SM1ZM) provides fine and accurate adjustment of image focus on CCD.

1418 **3.1.2.2 *the consideration for focusing and tilting alignment of op-*** 1419 ***tics***

1420 A retro-reflective mirror captures the output beam of the laser diode and
 1421 focuses it through the field of view at the target onto the lens of the telescope.
 1422 The CCD camera views the target through the telescope. Tilting alignment by
 1423 using fine adjustments on the side of the retro-reflecting mirror can be made
 1424 and the field of view can be adjusted by moving the imaging lens forwards or
 1425 backwards. The system is designed to make 6 possible alignment adjustments.
 1426 After the retro-reflecting mirror is moved forward or backward, the field of
 1427 view can also be adjusted. The maximum field of view that we can obtain is
 1428 ~ 5.0 cm diagonally. The distance d from the objective lens to the imaging
 1429 lens is related to the field of view at the target. For target to be in focus, one
 1430 must obey the lens formula,

$$1431 \quad \frac{1}{f} = \frac{1}{c} + \frac{1}{d} , \quad (3.5)$$

1433 where c is the distance from the target to the objective lens and d is the
 1434 distance from the objective lens to the camera.

3.1.2.3 *high speed cameras and light sources*

Table 3.1 gives the specifications of high speed cameras in terms of some selected attributes. Two FastVision cameras with CCD size of 15.4×12.3 mm run with a full 1280×1000 pixel resolution at a 0.5 kHz frame rate. One Olympus Encore PCI 8000S camera with 1/3 inch CCD size runs with a 480×420 pixel resolution at a 4 kHz recording rate. A high speed "Silica Mountain Devices (SMD)" 64KIM camera with a CCD size of 13.4×13.4 mm runs with a reduced single frame size of $(960 \times 960)/4$ pixel resolution at up to 1 MHz frame rate. For the three slower cameras, images collected by each individual imaging fiber overfill the CCD pixels by a factor of ~ 6 and ~ 3 , respectively, i.e. one fiber projected onto 6×6 and 3×3 CCD pixel area, respectively. However, for the SMD camera, each imaging fiber slightly underfills the CCD pixels by a factor of 0.83, i.e. one fiber projected onto nearly a single CCD pixel area. Due to the nature of spatial superposition, an array of imaging fibers imaged by an array of CCD pixels, some images might compose of a honeycomb pattern caused by this pixelation artifact. However, the artifact can be minimized by slightly defocusing the image on the CCD. However, the FastVision and Olympus CCDs are capable of recording at a frame rate higher than 500 Hz, the architecture for binning at reduced resolution requires a change of the zoom ratio on the image head doom. The SMD camera has a different but fixed binning architecture so that the full field of view is taken at a high speed frame rate with reduced resolution. Except for the SMD camera where images are frozen by the short 150 ns illumination laser pulses, all other

1458 images are arrested by the short adjustable electronic exposure time of $10 \sim$
 1459 $50 \mu\text{s}$ set on the CCDs.
 1460 Synchronized short laser light pulses are used to illuminate the target and
 1461 freeze the motion of the jet after the impact of the proton beam. For SMD cam-
 1462 era, the mask reduces the photosensitive area to 0.03 of the nominal pixel area.
 1463 The quantum efficiency of the photo-resistive area is 0.18 at 800 nm, and the
 1464 pixel fill is 200000 electrons. Therefore, a full exposure of a frame of the CCD
 1465 therefore requires $(960)^2 \times 200000 / 0.03 / 0.18 \approx 3.4 \times 10^{13}$ photons or 10 Watts
 1466 for 800 nm photons. For FastVision camera, the sensor is 1280×1024 pixel
 1467 (1.03 megapixel) of CCD of total area $15.36 \times 12.29 \text{ mm}^2$ in 8 bits at 500 frames
 1468 per second (10 bits at 400 frames per second). Maximum frame rate is 500,000
 1469 at 1×1280 . The mask reduces the photosensitive area to 0.4 of the nominal
 1470 pixel area. Based on the estimation of required photons, a full exposure of a
 1471 frame of the CCD therefore requires $1280 \times 1024 \times 200000 / 0.4 / 0.18 \approx 3 \times 10^{12}$
 1472 photons or 1 Watts for 800 nm photons.
 1473 Optical light pulses are sent through 15 meters of multi-mode illumination
 1474 fibers. The light sources used in the experiment are all Class 4 lasers, emit-
 1475 ting at wavelengths of 808 to 850 nm. Three lasers are capable of emitting a
 1476 peak optical power of 1 Watt (JDS Uniphase SDL-2300-L2) driven by three
 1477 independent current drivers (ThorLabs LDC220C). These 1 Watt lasers can be
 1478 operated from CW to a minimum programmable pulse width of $1 \mu\text{s}$ limited by
 1479 the trigger logic pulse. The 4th laser emits at a peak optical power of 25 Watt
 1480 (Bright Solution BDL20-808-F6) limited by the pulsed current driver (Avtech

AXOZ-A1A-B). It provides a current pulse of 150 ns and is capable of running at the maximum 1 MHz repetition rate, i.e. a frame rate of 1 μ s/frame.

The complete transmission of the imaging system is ~ 0.2 per Viewport channel, including 0.85 for the 15 meter long illumination fiber, 0.86 for the sapphire ball lens, 0.86 for each pass of the sapphire Viewport, 0.91 for the retro-reflector, 0.67 for the 10 meter long imaging fiber, and 0.86 for the grin lens and the relay lens. For the SMD camera, the imaging circle filled $\pi/4$ of the CCD array. A measured output energy of 3.5 μ J/pulse is obtained from the Bright Solution (BDL20-808-F6) laser illumination light source for Viewport 2. Therefore the calculated number of photons impinging on the SMD camera reaches 4.2×10^6 photons/pixel. After taking into account the 18% quantum efficiency of the CCD, 7.5×10^5 photoelectrons are generated at the full illumination intensity. Since the SMD camera has full well capacity of $2.2 \times 10^5 e^-$, there is a factor of ~ 3 on the optical power budget reserved for unanticipated optical power loss and for overcoming the possible attenuation due to ionization radiation. Similar calculations for Viewport channels 1 and 3 give a factor of ~ 10 on the optical power budget. This larger factor is mostly due to the long, 10 μ s, exposure time set on the FastVision cameras. Overall, the imaging system is designed to have sufficient optical power budget for the illumination of each Viewport throughout the entire experiment.

3.1.2.4 *radiation-hardness*

Because of the high radiation level in the beam tunnel and the activation of the mercury after the proton beam interactions, all optics placed inside the interaction beam tunnel are required to be radiation-hard. One complete set of optics was selected for radiation resistance test done at CERN. This complete set of optics included an Au-coated reflector, sapphire window, illumination fiber, imaging fiber, and Grin objective lens. The experiment has anticipated a total of 200 proton pulses at 14 and 24 GeV with a total of $\sim 3 \times 10^{15}$ protons. The calculated total radiation reaches ~ 1 Mrad equivalent radiation dose. Therefore, all optics except the grin objective lens were irradiated at CERN to a lower energy 1.4 GeV proton beam but up to an equivalent radiation dose of 5×10^{15} protons. Because we missed an opportunity to deliver the grin lens to the CERN irradiation facility, the grin objective lens was instead irradiated at BNL using a Co-60 source up to a total dose of ~ 3 Mrad. The reflectance of the Au-coated reflector and the transmittance of all other optics are measured at the wavelength of 830 nm before and after irradiation. Table 3.2 shows the effects of irradiation up to an equivalent radiation dose of 1 Mrad on the reflectance and transmittance of the components of the optical diagnostic system. No noticeable change in the reflectance was observed on the Au-coated reflector even though the substrate of the reflector has turned nearly opaque. The sapphire, 5 meter long of illumination fiber, and 0.3 meter long of imaging fiber do not show any additional insertion loss. They are all radiation hard up to a 1 Mrad dose. However, the small grin objective lens did suffer

radiation damage resulting in a 0.73 transmission. This tiny grin objective lens is made of silver-ion exchanged index modification internal to a glass substrate. Therefore it was not anticipated to have a high radiation resistance. However, it is well known that although glass (and silica fibers) lose its transmission in the visible wavelengths, near infrared (NIR) light can still has adequate light throughput for some applications (Kakuta, 1999). This is one of the reason we select NIR rather than visible laser light for back-illumination of the mercury jet. Since the back-illuminated NIR light passes the grin objective only once, the 0.27 transmission loss over the entire experiment is tolerable and can be recovered with the present designed laser capability. We should note that the integrity of the imaging properties of the grin lens was unchanged, i.e. no image distortion was observed after the 1 Mrad radiation resistance test.

3.1.2.5 *scintillating fiber channel*

A jacketed 2 meter long 1 mm diameter blue emitting scintillating fiber is attached along with the imaging head to register gamma emission during the proton beam and mercury jet interaction. A 12 meter long 1 mm diameter fiber patch-cord (ThorLabs BFH37-1000) carries the blue scintillated light signal and is fiber-coupled to an Avalanche photodiode (ThorLabs APD210), designated as channel 0. The overall transmission at the center wavelength of 480 nm of the fiber patch-cord is measured to be 0.77. The scintillating signal trace is displayed on an oscilloscope and data can be retrieved remotely from the control room. This scintillating signal serves to confirm the arrival of the

proton beam and has the potential to extract the proton intensity from the scintillating signal pulse level.

3.1.3 Schematic of electronic trigger and high speed camera control

Because we are using several high speed cameras from different vendors, we must use separate camera control software for each camera. The limitation on their exposure time also requires two different set of illumination laser pulse trains. A master trigger pulse, synchronized to the arrival of the proton bunch, is delivered to trigger the mercury loop system, the solenoid magnet system, and the optical diagnostic system together. The mercury jet reaches its steady state for 1 second when the solenoid magnet reaches the highest magnetic induction field of 15 T. However, there is a significantly long time lag of ~ 10 seconds for the solenoid system to power up to its full capacity. Therefore, the master trigger signal is first sent to a digital delay generator (Stanford Research DG535) to provide a sufficient long delay to synchronize with all other electronic components. These relative and absolute delays are measured by an oscilloscope. By adjusting each independent delay channel, complete synchronization of all cameras with the pulsing of the laser light sources can be achieved and verified by comparing the bright/dark image intensities of each frame of each CCD.

Fig. 3.5 shows the two sets of pulse sequences used to simultaneously trigger all cameras. The 25W infrared laser consisted of a 17 pulse sequence with a

pulse width of 150ns. This determines the exposure time of the SMD camera on the Viewport 2. The laser pulse period is set to match the frame rate of the images. The SMD camera collects 16 frames of image. Fig. 3.6 shows the traced signals on an oscilloscope when the beam and the beam triggering are delivered. After the master trigger from the synchrotron is delivered at time $t = 0$, the proton beam comes in $\sim 3 \mu s$. The photodiode response from scintillating fiber has a 20 ns rise time and the level indicates the beam intensity and beam position. The scintillating fiber signal gives the beam arrival time. Therefore, it is possible to set the trigger timing for the cameras and laser driver inputs, which is $\sim 2 \mu s$ after the master trigger from the proton synchrotron.

Three 1 Watt lasers pulsed to a 0.5 second duration are used to independently illuminate Viewport 1, Viewport 3, and Viewport 4, respectively. Typically the FastVision and Olympus cameras continuously collect 220 frames of images. The exposure times on the cameras are set at $10 \sim 50 \mu s$ respectively to give a sharp image quality. Although the sharpness of images increases with reduced exposure time, much more light is required for illumination. Therefore, a trade off between exposure time and laser intensity is made. On the contrary, the exposure time for SMD camera is determined by the laser pulse width. As the pulse width of the laser decreases, the laser intensity also decreases. In order to utilize the maximum allowable intensity of the 25W laser, the maximum pulse width of $0.15 \mu s$ is used. This pulse width should not seriously jeopardize the image quality even running at its highest frame rate

of 1 μ s/frame. A schematic diagram linking all cameras, triggering electronics, and controlling computers is shown in Fig. 3.7. 2 desktops reside in the control room to master the optical diagnostics system. All other electronics and desktops are placed in the TT2 tunnel adjacent to the interaction beam tunnel TT2A.

3.2 Windows Consideration as Viewports for Observation

The mercury jet target is observed through four windows. These windows must contain any possible spray of mercury due to intense beam energy deposition, and remain transparent after a radiation dose from the interaction of beam and mercury.

3.2.1 Fiducial mark on windows

We put fiducial mark on each sapphire window to use the magnitude of the referenced length. The size of fiducial on the back and front windows is varying on images according to the changing field of view. i.e, the back fiducial looks smaller than the front fiducial. Fig. 3.8 shows the artificially marked fiducial on the sapphire window. It gives referencing length scale when we measure the size of jet, velocity, rotation of windows, and the location of magnetic axis on images.

3.2.2 Impact resistance test

We used sapphire windows to obtain enough strength and did surface coating on both sides for anti-reflection at 800nm wavelength. In order to check the survival from mercury droplet impact, we tested sapphire window using a paint ball gun. A paint ball is a 2.75 gram sphere of radius 8.6 mm containing a colored gel that readily “splats” on impact. The velocity of a paint ball was 95m/s. The ratio of the force from a paint ball to that due to the dispersal of the entire mercury jet by the proton beam is

$$\frac{F_{paintball}}{F_{mercury}} = \frac{m_{paintball} v_{paintball}^2 r_{mercury}}{m_{mercury} v_{mercury}^2 r_{paintball}} . \quad (3.6)$$

The momentum of the paint ball is the same as that of a 7 mm diameter mercury drop at 95 m/s. The sapphire window survived in the test.

3.2.3 Pressure leaking test of sapphire windows

The primary containment is mostly welded and the window ports are sealed with rubber gaskets (BUNA-N). Each window is sealed with two sheets of rubber gaskets per port. 21 psi is loaded inside the primary containment to check the sealing of the primary containment. To locate leaks, a Metheson 8850 flammable gas sniffer, which has a 5ppm sensitivity, and Ar/Methane (90 % / 10 %) was used. All of 8 windows survived the 21 psi pressure for over 17 hours.

3.3 Integrated Experimental Setup for High Power Target

3.3.1 Mercury loop system in solenoid magnet

The cross-section and actual equipment for the mercury system with high field solenoid magnet is shown in Fig. 3.9. The horizontal line in Fig. 3.9(a) represents the proton beam. The Hg jet, which is ejected from right to left in Fig. 3.9(a), co-propagates with the proton beam. Four Viewports are shown within the solenoid bore, which represent viewing locations for observation of the Hg jet within its primary containment vessel (see Fig. 1.3). Viewport 2 is positioned at the center of the solenoid and is the location where the center of the proton beam interacts with the Hg jet. The Hg system provides for double containment vessel of the hazardous liquid metal, and can be inserted or removed from the solenoid bore without disassembly. A hydraulic syringe pump, with a piston velocity of 3 cm/s was used to pulse the mercury jet. This pump minimizes the heat added to the Hg as opposed to a centrifugal pump. The syringe pump also reduces the discharge pressure which is the limitation of a centrifugal pump. The Hg system provides a jet duration of a ~ 3 seconds of constant velocity profile. A total of 180 kg of Hg is loaded in the system. A 30 KW, 200 bar hydraulic power unit drives the syringe pump.

The pulsed solenoid incorporates a magnetic induction field ramp up of 10 seconds and is capable of sustaining its peak field for a duration of approximately 1 second. A 5.5 MW, 700 V power supply delivers 7500 A of current

to pulse the solenoid. The magnet is cryogenically cooled to 77 K prior to operation and warms up by 30 K during pulsing due to 30 MJ coil heating. Therefore, a 30 minute cooling time is needed for each single shot. The magnetic axis is positioned at an angle of 67 milliradian to the proton beam, with the tilt provided by a common baseplate supporting all the equipment (see Fig. 3.9(a)). The applied magnetic induction field has been measured with a gaussmeter placed both perpendicular and parallel to the magnetic induction field. The relationship between the measured magnetic induction field and the applied solenoid current was mapped to deduce the maximum magnetic induction field at the center of the solenoid. It was found that the maximum magnetic induction field reached 15 T at Plasma Science and Fusion Center in Massachusetts Institute of Technology.

3.3.1.1 *the considerations in nozzle design*

Better yields of low energy pions are obtained from the mercury jet target when the proton beam and target are tilted with respect to the axis of the capture solenoid magnet. Monte Carlo simulations have indicated that a tilt angle of about 100 milliradian between the mercury jet and the proton beam is optimal (Mokhov, 2000). However, jet motion in a magnetic induction field behaves differently, depending on the angle between the axis of the magnet and that of the jet, as a result of the differences in the magnitude of the components of the magnetic induction field (Samulyak, 2006). As the crossing angle increases, the transverse component of the magnetic induction field increases,

but with no significant change in the longitudinal component. The increase in the transverse component of the magnetic induction field raises the induced current on the Hg jet. Therefore, the angle of the Hg jet is launched at 33 milliradian with respect to the axis of the magnet, resulting in an interaction region about 30 cm long in case of a 1 cm diameter mercury jet with a 1.5 mm RMS diameter of proton beam. Since the proton beam in TT2A beamline at CERN is horizontal, the mercury jet should make a 34 milliradian angle with respect to the proton beam axis, and the magnetic axis should make an angle of 67 milliradian with respect to the proton beam. The mercury will flow from the upstream end of the magnet to the downstream end of the magnet. The jet velocity is designed to be 20 m/s and the center of the jet to intersect the center of the proton beam at center of magnet.

3.3.2 Water jet observation for nozzle performance test

Prior to mercury injection in the primary at Oak Ridge National Laboratory(ORNL), extensive optical diagnostics were carried out by pulsing water jets in the system using 4 different types of nozzle configurations. One nozzle showed the most stable shape of jet motion with fairly uniform velocity, ~ 10 mm diameter and 20m/s respectively.

Due to the spray and wetting of water on the interior of windows, only ambiguous shadow of the water jet was observed. A clear surface motion is required in order to obtain accurate velocity measurement. Therefore, only qualitative diagnostics was made on the water jet. The field of view of each Viewport is \sim

1696 50 mm. The diameter of the jet is measured by overlaying a grid of referenced
1697 field of view onto the images. The time lapse of each frame is read from the
1698 camera frame rates. The trajectory of the jet between several frames can then
1699 be measured and the velocity of the jet surface motion is estimated.
1700 These measurements of the water jet tests were done at ORNL. The observa-
1701 tions led us to select the design of the final nozzle for the subsequent jet runs.
1702 It was fabricated from Titanium and the assembly was anodized for electrical
1703 insulation.

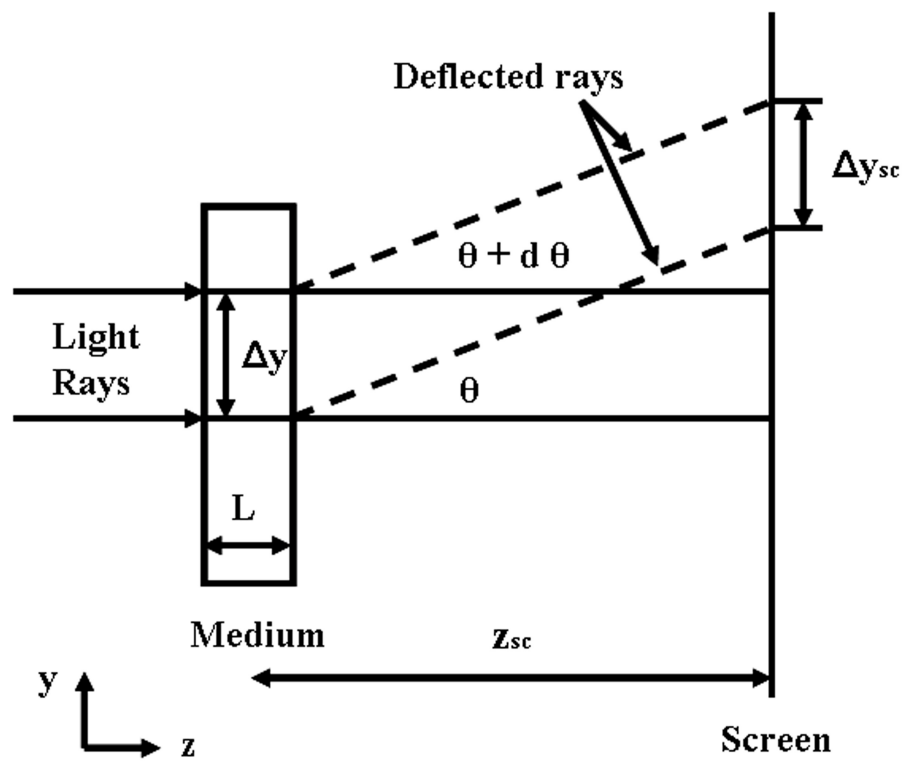


Figure 3.1: Displacement of light beam for shadowgraph.

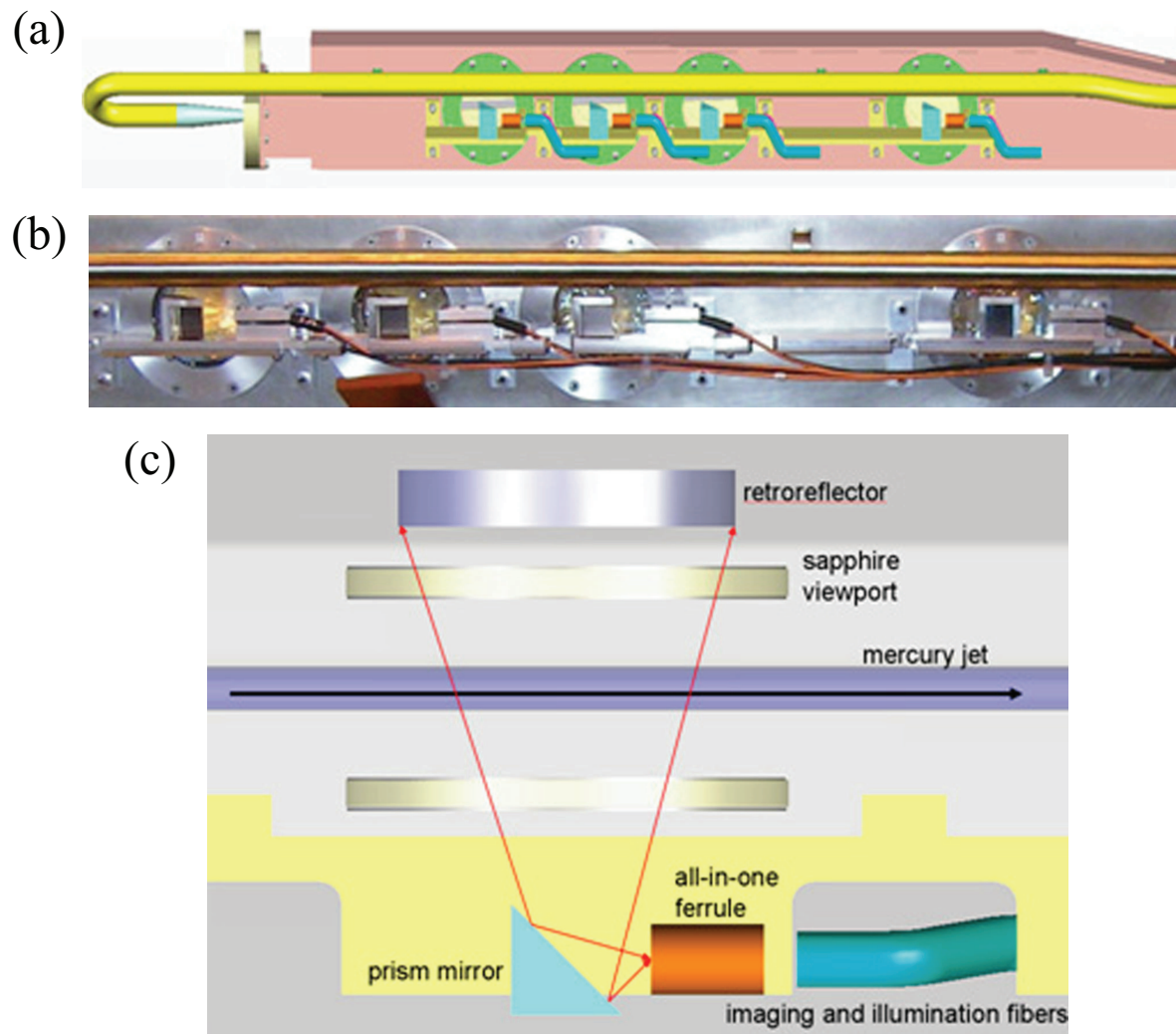


Figure 3.2: Design of optical layout and installation of 4 Viewports of primary containment vessel. a.) Conceptual integration of optics to primary containment vessel. b.) Photograph of installation of optics to primary containment vessel. c.) Schematic layout of optical components.

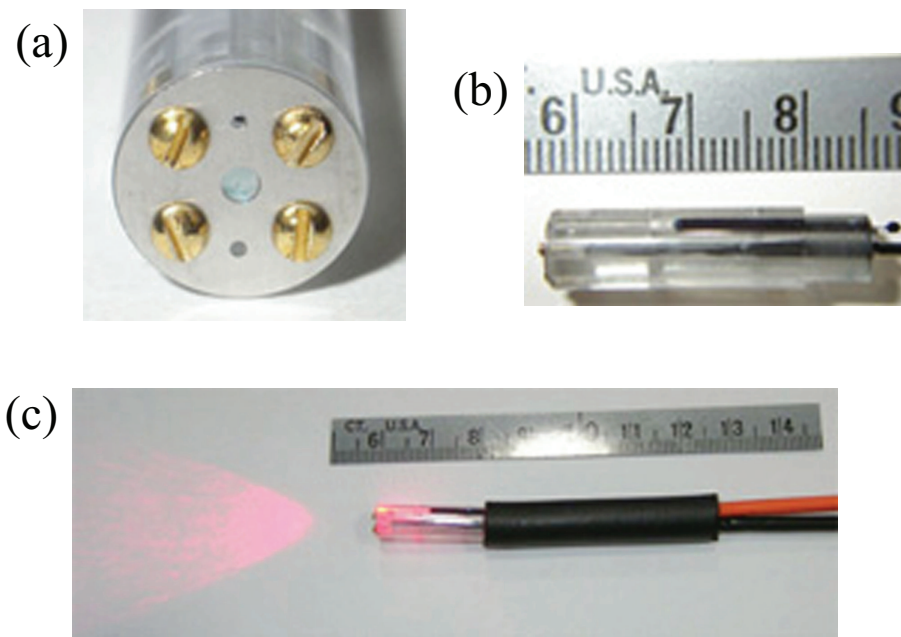


Figure 3.3: Photograph of optical head assembly and its illumination of laser. a.) Front view of optical head assembly. b.) Side view of optical head assembly. c.) Illumination of fiber-optics head assembly.

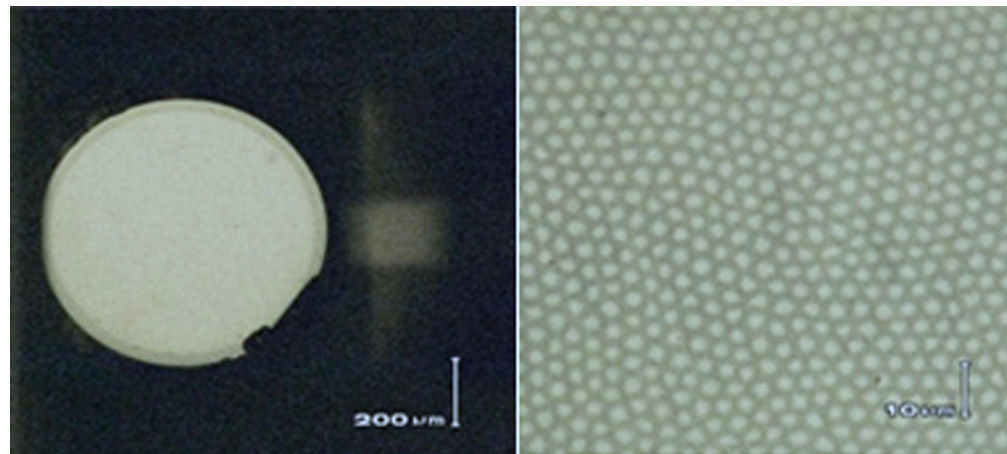


Figure 3.4: Polished fiber end, 50X and 800X magnifications, respectively

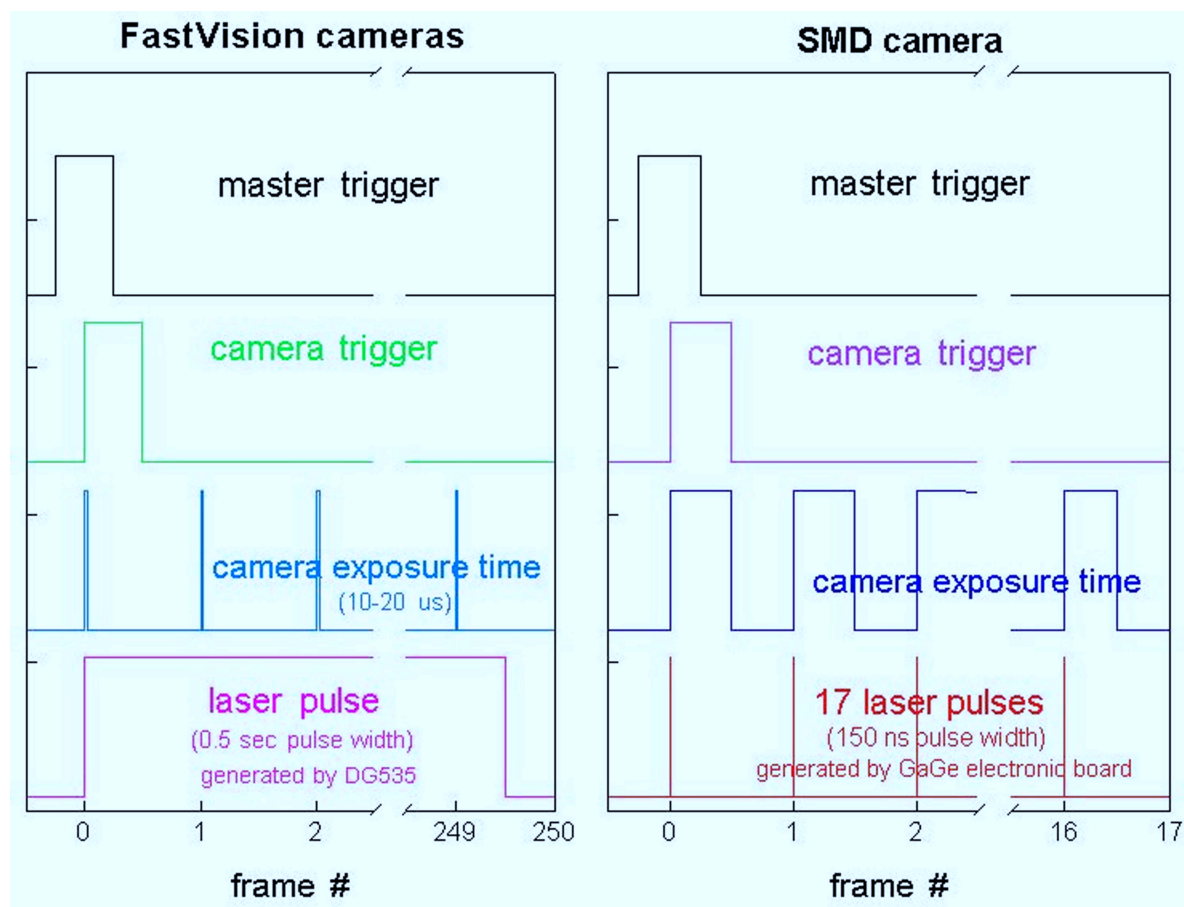


Figure 3.5: Schematic of synchronized signal of high speed camera and laser pulse.

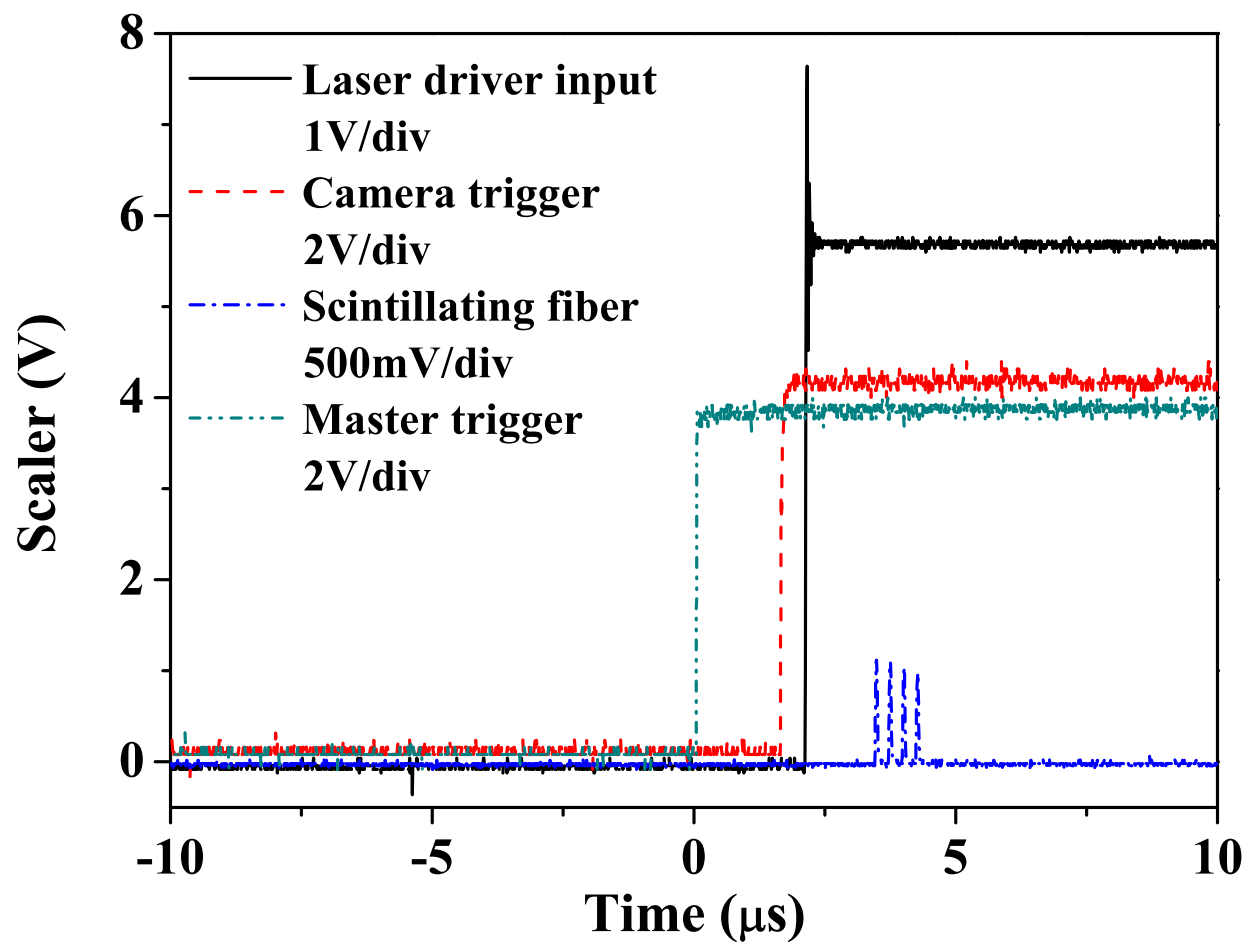


Figure 3.6: The triggering time for high speed camera upon beam arrival.

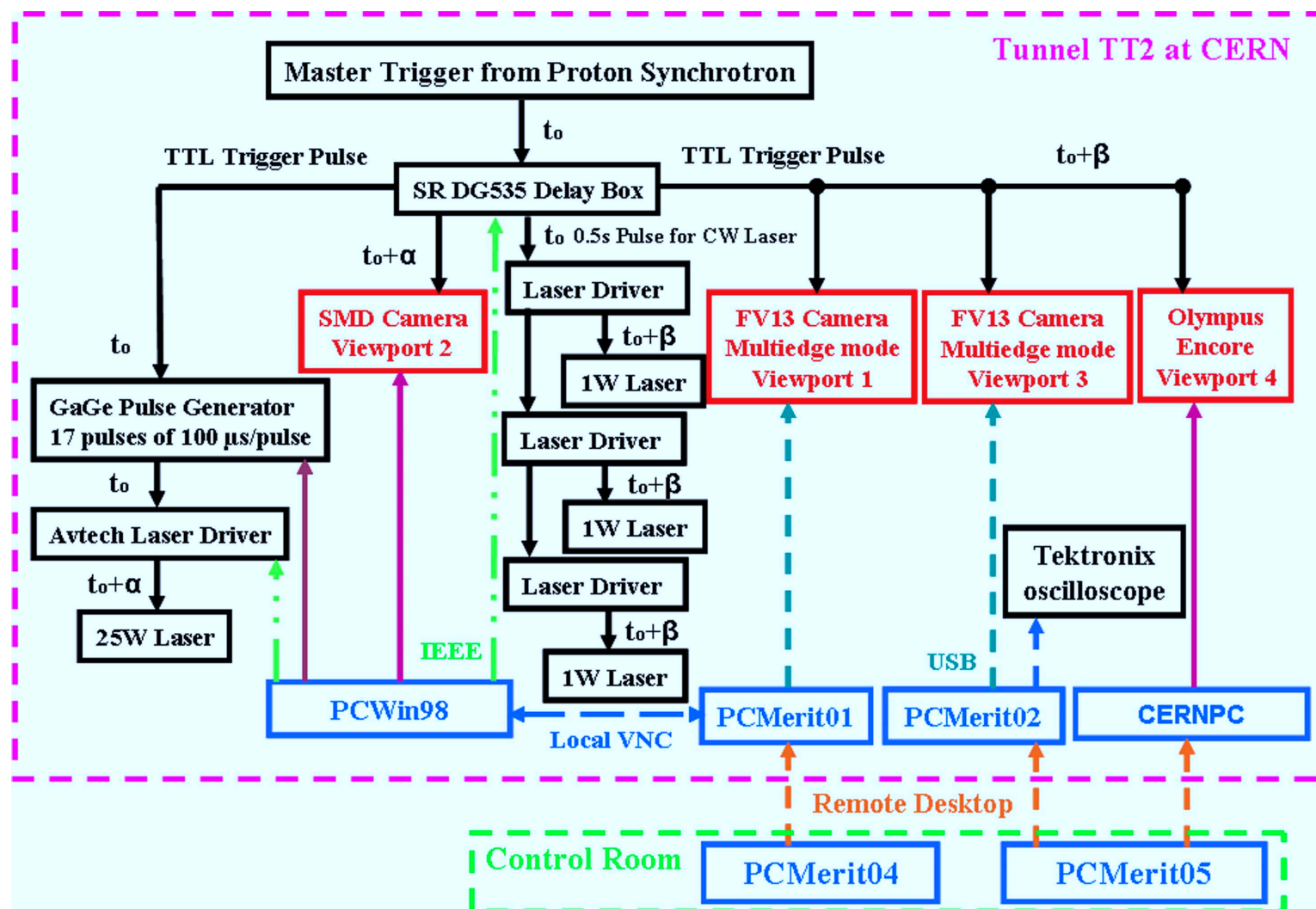


Figure 3.7: Schematic of electrical triggering and high speed camera control in tunnel for experiment.

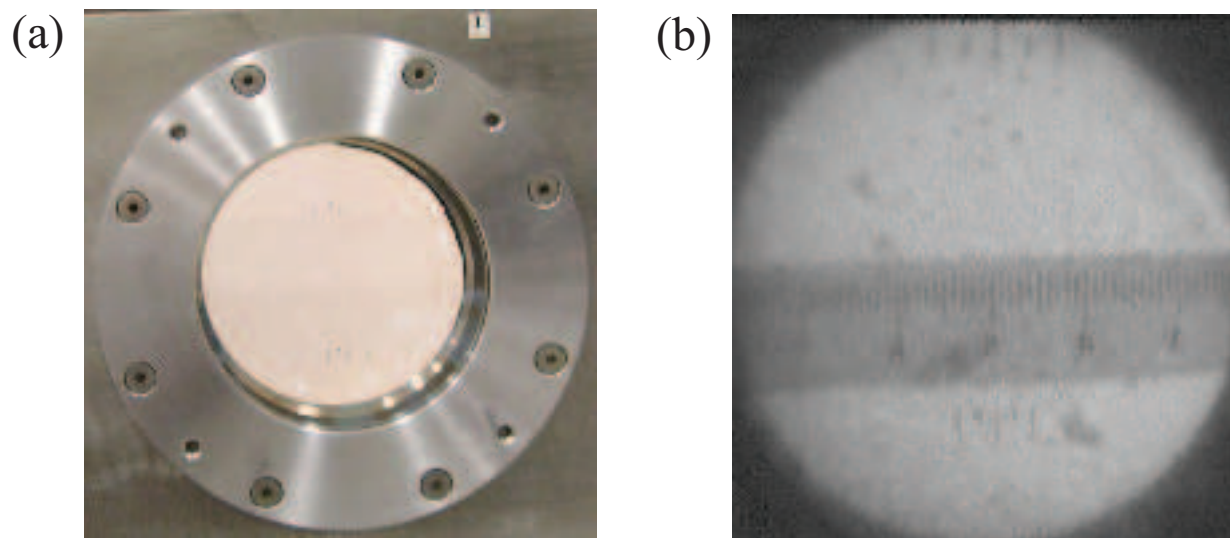


Figure 3.8: Top fiducial on the front window and bottom fiducial on the rear window. a.) Photo of fiducial on the sapphire window assembled in Viewport. b.) Image of fiducial captured by camera.

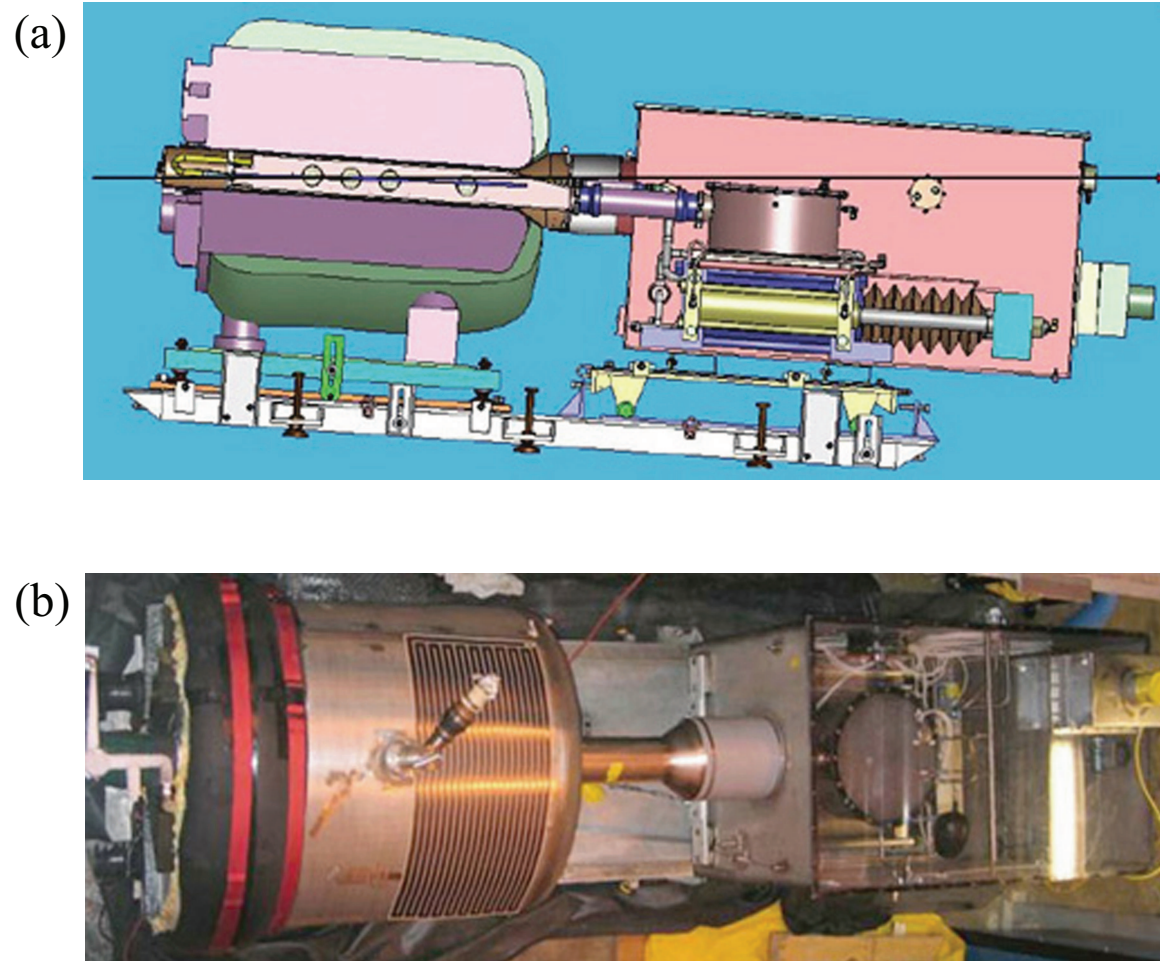


Figure 3.9: Photographs of the entire MERIT experiment. a.) Sectional side view of mercury loop system integrated with 15 T solenoid magnet. b.) Fabricated mercury loop system assembled with 15 T solenoid magnet (Top view).

Table 3.1: Specifications of high speed cameras.

Attributes	SMD 64KIM	FastVision	Olympus Encore PCI 8000S
CCD chip size	13.4 mm \times 13.4 mm	15.4 mm \times 12.3 mm	1/3 inch
Pixels	960 \times 960	1280 \times 1024	480 \times 420
Pixel size	14 μ m	12 μ m	13 μ m
Single frame	240 \times 240	1280 \times 1000	480 \times 420
Maximum frame rate	1 MHz ¹	0.5 kHz ²	4 kHz ³
Full well Capacity	220,000 e^-	\sim 1000 LSB/lux-sec	-
ADC	12 bit	8 bit	8 bit

¹ 16 frames.

² at full resolution.

³ 12.5 μ s electronic shutter, with reduced frame size.

Table 3.2: Effects of irradiation up to an equivalent radiation dose of 1 Mrad on the reflectance and transmittance of the components of the optical diagnostic system. Reflectance is inferred on the Au-coated mirror and transmittance is inferred on all other components.

Optical component	Before radiation	After radiation	% difference
Large Au-coated mirror	0.91	0.92	no change
Sapphire window(1-mm)	0.86	0.87	no change
Illumination fiber(5m)	1	1.02	no change
Imaging fiber (30 cm)	0.67	0.71	no change
Grin lens	0.90	0.66	73 %

Chapter 4

Experimental Investigation of Mercury Jet Flow in Magnetic Fields

In this chapter, the jet behavior in magnetic field are investigated. To do this, the collected images are read digitally and the characteristic jet parameters are evaluated based on the probability approach. It effectively diagnoses the jet condition on each collected image. Jet deformation such as the free jet surface deformation and surface stabilization is investigated by measuring the pixels on the collected images based on 2-D shadow photography. As a result, we will discuss the magnetic field effect to the dynamic behavior of freely moving jet in a solenoid magnetic field. The driving pressure of mercury flow entering inlet pipe is measured to monitor the effect of the magnetic field and assure if the input condition for driving the jet is affected. In order to diagnose the flow rate, the flow velocity in magnetic field is discussed and the deflection of jet size in various magnetic field is investigated. Based on the observed flow rate of jet, the shape of jet is suggested for the energy deposition calculation

by proton beam interaction with Hg jet target.

4.1 Image Analysis for Data Reduction

4.1.1 Image acquisition

~ 360 complete integrated tests (i.e., with magnet, proton beam, Hg loop system, and optical diagnostic system) were conducted at CERN (European Organization for Nuclear Research) with various values of the proton beam structure (8 harmonic and 16 hamonic) and the beam intensity up to 30×10^{12} protons and the beam energy (14 GeV/c and 24 GeV/c) and the the magnetic field (0T, 5T, 7T, 10T, and 15T) and two Hg jet velocities (15 m/s and 20 m/s). Fig. 4.4 and 4.5 are representative optical diagnostic results collected by the 3 cameras, with and without a magnetic induction field at Plasma Science and Fusion Center in Massachusetts Institute of Technology. Note that the Olympus Encore PCI 8000S camera for Viewport 4 was integrated in the beam interacting target study done at CERN.

The current in the magnet system generates heat, which is cryogenically removed using liquid nitrogen. As the magnet cools down, all Viewports become foggy up due to condensation. It was found out that $\sim 0.5 \ell$ of water (from nozzle performance test at Oak Ridge National Laboratory) was not removed from the system prior to loading Hg. Flexible heater strips were installed both on the exterior of the primary containment vessel and on the snout in order to prevent the condensation of the humid air on the Viewports. Although residual Hg droplets in sizes less than 1 mm often adhere to the

sapphire Viewports after every shot, jet motion with adequate image quality could still be collected.

4.1.2 Image processing

To measure the shape of the jet, 8 and 12 bit grey scaled TIF images are converted into digital forms. Background images are subtracted to reject the noise in the image digitization process. The residual data is then transformed into a 2 bit scaled image. Fig. 4.1 shows the collected image and its transformed 2 bit scaled image. Only the black and white colored pixels in the 2 bit depth images are used to differentiate the shadow of the jet and the background. Due to the image quality caused by the Hg droplet on window and the quality in fiber optic system, the noise such as black dots exists. A threshold is adjusted according to Otsu's method to highlight the interface between the mercury and background (Otsu, 1979). Otsu's method selects the threshold by minimizing the within-class variance and maximizing the between-class variance of the two groups of pixels separated by the thresholding operator. Otsu's method, which relies on the assumption that all image pixels belong to one of two classes, background or foreground, has been shown to be efficient in image segmentation for bi-level thresholding.

Fig. 4.2 show the sensitivity of 2 bit scaled image conversion to the measurement of jet height using Otsu's method. As the threshold level increases, the mean value of the jet height as well as the σ value of the jet height in measurement is approaching an asymptotic level. The optimally selected threshold

value by the Otsu's method in this example is 0.35.

The Hg jet was observed at upstream (Viewport 1), midstream (Viewport 2), and downstream (Viewport 3) locations from the nozzle exit. 220 images are collected at each run for both the upstream and downstream locations, with an image size of 1280×1000 pixels. The most probable transverse jet height within the longitudinal pixel range of 300 to 1000 is shown in the histogram of Fig. 4.3(a). Note that within this range, the transverse jet height probability P is obtained by counting the number of longitudinal pixel events in the jet image. If z denotes the transverse direction (in terms of pixels), the histogram in Fig. 4.3(a) can be written as (Eqn. (4.1)) using the least square curve-fairing approach:

$$P(z) = P_1 \frac{1}{\sqrt{2\pi}\sigma_1} e^{-\frac{(z-\mu_1)^2}{2\sigma_1^2}} + P_2 \frac{1}{\sqrt{2\pi}\sigma_2} e^{-\frac{(z-\mu_2)^2}{2\sigma_2^2}}, \quad (4.1)$$

where μ_1, μ_2 are the means, σ_1, σ_2 are the standard deviations, and P_1, P_2 are the a-priori count of the histogram distribution. Note that, in pixel units, $\mu_1=386$, $\mu_2=401$, $\sigma_1=3.8$, and $\sigma_2=21.6$. The number of background events (i.e., outside of the jet) is always larger than that within the jet because the portion of bright background on each image is larger than that of the black jet shadow. The distribution on the left in Fig. 4.3(a) (i.e., $0 < z < 200$) represents the background pixels and is not included in the faired curve in Fig. 4.3(b).

On the other hand, rather than using the fitting of the histogram of number of events, the number of pixels corresponding to the jet height is counted within

the longitudinal pixel range of 300 to 1000. Each counted pixel numbers are directly average to give a jet height measurement and then added up over ~ 200 images for 1 jet shot, where the time elapse corresponds to ~ 0.4 s at Viewport 1 and 3. Multiple shots are then used to add up all of the counted vertical jet height. The average of the individually counted vertical pixels is given to indicate the nominal jet height. In a mathematical form, the direct averaging method is described as Eqn. (4.2) and its measurement is shown at Fig. 4.7 (b).

$$D_{jet} = \frac{1}{i + j + k} \sum_1^i \sum_1^j \sum_1^k N_{vertical} \quad (4.2)$$

where D_{jet} and $N_{vertical}$ denote the averaged vertical jet height and a individually counted number of vertical pixels respectively. i, j, k represent the number of shots, images in a shot, and vertical lines in a image respectively.

On Viewport 2, 16 image files are collected at each run, with an image size of 316×316 pixels. The images are analyzed in the same manner as described above. Viewports 1 and 3 give the same resolution for the images: 1280×1000 . Thus, no image re-scaling is needed when comparing the pixel size for these images. However, Viewport 2 gives a resolution of 316×316 . Based on the 1 cm scale fiducial mark on the exterior of all Viewports, all images taken on this Viewport are re-scaled to match the resolution of Viewport 1 prior to comparison.

4.1.3 Study on the scaling length and the location of center of window

In order to relate the lengths on the collected images at each Viewport, the pixel length on the images has to be investigated. Since the image size corresponds to the CCD size, any discrepancy in horizontal and vertical pixel size is not considered. Viewports 1 and 3 give the same resolution for the images: 1280×1000 . Thus, no image re-scaling is actually needed when comparing the pixel size for these images but did the scaling to see any difference on the image length of Viewport 1 and Viewport 3. The fiducial length on the top front window and the bottom back window is measured and then interpolated to get the length at the mid-span on the primary containment. The interpolated pixel length at the mid-span corresponds to 1 cm at the mid-span of primary containment. Thus, in Viewport 3, a pixel length at the mid-span where the jet is moving is approximated ~ 0.05 mm. Same scaling was done at images in Viewport 3. The ratio of the pixel length in Viewport 3 to Viewport 1 is 1.06.

Viewport 2 gives a resolution of 245×252 . Based on the 1 cm scale fiducial mark on the exterior of all Viewports, all images taken on this Viewport are re-scaled to match the resolution of Viewport 1 prior to comparison. A pixel length at the mid-span is approximated ~ 0.21 mm. Viewport 4 gives a different resolution of images depending on the frame rate setting but typically the resolutions of 320×280 was used. A pixel length at the mid-span is approximated ~ 0.21 mm, which is same with Viewport 2.

The distance of the center position between the fiducial and the window is 0.75 inch apart. In order to locate the center of the window at the mid-span, the positions where 0.75 inch is apart from the top fiducial and bottom fiducial is found on each image and then the averaged difference in the located position is considered as the center of window.

Based on these scaling study, the measurement is performed for the following investigation. The measurement is averaged for ~ 200 images to give a result of the following investigation and the standard deviation is also calculated for the individual measurement respectively. Based on the standard deviation and the number of events, the error bar, σ/\sqrt{N} , is calculated to give error estimation for each measurement.

4.2 Motion of Mercury Jet and Stability in Magnetic Field

4.2.1 Jet deflection and surface flattening

When the jet is injected without an applied magnetic field, it is difficult to discern the jet surface because of blockage by Hg droplets on the window. Therefore, some errors in the measurement exists (see images Fig. 4.4(a) through Fig. 4.4(c) and 4.5(a) through 4.5(c)). On the contrary, when a magnetic field is applied, the measurement errors are significantly reduced, leading to significantly less intermittent jet boundaries.

The inertial forces appear to dominate the jet movement when the jet velocity is 15 m/s. The turbulent jet motion is unstable but becomes stabilized

as the magnetic field approaches 5 T. It has been reported that the radial force induced by the transverse component of magnetic field caused by the axially induced current due to the tilted jet angle can significantly increase the jet height (Gallardo *etal*, 2002). The phenomena of increasing jet thickness with high magnetic induction field is observed for the first time when the magnetic field exceeds 10T.

The Fig. 4.7 (a) shows the jet height variation by the magnetic field strength and the jet height is measured by fitting the histogram of number of events resulted from the image processing. The standard error is used to give the error bar, where the standard deviation is divided by the number of samples. The Fig. 4.7 (b) shows the jet height measurement by direct average of vertical jet height from scanned pixels on each image. The standard deviation is used to give the error bar. This two plot shows the extreme two conditions of evaluation of the measured jet height, but one can effectively observe the fluctuating amount relative to the nominal jet height according to the various magnetic fields.

At a jet velocity of 15 m/s, the relatively low inertial force reduces the extent of turbulent fluctuation. For this case, the magnetic field does not significantly affect the dynamics of the jet until the magnetic field strength of ~ 5 T reaches. Consequently, the height of the jet decreases only slightly until 5T since the magnetic field reduces the fluctuating surfaces and the jet is more likely to elongate axially to the jet axis. The results shown in Fig. 4.4 and 4.5 clearly suggest that the magnetic field has constrained (stabilized)

1878 the Hg jet flow by smoothing out the edges of the otherwise turbulent flow.
1879 At large number of the magnetic field (>10 T), stability is maintained at all
1880 Viewports. At 15 T, a larger height (cross sectional distortion) is observed on
1881 all Viewports.

1882 The fact that the Hg jet size is relatively reduced from 0 T to 5 T but
1883 increases from 10 T to 15 T suggests that the Hg jet might encounter a different
1884 type of instability at high field, namely a quadrupole effect. The quadrupole
1885 effect would alter the jet's circular cross-section to become elliptical. From
1886 the data obtained with a 15 m/s jet, the jet height at a 10 T is smaller
1887 than that at 15 T, which is manifested in the vertical elongation of the jet.
1888 However, the height at a 10 T is smaller than that at 5 T. The issues for such
1889 a behavior have to be addressed. There are two possibilities. First, the jet
1890 is elongating axially up to 10 T. The equivalence of hydrodynamic pressure
1891 with magnetic pressure is more dominantly affecting to the axial elongation of
1892 jet than the transverse pressure. Eqn. (2.76) shows the magnetohydrodynamic
1893 stress tensor, which indicates the ration of the axial pressure and the transverse
1894 pressure. The increasing axial pressure of jet is more elongating from 0 T to
1895 10 T. However, the transverse magnetic pressure becomes significant once the
1896 magnetic field exceeds 10 T. Thus, the jet at 15 T is experiencing the transverse
1897 deflection as well as axial deflection, but the the role of transverse deflection
1898 plays significantly on the behavior of jet. That can explain why the reduction
1899 of jet is appearing up to 10 T and then the expansion of jet is appearing at 15
1900 T.

1901 Second, the optical diagnostics depends only on the side sectional view of
 1902 jet movement. The reduction of jet size on the minor axis of the elliptical
 1903 core has to be accompanied by the gain in jet size on the major axis in order
 1904 to satisfy the continuity condition in flow. In other words, the cross-sectional
 1905 are in flow should be constant. Although the two dimensional nature of the
 1906 image data does not distinguish between an elliptical cross section and a cir-
 1907 cular one, occasional observation of a smaller jet thickness at 15 m/s with 10
 1908 T field as opposed to a 5 T indicates that the jet cross section might vary
 1909 between the major and minor axis of an elliptical core. It is important to note
 1910 that within the axial distance of interest, the jet diameter is approximately
 1911 constant. Therefore, references to "larger jet height" should be interpreted
 1912 to mean larger distortions of the jet cross section. Since the jet and solenoid
 1913 field are cylindrically symmetric, it is hard to estimate in what direction the
 1914 jet is going to be distorted but the ratio of the deflection can be determined
 1915 experimentally. The ratio also can be compared with the transverse magnetic
 1916 pressure $B^2/2\mu$ considering the reversed direction of deflection on each plot.
 1917 If then, the Fig. 4.7 (a) gives the deflection ratio with magnetic field in an in-
 1918 creasing sequence from 0 T to 15 T approximately consistent with the ratio of
 1919 magnetic pressure $B^2/2\mu$. Samulyak (2007) suggested that the deflection ratio
 1920 of jet size $\Delta R/R_o$ is proportional to the magnitude \mathbf{B}_o^2/U . by using the devel-
 1921 oped MHD code, where the governing MHD equations and free jet boundary
 1922 condition including Maxwell's equations using low magnetic Reynolds approx-
 1923 imation are employed and calculated the Hg jet deflection in magnetic field

using a hybrid of Eulerian and Lagrangian method, so called Front tracking method. Fig. 4.8(a) shows the deflection ratio of Hg jet along the distance from nozzle at 10 T and 15 T magnetic field. As shown in Fig. 4.4 and Fig. 4.5, the magnetic field stabilizes the Hg jet surface so that the jet surface is getting flattened. In MHD simulation, constant 1 cm diameter of Hg jet is considered. Although the magnetic field causes the jet surface flattening, the nature of turbulence such as growth of jet size is observed in experiment. Therefore, in order to avoid such a turbulent nature between simulation and experiment, the ration of jet deflection ratio between 10 T and 15 T is evaluated to see the comparison of the magnetic field effect \mathbf{B}_o^2/U between Fig. 4.8(a) and Fig. 4.7 (b), which is shown in Fig. 4.8(b). It shows somewhat consistency at upstream, but still the ratio diverges as the jet flows to downstream.

As expected, jet motion in a magnetic field behaves differently, depending on the angle between the axis of magnet and the axis of jet, as a result of the differences in the magnitude of components of magnetic field (Samulyak, 2006). Fig. 4.6(a) and 4.6(b) show the axial and radial components of the magnetic field in a solenoid. Fig. 4.6(c) and 4.6(d) show the transverse and longitudinal components of the magnetic field along the jet axis at different crossing angles. As the crossing angle increases, the transverse component of the magnetic field increases, but with no significant change in the longitudinal component of the magnetic field. An increase of the transverse component of the magnetic field raises the induced axial current on the Hg jet. Therefore, the angle of the Hg jet is launched at 33 milliradian with respect to the axis

1947 of solenoid magnet.

1948 The jet surface can readily be extracted from each collected image. The
1949 jet axis is approximated by fitting the averaged positions between top surface
1950 and bottom surface. This jet axis is moved with an offset until it interferes the
1951 top surface bottom surface. The amount of fluctuations of surface is measured
1952 by getting the difference between the fluctuation surfaces and the interfering
1953 jet axis on a RMS scale. Let $\delta(r, t)$ denotes the probability of turbulence at r ,
1954 such that δ is 0 in the non-turbulent fluid, where the background is considered
1955 here, and is 1 in the turbulent fluid, where the jet is considered here. Time av-
1956 erage of δ yields $\zeta(r)$, the intermittency factor at r . The turbulent fluctuations
1957 are produced by the intermittency effect and these fluctuations are significant
1958 for scalar quantities. The intermittency characteristics of the turbulence are
1959 the appropriate input to be used in defining rough surface for a scattering
1960 analysis. When the intermittency phenomenon is present, the conventional
1961 turbulent fluctuation is modified by the intermittency function and there is
1962 an additional contribution depending on the difference between the mean tur-
1963 bulent quantity and the non-turbulent quantity (Yen, 1967). However, the
1964 probability of the fluctuating jet surface area is introduced to define the in-
1965 termittency in the following work. The pixel information along the jet axis
1966 by changing the translational offset is added to represent the intermittency of
1967 jet on the top/bottom surface. The intermittency within the jet represents 1
1968 and it is gradually decrease to 0 at the background. The intermittency is be-
1969 tween 0 and 1 at the jet surface depending on the surface fluctuations. Fig. 4.9

1970 shows the intermittency as a function of magnetic field and time. Total eval-
1971 uated time is $160 \mu s$. Without magnetic field, the slope of intermittency at
1972 the jet surface is broad and it is oscillating as a function of time. With higher
1973 magnetic field, the slope of intermittency at the jet surface is more steep and
1974 it keeps same shape with respect to time. This result clearly tells that the
1975 magnetic field suppresses the fluctuation of jet surface.

1976 The Fig. 4.10 shows the measured fluctuations on the jet surface. Surface
1977 fluctuations is monotonically decreasing and the surface is flattened approx-
1978 imately at 5 T. The fluctuations at Viewport 3 (downstream) is larger than
1979 that at Viewport 1 (upstream) since the tendency to be more turbulent grows.
1980 The amount of fluctuations at top surface and bottom surface of jet is almost
1981 same, though the magnetic field is varied. Thus, the symmetry on the jet
1982 surface in terms of the surface variations such as fluctuations and wave am-
1983 plitude is valid. The amount of difference of surface fluctuations at Viewport
1984 1 and Viewport 3 becomes same. It indicates that the jet surface becomes
1985 flattened at 5 T in flow velocity 15 m/s. The decreased amount of surface
1986 fluctuation at Viewport 1 and Viewport 3 is ~ 0.5 and 1.5 mm RMS respec-
1987 tively. This explains why the jet height is reducing from 0 T to 5 T in Fig. 4.7
1988 (a). The magnetic field makes the wavelength on the jet surface increases.
1989 Correspondingly, the wave propagation speed is increasing. Thus, it causes
1990 Re_{cr} to increase and the flow becomes laminar due to the stabilization by the
1991 magnetic field. The transverse component of magnetic field prevails more over
1992 the jet stabilization. Though there is some measurement errors due to the

1993 saturation in image brightness, the measurement could show the field effect to
 1994 the reduction of fluctuation on jet surfaces.

1995 The these observations are supported by previous results. For example,
 1996 several investigations have suggested that magnetic field suppresses turbulent
 1997 fluctuations in conducting liquid by stabilizing the flow (Shercliff 1956, Gold
 1998 1962, Kozyrev 1981, Bernshtam 1982), where stabilization is judged by an
 1999 increase in the characteristic wavelength of the flow.

2000 **4.2.2 Trajectory of mercury jet projectile in magnetic** 2001 **field**

2002 The Hg jet and the beam are launched at 33 and 67 milliradian with respect
 2003 to the magnetic axis respectively. The trajectory of Hg jet projectile is acted
 2004 upon by gravity, which is represented as follow:

2005

$$\begin{aligned}
 t &= \frac{x}{v_o \cos \theta} , \\
 y &= -\frac{g}{2} t^2 + v_o \sin \theta t + y_{nozzle} , \\
 |v| &= \sqrt{v^2 - 2gx \tan \theta + \left(\frac{gx}{v \cos \theta}\right)^2} , \tag{4.3}
 \end{aligned}$$

2006

2007 where x is the jet traveling distance, y is the height at x, y_{nozzle} is the
 2008 vertical position of nozzle, v_o is the launched velocity, and θ is the launched
 2009 angle of Hg jet.

2010 The distance of jet elevation is determined by measuring the distance from
 2011 the magnetic axis at center of each window to the jet axis, which is approxi-
 2012 mated by fitting the averaged positions between top surface and bottom sur-

face. The Fig. 4.11 shows the trajectory of Hg jet and it's effect by the magnetic field and gravity. The solid line represents the globally fitted value using the trajectory of projectile with different initial launching speed of jet for the case of 15 m/s and 20 m/s respectively. It shows that the trajectory of Hg flow approximately agrees well with the trajectory of projectile for both 15 m/s and 20 m/s shots. Experiment shows that the trajectory of the Hg jet is parabolic. The magnetic field caused some elevation of Hg jet closer to the center of magnetic field. As the jet moves to downstream, magnetic field effect is more clearly shown up since the jet is more likely to elongate to the axial direction (Davidson, 1999). The longitudinal magnetic force is more increasing as one can see the magnetic pressure term in the longitudinal direction increasing at Eqn. (2.76). Therefore, it is observed that the jet is behaving more like straight at Viewport 4 with higher magnetic field. At 15 T, the elevation of jet is observed from Viewport 1 to Viewport 4. It shows that the magnetic force is overcoming the inertia force at 15 T similarly as there is the increase in jet height at 15 T. The overall increase of the jet elevation in upstream, mid-stream, and downstream at 15 T may have been caused by the asymmetric change of jet height. Possibly the stable equilibrium between magnetic force and gravitational force could be varying according to the variation of magnetic field (Geim, 1999).

The beam trajectory is also given to show the overlap with the Hg jet. It is shown that the overlap length is ~ 30 cm when we consider the height of jet at various position with various magnetic field.

2036 Based on the result of the jet trajectory, the angle of jet axis at Viewport 2
 2037 (midstream) is determined by the trigonometric approach using the elevation of
 2038 jet and the distance along the magnetic axis between Viewport 1 and Viewport
 2039 3. Fig. 4.12 shows the estimation of jet angle at center of magnetic axis
 2040 (Viewport 2), which is approximately $7 \sim 11$ milliradian. The jet angle is
 2041 slightly decreasing with higher magnetic field, which indicates that the jet is
 2042 more likely to move horizontally following the field line direction.

2043 4.3 Dynamics of Liquid Jet Flow From Nozzle

2044 4.3.1 Jet equations for analysis

2045 Lee (1977) investigated the phenomenon of air wake caused by a cylindrical
 2046 jet emerging from a nozzle and showed the boundary layer of jet by applying
 2047 continuity of jet mass and matching the loss of jet momentum with air drag on
 2048 the jet. Fig. 4.13 depicts schematically the boundary layer of jet emerging from
 2049 a nozzle. The conservation of axial momentum and the rate of momentum loss
 2050 to the skin friction on the jet and the continuity of the liquid jet are expressed
 2051 as follows:

$$2052 \quad 2\pi\rho_a \int_0^{\delta(x)} [a(x) + y]v^2(x, y)dy + \rho_l\pi a^2(x)v_l^2(x) = \rho_l\pi a_o^2v_{lo}^2. \quad (4.4)$$

$$2054 \quad \frac{d}{dz}[\pi\rho_l a^2(x)v_l^2(x)] = 2\pi a(x)\mu_a \frac{\partial v}{\partial y}|_{y=0}. \quad (4.5)$$

2056

2057

$$\pi a^2(x)v_l(x) = \pi a_o^2 v_{lo}. \quad (4.6)$$

2058

2059

2060

2061

2062

2063

2064

2065

2066

2067

2068

$$\frac{\delta(x)}{a(x)} = e^{\beta(x)} - 1. \quad (4.8)$$

2069

2070

2071

2072

2073

$$\bar{v}_l(barx) = \frac{v_l(barx)}{v_{lo}} = \frac{1}{1 - \bar{\rho}[1 + \frac{1}{\beta} - \frac{1}{2\beta^2}(e^{2\beta} - 1)]}, \quad (4.9)$$

2074

2075

2076

2077

where velocity, density, and viscosity are denoted by v , ρ , and μ , respectively, with subscripts a and l for air and liquid, respectively. The subscripts o denotes the initial values at the nozzle. For boundary layer analysis of cylindrical objects, because of the diverging flux characteristics in radial direction, a logarithmic profile is the most appropriate (Stewartson, Glanert, 1955). Thus, the velocity profile of the air induced by the liquid jet is assumed to be as follow:

$$v(x, y) = v_l(z)\{1 - \frac{1}{\beta(x)} \ln[1 + \frac{y}{a(x)}]\}.$$

Substitution of Eqns. (4.7) into Eqns. (4.4) Eqns. (4.6) results in

$$\frac{d\beta(barx)}{dbarx} = \frac{\beta^2 - bar\rho[\beta^2 + \beta - \frac{1}{2}(e^{2\beta} - 1)]}{\beta(1 + e^{2\beta}) - (e^{2\beta} - 1)}, \quad (4.10)$$

where $barx = \frac{4x}{Re_e a_o}$, $Re_e = \frac{2a_o \rho_a v_{lo}}{\mu_a}$, and $bar\rho = \frac{\rho_a}{\rho_l}$. For a given value of ρ , the stream velocity $barv_l(barx)$ and boundary layer thickness $bar\delta(x)$ are obtained. As seen in Fig. 4.14, the Reynolds number plays its role implicitly and this makes the density ratio $bar\rho$ to be varied. Since the cylindrical jet has

larger volumes, for the initial momentum of the jet to be maintained, the liquid density must be reduced and the value of the density parameter to be used must be modified to $\bar{\rho} = \rho_a D^2 / (\rho_l d_o^2)$, where D and d_o denote diameter of jet and nozzle, respectively.

4.3.2 Pressure loss and magnetic effect to the Hg delivery pipe

Fig. 4.15 (a) and 4.15 (b) show the pipe inlet pressure for driving jet in various magnetic field strength. The Hg jet is driven by the piston in syringe and the piston velocity is measured by position sensor. The piston velocity determines the flow rate so that the dynamic pressure head at pipe inlet is determined using the conservation of flow rate. The pressure sensor installed at the pipe wall measures the static pressure. No significant pressure drop is observed at the pipe inlet in magnetic field strength. It indicates that the driving pressure in pipe for nozzle is at same condition regardless of the magnetic field variation.

To obtain the jet velocity, the distance traveled by a fixed point on the jet surface is tracked over a given time period. Fig. 4.16 (a) shows the jet velocity measured at Viewport 1, Viewport 2, Viewport 3, and Viewport 4 in various magnetic field strength. Note that this velocity does not change with the imposition of a magnetic field. Therefore, considering the measurement error in Fig. 4.16 (a), the averaged flow velocity, regardless of magnetic fields, can reasonably indicate the flow velocity given in Fig. 4.16 (b). This explains

2100 why the pressure is approximately constant in the pipe, consistent with the
2101 report (Graves, 2007).

2102 Another interesting result is that the cross section of Hg jet is more likely to
2103 be elliptical since the longitudinal jet flow velocity is constant from upstream
2104 to downstream. Regardless of the magnetic field, the Hg jet does not show jet
2105 velocity change. Thus, the jet is changing its shape once it leaves the nozzle
2106 from circular to elliptical. Hence, the result in Fig. 4.7 (a) should be again
2107 interpreted by the result in Fig. 4.16 in the manner that the jet height at 5
2108 T is elongated on the minor axis followed by the reduction of jet height on
2109 the major axis of the elliptical core, and the jet is deflecting further at 10
2110 T. However, the jet height at 15 T is elongated on the major axis, which is
2111 manifested by the comparison between the ratio of the reduction of jet height
2112 and the increased ratio of the jet height at 15 T. This approach is already
2113 mentioned in the above, but it is examined again.

2114 Considering that the driving pressure and the jet velocity are not signifi-
2115 cantly changed in various magnetic field, it is concluded that the longitudinal
2116 magnetic field does not affect to the pressure loss or velocity degradation while
2117 Hg passes the solenoid magnet two times along with the direction of magnetic
2118 field line. It is reported that the gradient of longitudinal jet velocity depends
2119 on the integration of gradient of longitudinal magnetic field along the magnetic
2120 axis plus it's multiplication to longitudinal magnetic field itself. (Gallardo *etal*,

2121 2002) It is expressed as follow:

2122

2123
$$\Delta v(x) = \frac{\kappa r_o^2}{\rho} \left(\int_{x_1}^{x_2} \left(\frac{dB_x}{dx} \right)^2 + \frac{d}{dx} \left(B_x \frac{dB_x}{dx} \right) dx \right) , \quad (4.11)$$

2124 where r_o is the radius of jet and κ is electrical conductivity. Since the gradient
 2125 of magnetic field is increasing (plus) at entrance and decreasing (minus) at
 2126 exit, it seems that there is an increasing velocity gradient (acceleration) at
 2127 upstream and decreasing velocity gradient (deceleration) at downstream but
 2128 it is ≤ 0.5 m/s due to the relatively high density comparing with the electrical
 2129 conductivity only if we consider the effect by the magnetic field. The exper-
 2130 imental result shows slight effect of magnetic field but is consistent with the
 2131 reported result in terms of the gradient of longitudinal velocity in magnetic
 2132 field.

2133 4.3.2.1 *pressure loss in pipe flow*

2134 Schematic pipe geometry is given in Fig. 1.3, where the pipe is connected
 2135 from the syringe pump to nozzle and it is passing parallel with solenoid mag-
 2136 netic field line next to the primary containment. A loss coefficient is defined
 2137 as follows:

2138

2139
$$(h_{loss}) = K_1 \frac{v_1^2}{2g} + K_2 \frac{v_2^2}{2g} + \dots + K_N \frac{v_N^2}{2g} ,$$

$$A_1 v_1 = A_2 v_2 = \dots = A_N v_N = A_R v_R , \quad (4.12)$$

2140 where the subscript R signifies a reference location and K represents the
 2141 loss coefficient.

2142 The general thermodynamic loss, so called the head loss h_{loss} is defined as
 2143 follow:

2144

$$2145 \int_1^2 \delta F = (h_{loss})_{1,2} = \frac{p_1 - p_2}{\rho g} + \frac{v_1^2 - v_2^2}{2g} + (z_1 - z_2) . \quad (4.13)$$

2146 Darcy-Weisbach equation is given to express the head loss of wherever
 2147 the density is constant, when the pipe diameter is constant and the pipe is
 2148 horizontal.

2149

$$2150 \frac{\Delta p}{\rho g} = f \frac{L}{d} \frac{U^2}{2g} , \quad (4.14)$$

2151 where f , L , d are friction factor, the pipe length, and the diameter of
 2152 pipe respectively. Considering that the $Re = 1800000$ and $e/d = 0.002$ for
 2153 commercial steel in terms of Nikuradse's sand grain scale, turbulent friction
 2154 factor f via Moody plot or by Colebrook Eqn. (4.15) is approximated to 0.024.
 2155 Colebrook simply combined the expressions for the friction factor for smooth
 2156 and rough pipes into a single transition equation of the equivalent form.

2157

$$2158 \frac{1}{\sqrt{f}} = 1.74 - 2 \log \left(2 \frac{e}{d} + \frac{18.7}{Re \sqrt{f}} \right) . \quad (4.15)$$

2159 Note that Colebrook's expressions for the friction factor in the transition
 2160 region reduces to Prandtl's smooth pipe equations when the relative roughness
 2161 approaches zero, and reduce to von Karman's fully rough pipe equation at very
 2162 high pipe Reynolds number.

2163 The loss coefficients for elbows are presented as follows, where a and R
 2164 represent the inside radius of the elbow and the radius of curvature of the

centerline of the elbow respectively. For $\text{Re}(a/R)^2 > 91$, the loss coefficient is expressed as follow (Ito, 1960):

$$K_{elbow} = 0.00241 \alpha \theta \left(\frac{R}{a} \right)^{0.84} \text{Re}^{-0.17} , \quad (4.16)$$

where θ is the bend angle in degrees and α is an empirical factor given by Ito as,

$$\alpha_{\theta=90^\circ} = 0.95 + 17.2 \left(\frac{R}{a} \right)^{-1.96} . \quad (4.17)$$

Inputting $R = 1.942$ and $a = 0.442$, $\alpha = 1.9$ and $K_{elbow} = 0.1232$.

A correction term is applied to the 90° elbow to determine the loss coefficient for arbitrary angle of elbow (SAE, 1960).

$$K_\theta = (C_\theta)_{elbow} K_{90^\circ} , \quad (4.18)$$

where C_{elbow} is given in the referenced manual (SAE, 1960). The C_θ is 0.28 at $\theta = 23^\circ$ and $K_\theta = 0.0345$.

The loss coefficient for the reducer or well-rounded inlet loss is $K_{reducer} = 0.05$ based on the flow area of the smaller piping section (Benedict, 1980).

The loss coefficient for the abrupt enlargement is determined by combining the momentum balance over the area of interest. Then, it yields the Carnot-Borda equation, which shows the head loss in the abrupt enlargement. By equating it to the head loss equation Eqn. (4.12), the loss coefficient is given

2185 based on the inlet velocity as follow:

2186

$$K_{enlargement} = (1 - \frac{v_2}{v_1})^2 = (1 - \frac{A_1}{A_2})^2 = (1 - \beta^2)^2 ,$$

2187 $\frac{p_1}{p_2} = 1 + (\frac{1 - G_1}{G_1})(2\beta^2 - 2\beta^4) ,$ (4.19)

2188 where G_1 is the inlet pressure ratio of static pressure to total pressure,
2189 p_t/p_{t1} . The fluid experiences pressure loss when going from a piping system
2190 to a plenum, so called exit loss. According to Eqn. (4.19), the loss coefficient
2191 for exit K_{exit} is 1, where $\beta = 0$. It applies regardless of whether the pipe
2192 protrudes into the exit plenum, is well rounded at exit, or is flush.

2193 Finally, the loss coefficient for the abrupt contraction is given based on the
2194 velocity at exit as follow (Benedict, 1980):

2195

$$K_{contraction} = (\frac{1}{C_D^2} - 1)(1 - \beta^4) ,$$

2196 $C_D = \frac{Q_{acutal}}{Q_{ideal}} ,$ (4.20)

2197 where the discharge coefficient C_D is given in reference (Benedict, 1980).
2198 The mean discharge coefficient is given as 0.815 based on the water tests in
2199 short pipes. According to Eqn. (4.20), this yields a maximum loss coefficient
2200 at $\beta = 0$ of 0.506. Assuming $\beta = A_2/A_1 = 0.9$, $K_{contraction}$ yields 0.1738.

2201 The head losses and the contribution of each geometry are given in Ta-
2202 ble 4.2. Total length of pipe is 87.1 inch. The diameter of inside pipe is 0.884
2203 inch. The diameter of inside nozzle is 0.4 inch. Total pressure head loss is

2204 4.5344 m., which corresponds to ~ 30 % of input pressure head. The main
2205 loss is caused by the exit from nozzle, which is over ~ 50 %. The following
2206 loss is caused by the friction due to the large length, which is ~ 27 %. The
2207 loss from pipe bend is somewhat low comparing with others.

2208 Based on the calculated head loss, the jet velocity at nozzle is determined
2209 assuming the pressure right after the nozzle is atmospheric. The pipe inlet
2210 pressure is given in Fig. 4.15 (a) and 4.15 (b). The elevation of the pipe inlet
2211 and the nozzle is 2.9 inch. The calculated jet velocity from nozzle including the
2212 pressure loss in pipe is 13.4 m/s, which is consistent with the measured result
2213 in Fig. 4.16 where the jet velocity is ~ 13.5 m/s. According to Eqn. (2.76), the
2214 magnetic field increases the fluid pressure by an amount $B^2/2\mu$, in directions
2215 perpendicular to the magnetic field, and decreases the fluid pressure by the
2216 same amount, in the parallel direction of the magnetic field. The fluid pressure
2217 including the magnetic pressure has to balance with the atmospheric pressure
2218 and surface tension of jet and satisfy the continuity condition. The fluid
2219 pressure will find equilibrium point since the fluid pressure perpendicular to the
2220 magnetic field line is mutually symmetric. Therefore, the jet is changing to be
2221 elliptical in Fig. 4.7 (a). Hence, the pressure drop is not occurred significantly
2222 and correspondingly the longitudinal jet velocity is not changed with magnetic
2223 field in Fig. 4.16.

2224 4.3.2.2 the measurement of wall tap pressure

2225 Wall taps is used in order to sense static pressure, wherein small pressure
2226 taps are located at a point on such surface as cylindrical pipe so that it does
2227 not disturb the fluid. Tap size error arises because of a local disturbances of
2228 the boundary layer.

2229

$$\begin{aligned} \text{Re}_d^* &= \frac{v^* d_{tap}}{\nu} , \\ \text{Re}_d^* &= \sqrt{\frac{f}{8}} \left(\frac{d_{tap}}{d} \right) \text{Re} , \end{aligned} \quad (4.21)$$

2231 where d_{tap} is the tap diameter, Re_d^* is the tap Re number, and v^* is the
2232 friction velocity. The friction factor is 0.024. The tap inside diameter and pipe
2233 inside diameter are 0.5, 0.884 inch respectively, which yields $\text{Re}_d^* = 55764$.

2234 At tap Re greater than 385, the error in static pressure caused by the tap
2235 size is given as follow:

2236

$$\frac{e_{tap}}{\tau} = 0.269 (\text{Re}_d^*)^{0.353} , \quad (4.22)$$

2238 where $\frac{e_{tap}}{\tau} = 12.74$.

2239 Combining the Darcy friction factor with the wall shear stress yields

2240

$$f = 4 \left(\frac{\tau}{\rho v^2 / 2g} \right) . \quad (4.23)$$

2242 Therefore, the error in a static pressure can be expresses as non-dimensionalized

2243 form by the dynamic pressure $p_{dynamic}$.

2244

2245
$$\frac{e_{tap}}{p_{dynamic}} = \left(\frac{e_{tap}}{\tau}\right)\frac{f}{4}, \quad (4.24)$$

2246 where $\frac{e_{tap}}{p_{dynamic}} = 0.0764$. The error of static pressure in Fig. 4.15 (a) is

2247 estimated to give 7.64 % uncertainty of the dynamic pressure in Fig. 4.15 (b).

Table 4.1: Error estimation of fiducial length at each viewport.

Viewport number	Fiducial length (cm)	Scaling factor
1	1.0 ± 0.095	1.0 (reference)
2	1.0 ± 0.091	4.3 ± 0.81
3	1.0 ± 0.062	1.0 ± 0.16
4	1.0 ± 0.067	4.3 ± 0.70

Table 4.2: Pressure head losses by geometry in pipe for mercury loop.

Geometry in pipe for mercury loop	Calculated pressure head loss	Percentage in total pressure head loss (%)
Friction by surface roughness	1.4176	60.7
Elbows in pipe bend ($3 \times 90^\circ$, $2 \times 23^\circ$)	0.2629	11.3
Reducer, Contraction in nozzle	0.6553	28

Table 4.3: Parameterized coefficients, its error, and statistics summary of fit function in figures.

Figure	1	2	3	4	5	6	7	8	9	10
4.11(B=0T,V=15m/s)	-0.01448	9.97E-04	0.03375	0.00379	-	-	-	-	13.6445	0.85213
4.11(B=5T,V=15m/s)	-0.01448	9.97E-04	0.03375	0.00379	-	-	-	-	13.85258	0.89937
4.11(B=10T,V=15m/s)	-0.01448	9.97E-04	0.03375	0.00379	-	-	-	-	14.13407	0.96089
4.11(B=15T,V=15m/s)	-0.01448	9.97E-04	0.03375	0.00379	-	-	-	-	14.48514	0.99102
4.11(B=15T,V=20m/s)	-0.01448	9.97E-04	0.03375	0.00379	-	-	-	-	18.85852	2.2851
Figure	11	12	13	14	15	16	17	18	19	
4.11(B=0T,V=15m/s)	-	-	-	-	20	13	25.15504	0.92629	0	
4.11(B=5T,V=15m/s)	-	-	-	-	20	13	25.15504	0.92629	0	
4.11(B=10T,V=15m/s)	-	-	-	-	20	13	25.15504	0.92629	0	
4.11(B=15T,V=15m/s)	-	-	-	-	20	13	25.15504	0.92629	0	
4.11(B=15T,V=20m/s)	-	-	-	-	20	13	25.15504	0.92629	0	

1 : A1 value, **2** : A1 standard deviation,

3 : B1 value, **4** : B1 standard deviation, **5** : B2 value, **6** : B2 standard deviation,

7 : B3 value, **8** : B3 standard deviation , **9** : C1 value, **10** : C1 standard deviation,

11 : C2 value, **12** : C2 standard deviation, **13** : C3 value, **14** : C3 standard deviation,

15 : Number of points, **16** : Degrees of freedom, **17** : Reduced χ^2 , **18** : Adjusted \mathbf{R}^2 , **19** : χ^2 probability.

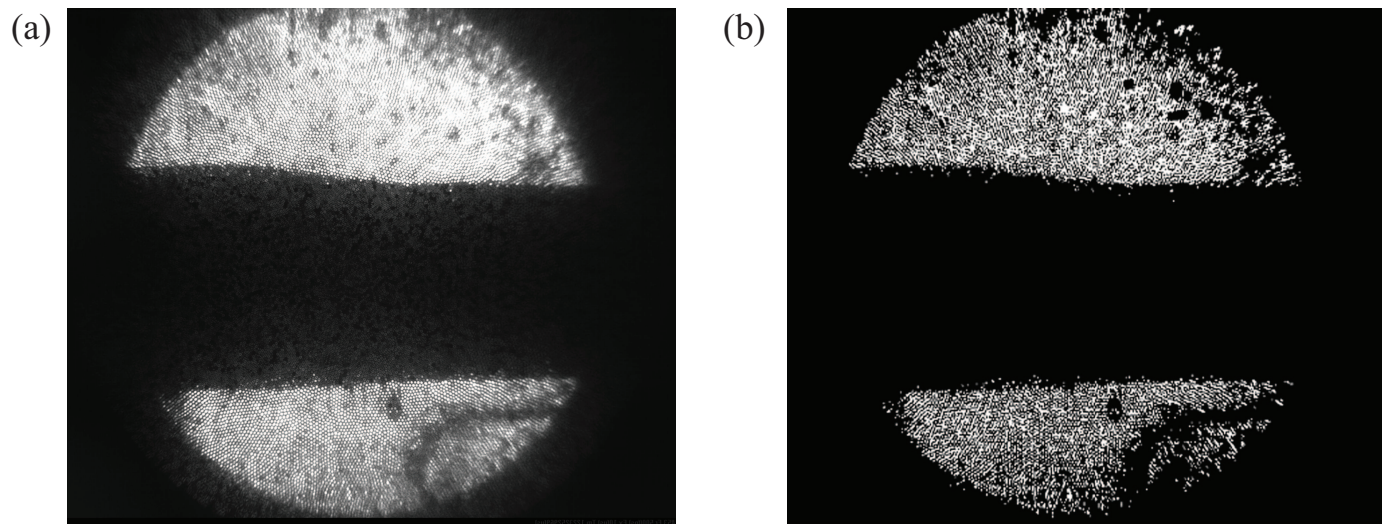


Figure 4.1: Image data conversion for image analysis. a.) Collected image data. b.) 2 bit scaled image data.

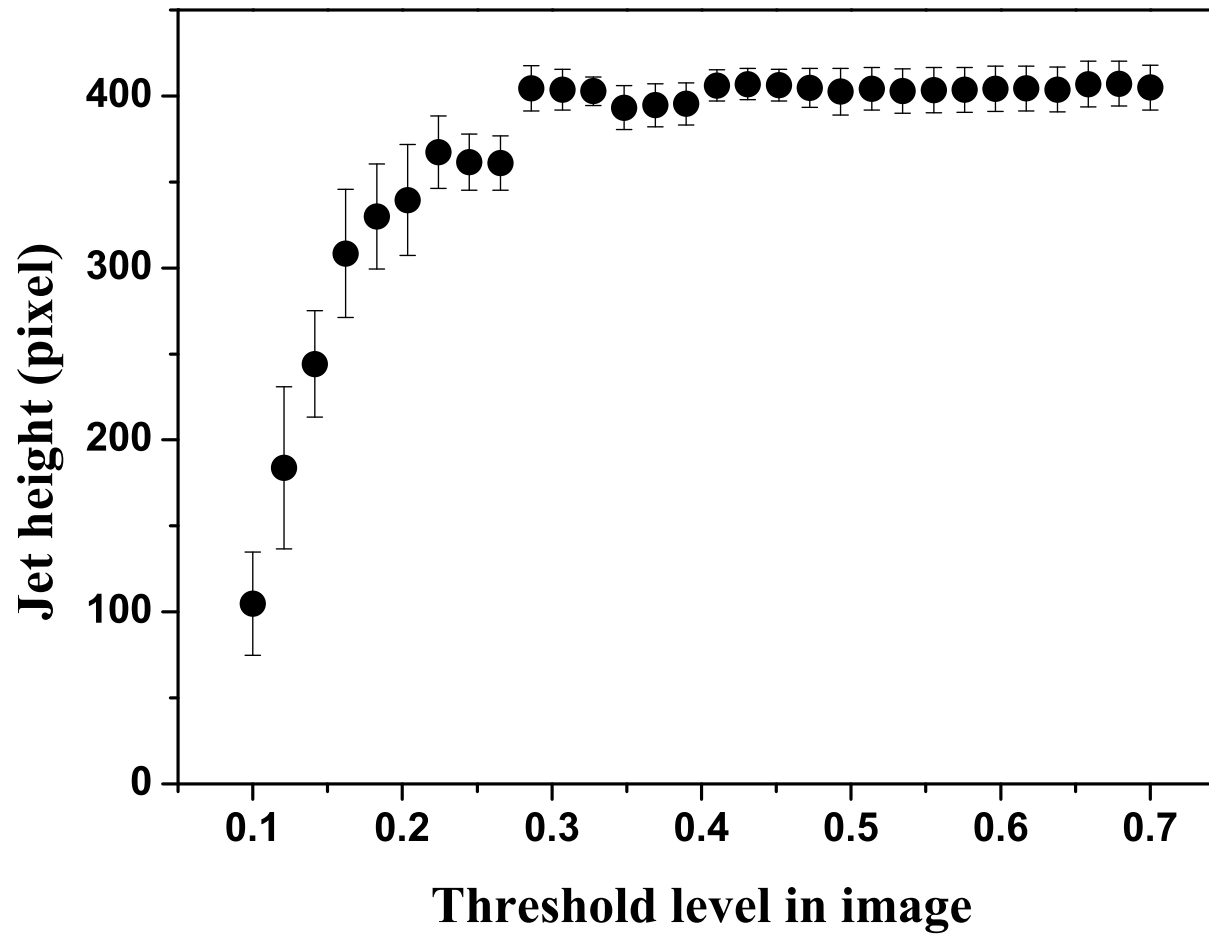


Figure 4.2: Sensitivity of threshold in a 2 bit scaled image conversion.

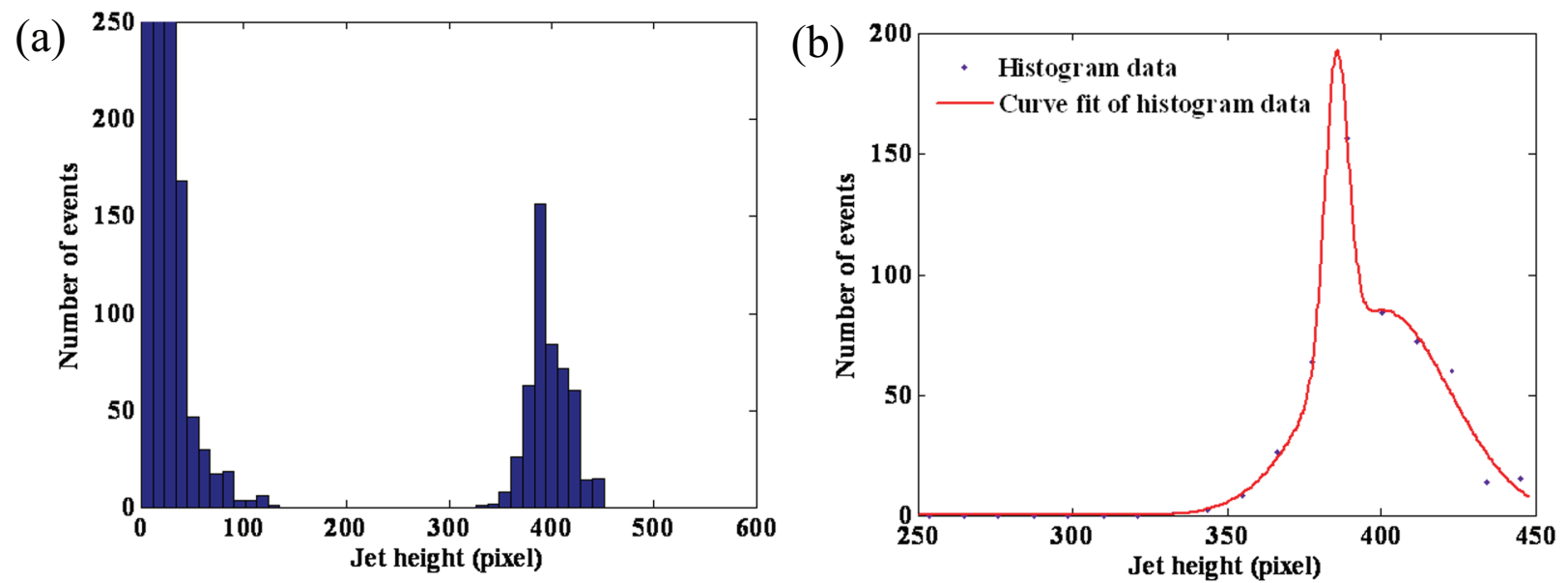


Figure 4.3: Jet height determination from image analysis. a.) Histogram of number of events in the jet height measurement. b.) Fitted histogram distribution.

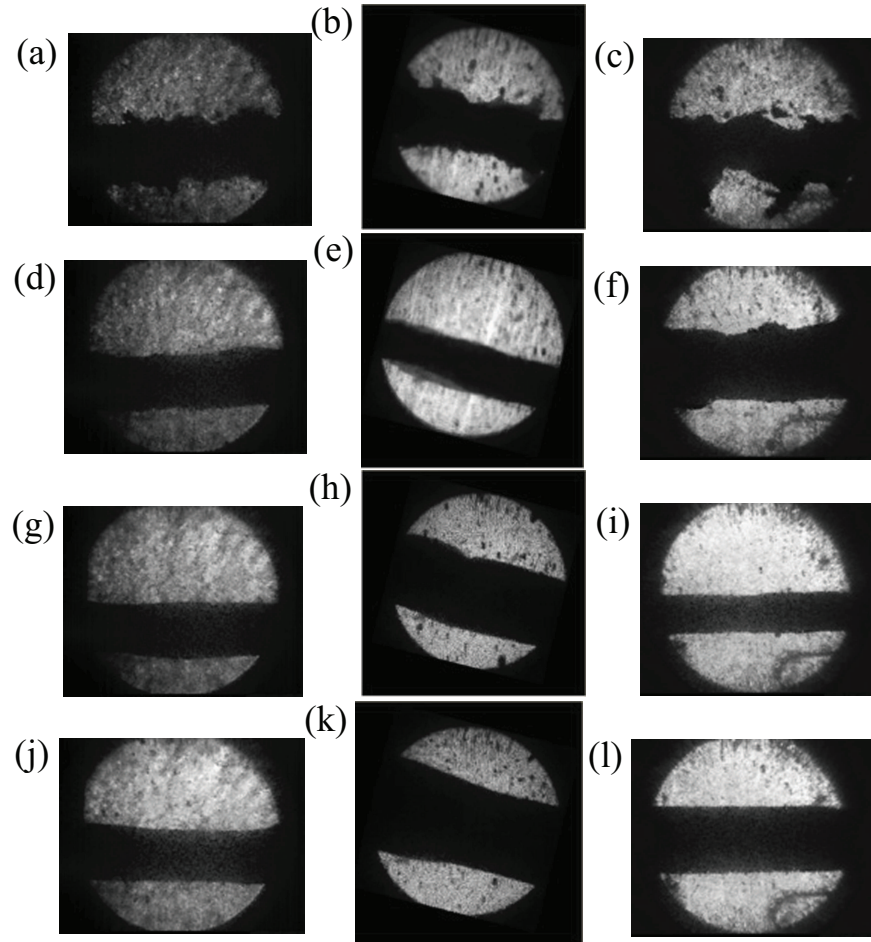


Figure 4.4: Mercury jet flows as observed from the 3 Viewports. The jet flows from left to right on each image. The first, second, and third columns represent Viewport 1, 2, and 3, respectively. The individual caption shows the applied magnetic induction field. The jet velocity is 15m/s. Images on Viewport 2 has a 14° clockwise rotation due to the SMD software. a.) $B=0\text{T}$. b.) $B=0\text{T}$. c.) $B=0\text{T}$. d.) $B=5\text{T}$. e.) $B=5\text{T}$. f.) $B=5\text{T}$. g.) $B=10\text{T}$. h.) $B=10\text{T}$. i.) $B=10\text{T}$. j.) $B=15\text{T}$. k.) $B=15\text{T}$. l.) $B=15\text{T}$.

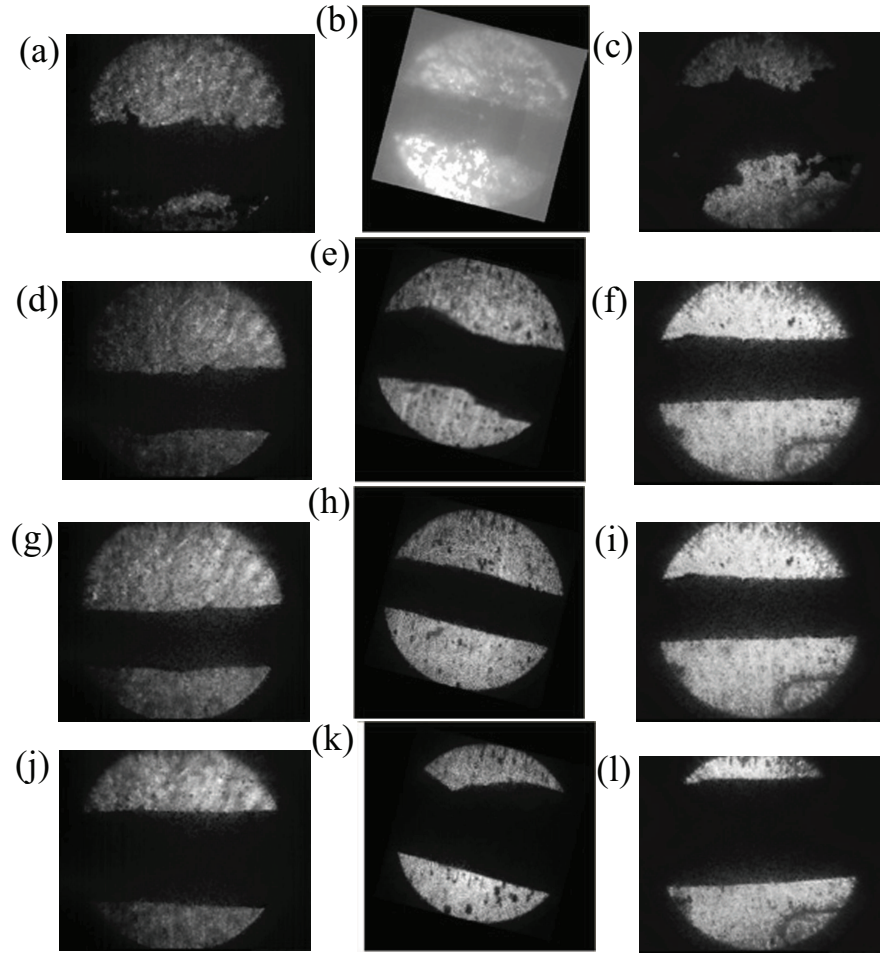


Figure 4.5: Same as Fig. 4.4 but with a jet velocity of 20 m/s. a.) $B=0\text{T}$. b.) $B=0\text{T}$. c.) $B=0\text{T}$. d.) $B=5\text{T}$. e.) $B=5\text{T}$. f.) $B=5\text{T}$. g.) $B=10\text{T}$. h.) $B=10\text{T}$. i.) $B=10\text{T}$. j.) $B=15\text{T}$. k.) $B=15\text{T}$. l.) $B=15\text{T}$.

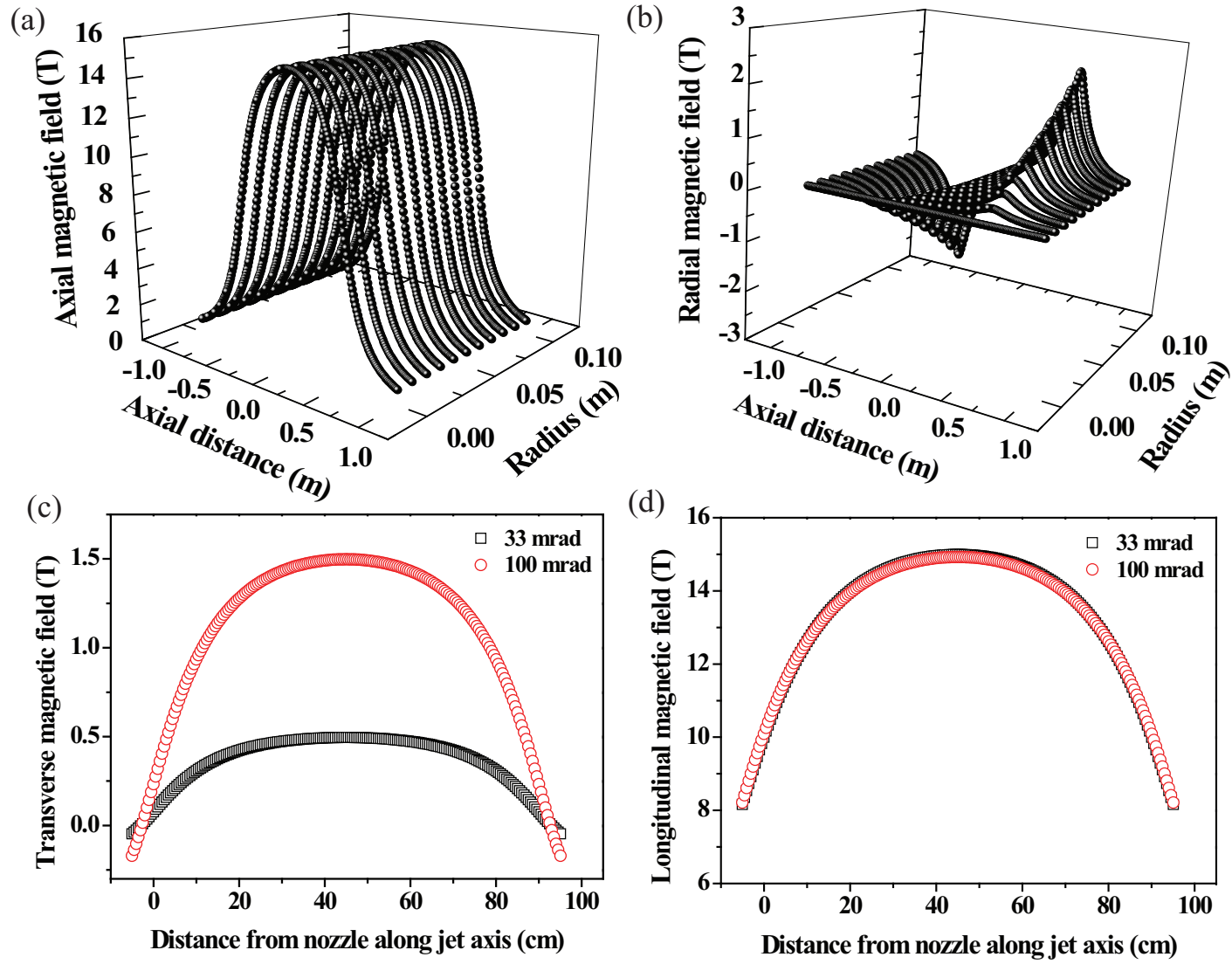


Figure 4.6: Calculated solenoid magnetic induction field map. a.) Radial field map. b.) Axial field map. c.) Transverse component of magnetic induction field along jet axis. d.) Longitudinal component of magnetic induction field along jet axis.

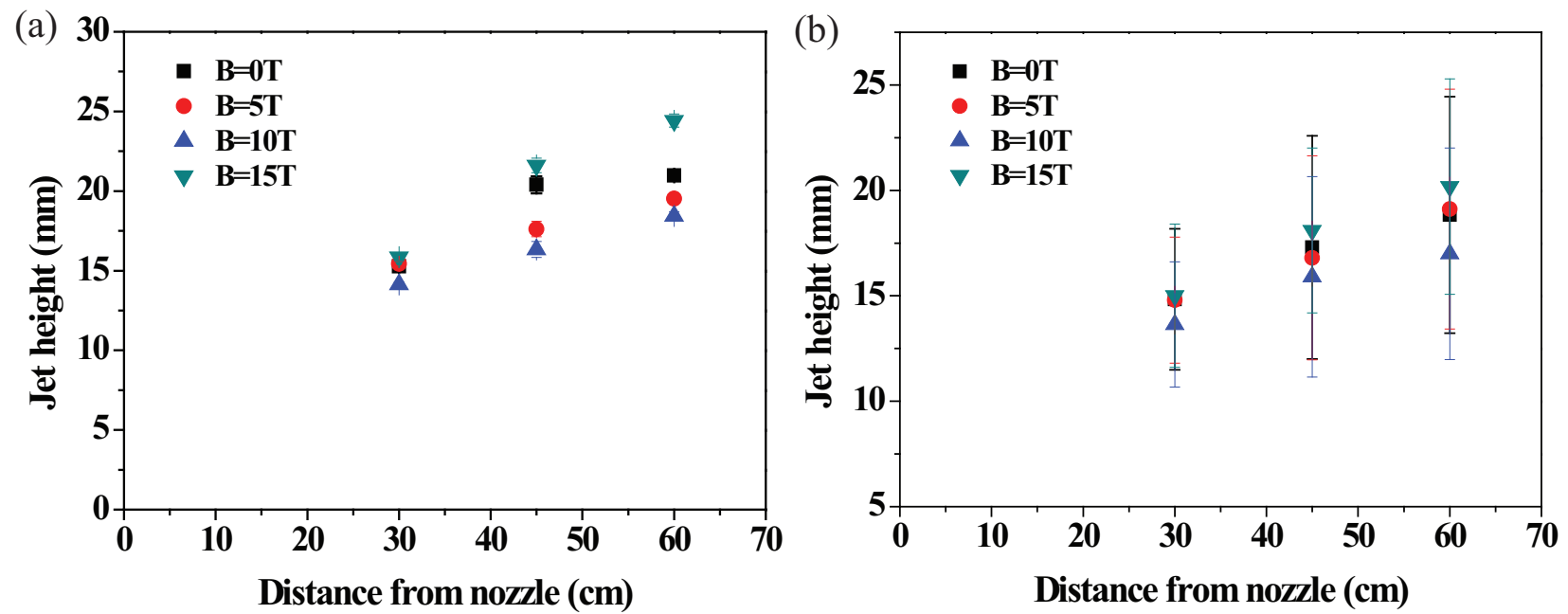


Figure 4.7: Hg jet height measurement in magnetic fields. a.) Histogram fitting of number of events. b.) Direct average of vertical height on each image.

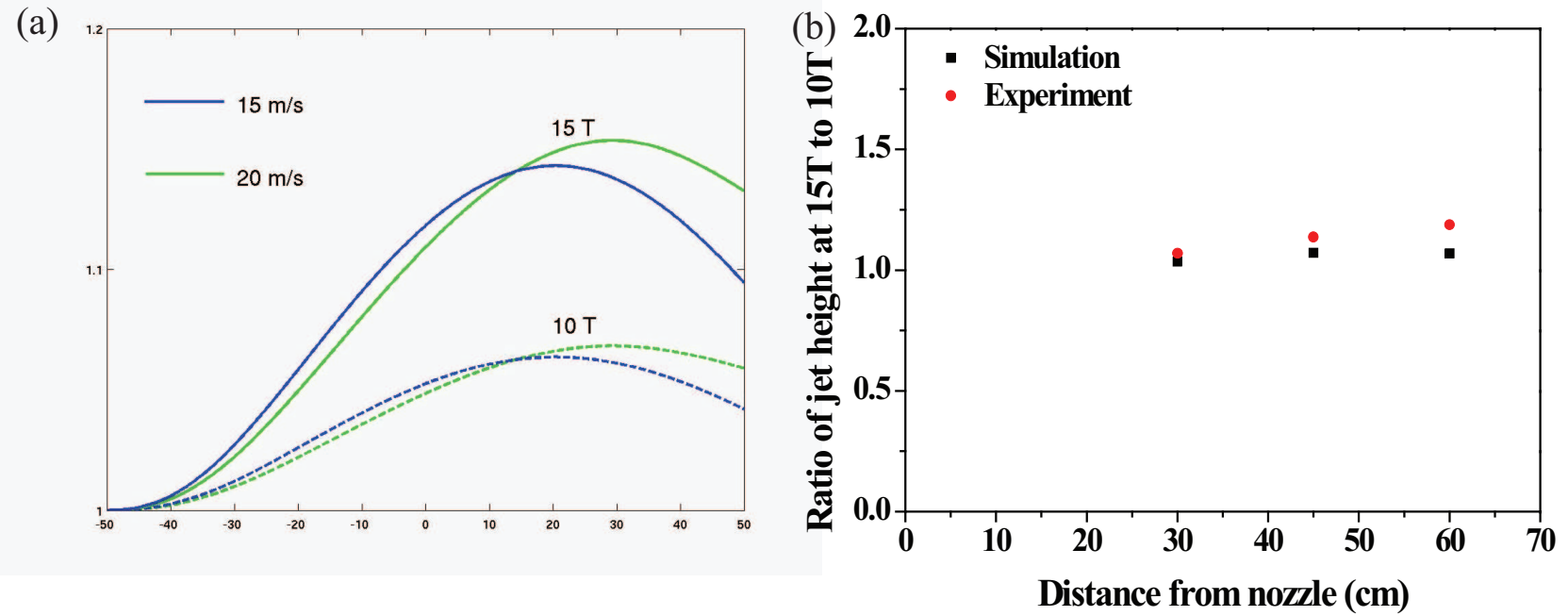


Figure 4.8: Comparison of Hg jet deflection ratio at 15 T to that at 10 T. a.) Numerical calculation of deflection ratio. b.) Comparison of ratio of jet deflection.

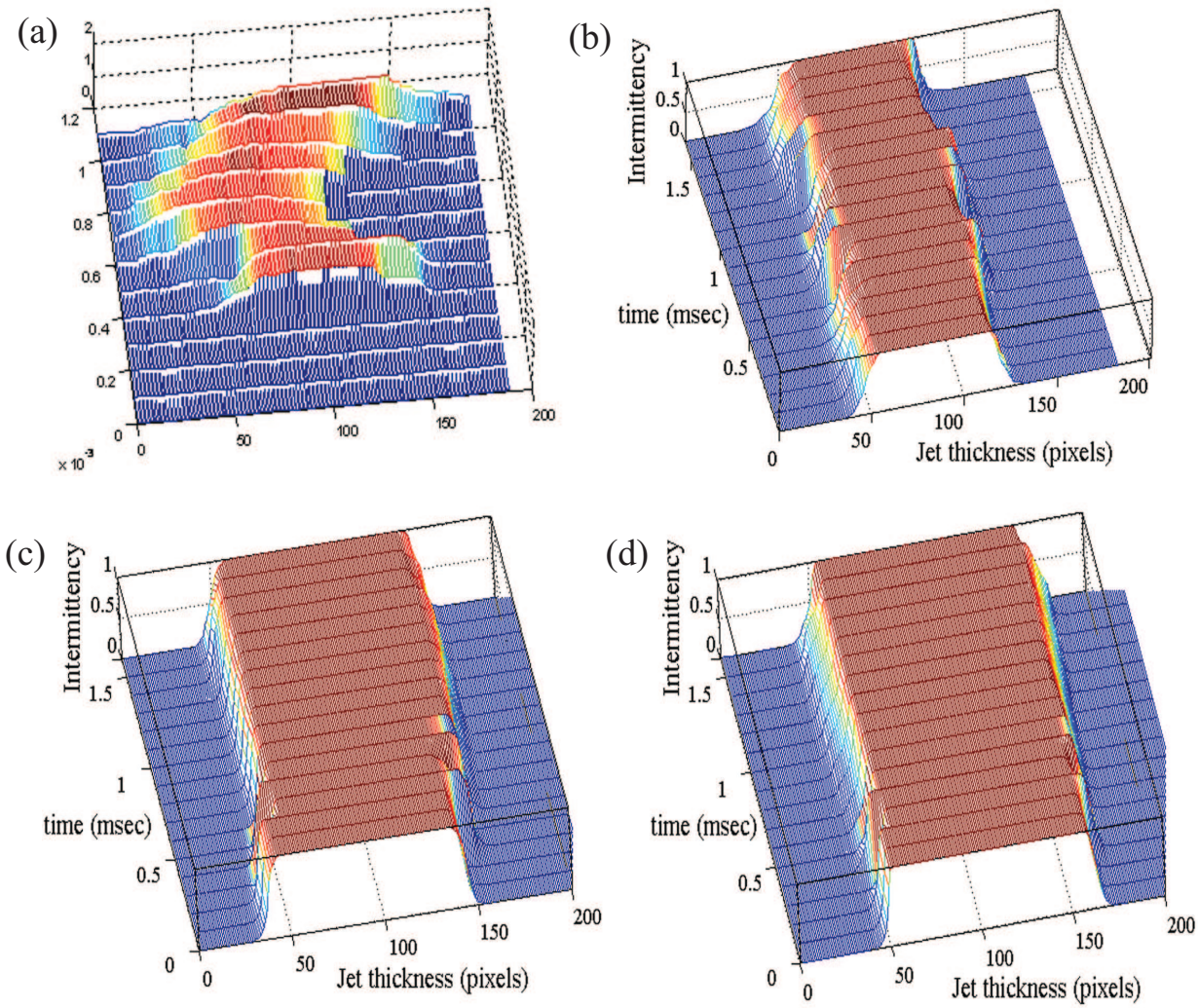


Figure 4.9: Intermittency of Hg jet at Viewport 2. The jet velocity is 15 m/s. a.) $B=0\text{T}$. b.) $B=5\text{T}$. c.) $B=10\text{T}$. d.) $B=15\text{T}$ (continued).

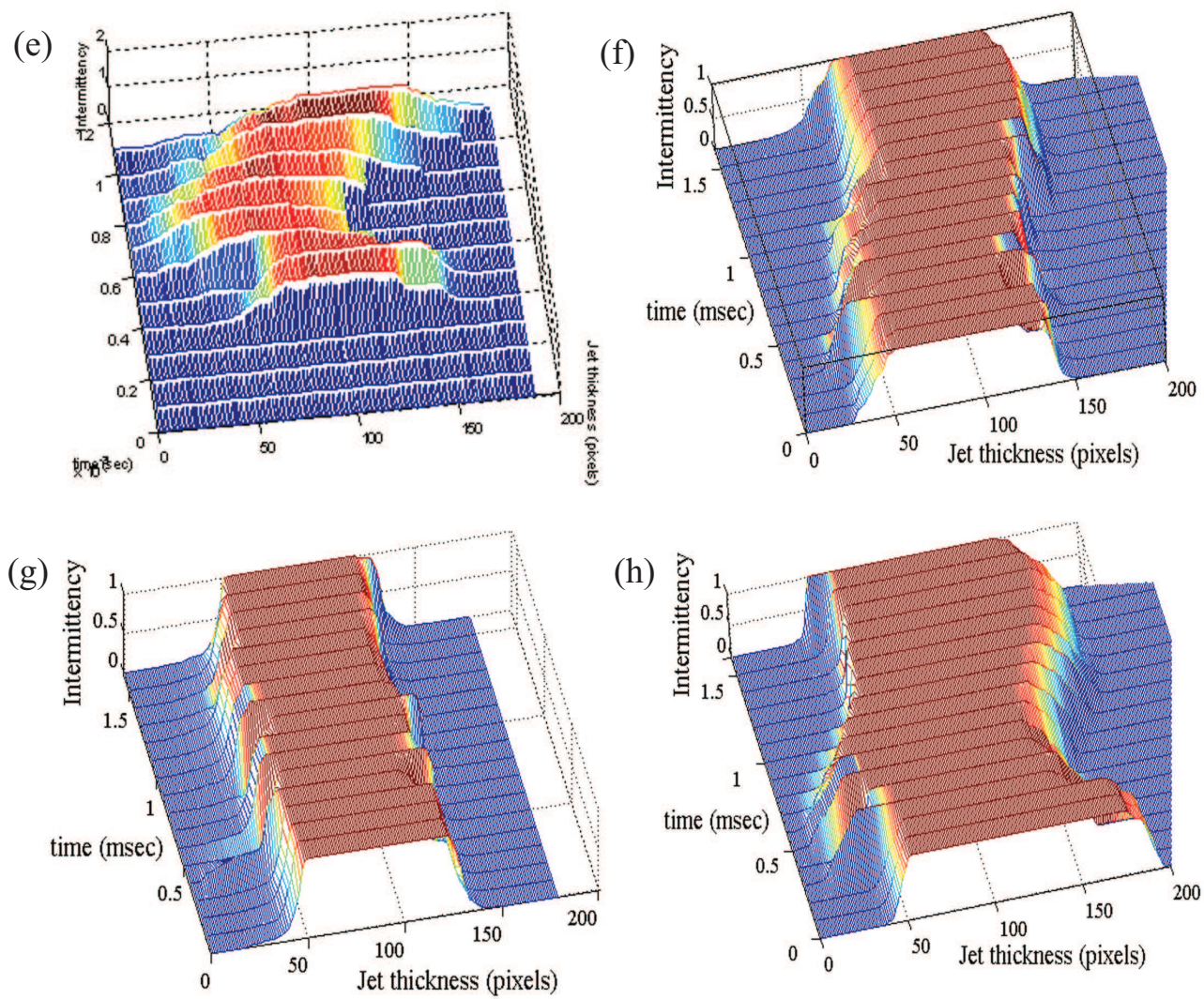


Figure 4.9: Intermittency of Hg jet at Viewport 2. The jet velocity is 20 m/s. e.) $B=0\text{T}$. f.) $B=5\text{T}$. g.) $B=10\text{T}$. h.) $B=15\text{T}$.

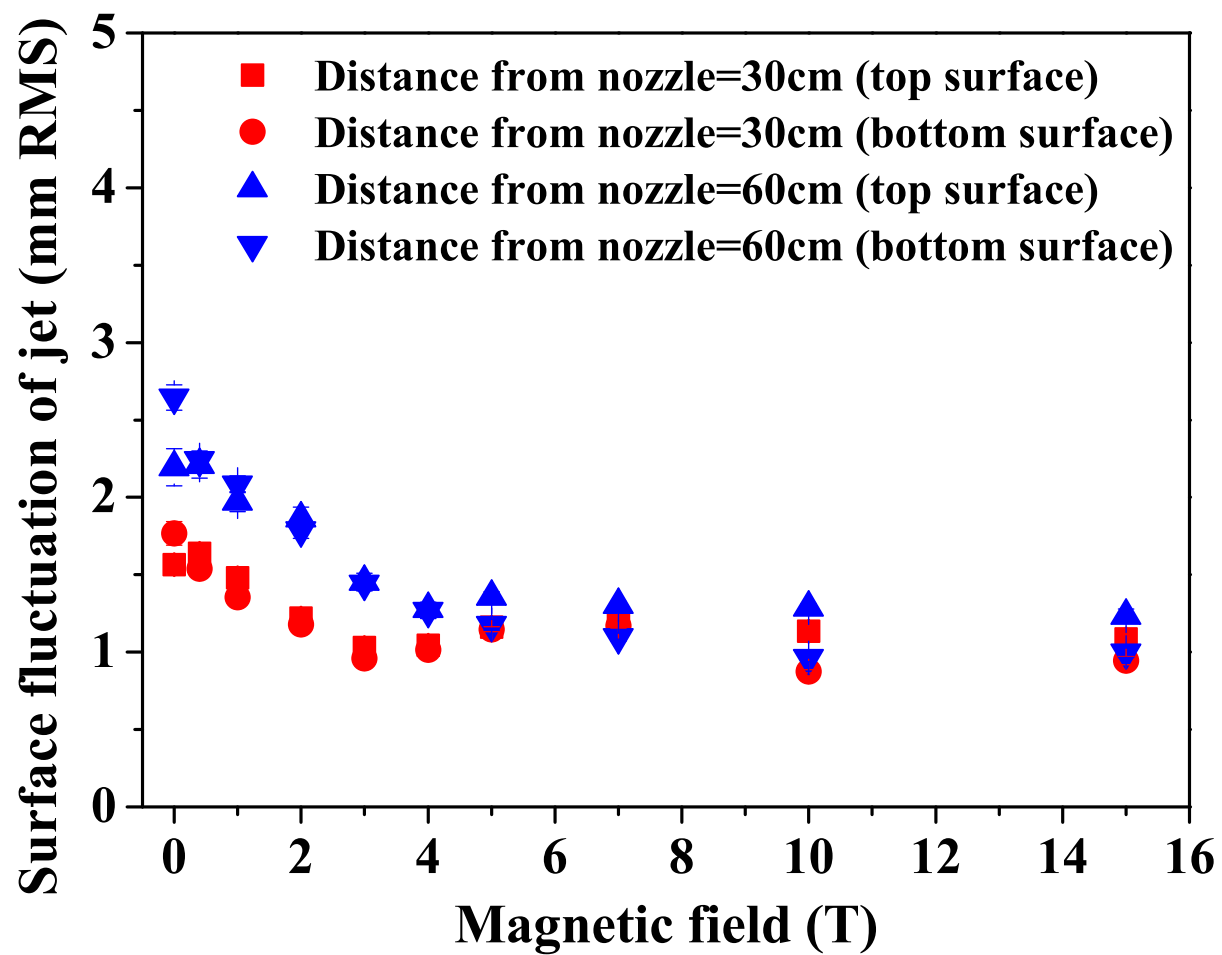


Figure 4.10: Surface fluctuations in a magnetic field.

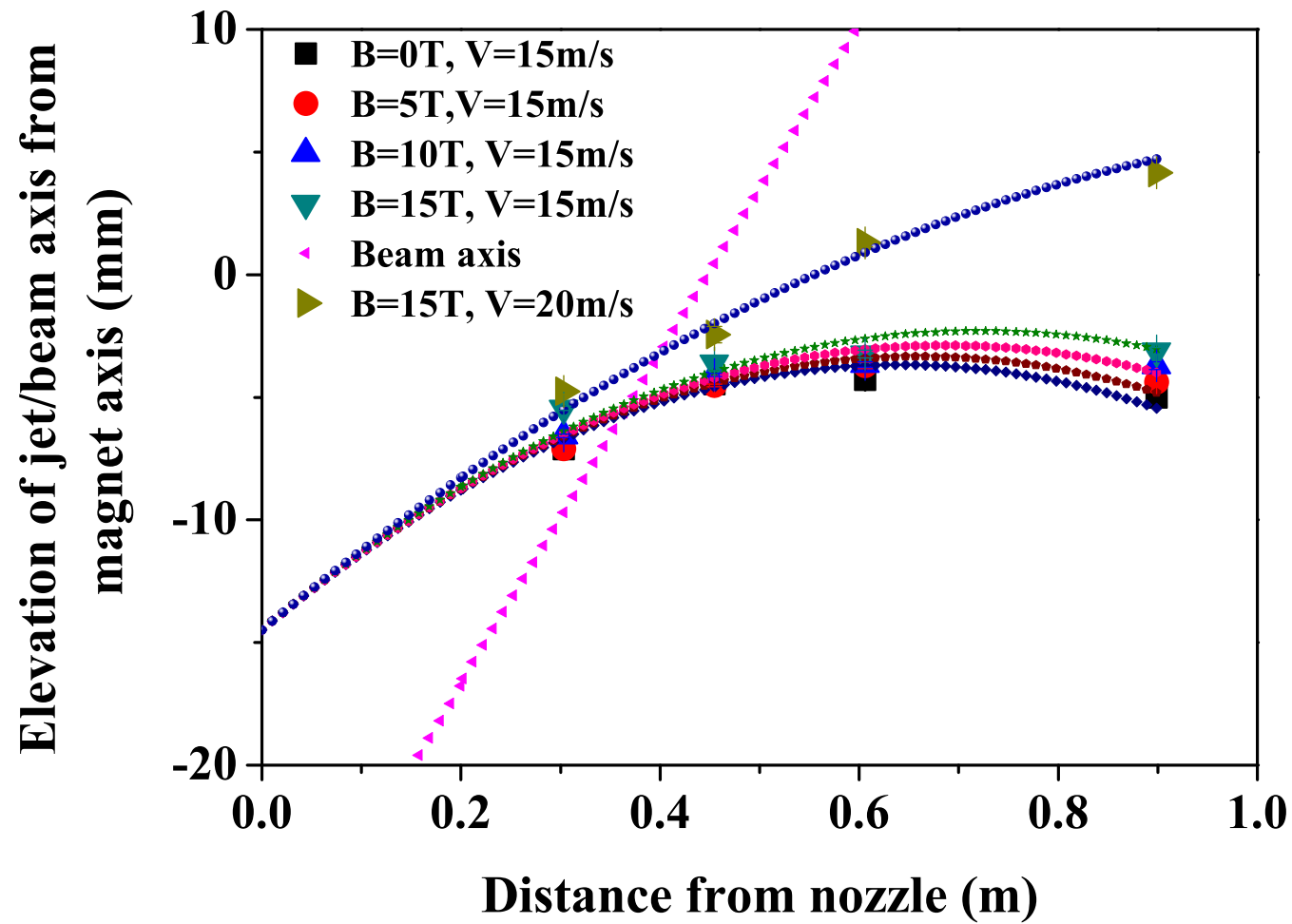


Figure 4.11: Trajectory of beam axis and Hg jet axis projectile with respect to magnetic axis in magnetic field. Solid line represents the simulated value using trajectory of projectile with different velocity.

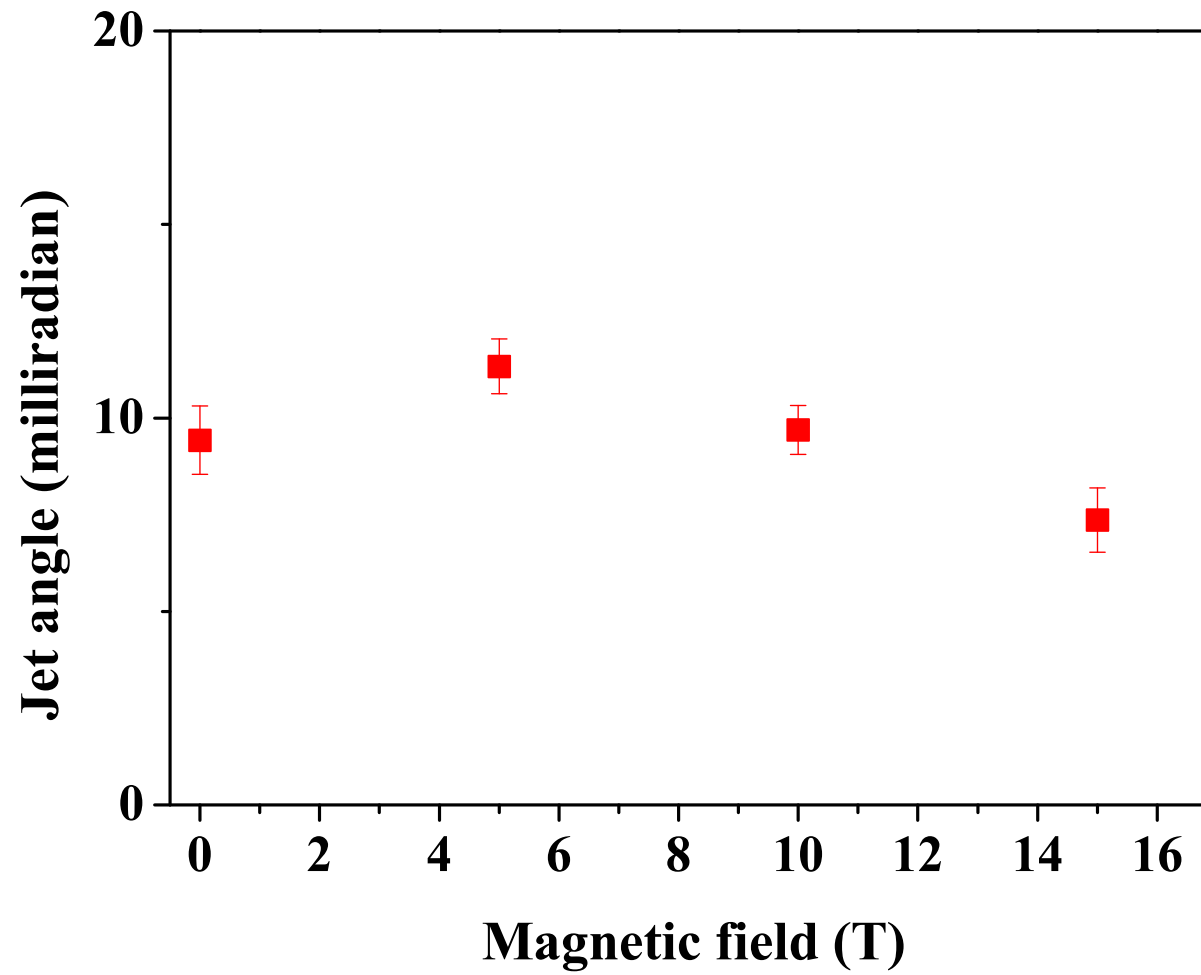


Figure 4.12: Hg jet angle at the center of magnetic axis (Viewport 2) as a function of magnetic field.

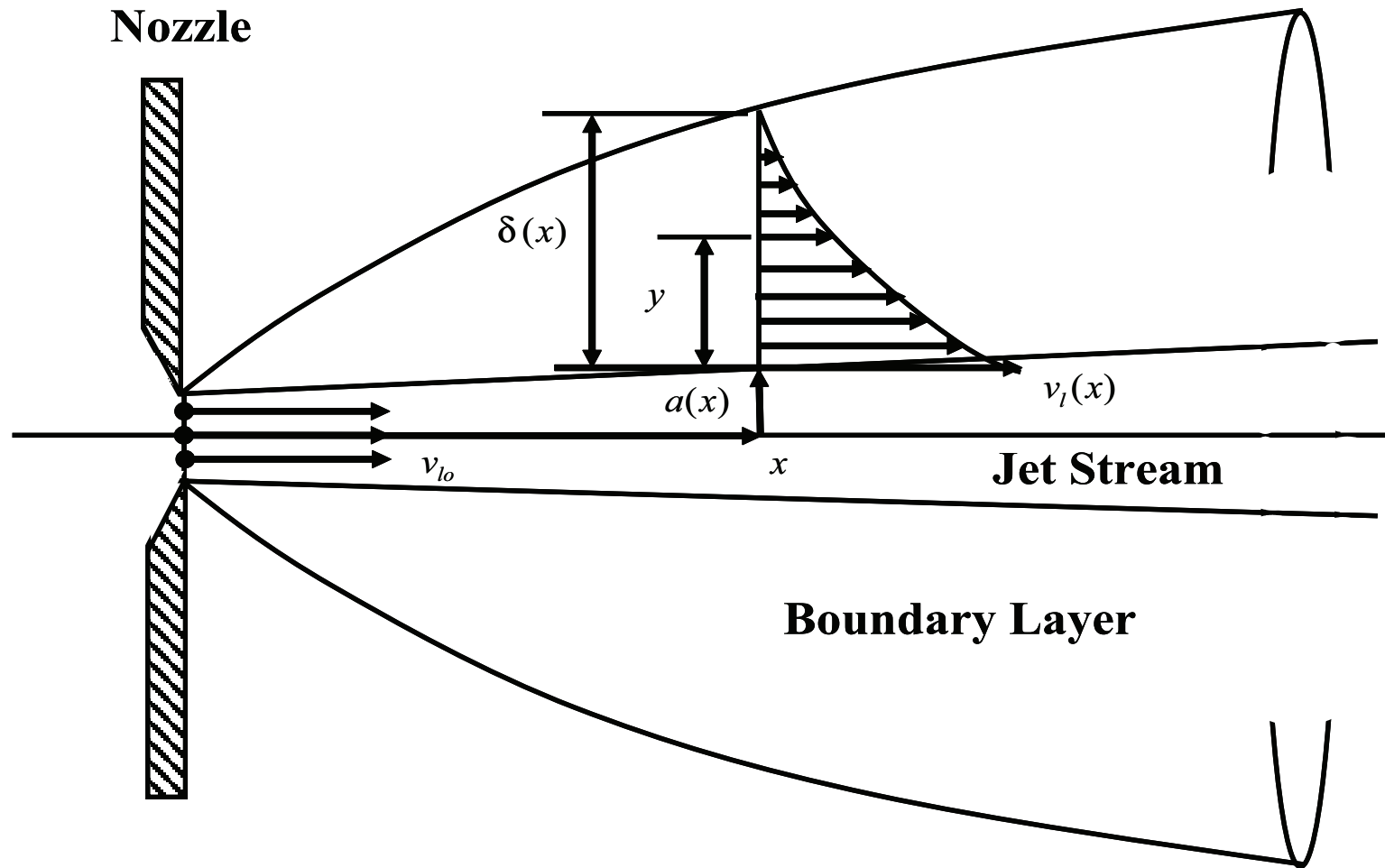


Figure 4.13: Boundary layer induced by a jet emerging from a nozzle.

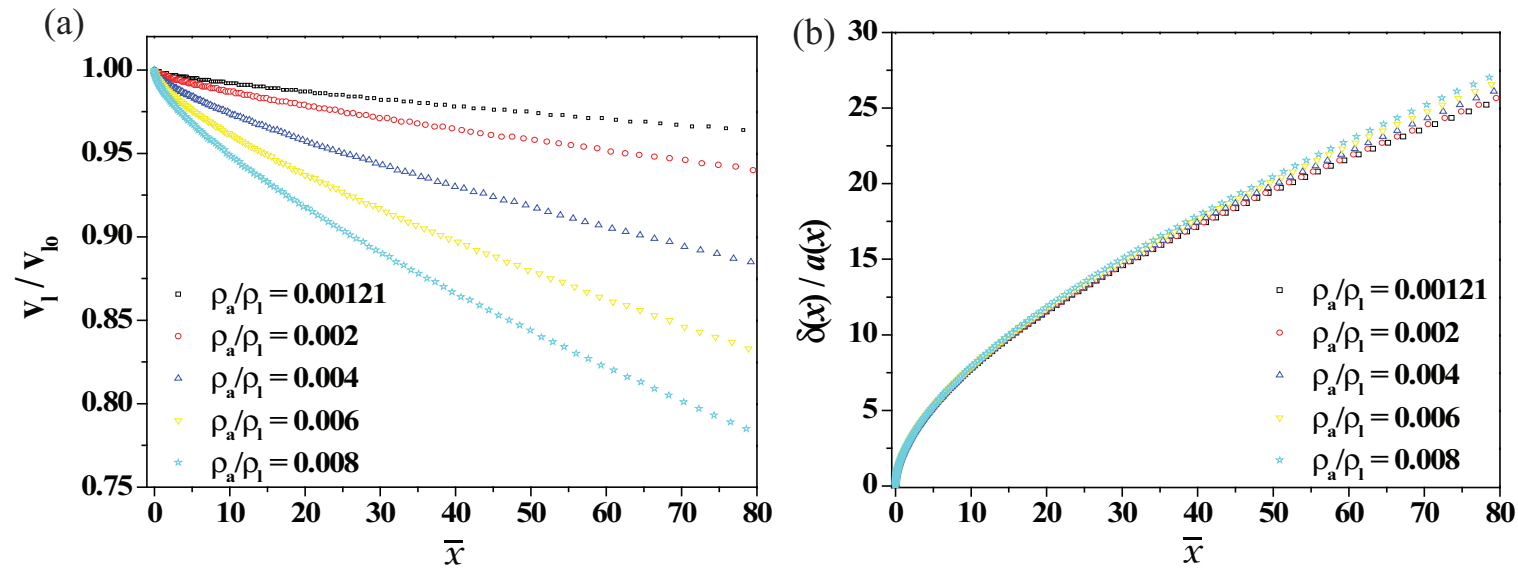


Figure 4.14: Stream velocity and boundary layer thickness for various values of density ratio.

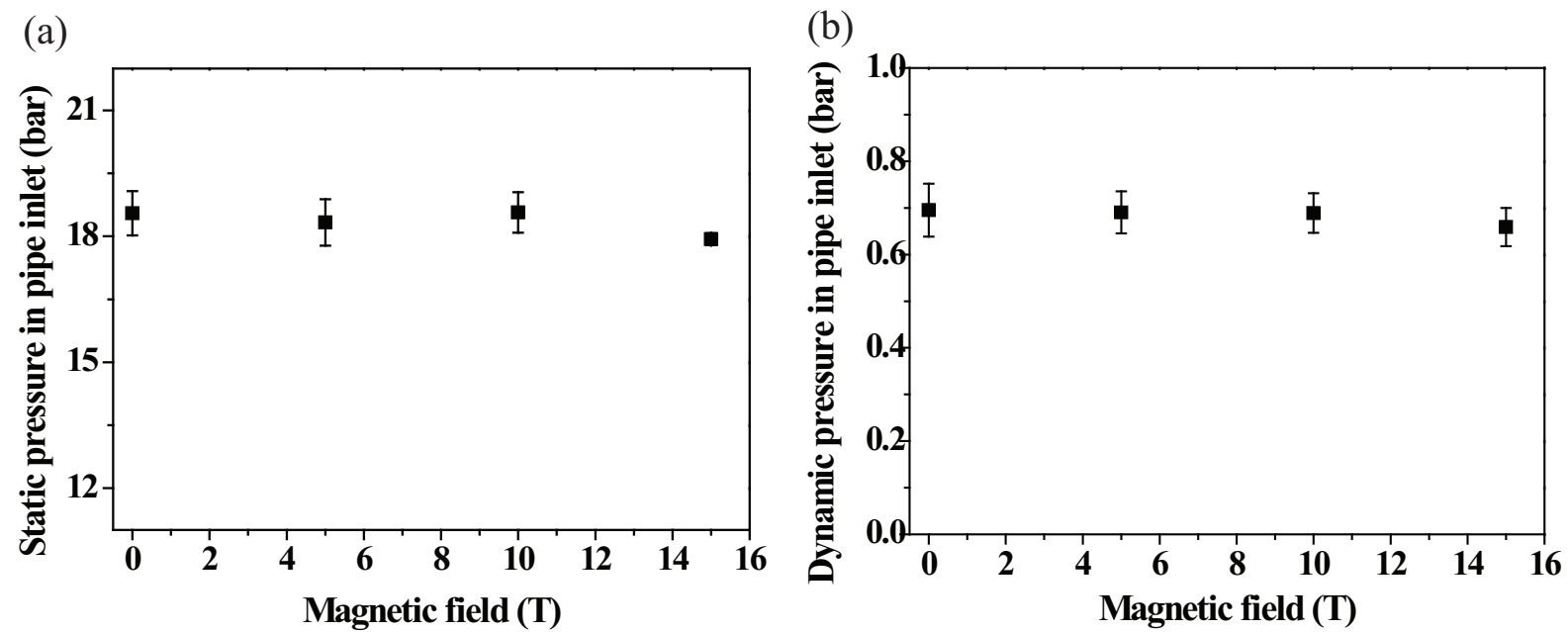


Figure 4.15: Pipe inlet pressure for driving Hg jet. a.) Static pressure. b.) Dynamic pressure.

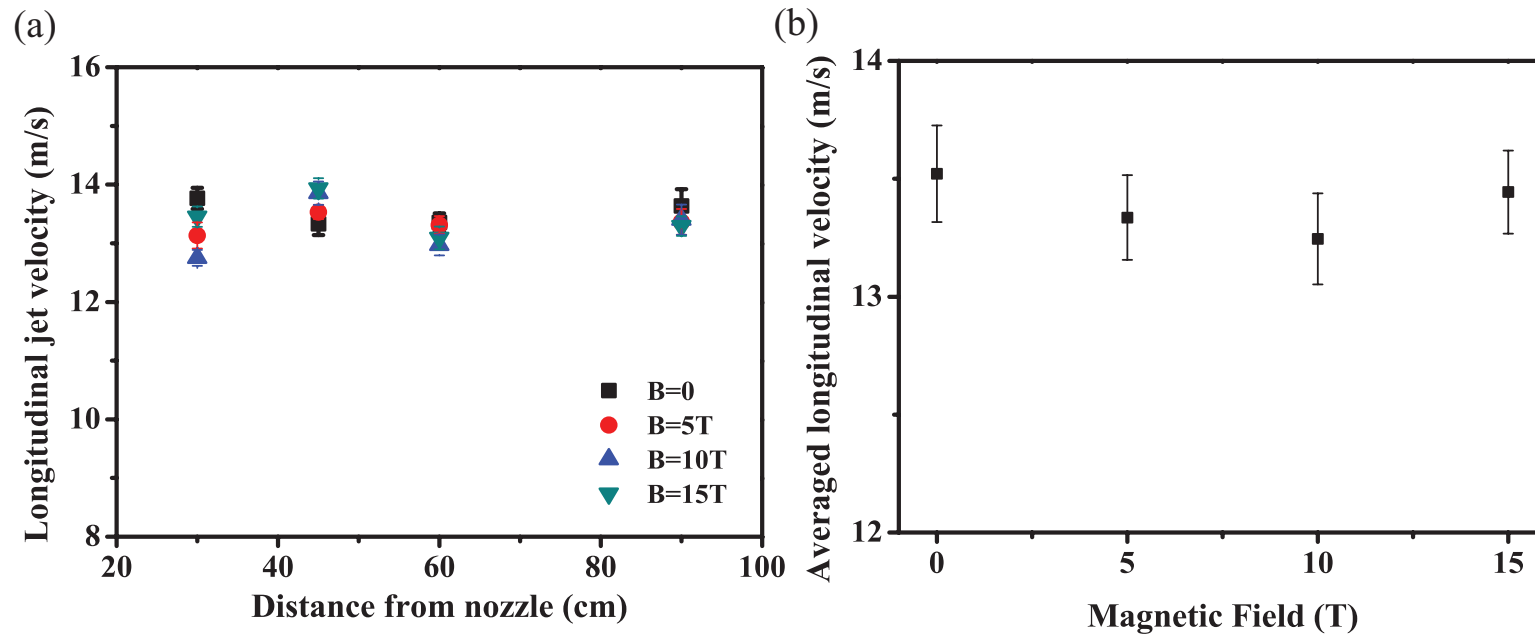


Figure 4.16: Longitudinal Hg jet flow velocity in magnetic field. a.) Velocity at each Viewport dependent of magnetic field. b.) Averaged velocity at each Viewport independent of magnetic field.

2248 Chapter 5

2249 Interaction of an Intense Proton 2250 Beam with Hg Jet in Magnetic 2251 Field

2252

2253 In this chapter, the jet's interacting characteristics in magnetic field are in-
2254 vestigated. The disruption of the jet interacting with various beam intensities
2255 and beam energy is observed and the magnetic suppression to it is discussed.
2256 The captured images show the mechanism of the beam-jet interaction and the
2257 qualitative consistency with the distribution of calculated energy deposition
2258 is discussed. The energy deposition induced by the proton beam generates
2259 filaments on the Hg jet surface due to thermal stresses. The filaments velocity
2260 and its reduction by magnetic field are discussed. It explains that the joule
2261 damping dissipates the kinetic energy on a time scale of joule damping term.

2262 5.1 High Energy Proton Beam Structure

2263 5.1.1 Proton synchrotron machine

2264 Neutrino factories requires a large number of muons, which are obtained
2265 from the decay of pions. Efficient production of pions can be achieved by

colliding an intense proton beam with a high-Z target. An important consideration is the problem of removing the power deposited by the proton beam without interfering with the process of extracting the end-product, which is the muon beam. The response of a liquid target in a high-magnetic induction field will have beam energy effects, which is investigated experimentally. Experiments on the interaction of a 14 GeV/c and 24 GeV/c proton beam with pulse structures of 4 to 16 bunches per pulse and the spot sizes in the order of 2 to 10 mm^2 RMS up to 30 tera-protons(TP) per pulse in magnetic field up to 15 T has been carried out at CERN. Fig. 5.1 (a) shows the infrastructures for experiment at CERN. All equipments for experiment are installed at tunnel TT2/TT2A and these are controlled remotely at control room. The proton beam is delivered from proton synchrotron ring and the beam setup is schematically shown in Fig. 5.1 (b). The PS machine is set up in harmonic 16 bunches and the extracted protons fill the machine in bunch pairs. A bunch in harmonic 8 mode is consisted of a bunch pair. Therefore, a bunch period in harmonic 8 mode is two times of a bunch period in harmonic 16 mode. Each bunch can fill protons up to 2.5×10^{12} . Therefore, the maximum beam intensity can be achieved up to 32×10^{12} protons. Fig. 5.2 shows the layout of tunnel at CERN, where equipments for experiment are installed. Electronic equipments for optical diagnostics, hydraulic power unit, and cryogenic system are positioned at tunnel TT2. Hg loop system, solenoid magnet, and beam diagnostic system are positioned at tunnel TT2A. The fibers for optical diagnostics of Hg target in solenoid magnet and cables for controlling the Hg loop

2289 system and solenoid magnet are connected between TT2 and TT2A passing
2290 through an artificially drilled hole.

2291 5.1.2 Proton beam pulse length

2292 In order to produce the design number of $10^{21} \text{muons/year}$ in the muon
2293 storage ring, 4MW of proton beam power is desired. For our experiment, the
2294 CERN PS ran typically in a harmonic 16 mode. Hence, it is possible to fill with
2295 2×10^{12} protons/bunch and therefore up to 32×10^{12} protons/spill. One beam
2296 pulse consists of several beam bunches. The bunch lengths for harmonic 16
2297 mode are 50 ns and 30 ns at full width at half maximum (FMWH) respectively.
2298 The bunch lengths for harmonic 8 mode are 70 ns and 40 ns at full width
2299 at half maximum (FMWH) respectively. The bunch-to-bunch differences for
2300 harmonic 16 mode and harmonic 8 mode are multiples of 131 ns and 262 ns
2301 respectively. The proton beam pulse structure of harmonic 8 and harmonic 16
2302 in 14 GeV, 6 TP is shown in Fig. 5.18. The spot size at the experiment is in
2303 the order of 2 to 10 mm^2 RMS. This allows to place up to 32×10^{12} protons
2304 on the mercury target, generating a peak energy deposition of $\sim 150 \text{ J/g}$.
2305 Power consumption is dominated by the repetition rate. Thus, the capability
2306 to replace the disrupted jet determines the ultimate beam power. The optimal
2307 interaction length for the 24 GeV beam energy is in the region of 30 cm which
2308 corresponds to approximately 2 interaction length for mercury (Kirk *et al*,
2309 2008). For a 20 m/s jet velocity, replacing two interaction lengths will be
2310 taken in 14 ms thus allowing for operations with a repetition rate of up to 70

2311 Hz. The beam energy per pulse is 115 kJ for a beam of 30×10^{12} protons with
2312 24 GeV beam energy. The disruption length at 30×10^{12} protons with 24 GeV
2313 beam energy in a magnetic field of 15 T is less than 20 cm at 24 GeV beam
2314 energy in Fig. 5.21, thus preserving the 70 Hz beam repetition rate option. It
2315 yields the key result that a target system capable of supporting proton beams
2316 with powers of up to 8 MW (Kirk *et al.*, 2008).

2317 **5.1.3 Proton beam envelope by optics and camera screen**

2318 The proton beam with 14 GeV and 24 GeV beam energy is employed in the
2319 experiment. As the number of protons in a beam pulse increases, it is reported
2320 (Efthymiopoulos, 2008) that the beam spot size increases. The beam spot size
2321 is calculated by CERN using the measured beam emittance, dispersion, and
2322 the momentum spread of the beam particle. The emittance is measured by
2323 measuring the beam profile in a position of known beam parameters based
2324 on optics. Fig. 5.4 shows the estimated 1σ beam spot size at the center of
2325 target based on optics (Efthymiopoulos, 2008). Fig. 5.5 shows the measured
2326 1σ beam spot size at the phosphor camera screen installed ~ 4.2 m away
2327 from the center of magnet before entering the magnet (Skoro, 2008). It is also
2328 reported (Skoro, 2008) that the beam spot size increases as the number of
2329 protons increases. Due to the saturation of image, the measured size is shown
2330 as ~ 2 times larger than the estimated beam spot size from optics. Fig. 5.6 (c)
2331 shows the beam sizes distribution measured by phosphor screen monitor as a
2332 function of time interval between beam shots, where the histogram for events

of beam size in horizontal plane is shown in Fig. 5.6 (a) and the histogram for events of beam size in vertical plane is shown in Fig. 5.6 (b). This plots show that the possible residual saturation of image by phosphor screen monitor is not related with time interval between each beam shot. The distribution of beam spot size is uniform regardless of the possible residual saturation by screen monitor.

5.2 MARS Simulation for Energy Deposition to Mercury Jet by Proton Beam

5.2.1 Physics model

MARS is a Monte Carlo code for inclusive and exclusive simulation of 3D hadronic and electromagnetic cascades, muon and heavy ion transport in accelerator, detector, and shielding components in the energy range from a fraction of an electronvolt up to 100 TeV. In MARS code, hadron production, neutrino interactions, electromagnetic interactions of heavy particles, and electromagnetic showers are considered. For hadron production, information on the nuclides generated in nuclear collisions is scored, or reported in the results of the simulation, which covers a hadron kinetic energy range up to 100 TeV. For neutrino interactions, the model permits the selection of the energy and angle of each particle (ν, e, μ) emanating from a simulated interaction. These particles, and the showers initiated by them, are then further processed in the code. Four types of neutrino interactions are distinguished ($\nu_\mu, \bar{\nu}_\mu, \nu_e, \bar{\nu}_e$) and the model identifies all possible types of neutrino interactions with nuclei. The

corresponding formulas for these processes as well as results of Monte Carlo simulations are considered. For electromagnetic interactions of heavy particles, electromagnetic interactions of muons and charged hadrons in arbitrary materials are simulated. Radiative processes and atomic excitation and ionization with energy transfer are considered. The electromagnetic showers are based on the physics of electromagnetic interactions and it gives electron and photon interactions in composite solid, liquid and gaseous materials (Mokhov, 2000).

5.2.2 Mercury jet modeling in MARS code

Using MARS code, Calculation of energy deposition is performed at Fermi National Accelerator Laboratory (Striganov, 2009). For the modeling of jet in MARS, the experimentally measured Hg jet size and trajectory in magnetic field with assumption of sectionally elliptic jet shape and circular jet shape with equivalent reduced mass density to the initial flow rate from nozzle. The proton beam is passing through the center of magnetic axis. For simplicity, the z coordinate of modeling in MARS defines as 0 at the center of magnetic axis along the direction of magnetic field. Accordingly, the x coordinate of modeling in MARS defines as the vertical direction perpendicular to the direction of magnetic field. The experimentally measured jet size and vertical position to the center of magnetic axis is shown at Fig. 4.7 and Fig. 4.11. The vertical distance in cm in MARS code between center of jet and magnetic axis is employed by using Eqn. (5.1). The experimental measurement of vertical

distance between magnetic axis and the center of jet is given in Table 5.1, where the experimentally measured jet size as well as approximated mass density for the simulation of circular jet case are also given.

$$x_{vert} = -1.4522 - 3.65 \times 10^{-2} \times zz - 3.1672 \times 10^{-4} \times zz^2 + 5.4206 \times 10^{-9} \times zz^4, \quad (5.1)$$

where $zz = z - 46$ in cm.

Fig. 5.7 (a), (b) show the sectional view of elliptic/circular jet and Fig. 5.7 (c) shows the side view of jet interacting with proton beam in magnetic field, which is indicated as arrows. Using MARS code, Calculation of energy deposition with various magnetic field strength and beam intensity is performed at Fermi National Accelerator Laboratory (Striganov, 2009).

5.2.3 Energy deposition to mercury jet

5.2.3.1 *energy deposition in magnetic field*

Fig. 5.8 shows the averaged energy deposition along the jet axis for the case of 3 Tp according to the variation of magnetic field. Calculated energy deposition in each meshed volume is averaged along the jet axis using Eqn. (5.2).

$$\frac{1}{N_{\theta}^r} \sum_r \sum_{\theta=0}^{2\pi} E_{\theta}^r, \quad (5.2)$$

where N_{θ}^r , E_{θ}^r represent the number of meshes along radial angle at each radial distance and its energy deposition respectively. As the magnetic field

increases, the distribution of energy deposition over the jet increases. This indicates interaction of charged particles with magnetic field, so that more atomic excitation and ionization with energy transfer occurs in higher magnetic field. Also, the electromagnetic shower produced by a particle that interacts via the electromagnetic force gives electron and photon interactions in mercury. From the equation of particle motion and Lorentz force in Eqn. (5.3), the momentum of charged particle has an influence of the intensity of magnetic field followed by Maxwell's equations.

$$\frac{d\mathbf{p}}{dt} = e[\mathbf{E} + \mathbf{v} \times \mathbf{B}], \quad (5.3)$$

where e is the charge on the particle and \mathbf{v} is the particle velocity.

5.2.3.2 *geometric distribution of energy deposition in elliptic Hg jet cross section*

Fig. 5.9 (a) shows the radially averaged energy deposition over the orientation in sectional jet area along the jet axis for the case of 3 Tp in 5 T. Calculated energy deposition in each meshed volume is averaged along the jet axis using Eqn. (5.4).

$$\frac{1}{N_{\theta}^r} \sum_r E_{\theta}^r. \quad (5.4)$$

The larger distribution of energy deposition occurs at bottom ($\sim 270^\circ$) of jet where the beam enters. Gradually the larger distribution moves to the top ($\sim 90^\circ$) of jet where the beam leaves. It again gives the consistent result with

Fig. 5.15 (a) and Fig. 5.16 (a), where the profile of energy deposition shows its changes along with the beam path through Hg jet.

Fig. 5.9 (b) shows the axially averaged energy deposition over the variation of magnetic field along the orientation in sectional jet area for the case of 3 Tp. Calculated energy deposition in each meshed volume is averaged along the orientation in sectional jet area using Eqn. (6.2).

$$\frac{1}{N_z^r} \sum_z \sum_r E_z^r, \quad (5.5)$$

where N_z^r , E_z^r represent the number of meshes along axial jet axis at each radial distance and its energy deposition respectively. The larger axially averaged energy deposition is at bottom ($\sim 270^\circ$) of jet and the distribution of energy deposition increases as the magnetic field increases. The geometrical distribution of energy deposition depending on the applied magnetic field does not changes but keeps uniform profile of distribution, which indicates that the profile of distribution is most likely dependent to the shape of Hg jet.

5.2.3.3 *proton beam spot size to the energy deposition*

Fig. 5.11 shows the averaged energy deposition density along the jet axis using Eqn. (5.2) according to the variation of number of protons in 10 T. As shown in Fig. 5.4, the beam spot size increases as the number of protons increase. As a result, the energy deposition density (per proton) decreases due to the decrease of beam intensity caused by increasing beam spot size. Fig. 5.12 shows the variation of peak energy deposition density with respect

to the beam sectional area and magnetic field. The total energy deposition amounts to $\sim 6 \sim 8$ % of the incident beam energy and the total energy deposition is same regardless of the variation of beam spot size. However, the total energy deposition increases as the magnetic field increases. As discussed in Fig. 5.8, it again indicates interaction of charged particles with magnetic field, so that more atomic excitation and ionization with energy transfer occurs in higher magnetic field. Since the beam spot area increases parabolically, the peak energy deposition density decreases parabolically accordingly. The solid line represents the fit of calculation of peak energy deposition density using Eqn. (6.1).

$$E_{peak} = \frac{E_{peak, N=threshold} A_{beam, optics, N=threshold}^{\frac{1}{x}}}{A_{beam, optics}^{\frac{1}{x}}}, \quad (5.6)$$

where $x = 2.6$ is used for fitting of calculated energy deposition in Fig. 5.12. The peak energy deposition density is estimated by fitting using the peak energy deposition density and the estimated beam cross sectional area at threshold beam intensity, so that the peak energy density can be estimated as a function of beam cross sectional area. Based on the result in Fig. 5.12, the number of protons is multiplied to the energy deposition density, which yields the result in Fig. 5.13. The peak energy deposition with respect to the number of protons increases parabolically due to the increase of parabolically approximated beam cross sectional area, which directly influences to the peak energy deposition to Hg jet. Also, the higher magnetic field again results in larger peak energy deposition to Hg jet. As expected, the smaller peak energy de-

position is resulted when the beam spot size from camera is considered, since the larger beam spot size reduces the beam intensity. This study is useful since it allows one to extrapolate the trend for estimation of profile of energy deposition, so that one can approximate the profile of energy deposition over all of the region of Hg jet based on the previous characteristics of relations in energy deposition to magnetic field, beam intensity, and Hg jet shape.

5.3 Observation of Interaction and Hg Jet Response to The Energy Deposition by Proton Beam

5.3.1 Hg jet pressurization by energy deposition of proton beam

The target material is mercury, whose ρ is 13.6 g/cm^3 . The density of the energy deposition E_{dep} due to ionization losses of the protons is $\sim 33 \text{ J/g}$. Additional ionization due to secondary particles from interactions of the protons in the target raises this to a peak of $\sim 100 \text{ J/g}$ at 10 cm into the target (McDonald, 2000). The energy deposition, E_{dep} , leads to peak pressure P that can be estimated as follow:

$$P \approx K \alpha_v \Delta T = \frac{\alpha_v K E_{dep}}{c_p} , \quad (5.7)$$

where α_v is the thermal volumetric expansion coefficient, which corresponds to 3 times of thermal linear expansion coefficient, K is the bulk modulus, E_{dep} is the energy deposition, and c_p is the specific heat capacity. For mercury,

2486 $\alpha_v = 180 \times 10^{-6}/K$, $E_v = 25GPa$, $c_p = 138J/(K\ kg)$. A peak value of
 2487 $E_{dep}=100J/g$ corresponds to a peak stress of ~ 3000 MPa. The mercury target
 2488 will be disrupted by the proton beam, leading to a breakup into droplets. The
 2489 strain energy is built up in the jet due to compression (Sievers and Pognat,
 2490 2000). The strain energy per unit volume can be estimated as follow based on
 2491 the relationship between pressure thermal expansion:

2492

$$2493 \quad E_{strain} = \frac{K}{2}(\alpha\Delta T)^2. \quad (5.8)$$

2494 This deposited strain energy will be released as kinetic energy such as the
 2495 generation of filaments on the jet surface. Hence, it indicates that the thermal
 2496 volumetric expansion is possibly proportional to the jet expansion velocity
 2497 with the coefficient of compressibility of jet material.

2498 **5.3.2 Observation of proton beam interaction and jet** 2499 **breakup**

2500 Fig. 5.14 is the photographs of the typical Hg jet interacting mechanism
 2501 with a 16 TP, 14 GeV/c proton beam at 5 T captured at Viewport 3 at a
 2502 500 μs frame rate, which shows clearly how the Hg jet is responding from the
 2503 sudden energy deposition by the proton beam. The beam hits the Hg jet at
 2504 the bottom surface, passing through the center of jet at Viewport 2, leaving
 2505 the Hg jet on the top surface. The captured photos show the response of the
 2506 Hg jet upstream, midstream, and downstream with the interaction of proton
 2507 beam. There are filaments on the top surface of jet downstream, where the

beam is leaving, and on the bottom surface of the jet upstream, where the proton beam is hitting, entering the target. The jet break up voids midstream where the beam is passing through, possibly caused by the cavitations from energy deposition.

5.3.2.1 *energy deposition calculation with low intensity of proton beam and its observation*

Fig. 5.15 (a) shows the distribution of energy deposition by 24 GeV, 3 Tp intensity proton beam in 5 T. Calculated energy deposition in each meshed volume is averaged along the jet axis and vertical radius of jet using Eqn. (5.9).

$$\frac{1}{N_{\theta}^r} \sum_{\theta=0}^{2\pi} E_{\theta}^r, \quad (5.9)$$

where N_{θ}^r , E_{θ}^r represent the number of meshes along radial angle at each radial distance and its energy deposition respectively.

The spot size from optics is used. The energy density distribution is plotted depending on the radial position of Hg jet from jet center. Therefore, the peak of energy density exists respectively depending on the radial position in analysis. It shows that the maximum energy deposition density is obtained at the bottom surface of jet at ~ 13 cm from the center of magnet, where Viewport 1 is actually positioned, and the peak energy deposition density moves to the center of the Hg jet followed by the larger energy deposition density is located at the top surface of the Hg jet. The peak energy deposition density is moving corresponding to the beam crossing trajectory in Hg jet. The

most dense energy deposition is distributed at the center of Hg jet between upstream and midstream, where the Hg jet breaks. The collected photos in Fig. 5.15 (b) clearly supports these simulation results, where the frame rate is 2 ms and measured disruption length at Viewport 3 is 11 cm.

5.3.2.2 *energy deposition calculation with high intensity of proton beam and its observation*

Fig. 5.16 (a) shows the distribution of energy deposition by 24 GeV, 10 Tp intensity proton beam in 5 T. Averaged energy deposition is also calculated using Eqn. (5.9). The distribution profile of energy deposition throughout Hg jet is similar with low intensity of beam. The collected photos in Fig. 5.16 (b) clearly supports these simulation results again, where the frame rate is 2 ms and measured disruption length at Viewport 3 is 17 cm. However, the jet breakup voids the midstream where the beam is passing through, which is different with comparing with the observation of low intensity beam. These voids are not observed at 3 Tp intensity of beam, possibly indicates threshold of the existence of cavitation induced by energy deposition.

5.3.3 Hg jet disruption and magnetic suppression of the disruption

The disruption length is determined by counting the number of frames at Viewport 3 where the complete disruption of the jet is observed. The time delay between Viewport 2 and Viewport 3 is 10 ms. Thus, the disruption generated at Viewport 2 by the beam could be observed at Viewport 3 after 10

ms, where the jet is moving with a velocity of 15 m/s. Each image is separated into 10 segments vertically in order to locate the position of disruption. Thus, the accuracy of the measurement to define the location of starting(ending) disruption in measurement could be increased. The disruption length is given by multiplying the frame rate by the counted number of images and investigated with the beam energy, beam intensity, and magnetic field. 230 events out of 360 beam shots are evaluated for the disruption length. About 130 events out of 360 beam shots are evaluated for the detection of particles without Hg jet. Thus, the images for these events are not collected. Fig. 5.17 shows the standard deviation of the evaluated disruption lengths with respect to the disruption length. The solid line represents the curve fitted approximation of the reduced data distribution, where the line asymptote logarithmic. This curve fitted line is used for estimation of the standard deviation of the disruption length at respective disruption length. Correspondingly, the error bar is determined by dividing the the estimated standard deviation by the root square of the number of samples N for each data point.

5.3.3.1 *characteristics of beam structure in disruption length, harmonic 8 and 16*

The proton beam pulse structure of harmonic 8 and harmonic 16 in 14 GeV, 6 Tp is shown in Fig. 5.18. Fig. 5.19 shows the dependence of the disruption length of the Hg jet on the proton beam pulse structure with a 14 GeV beam in 5 T. A pulse contains same total protons. Doubled bunches shows doubled disruption length. It indicates that the energy deposition by

the collision of Hg and protons is same, but the disruption of Hg jet is more likely affected by the number of protons in each bunch and time difference in a pulse due to the different bunches, i.e, 8 bunches and 16 bunches, though there are same protons in a pulse. The disruption on the Hg jet surface disappears when the beam intensity is less than ~ 4 Tp in Fig. 5.20. The threshold of beam intensity is ~ 4 Tp at 14 GeV in 5 T. Fig. 5.19 also indicates that the harmonic 8 pulse structure can increase the threshold of disruption for a bunch of beam intensity. Considering that the different beam pulse structure results in different disruption to Hg due to the time difference of bunches in a pulse structure, we consider only harmonic 16 pulse structure for the following experiment.

5.3.3.2 *disruption length with 14 GeV proton beam*

Fig. 5.20 shows the disruption length with beam intensities up to 30 Tp for a 14 GeV beam. The peak energy deposition to Hg with 14 GeV beam energy at 30 Tp is ~ 70 J/g by approximating it from Fig. 5.13 and the ratio of energy deposition by 14 GeV and 24 GeV respectively, where the disruption length corresponds to ~ 23 cm \pm 5 cm for 10 T to ~ 18 cm \pm 5 cm for 15 T respectively. At high intensities of beam, the disruption length appears to be approaching an asymptotic level. The magnetic field reduces effectively weak disruption such as the generation of the filaments on the jet surface. The threshold of the disruption for beam intensity is around 4 Tp at 5 T and the magnetic field can increases it, though the effect is not clear in Fig. 5.20 due to

the difficulty in quantifying and measuring the small amount of the disruption length.

5.3.3.3 *disruption length with 24 GeV proton beam*

Fig. 5.21 shows the disruption length with the beam intensities up to 30 Tp for a 24 GeV proton beam. The disruption length is estimated by measuring the extent of energy level of Hg jet larger than the energy experimentally determined by threshold intensity of beam as follow :

$$L^{disruption} \text{ over } E \geq E_{threshold}^{peak}, \quad L_{E_{threshold}^{peak}}^{disruption} = 0, \quad (5.10)$$

where $L^{disruption}$, $E_{threshold}^{peak}$ represent the length of disruption and peak energy of thresholding intensity of beam experimentally determined for jet disruption.

According to Fig. 5.13, the peak energy deposition to Hg with 24 GeV beam energy at 30 Tp in 10 T is ~ 130 J/g, where the disruption length corresponds to ~ 22 cm \pm 5 cm for 10 T to ~ 17 cm \pm 5 cm for 15 T respectively. The results show that the magnetic field suppresses the disruption length. The disruption length appears to be approaching an asymptotic level. If there is no magnetic field, the disruptions are always generated by proton beam regardless of the beam intensities, though very weak disruptions on the Hg jet surface are observed with low beam intensities. The threshold of the disruption for beam intensity is ~ 2 Tp at 5 T but the higher magnetic field increases it. The estimation of disruption length in 10 T based on the calculation of energy deposition using the beam spot size from optics is well agreed with the exper-

imental measurement, but the estimation in 0 T based on the beam spot size from optics underestimates the experimental results. Possibly, the difference in MARS model may cause the difference of energy deposition calculation and the beam spot size is more likely to be larger at 0 T. Therefore, possibly the estimation by energy deposition from larger beam spot size is more likely to be fit to the experimental measurement. However, the estimation in 0 T based on the beam spot size from camera screen is well agreed with the experimental measurement at 0 T. For theses estimations, the independent threshold of beam intensity is chosen individually from the experimental results depending on the conditions of individual cases for estimation. Therefore, the energy for threshold is differently used for the case of estimation using the beam size from optics and camera. For the case of estimation of 0 T , 5 T, and 10 T, 0.8 Tp, 1.5 Tp, and 3.7 Tp of threshold beam intensity is chosen respectively.

5.3.3.4 *validation of measurements of Viewport 3 through comparison with Viewport 4*

In order to validate measurements of the disruption length at Viewport 3, measurements of disruption lengths at Viewport 4 are also performed. Fig. 5.22 (a) shows the disruption length at Viewport 3 for 23 events with a harmonic 16 beam structure, 16 Tp, 14 GeV beam energy in 5 T. Fig. 5.22 (b) shows the disruption length at Viewport 4 for the same events. Fig. 5.22 (c) shows the difference of disruption length between Viewport 3 and Viewport 4 for the same events. The solid line represents the average and distribution of the disruption length difference. The difference of measured disruption length

2642 between Viewport 3 and Viewport 4 is 1.3 ± 3.5 cm. The reason for the differ-
2643 ence of the disruption length measurement between Viewport 3 and Viewport
2644 4 is mainly caused by the fluctuation of the proton beam and the Hg jet in
2645 a magnetic field. The reduction of surface instabilities by the presence of a
2646 static magnetic field is a consequence of magnetic damping. Also, surface
2647 structure is frozen by magnetic field. Therefore, the same disrupted shape on
2648 the jet surface at Viewport 3 is observed at Viewport 4 without variation of
2649 the disruption length.

Table 5.1: Measurement of vertical distances of center of jet from magnetic axis and jet size for modeling in MARS code for the cases of elliptic and circular jet sectional shape.

1 (T)	2 (mm)	3 (mm)	4 (mm)	5 (mm)	6 (mm)	7 (mm)	8 (g/cm^3)
Elliptic jet shape							
0	7.11	4.46	4.28	5.01	8.65	2.9	13.55
5	7.1	4.52	3.7	4.38	8.4	3.0	13.55
10	6.57	4.08	3.66	3.71	7.95	3.15	13.55
15	5.45	3.6	3.24	3.11	9.05	2.76	13.55
Circular jet shape							
0	7.11	4.46	4.28	5.01	8.65	8.65	4.50
5	7.1	4.52	3.7	4.38	8.4	8.4	4.77
10	6.57	4.08	3.66	3.71	7.95	7.95	5.32
15	5.45	3.6	3.24	3.11	9.05	9.05	4.11

-
- 1** : Magnetic field
2 : Vertical distance at Viewport1
3 : Vertical distance at Viewport2
4 : Vertical distance at Viewport3
5 : Vertical distance at Viewport4
6 : Vertical radius of jet
7 : Horizontal radius of jet
8 : Hg density

Table 5.2: Parameterized coefficients, its error, and statistics summary of fit function in figures.

Figure	1	2	3	4	5	6	7	8	9	10
5.12a	0.74078	0.03855	-0.06864	0.01598	0.50641	0.05307	-	-	1.48078	0.0158
5.12b	0.02228	8.60E-04	-1.09835	0.36388	0.0613	0.00759	-5.49E-04	1.62E-04	1.36185	0.01097
5.13a	0.06023	0.0073	0.80386	0.0105	-	-	-	-	1.5568	0.04025
5.13b	3.52931	0.3187	0.88872	0.01003	0.02553	0.01138	0.3758	0.16582	1.4208	0.02953
5.19a	1.43E-04	1.86E-05	647.56071	89.38814	-	-	-	-	-	-
5.19b(H8)	1.70E-04	3.77E-05	638.26526	126.57444	-	-	-	-	-	-
5.19b(H16)	1.39E-04	2.18E-05	680.28969	113.41709	-	-	-	-	-	-
5.24	0.00649	0.00348	338.24297	15.76037	115.38009	47.56862	0.82899	0.22938	1.92463	0.29005
Figure	11	12	13	14	15	16	17	18	19	
5.12a	-	-	-	-	32	28	14.67464	0.99691	0	
5.12b	0.91711	0.10273	-	-	32	26	256.24604	0.99909	0	
5.13a	-	-	-	-	32	29	95.44974	0.99168	0	
5.13b	-	-	-	-	32	27	3972.28821	0.99628	0	
5.19a	-	-	-	-	11	9	1.84	0.85406	0.056	
5.19b(H8)	-	-	-	-	5	3	1.97369	0.82927	0.1155	
5.19b(H16)	-	-	-	-	6	4	1.77779	0.88853	0.1301	
5.24	0.03939	0.01079	0	0	36	30	1.82037	0.88724	0.0039	

1 : A1 value, **2** : A1 standard deviation,

3 : B1 value, **4** : B1 standard deviation, **5** : B2 value, **6** : B2 standard deviation,

7 : B3 value, **8** : B3 standard deviation , **9** : C1 value, **10** : C1 standard deviation,

11 : C2 value, **12** : C2 standard deviation, **13** : C3 value, **14** : C3 standard deviation,

15 : Number of points, **16** : Degrees of freedom, **17** : Reduced χ^2 , **18** : Adjusted \mathbf{R}^2 , **19** : χ^2 probability.

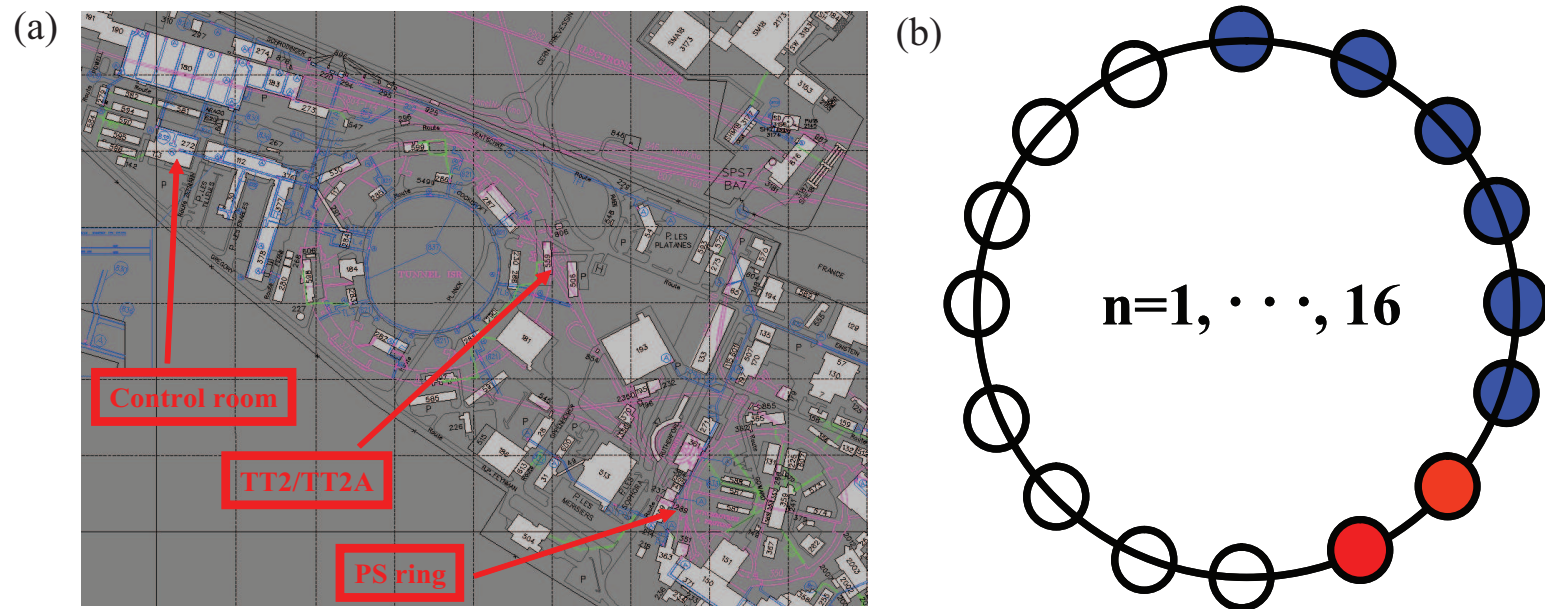


Figure 5.1: Infrastructures for experiment at CERN. a.) Proton synchrotron and TT2 tunnel for experiment. b.) 16 harmonics of beam extraction in proton synchrotron.

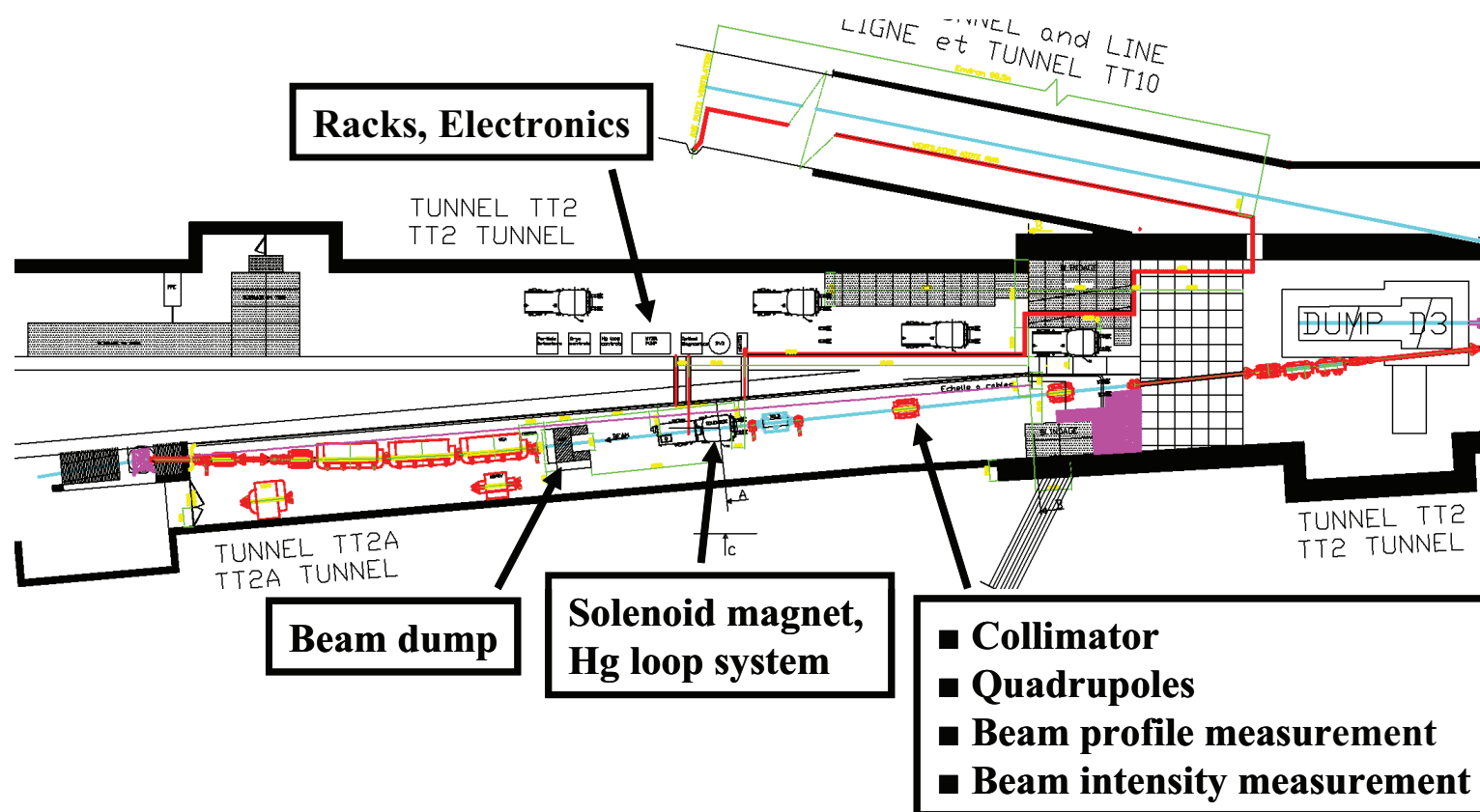


Figure 5.2: Installation of integrated experimental components in tunnel TT2/TT2A for high power target experiment. Extracted proton beam comes from right to left in tunnel TT2A.

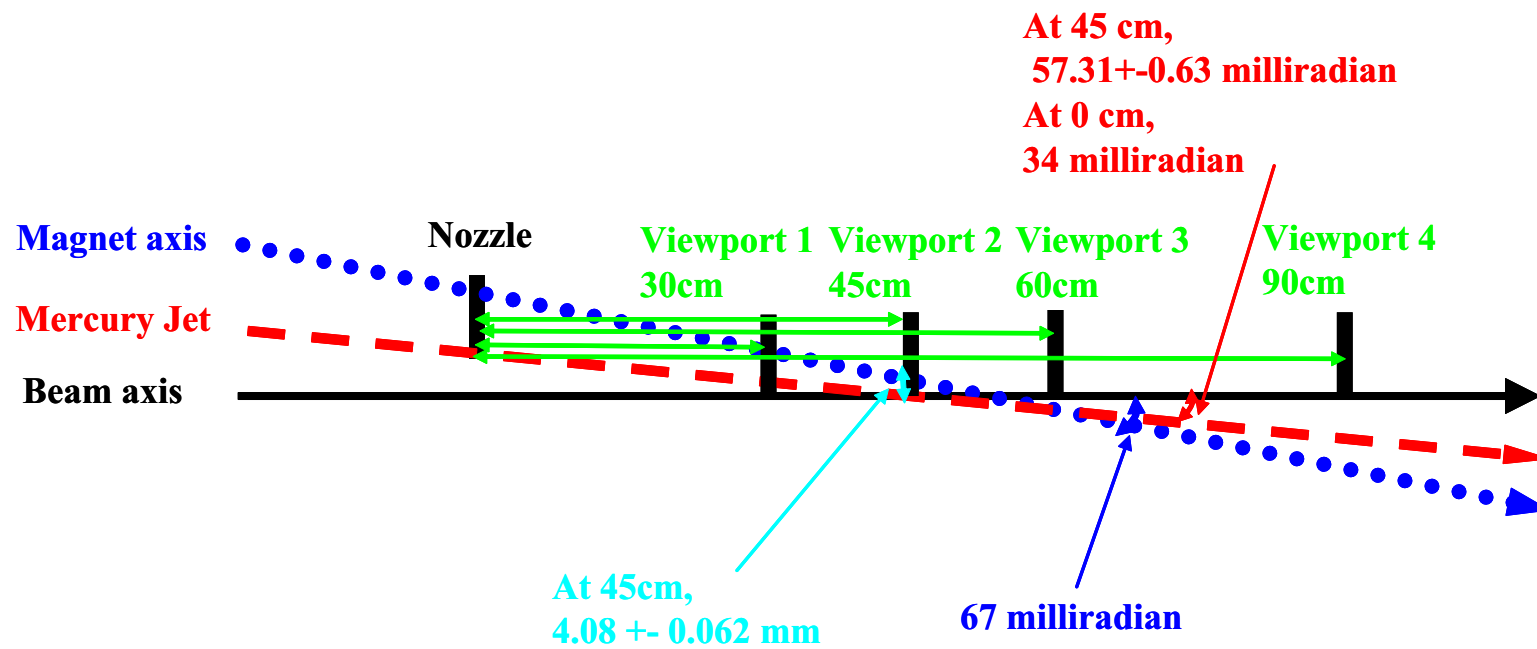


Figure 5.3: Schematics of beam to jet interaction in magnetic field and the location of each Viewport.

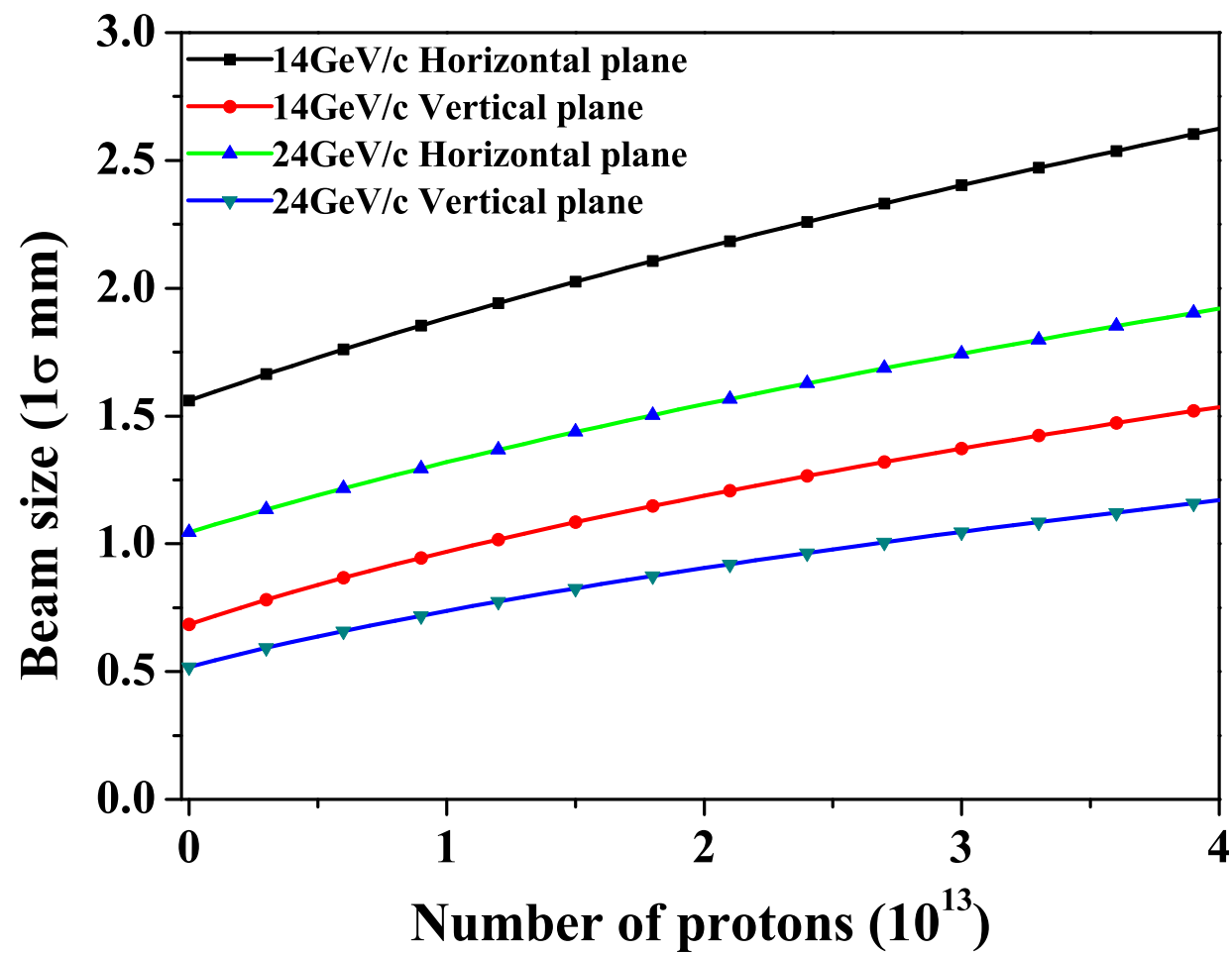


Figure 5.4: 1σ proton beam size at the center of magnet by optics (Efthymiopoulos, 2008).

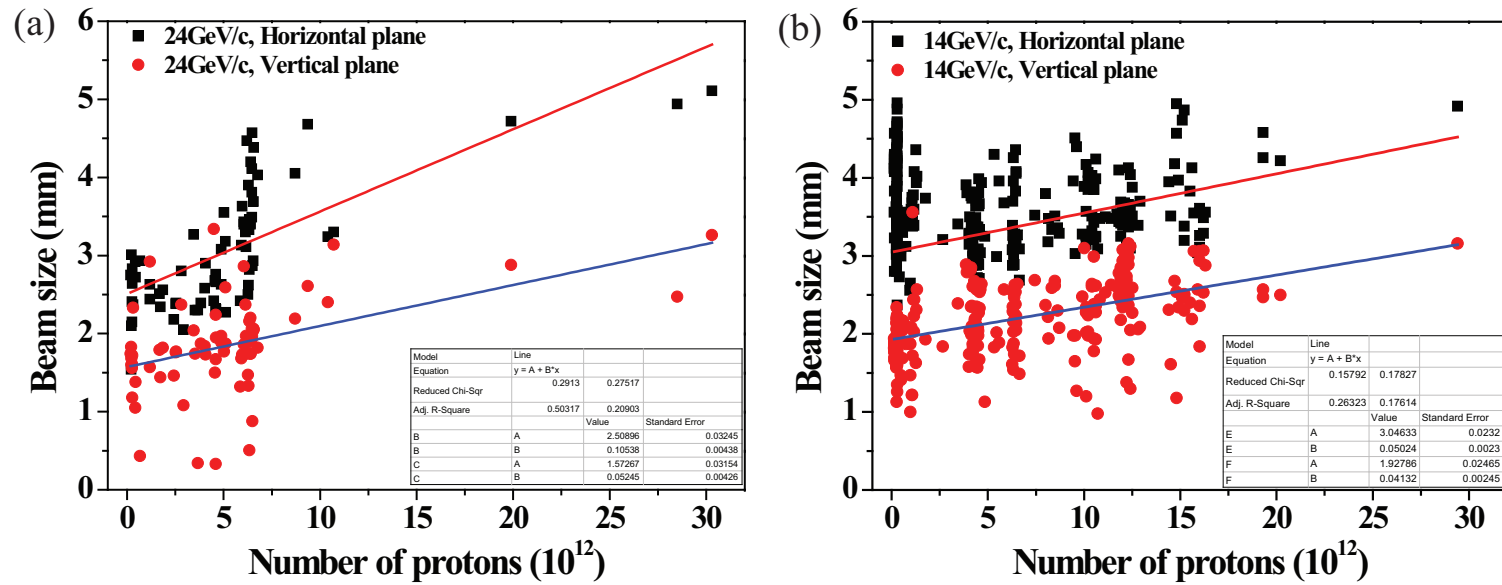


Figure 5.5: 1σ proton beam size by camera screen (Skoro, 2008). a.) 14 GeV beam. b.) 24 GeV beam.

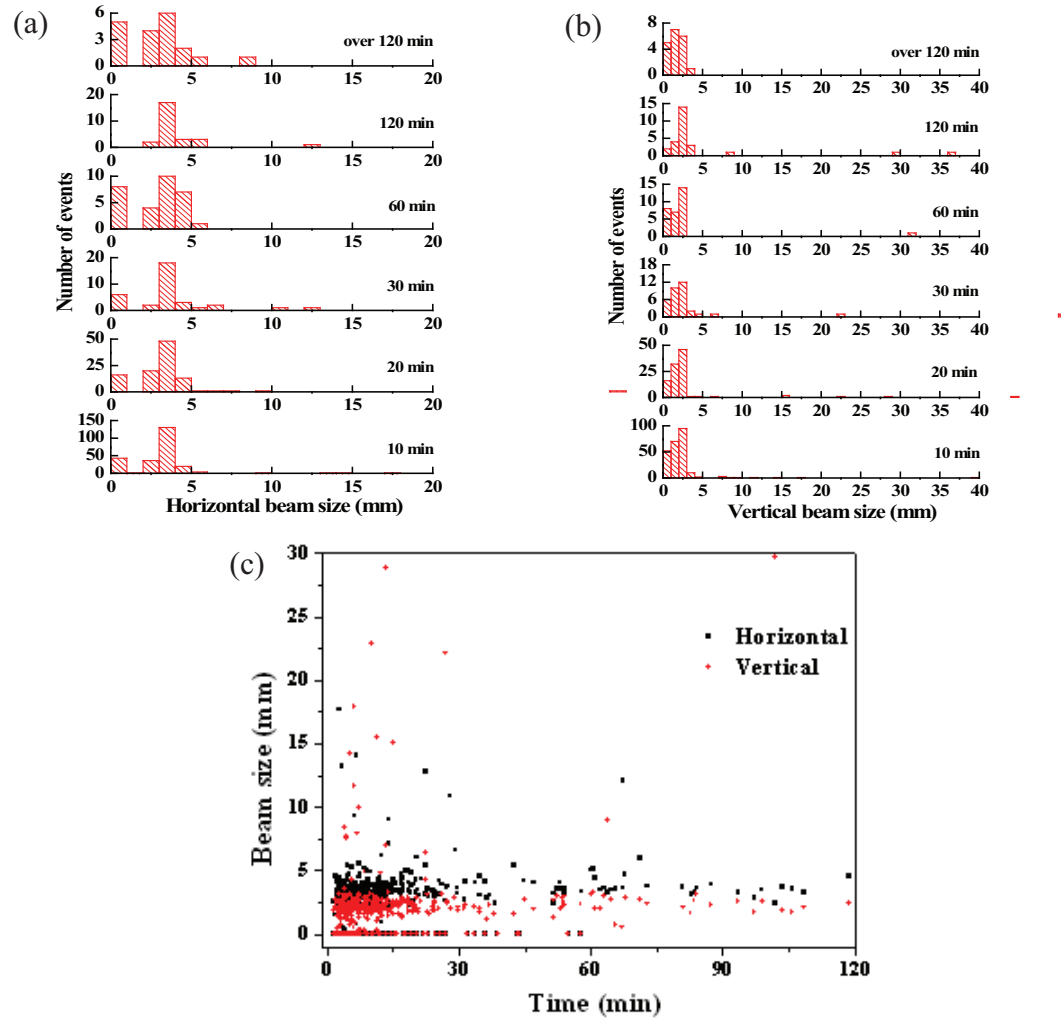


Figure 5.6: Beam size measured by phosphor screen monitor as a function of time interval between beam shots. a.) Histogram of beam size in horizontal plane. b.) Histogram of beam size in vertical plane. c.) Beam sizes distribution.

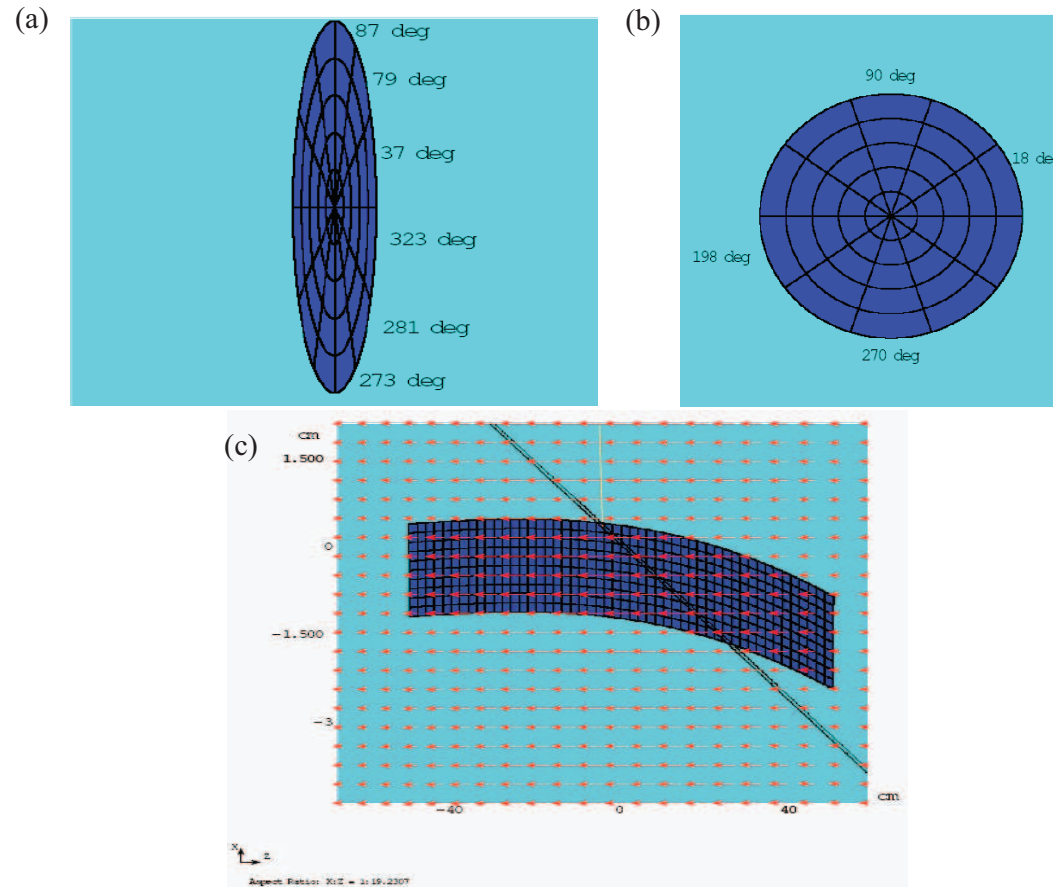


Figure 5.7: Modeling in MARS code for energy deposition calculation (Striganov, 2009). a.) Sectional view of elliptic jet. b.) Sectional view of circular jet. c.) Side view of mercury jet.

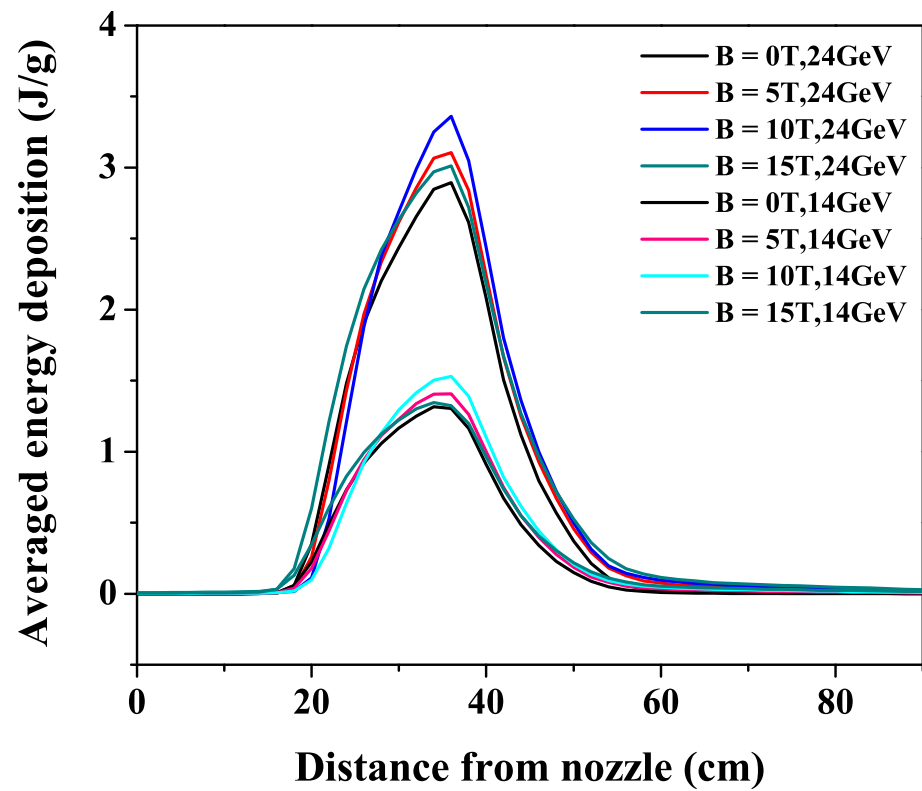


Figure 5.8: Influence of magnetic field to the energy deposition distribution to Hg jet considering experimentally measured jet parameters.

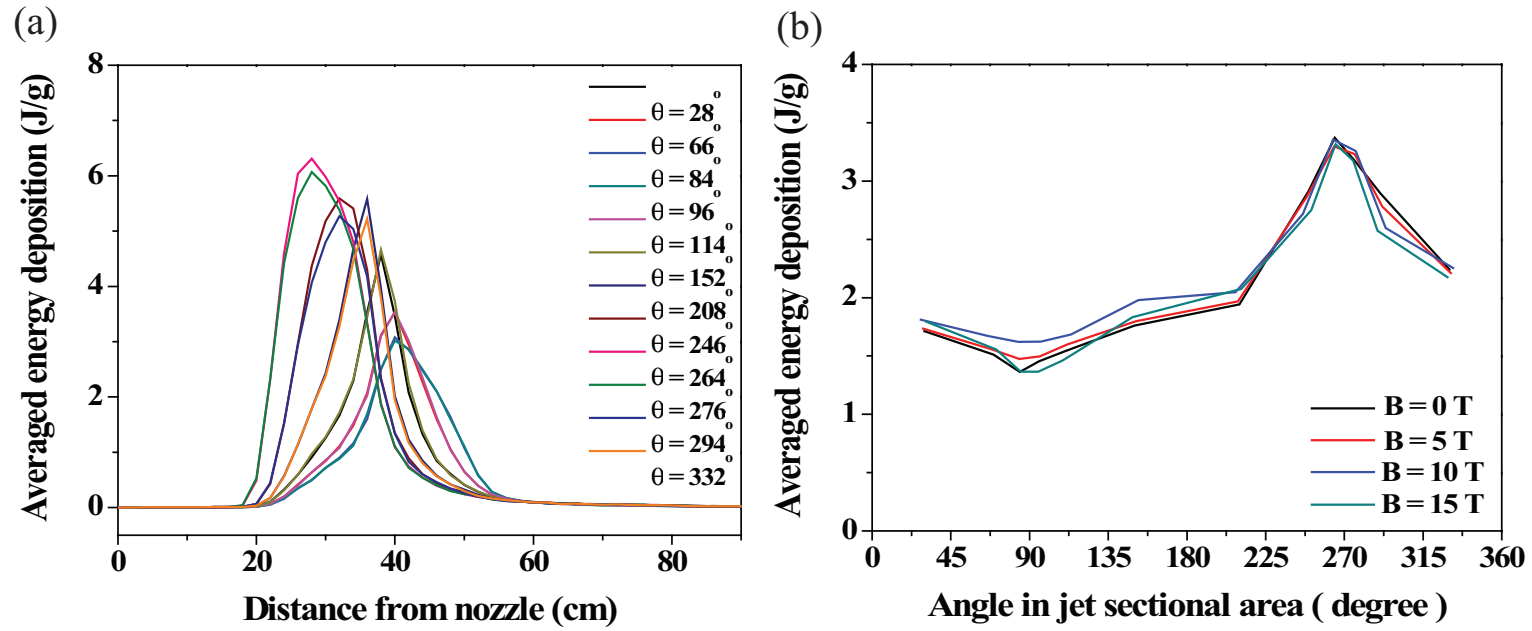


Figure 5.9: Radial energy deposition distribution along jet axis interacting with 24 GeV proton beam. a.) Along jet axis. b.) Along radial angle in jet cross section.

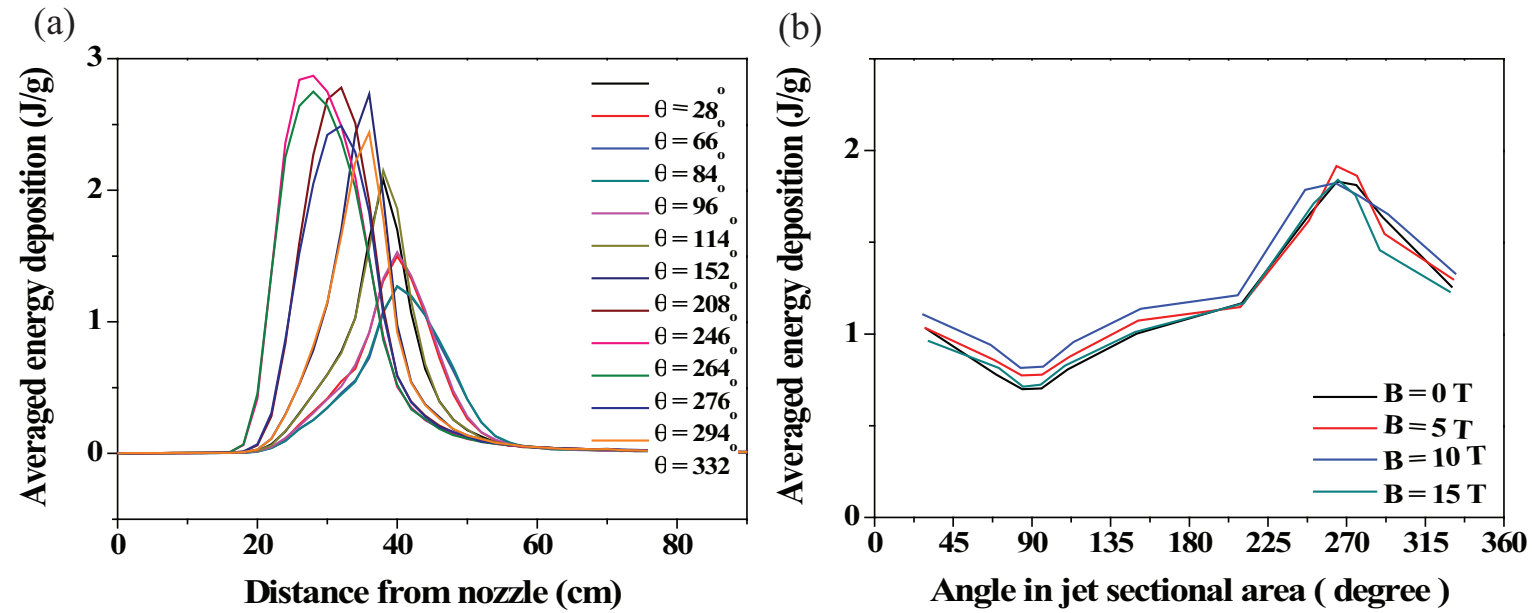


Figure 5.10: Radial energy deposition distribution along jet axis interacting with 14 GeV proton beam. a.) Along jet axis. b.) Along radial angle in jet cross section.

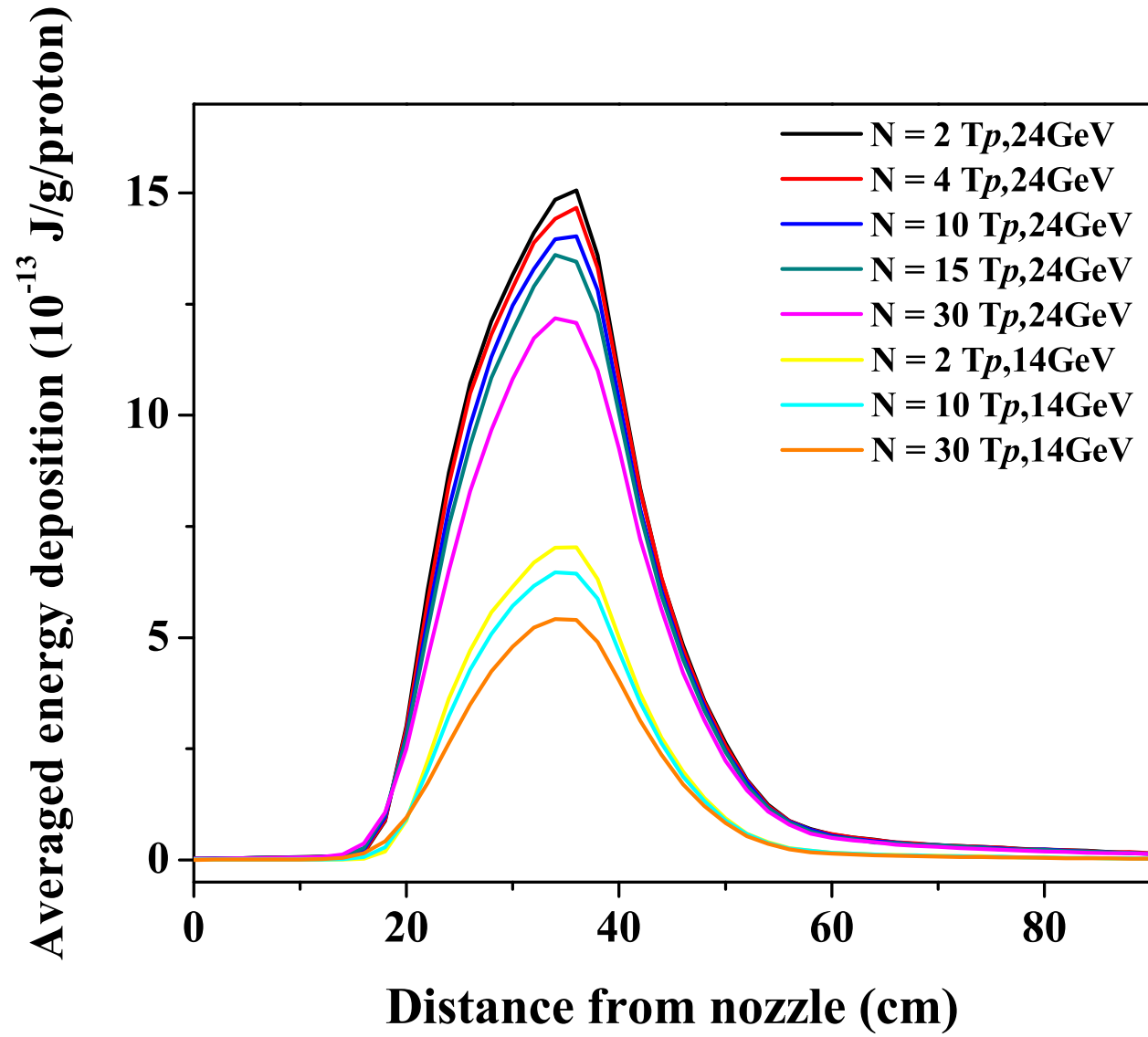


Figure 5.11: Energy deposition distribution per proton according to the variation of beam spot size along jet axis.

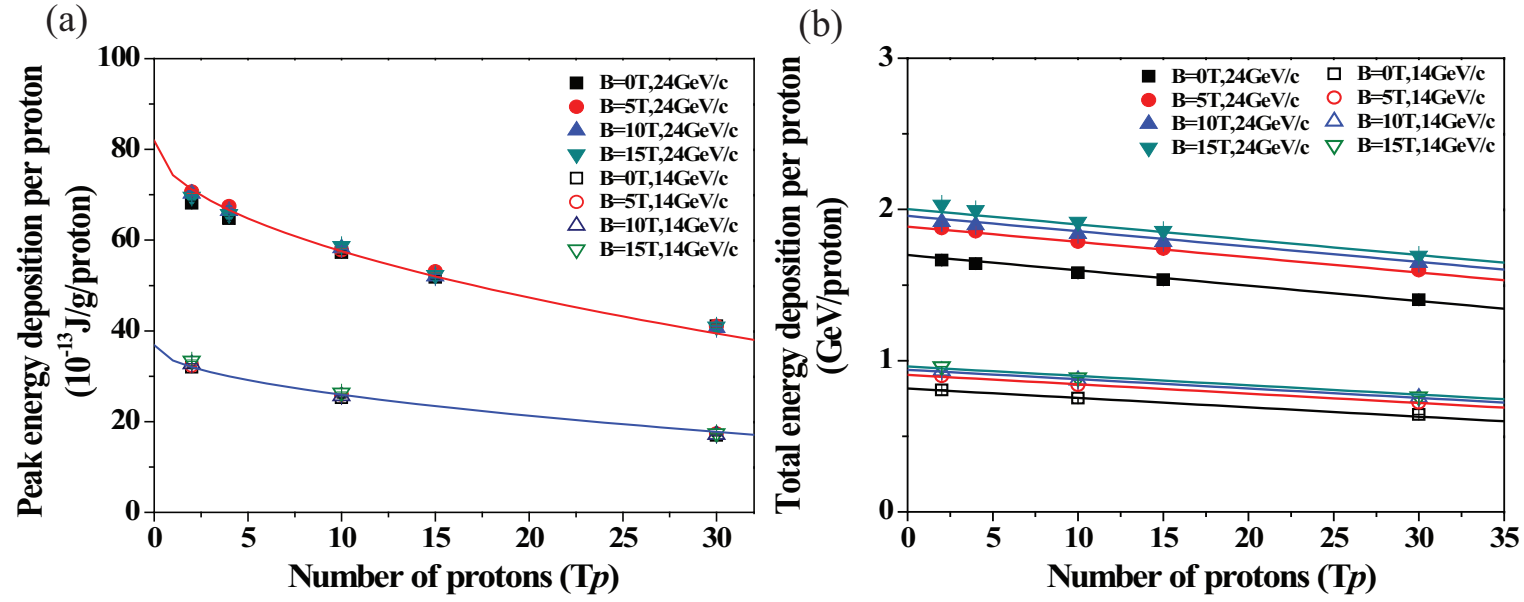


Figure 5.12: Peak energy deposition per proton and total energy deposition per proton according to the beam spot sizes by beam intensities. a.) Peak energy deposition per proton. b.) Total energy deposition per proton.

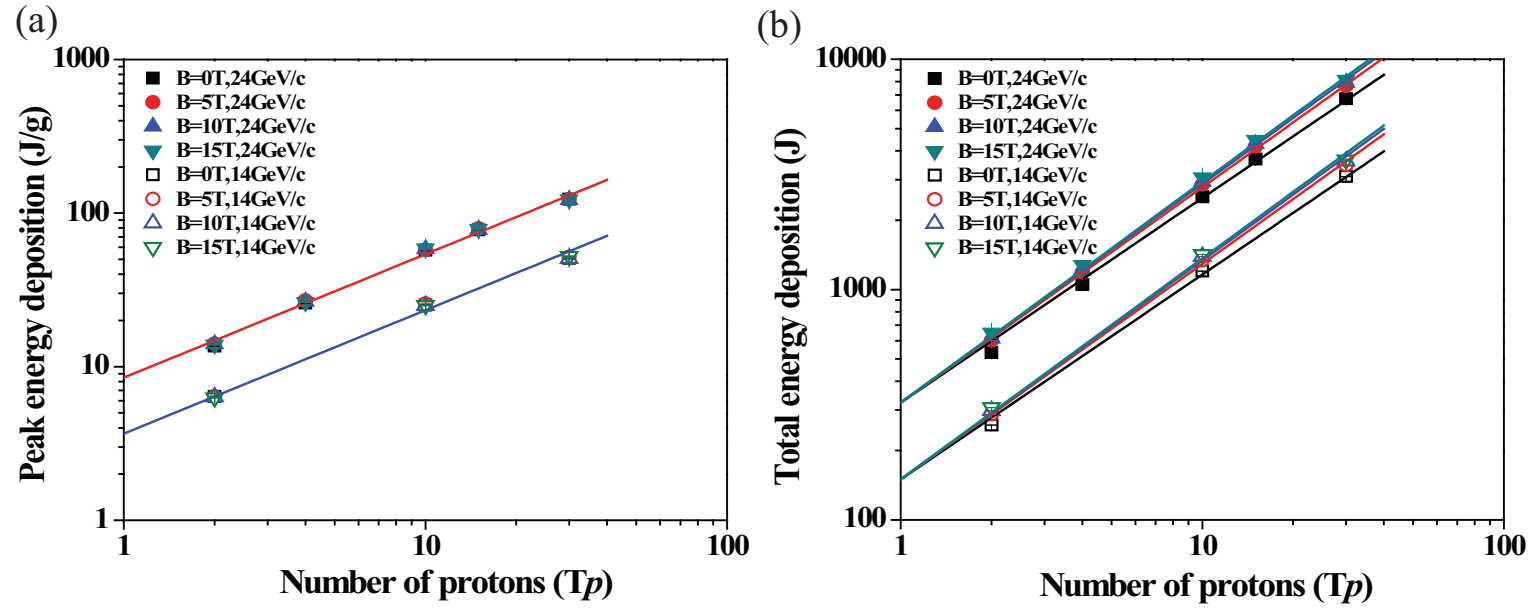


Figure 5.13: Peak energy deposition and total energy deposition in total number of protons. a.) Peak energy deposition. b.) Total energy deposition.

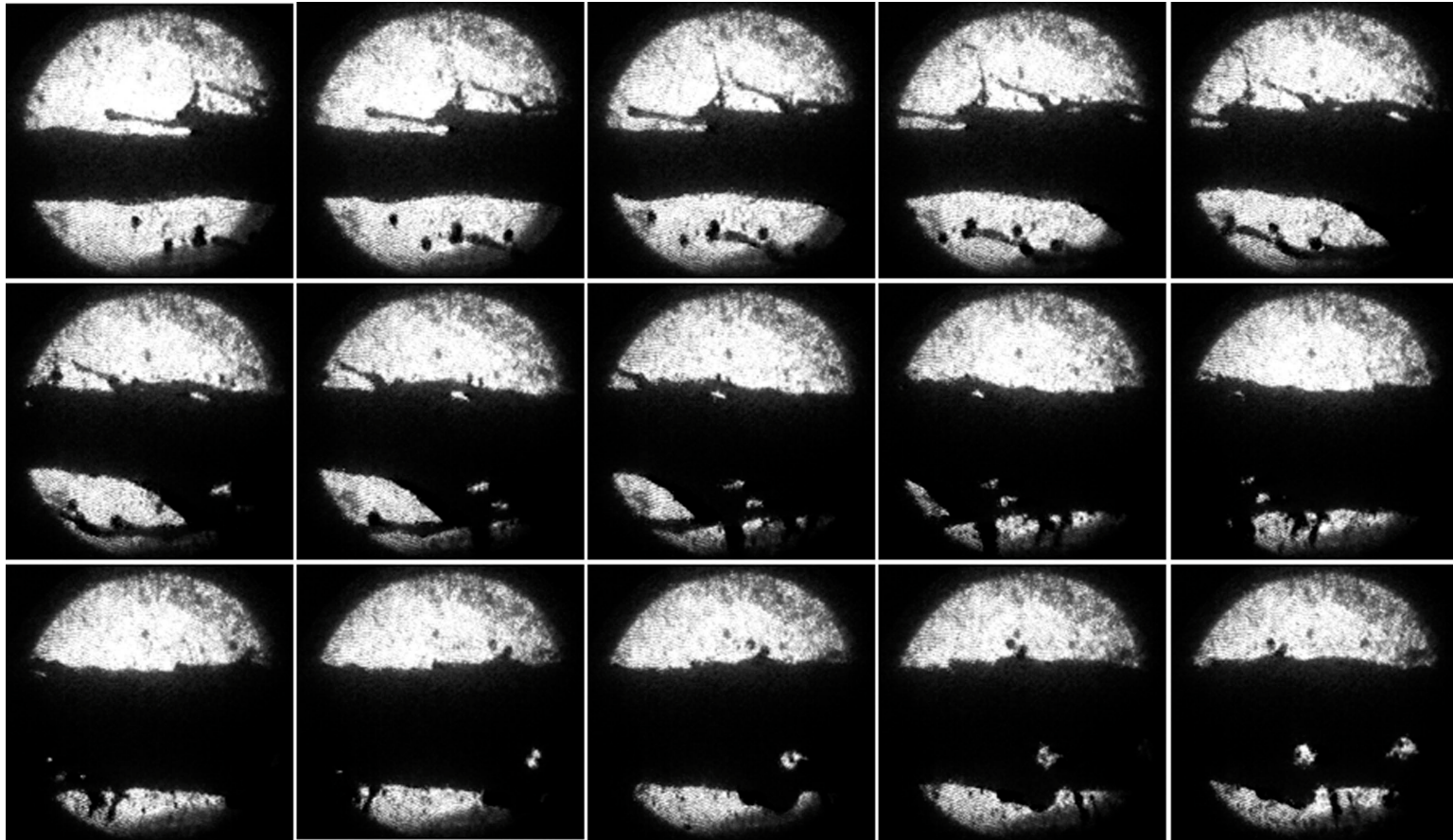


Figure 5.14: Photographs of the Hg jet interaction with 16 TP, 14 GeV proton beam at 5 T. Captured at Viewport 3 at $500 \mu\text{s}$ frame rate (continued).

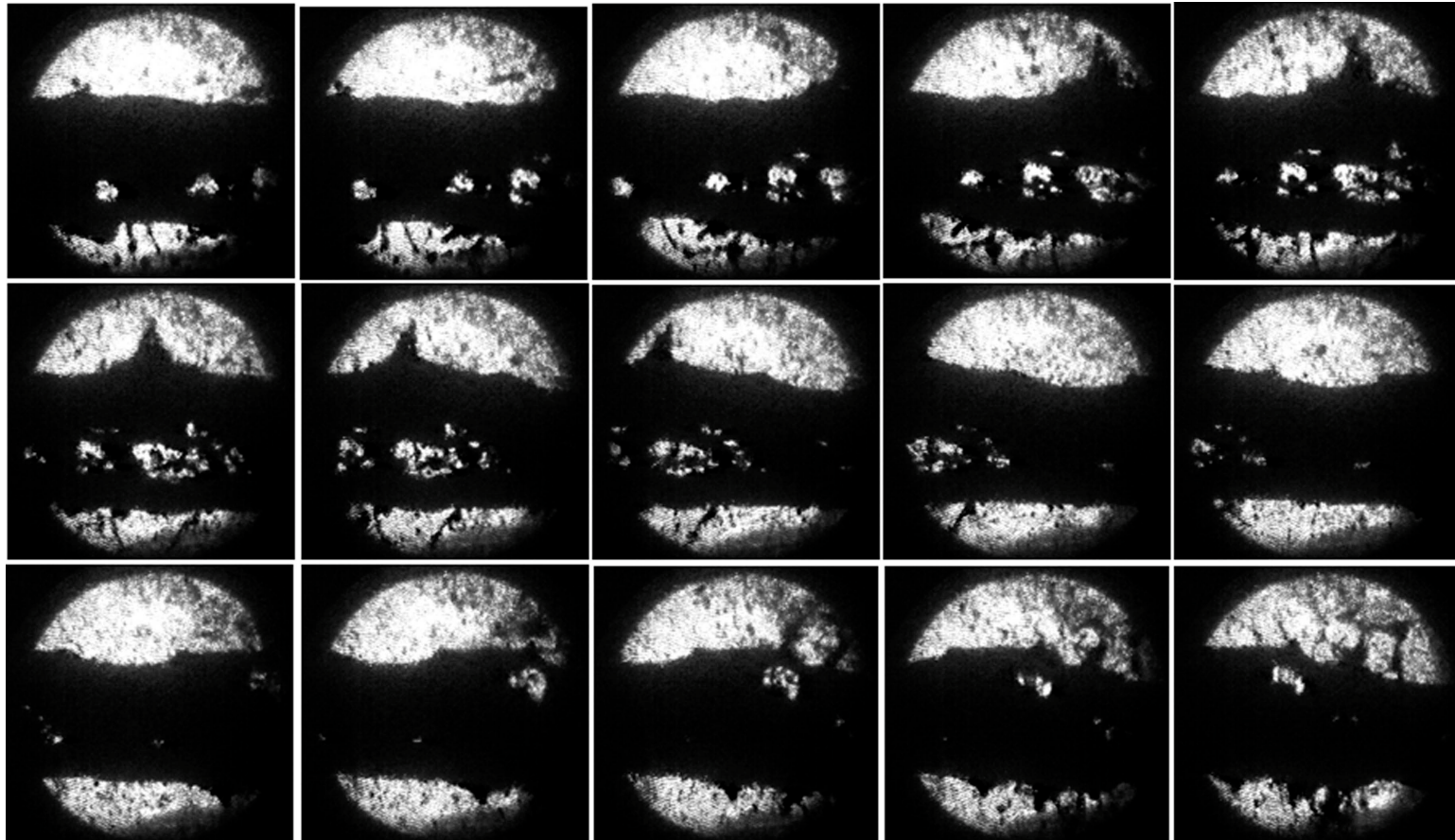


Figure 5.14: Photographs of the Hg jet interaction with 16 TP, 14 GeV proton beam at 5 T. Captured at Viewport 3 at $500 \mu\text{s}$ frame rate (continued).

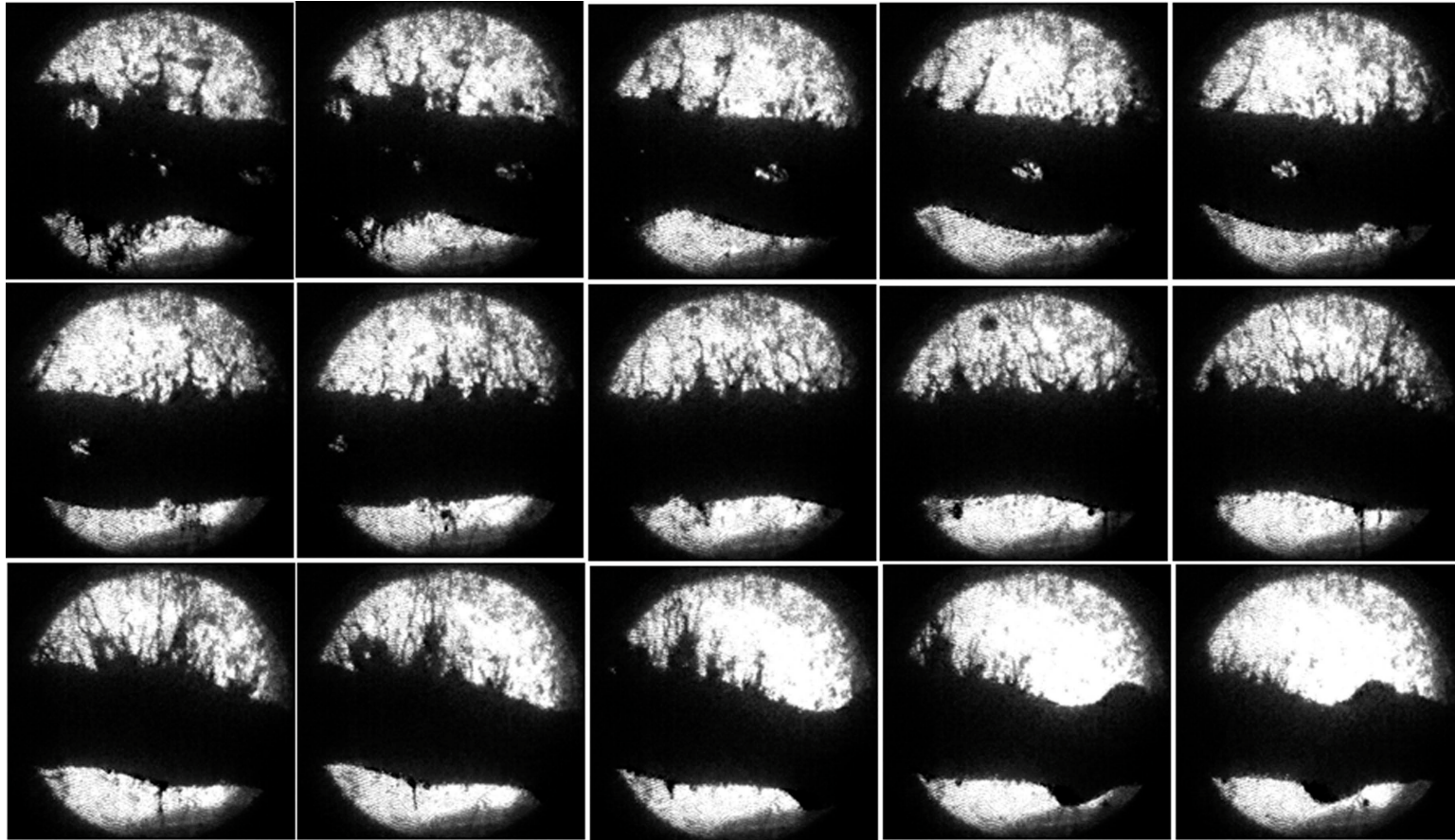


Figure 5.14: Photographs of the Hg jet interaction with 16 TP, 14 GeV proton beam at 5 T. Captured at Viewport 3 at $500 \mu\text{s}$ frame rate.

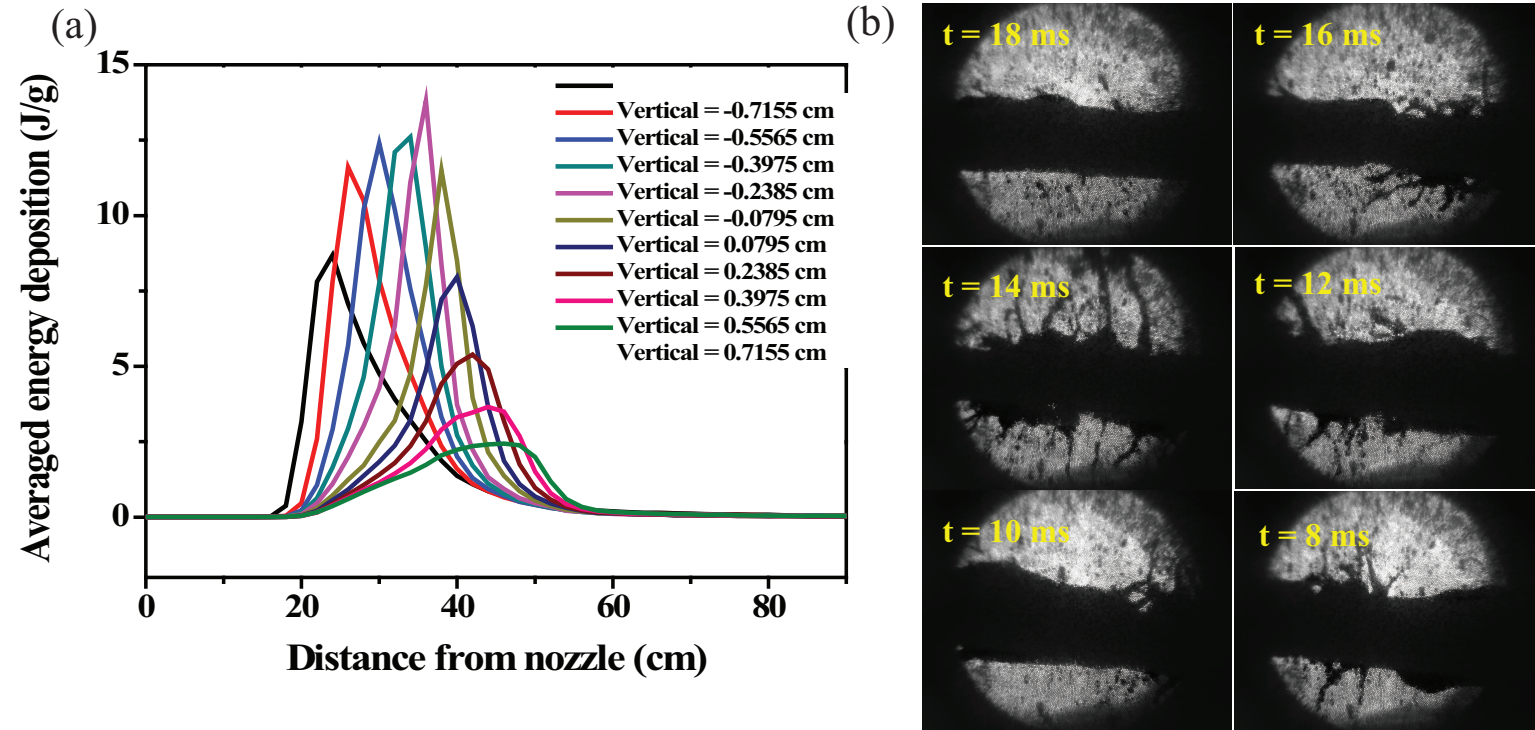


Figure 5.15: Qualitative comparison of the jet response incident by interaction of low intensity (3 Tp) of beam at 5 T. a.) Calculated averaged energy deposition profile to mercury jet according to the distance from jet center. b.) Jet response by captured image.

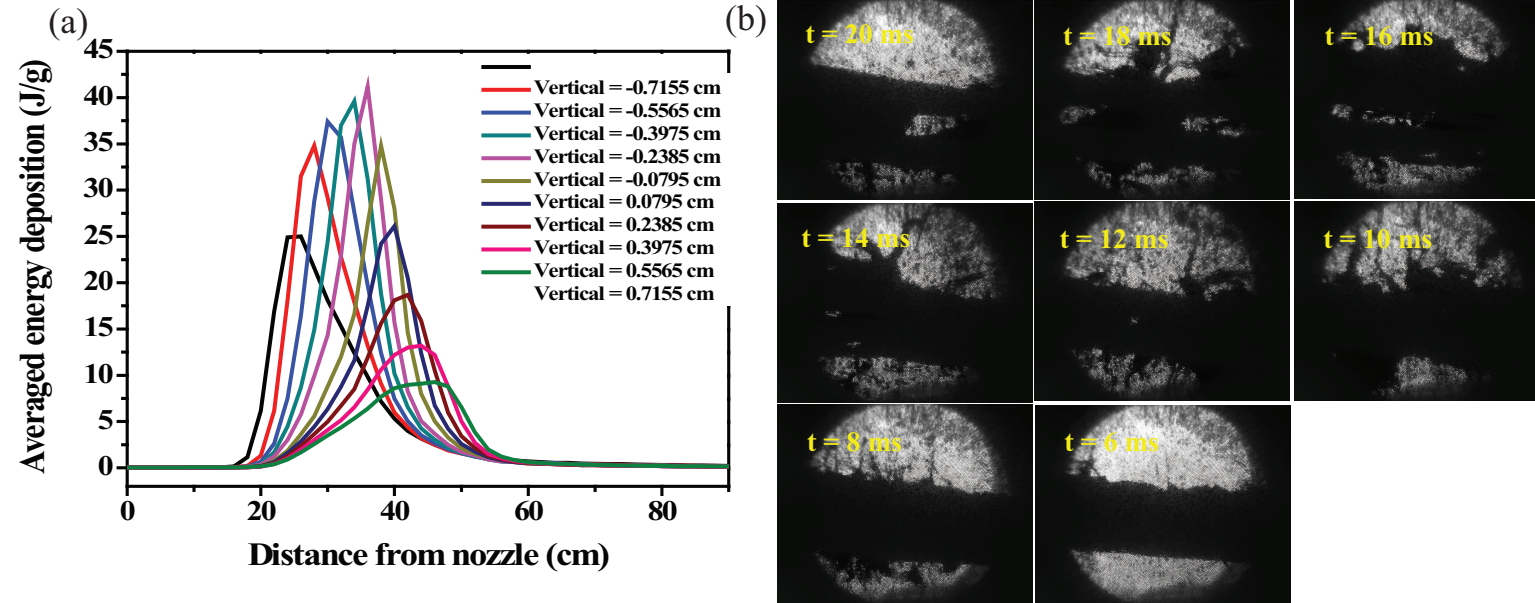


Figure 5.16: Qualitative comparison of the jet response incident by interaction of high intensity (10 Tp) of beam at 10 T. a.) Calculated averaged energy deposition profile to mercury jet according to the distance from jet center. b.) Jet response by captured image.

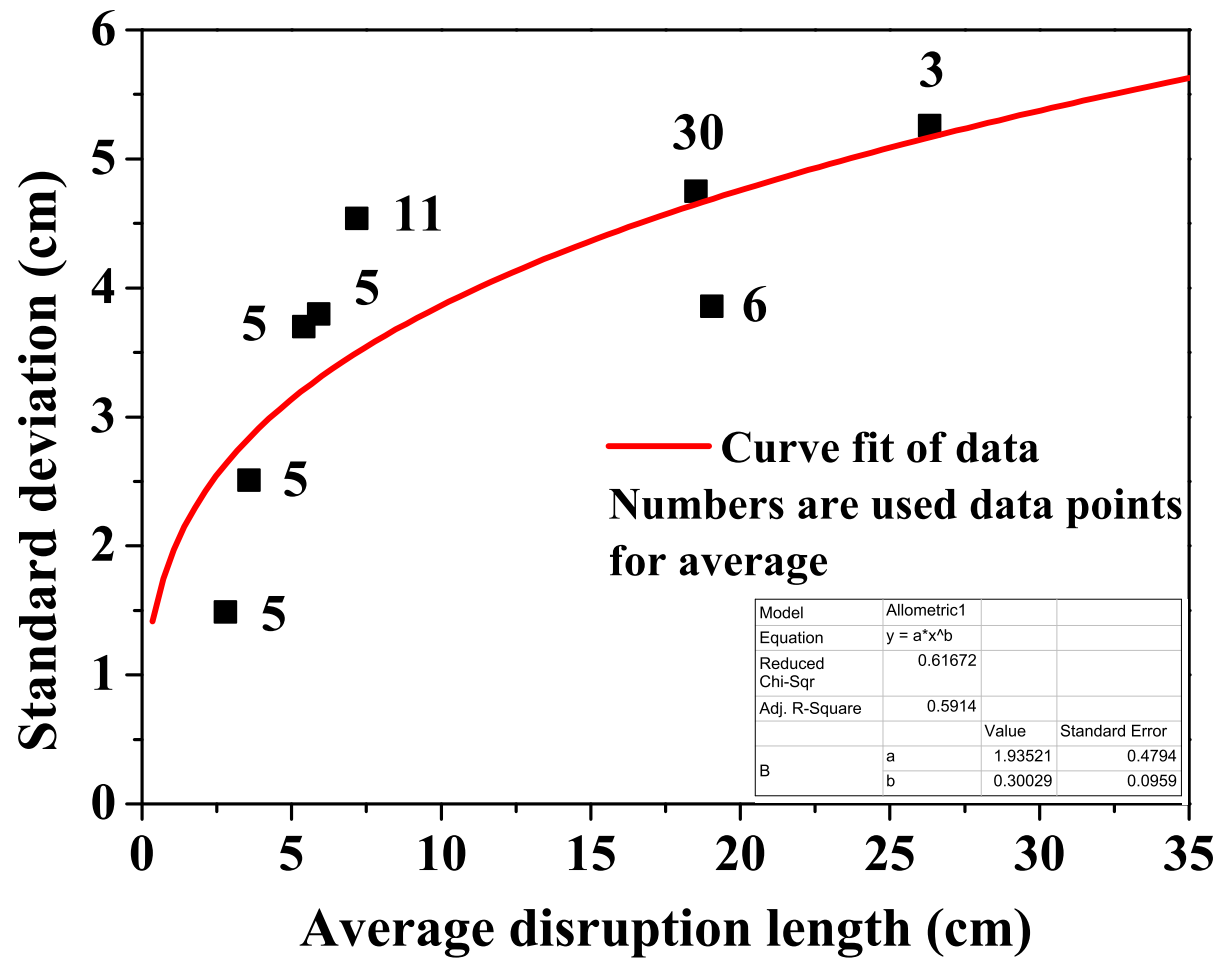


Figure 5.17: Standard deviation of disruption length as a function of disruption length and the function of fitted curve. The fitted curve is $\sigma_{disruption} = 1.9352L_{disruption}^{0.3}$.

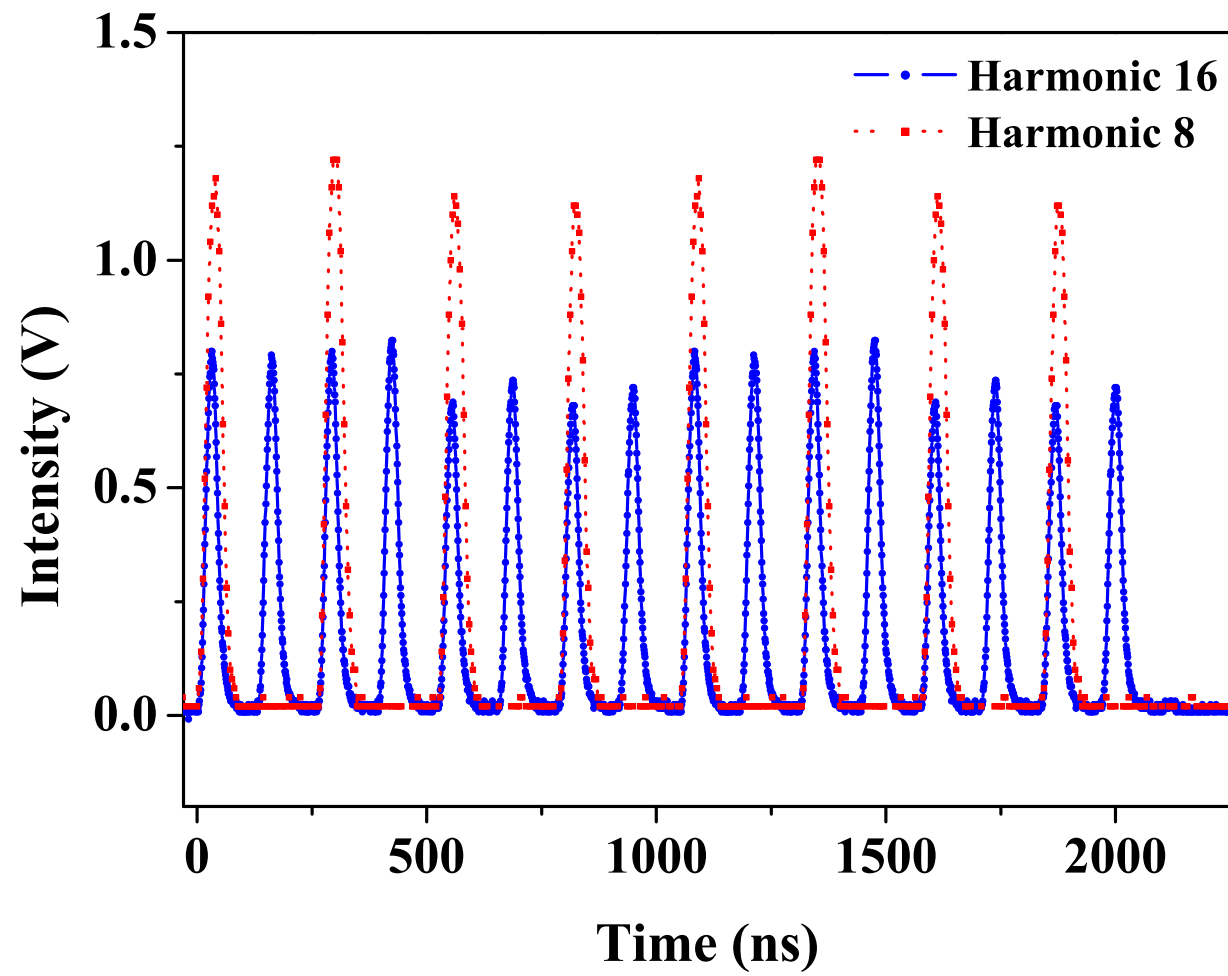


Figure 5.18: Proton beam pulse structure of harmonic 8 and harmonic 16 in 14 GeV and 6 TP.

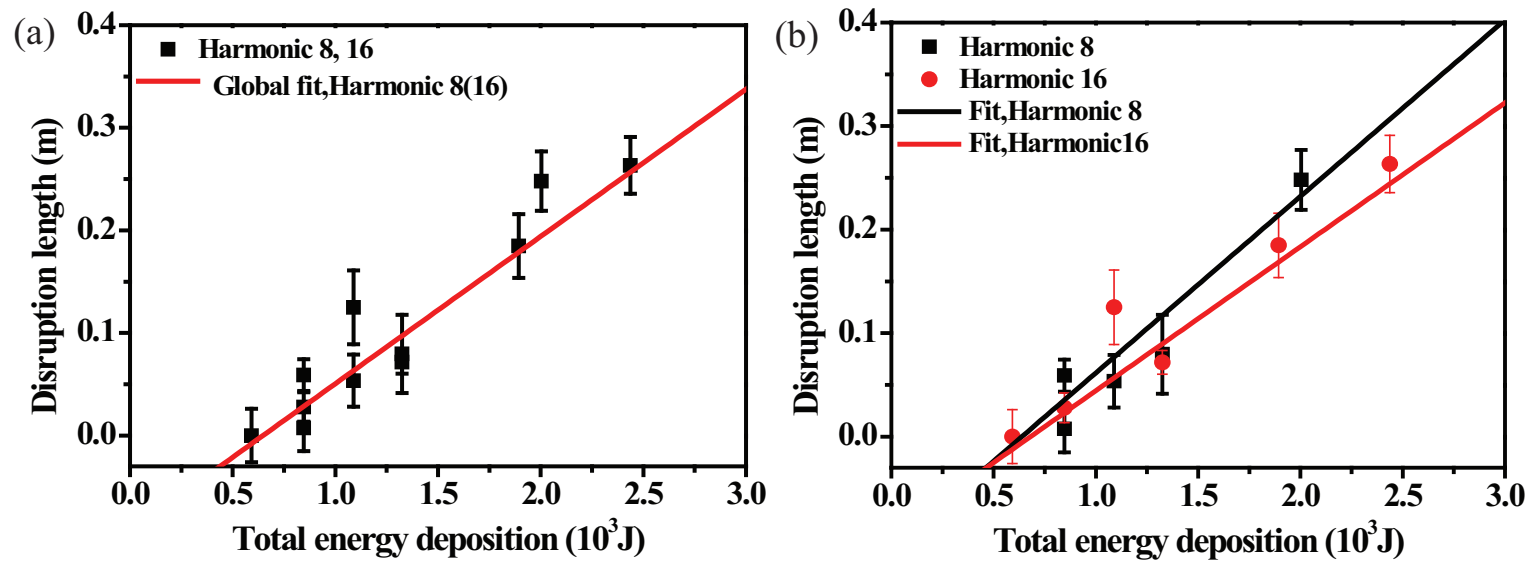


Figure 5.19: Disruption length of Hg jet depending on the beam pulse structure as a function of 14 GeV beam intensity in 5 T. $T_p = 10^{12}$ protons. a) Global fit of harmonic 8 and 16. b.) Independent fit of harmonic 8 and 16.

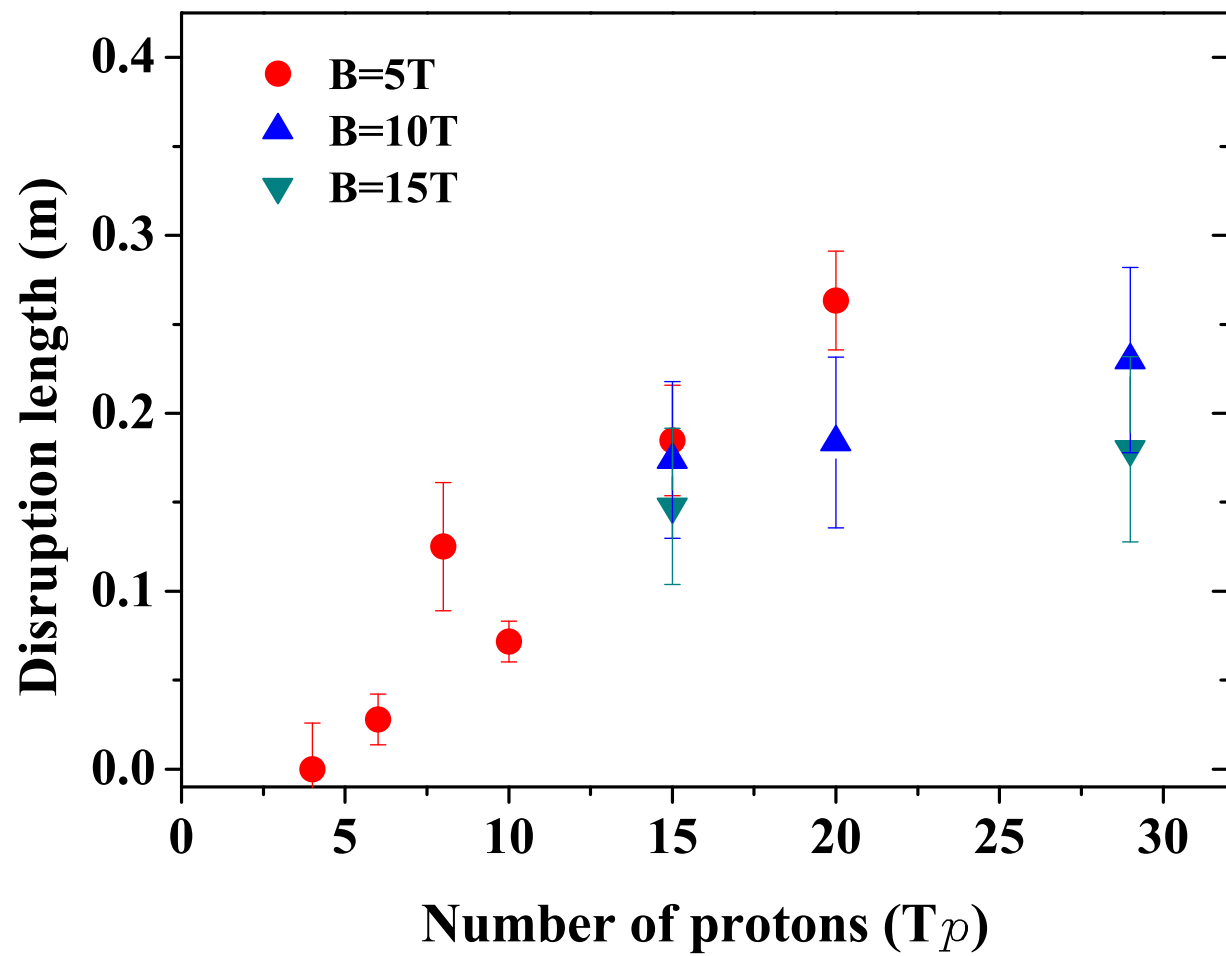


Figure 5.20: Disruption length of Hg jet as a function of 14 GeV beam intensity and magnetic field. Harmonic 16 with 16 bunches is used.

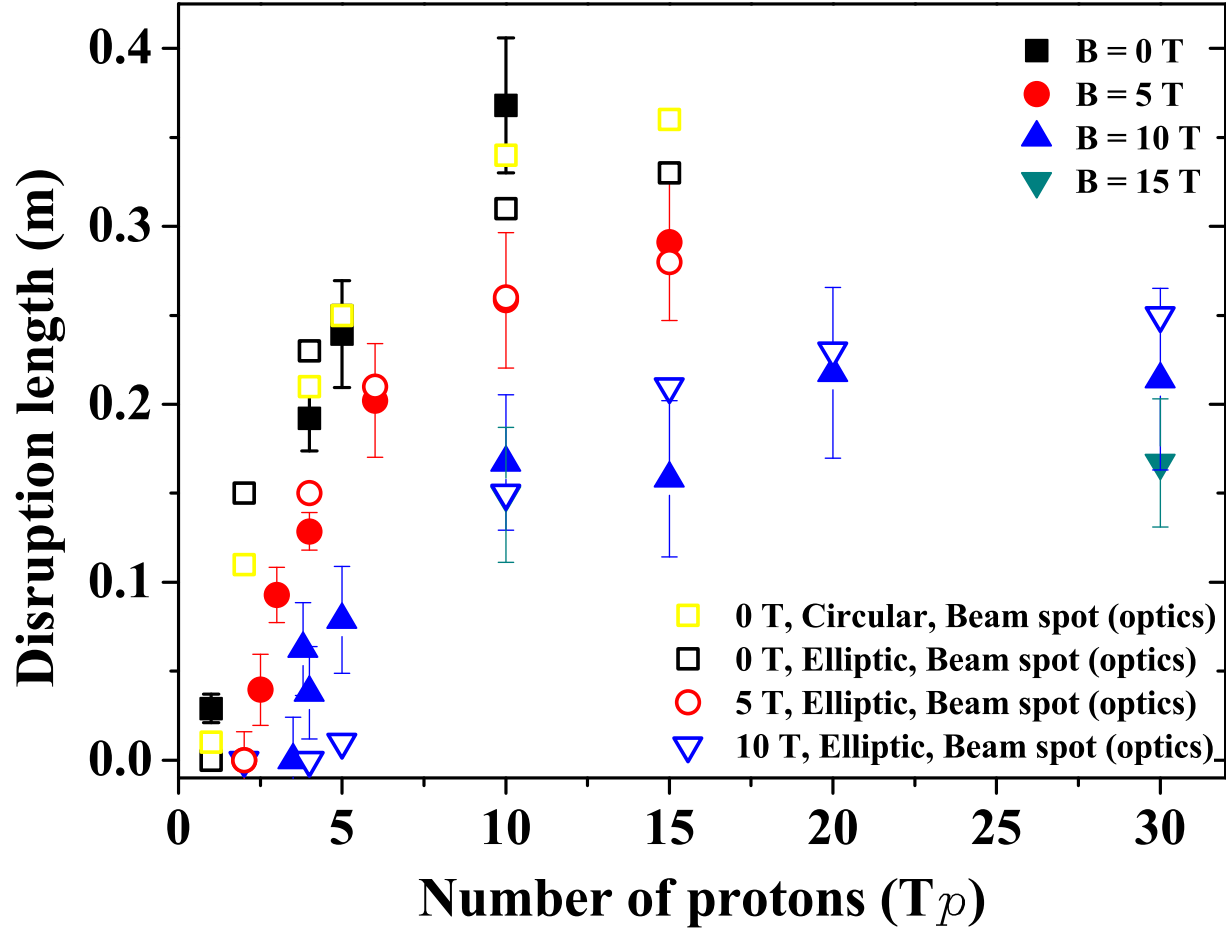


Figure 5.21: Disruption length of Hg jet and its estimation as a function of 24 GeV beam intensity and magnetic field. The estimation of disruption length by energy deposition calculation is compared.

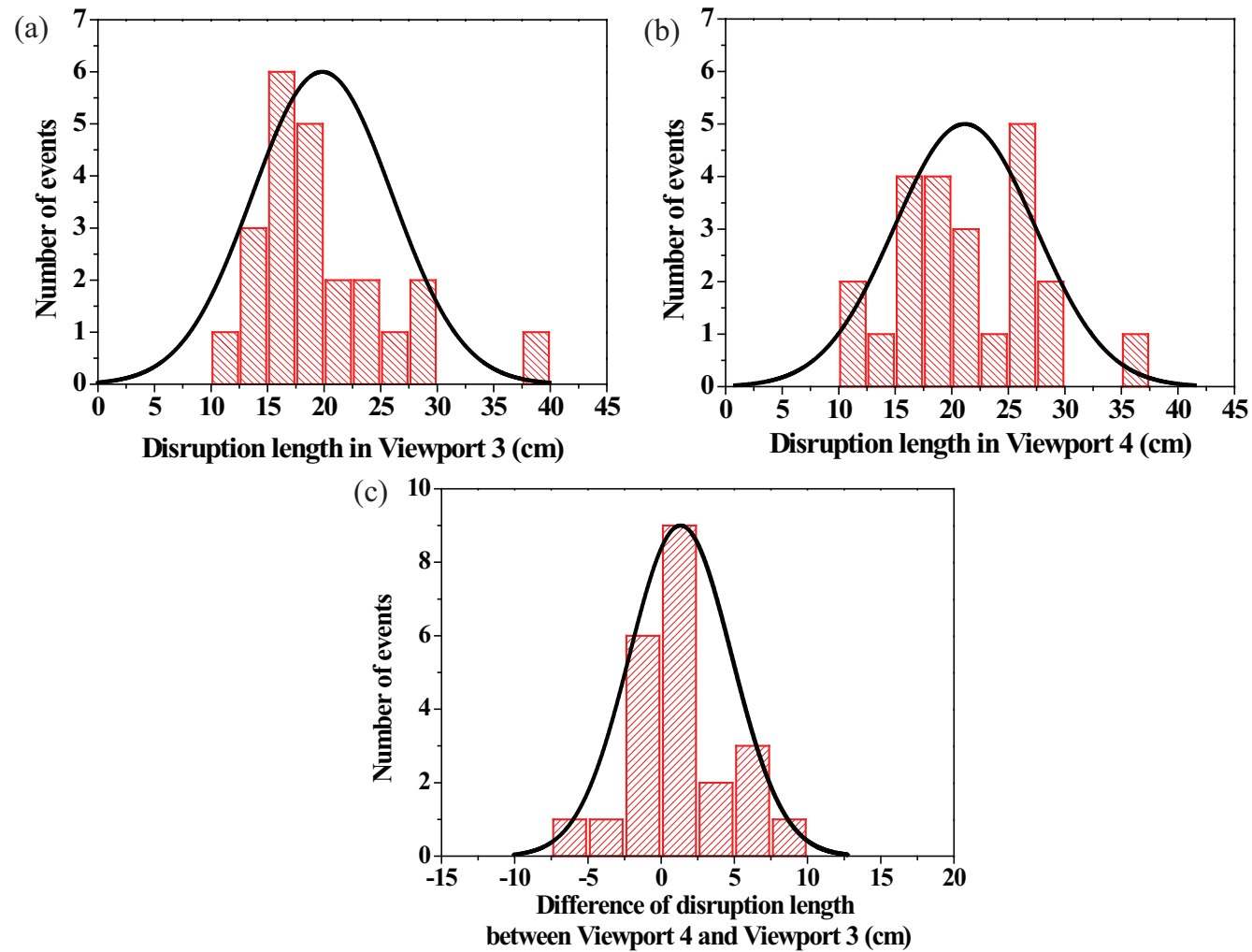


Figure 5.22: Validation of disruption measurement for the evaluation of evolution of disruption length from Viewport 3. a) Disruption length at Viewport 3. b.) Disruption length at Viewport 4. c.) Difference of the disruption length at Viewport 3 and Viewport 4.

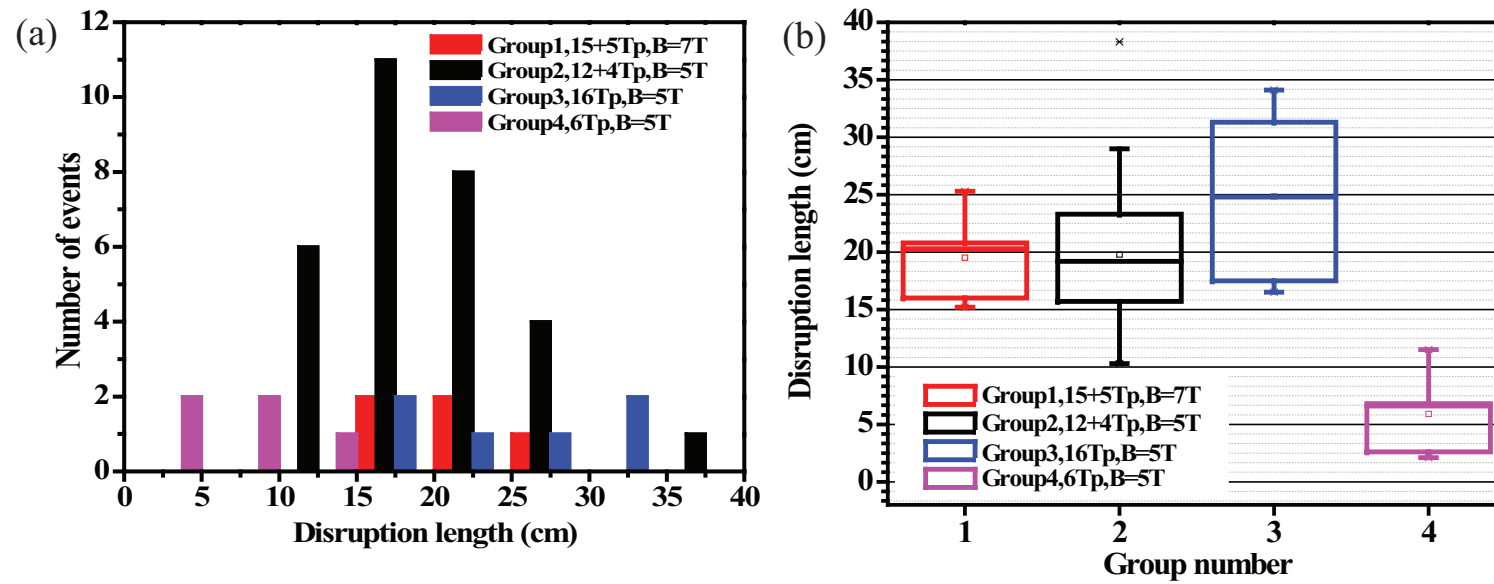


Figure 5.23: Disruption length distribution measurement in a same condition. Pump probe conditions with harmonic 8 and 16 bunches are used.

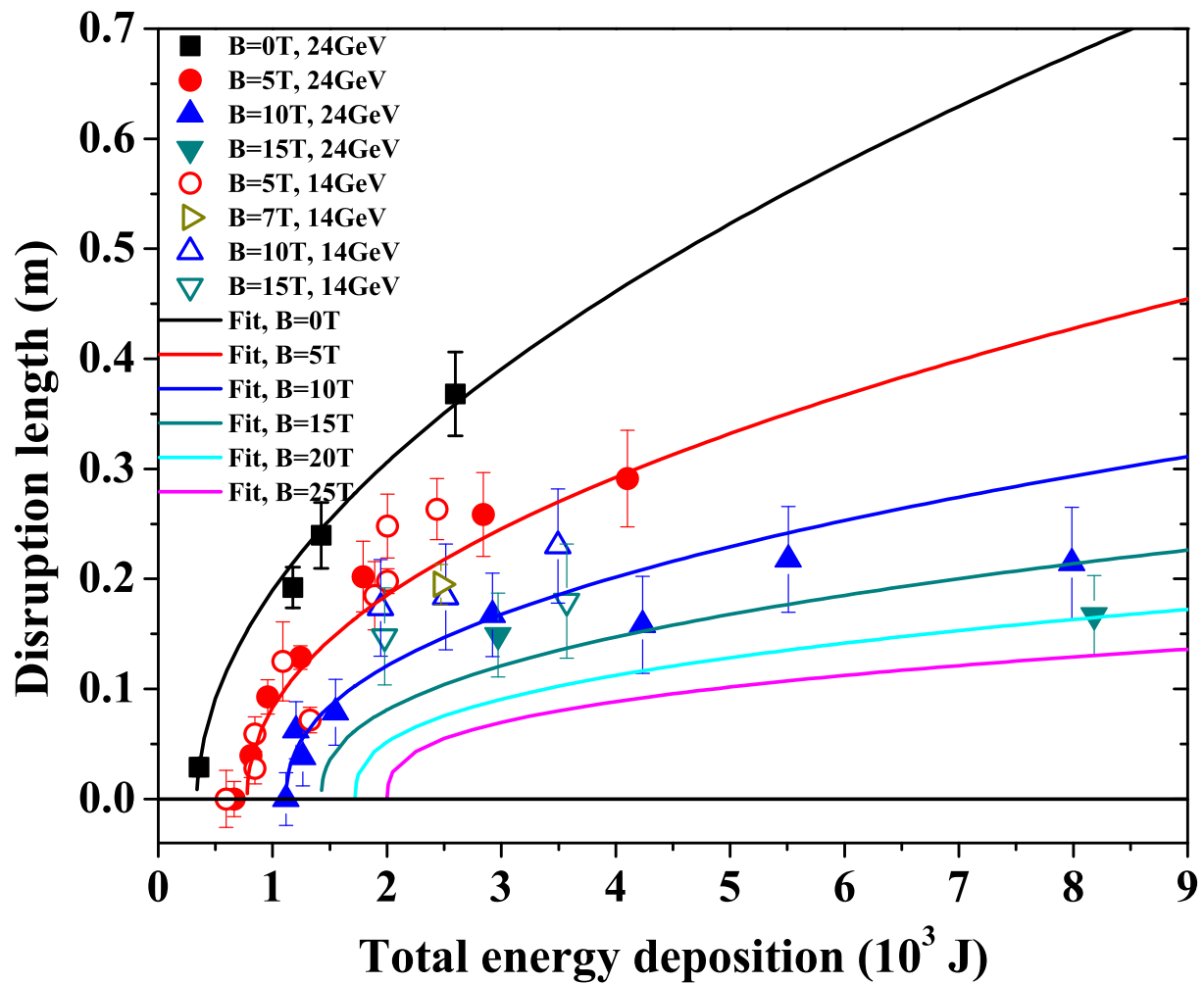


Figure 5.24: Disruption of mercury jet in magnetic fields as a function of total energy deposition and its extrapolation.

Chapter 6

Mercury Jet Surface Development in Magnetic Field

In this chapter, the motions of filaments emanating from jet surface caused by disruption in magnetic field are investigated. The energy deposition induced by the proton beam generates filaments on the Hg jet surface due to thermal stresses. The filaments velocity leaving from the jet surface and the effect of magnetic field to it are discussed. It explains that the joule damping dissipates the kinetic energy on a time scale of joule damping term.

6.1 Filament Model on Jet Surface

6.1.1 Geometry of viewing mercury filaments

It is investigated (McDonald, 2009) that the observed motion of filament by images has geometric relation with the viewing angle by focal length in optics. The filaments ejected from mercury jet by the proton beam interaction are viewed via shadow photography from a focal length $f = 9.15$ cm from the center of the jet. The jet is supposed to have elliptical cross section. The

schematic geometry of viewing mercury filaments is shown in Fig. 6.1. The measurements describes the projection $y_m(t)$ onto the y axis of a ray from the observer to the surface. McDonald (2009) assumes that the filaments leave perpendicularly as shown in Fig. 6.1. The elliptic expression is given as Eqn. (6.1).

$$\frac{x^2}{a^2} + \frac{y^2}{b^2} = 1, \quad (6.1)$$

where the jet is circular with radius b if $a = b$. Suppose a filament leaves the surface with velocity v_o at time t_o from point (x_o, y_o) , at time $t > t_o$, the travel distance d is then $v_o(t - t_o)$ assuming that the velocity is constant. The position of the filament is $x_d = x_o + d \sin(\theta)$, $y_d = y_o + d \cos(\theta)$. Using the trigonometric notation of slope at point (x_o, y_o) , the position of the filament, y_m , as projected onto the y axis is

$$\begin{aligned} y_m &= y_d \frac{f}{f - x_d} \approx y_d \left(1 + \frac{x_d}{f}\right) \\ &= b \cos \theta + v_o(t - t_o) \cos \theta + \frac{[a + v_o(t - t_o)][b + v_o(t - t_o)]}{2f} \sin 2\theta. \end{aligned} \quad (6.2)$$

Thus, the apparent velocity of the filament along y axis is

$$v_m = \frac{dy_m}{dt} \approx v_o \left[\cos \theta + \frac{a + b + 2v_o(t - t_o)}{2f} \sin 2\theta \right]. \quad (6.3)$$

The earliest time t_{om} that a filament can be seen vis projected shadow

2686 photography when $y_m = b$ is given as

2687

$$2688 \quad t_{om} \approx t_o + \frac{b(1 - \frac{v_m}{v_o})}{v_m} \quad (6.4)$$

2689 and

2690

$$2691 \quad v_m \approx \frac{v_o}{1 + v_o \frac{(t_{om} - t_o)}{b}}. \quad (6.5)$$

2692 6.1.2 Distribution of filaments on jet surface

2693 McDonald (2009) suggested three cases of possible distribution of filaments
 2694 on the jet surface, which can indicate the probable existence of filaments in
 2695 observation depending on the assumed orientation of the filaments. First, in
 2696 case that the filaments are distributed uniformly in angle θ , the probability of
 2697 the existence of the filaments is

2698

$$2699 \quad P(\theta)d\theta = \frac{d\theta}{2\pi}. \quad (6.6)$$

2700 Second, in case that the filaments are distributed uniformly in angle θ , the
 2701 probability of the existence of the filaments is

2702

$$2703 \quad P(\theta)d\theta = \frac{d\phi}{2\pi} = \frac{ab}{a^2 \sin^2 \theta + b^2 \cos^2 \theta} \frac{d\theta}{2\pi}. \quad (6.7)$$

2704 Third, in case that the filaments are distributed uniformly in position s
 2705 around the circumference C of the ellipse, the probability of the existence of

the filaments is

$$P(\theta)d\theta = \frac{ds}{C} \approx \frac{2\sqrt{a^2 \cos^2 \theta + b^2 \sin^2 \theta}}{3(a+b) - \sqrt{(3a+b)(a+3b)}} \frac{d\theta}{2\pi}. \quad (6.8)$$

6.1.3 Approximation of filaments velocity

6.1.3.1 *first order approximation*

Sievers and Pognat (2000) reported the response of solid and liquid target to rapid heating by the incident proton beam. The parabolic radial energy deposition density E_{beam} is considered, dropping to 0 at the outer radius $a = 1$ cm as follow :

$$E_{beam} = E_o[1 - (r/a)^2]. \quad (6.9)$$

The increase in temperature causes pressure rise. It is assumed that the rise time for the temperature is of the same order of magnitude with the beam energy deposition, 10^{-9} s, thermal expansion is initially prevented by the mass inertial of the material. From the definition of bulk modulus K , the resulting instantaneous thermal pressure for mercury is

$$\Delta p(r) = K\alpha_v \Delta T(r). \quad (6.10)$$

If the thermal heating occurs very slowly comparable to the material's dynamic frequency, it would correspond to quasi-static thermal expansion. It is believed that the energy stored in the material due to the initial thermal

2727 expansion may be converted into kinetic energy bombarding the liquid flow
 2728 away. Corresponding to the thermal expansion caused by the pressure rise,
 2729 strain energy is stored in the liquid flow due to the compression, which is
 2730 expressed as

2731

$$2732 \quad \frac{E_c}{V} = \frac{K(\alpha_v \Delta T(r))^2}{2}, \quad (6.11)$$

2733 where E_c represents the converted beam energy. The order of the velocity
 2734 with which the boundary of the liquid material is given by the thermal expan-
 2735 sion at the boundary divided by the time over which the sound travels across
 2736 the radius of the jet, which is in units of $c\alpha_v T_o$. The pressure and the velocity
 2737 at the boundary are reduced by extending the time of heating, which depends
 2738 on the compressibility like

2739

$$2740 \quad p \sim \frac{1}{\kappa} \quad , \quad v \sim \frac{1}{\sqrt{\kappa}}, \quad (6.12)$$

2741 where κ is the compressibility of material.

2742 **6.2 Observation of Filaments Development on** 2743 **Mercury Jet Surface**

2744 **6.2.1 Image calibration**

2745 **6.2.1.1 *image calibration with proton beam arrival signal***

2746 In order to investigate the time response of filaments, we need to establish
 2747 the accuracy and calibration of the measurement based on the experimental

setup. Fig. 3.6 shows the traced signals on an oscilloscope when the beam and the beam triggering are delivered. The scintillating fiber signal gives the beam arrival time. Therefore, it is possible to set up the trigger timing for the cameras and laser driver inputs, which is $\sim 2 \mu s$ after the master electronic triggering signal from the proton synchrotron. Therefore, the first image of the SMD camera tells the status of jet for the time before the beam arrives since the exposure time of SMD camera is 150 ns. All of the electronic delays including the cable delays are less than $1 \mu s$. The maximum frame rate of SMD camera is up to 1 MHz. The accuracy of camera frame rate is checked by using laser pulses. Laser pulses with certain periods are generated and then monitored at oscilloscope through photodiode. The frame rate of camera is set at the corresponding values of laser pulse period. The frame rate is checked by monitoring the variation of intensity of image captured from camera, which is judged as negligibly uniform.

6.2.1.2 *time delay structure of proton beam to light source triggering*

Fig. 6.2 shows the time structures between freezing image after laser enabling and proton beam arrival. Fig. A.1 shows the specifications of 25 W laser, where the response time to reach the peak laser, wavelength of laser, and optical power for various pulse rates are shown (Tsang, 2006). Laser emits ~ 250 ns after receiving the 16 pulse trigger from the pulse generator. The time of flight of light to the primary vessel is ~ 60 ns. Once the light source arrives at the primary vessel, the freezing image of mercury jet flow

is instantaneously generated and it is then transmitted through the optical fiber corresponding to the light speed ~ 4 ns/m, where ~ 60 ns is taken for the used imaging fiber length. From the traced signals in Fig. 3.6, the proton beam arrival time is measured. Considering the time of flight from primary vessel through scintillating fiber, ~ 60 ns delay is estimated, so that the time delay between the 1st acquired image and the actual proton beam arrival is given as $T_3 - T_2$ in Fig. 6.2, which is considered for the velocity analysis of filaments.

6.2.2 Parameter optimization with uncertainty

6.2.2.1 *linear curve fit for estimation of model*

Selecting a model of the right form to fit a set of data requires the use of empirical evidence in the data, knowledge of the process and some trial-and-error experimentation. Much of the need to iterate stems from the difficulty in initially selecting a function that describes the data well. Some scientific theory describing the mechanics of a physical system provide a functional form for the process, which type of function makes an ideal starting point for model development. So, a practical approach is to choose the simplest possible functions that have properties ascribed to the process. Complex models are fine, but they should not be used unnecessarily. Fitting models that are more complex than necessary means that random noise in the data will be modeled as deterministic structure. This will unnecessarily reduce the amount of data available for estimation of the residual standard deviation, potentially increas-

ing the uncertainties of the results obtained when the model is used. Numerical methods for model validation, such as R^2 statistic, are useful. Graphical methods have an advantage over numerical methods for model validation because they illustrate a broad range of complex aspects of the relationship between the model and the data. Numerical methods tend to be focused on a particular aspect of the relationship between the model and the data and try to compress that information into a single descriptive number. The residuals from a fitted model are the differences between the responses observed at each combination values of the explanatory variables and the corresponding prediction of the response computed using the regression function.

The linear regression model is

$$\mathbf{Y} = f(\mathbf{X}, \Theta) + \epsilon, \quad (6.13)$$

where $\mathbf{X} = (x_1, x_2, \dots, x_m)$ are independent variables and $\Theta = (\Theta_1, \Theta_2, \dots, \Theta_k)$ are parameters and ϵ is the random error assuming the mean is equal to 0 with normal distribution, where k is the degree. A measure of the quality of non-linear fitting parameters is the chi-square value :

$$\chi^2 = \sum_{i=1}^n w_i (y_i - \hat{y}_i)^2, \quad (6.14)$$

where w_i is the weighting coefficient, y_i are the experimental data points, and \hat{y}_i are the theoretical points. To fit the model, the residual is defined as

$$r_i = y_i - \hat{y}_i. \quad (6.15)$$

2816 It conforms to a normal distribution with the mean equal to 0 and the vari-
 2817 ance equal to σ_i^2 . Then the maximum likelihood estimates of the parameters
 2818 Θ_i can be obtained by minimizing the chi-square value , defined as

$$2819 \chi^2 = \sum_{i=1}^n \frac{(y_i - \hat{y}_i)^2}{\sigma_i^2}. \quad (6.16)$$

2821 If the error is treated as weight, $w_i = \frac{1}{\sigma_i^2}$ can be defined in the chi-square
 2822 minimizing equation, where σ_i are the measurement errors. The quality of
 2823 regression can be measured by the coefficient of determination, R^2 , which is
 2824 defined as

$$2825 R^2 = 1 - \frac{w_i(y_i - \hat{y}_i)^2}{\sum_i^n (y_i - \bar{y})^2}. \quad (6.17)$$

2827 In order to express the relationship between independent variables and de-
 2828 pendent variables and a degree of confidence in regression model, the adjusted
 2829 R^2 for validation of goodness of fit measurement is defined as

$$2830 \bar{R}^2 = 1 - \frac{\frac{w_i(y_i - \hat{y}_i)^2}{n^* - k}}{\frac{\sum_i^n (y_i - \bar{y})^2}{n^*}}. \quad (6.18)$$

2832 Note that if intercept is included in the model, the degree of freedom is
 2833 $n^* = n - 1$. Otherwise, $n^* = n$. The adjusted R^2 will avoid the effect of the
 2834 degrees of freedom by adding variables in the model, which results in rising of
 2835 R^2 . Therefore, the adjusted R^2 overcomes the rise in R^2 when fitting a small
 2836 sample size by multiple predictor model.

2837 The covariance value indicates the correlation between two variables, and

the matrices of covariance in regression show the inter-correlations among all parameters. The correlation matrix rescales the covariance values. The covariance matrix of the regression and correlation between parameters are defined as

$$Cov (\Theta_i, \Theta_j) = \sigma^2 (X' X)^{-1} \quad (6.19)$$

and

$$Cor (\Theta_i, \Theta_j) = \frac{Cov (\Theta_i, \Theta_j)}{\sqrt{Cov (\Theta_i, \Theta_i)} \sqrt{Cov (\Theta_j, \Theta_j)}}. \quad (6.20)$$

Parameter errors are equal to the square root of the covariance matrix diagonal values.

6.2.2.2 *Levenberg-Marquardt minimization*

To estimate the $\hat{\Theta}$ value with the least square method, we need to solve the normal equations which are set to be zero for the partial derivatives of χ^2 with respect to each $\hat{\Theta}_p$:

$$\frac{\partial \chi^2}{\partial \hat{\Theta}_p} = 0. \quad (6.21)$$

Employing an iterative strategy to estimate the parameter values, it starts with some initial values Θ_o . With each iteration, χ^2 value is computed and then the parameter values are adjusted to reduce the χ^2 . When χ^2 values computed in two successive iterations are small enough compared with the tolerance, the fitting is converged. The Levenberg-Marquardt algorithm is employed for an

iterative technique that locates a local minimum of a multivariate function that is expressed as the sum of squares of nonlinear function. Levenberg-Marquardt is considered as a combination of steepest descent and the Gauss-Newton method. When the solution is far from a local minimum, the algorithm behaves like a steepest descent method. When the solution is close to a local minimum, it becomes a Gauss-Newton method and exhibits fast convergence.

Given the residuals r_i ($i = 1, \dots, n$) of parameters $\Theta = (\Theta_1, \Theta_2, \dots, \Theta_p)$, with $n \geq k$, the Gauss-Newton algorithm finds the minimum of χ^2 given in Equation (6.16). Starting with an initial guess Θ_o for the minimum, the method proceeds by the iteration $\Theta^{s+1} = \Theta^s + \delta\Theta$ with an increment $\delta\Theta$ satisfying the normal equation given as Equation (6.22) using Equation (6.21).

$$(\mathbf{J}_r^T \mathbf{J}_r) \delta\Theta = -\mathbf{J}_r^T \mathbf{r}, \quad (6.22)$$

where \mathbf{r} is the vector of r_i and \mathbf{J}_r is the Jacobian of \mathbf{r} with respect to Θ . The residuals r_i are defined as $r_i(\Theta) = y_i - f(x_i, \Theta)$. In order to find the parameters Θ that a given model function $y = f(x, \Theta)$ fits best data points, the increment $\delta\Theta$ can be expressed in terms of Jacobian of the function as follow:

$$(\mathbf{J}_f^T \mathbf{J}_f) \delta\Theta = \mathbf{J}_f^T \mathbf{r}, \quad (6.23)$$

The Levenberg-Marquardt iteration is a variation on the Newton iteration. The normal equations $\mathbf{N} \delta\Theta = \mathbf{J}_f^T \mathbf{J}_f = \mathbf{J}_f^T \mathbf{r}$ are augmented to $\mathbf{N}' \delta\Theta = \mathbf{J}_f^T \mathbf{r}$ where $N'_{ij} = (1 + \delta_{ij} \lambda) N_{ij}$ with δ_{ij} the Kronecker delta. The λ is initialized

to a small value, e.g. 10^{-3} . If the value obtained for $\delta\Theta$ reduce the residuals, the increment is accepted and λ is divided by 10 before the next iteration. If the residuals increase then λ is multiplied by 10 and the augmented normal equations are solved again until an increment is obtained that reduces the residuals. For large λ , the iteration approaches a steepest descent.

6.2.3 Filaments distribution and uncertainty of measurement

6.2.3.1 *onset of filamentation on jet surface*

Fig. 6.3 shows photographs of filament evolution on the Hg jet surface at 25 μs frame rate, where the beam is 10 Tp, 24 GeV and the magnetic field is 10 T. Fig. 6.4 shows the locations of filaments where the individual velocity is measured as a function of time, shown in Fig. 6.6, Fig. 6.7 (a), (b). The first collected image among 16 images is brighter than the rest of 15 images. It indicates that the radiation generated by the interaction of Hg with proton beam affects the transmittance and/or reflectance of optical components, resulting in the production of darker images as one sees at the rest of collected 15 images.

6.2.3.2 *measurement of traveled distance of filament*

To obtain the vertical filament velocity, the distance traveled by a fixed point on the jet surface is tracked over a given time period. The jet volume, where the maximal energy is deposited, results in the initial generation of the filaments. The higher jet velocity occurs when the filaments is initially

2905 protruded out of the jet surface and then the jet velocity decreases due to the
2906 magnetic damping and viscous dissipation. So, the velocity at steady state
2907 is obtained in order to evaluate the relationship with the beam intensity and
2908 magnetic field.

2909 The quality of optical images varies from shot to shot since the radiation or
2910 jet dispersion may make image quality varies. The most difficulty in measure-
2911 ment is to discern the edge of filaments as it moves somewhat far away from
2912 surface because the initial jet filament edge is dense (clearly black) but it looks
2913 like dissipating, dilute, disappearing (grey or similar with background) as it
2914 moves further. Because measurement is done in several points, there may be
2915 some error in measurement after some steady velocity (constant peak velocity)
2916 at weak filament velocity measurement.

2917 The image size at Viewport 2 is 240 by 240. Using graphic software, pixels
2918 on image is picked to locate the edge of filament. Therefore, the uncertainty
2919 while locate the position y_m is reported to be ± 2 pixels, which corresponds
2920 to the difference of $\sim \pm 17$ m/s filaments velocity. This uncertainty can occur
2921 randomly uniformly. The peak strong filament which gives constant velocity
2922 within ± 2 pixels until the end of 15 frames is assumed to be considered as there
2923 is constant uncertainty, ± 2 pixels. The weak filament which gives constant
2924 velocity within ± 2 pixels until the filament reaches some frames, for example, 3
2925 ~ 7 frames, is also assumed to be considered as there is constant uncertainty,
2926 ± 2 pixels, where the black edge of filament is clearly observed. However,
2927 after the some frames, for example, 3 ~ 7 frames, because the original edge

of filament dilute or dissipates or disappear, the uncertainty in measurement may not be constant. In this case, measurement is stopped at that frames.

6.2.4 Linear regression with the first order polynomial

6.2.4.1 *curve fit function*

The heaviside step function is defined as the integral of the Dirac delta function as follow:

$$H(t) = \int_{-\infty}^t \delta(\xi) d\xi. \quad (6.24)$$

The ramp function is the antiderivative of the Heaviside step function:

$$R(t) = \int_{-\infty}^t H(\xi) d\xi = tH(t). \quad (6.25)$$

In discrete form, it is now defined as an alternative form for our linear regression model as follow:

$$R(t) = \begin{cases} y_m = s, & t \leq t_o \\ y_m = s + v(t - t_o), & t > t_o \end{cases}, \quad (6.26)$$

where y_m , s , v , t_o denote the measured position of the filament as projected onto the y axis in image, the position of jet surface before the filaments developed, the apparent velocity of the filament along the y axis, and onset time delay of filaments respectively.

6.2.4.2 *parameter estimation using multiple data points*

Shot 11019 is chosen for illustration. Using Equation (6.26) for linear regression model with measured data points y_m and t , minimizing R^2 yields s , v , and t_o . Fig. 6.5 (a) shows the illustration of multiple data points where the intercept of x axis and slope approximate the onset time of filament and apparent velocity projected on y axis in image, which are $t_o = 43.6 \pm 4.5 \mu s$ and $v = 55.5 \pm 0.8 \text{ m/s}$ respectively. The reduced R^2 value and adjusted \bar{R}^2 values are 1.749 and 0.998 respectively. In case of larger velocity of filaments, maximally measurable data points are limited to $\sim 2 \sim 3$ points due to the limited field of view in optical diagnostic image. Fig. 6.5 (b) shows the illustration of 3 data points. The onset time from regression model yields underestimated value such as negative time delay because the data point is equal or smaller than the number of data points. Thus, we assumed the real onset time should be between typical onset time $50 \mu s$ and $0 \mu s$, which yields the onset time of $25 \pm 25 \mu s$. Therefore, the slope of fit curve is determined by fixing the assumed onset time accordingly, which yields the filament velocity of $148 \pm 24.5 \text{ m/s}$. The error is determined directly by dividing approximated filament velocity of the cases of $t_o = 0$ and $t_o = 50 \mu s$ by 2. The shot 10008 is chosen for the illustration of parameter estimation of 3 data points.

6.2.4.3 *filaments velocity distribution on jet surface*

Fig. 6.6 (a) shows the approximated velocity distribution of filaments over the jet surface shown in Fig. 6.3. Fig. 6.6 (b) shows the approximated onset

time distribution of filaments according to the approximated velocity of filaments. As the approximated apparent velocity of filaments projected on y axis in image increases, the approximated onset time of filaments decreases. This shows the evidence of the geometric effects of viewing of filaments. Assuming the filaments are generated perpendicular to the jet surface, as the filaments leaves farther from the jet surface, it takes more time to make an initial observation in images. Thus, it is possible to consider the low velocity of filaments with large onset time leaves from more close to the center of jet normal to the side view shown in images. Note that the velocity of each filament is approximated with uncertainty by doing linear regression using the fit function in order to give one representative velocity according to each filament. Low velocity of filaments close to 0 showed larger error of approximation of onset time due to the uncertainty of the very small observed traveling distance of filaments.

Each filament used for measurement of velocity in Fig. 6.3 has been numbered in Fig. 6.4 for particular indication of each filament. According to the notation in Fig. 6.4, Fig. 6.7 (a) shows the velocity of filaments on the upper free surface of jet as a function of time and Fig. 6.7 (b) shows the velocity of filaments on the lower free surface of jet as a function of time. Note that the instantaneous velocity as defined in Equation (6.28) is used for measurement in Fig. 6.7. The onset time of filament increases as the peak velocity of filament decreases, which indicates the possible evidence of the geometric effect of viewing of filaments.

2992 **6.3 Velocity of Filaments on Mercury Jet Sur-** 2993 **face**

2994 **6.3.1 Magnetic dissipation of energy**

2995 As a conducting liquid moves through a static magnetic field, electric cur-
2996 rents are generated. This, in turn, leads to ohmic heating such as Joule dis-
2997 sipation. As the thermal energy of the fluid rises, there is a corresponding
2998 filament in its kinetic energy, and so the fluid decelerates. This results in a
2999 suppression of the motion of liquid jets. According to P. A. Davidson's ap-
3000 proximation (1999), the Eqn. (2.42) shows the energy decay with respect to
3001 time depending on the magnetic damping time constant, where $\tau = \rho/\sigma B^2$.
3002 This implication is that the filaments decelerates on a time scale of τ . Fig. 2.3
3003 (a) shows the decay of the normalized energy of flow in magnetic fields with
3004 respect to time due to the magnetic damping. Higher magnetic field dissipates
3005 energy faster. Fig. 2.3 (b) shows the integral calculation of energy with respect
3006 to time. Thus, it represents the total energy of flow by the certain time.

3007 **6.3.2 Time response of filaments in magnetic field**

3008 **6.3.2.1 *averaged time response of filament in magnetic field***

3009 Since the camera is triggered before beam arrives at the Hg jet and the
3010 laser pulse width is 150 ns, the first collected image shows the status of Hg jet
3011 before beam comes. Thus, the velocity of filament can always be judged as 0
3012 m/s in the following Fig. 6.8. Fig. 6.8 represents the time response of filament

average velocity as a function of magnetic field with 14 GeV, 20 TP beam and 24 GeV, 10 TP beam respectively. The expression for the calculation of average velocity is

$$v_n^{avg} = \frac{1}{T_n - T_o} \int_{T_o}^{T_n} v(t) dt = \frac{y_m(T_n) - y_m(T_o)}{T_n - T_o}, \quad (6.27)$$

where T_n, T_o denotes the time taken in each framed image and the initial time of the first image respect to the proton beam arrival time respectively. Since the joule damping dissipates the energy with an exponential factor, the energy dissipation arises rapidly in the beginning depending on the magnetic field term B^2 . Thus, higher magnetic field will have higher damping effect so that it takes more rising time. Therefore, the slope of rising velocity in Fig. 6.8 is varying depending on the magnetic field proportional to B^2 in exponential function. The magnitude of steady peak velocity is reduced by increased applied magnetic field strength, which is possible indication of the magnetic damping role induced by the joule damping dissipation. Again, in Fig. 6.8 (a), the delay of onset time of filament causes reduced steady peak velocity in same 5 T, which again indicates the fluctuation of jet flow in magnetic field and the geometric effect of viewing of filaments in shadow photography as well.

6.3.2.2 *instantaneous time response of filament in magnetic field*

Fig. 6.9 represents the time response of instantaneous filament velocity as a function of magnetic field with 14 GeV, 20 Tp beam and 24 GeV, 10 Tp beam respectively, which are reinterpretation of Fig. 6.8 in terms of instantaneous

velocity analysis. The expression for the calculation of instantaneous velocity assuming ΔT_n is small enough is

$$v_n = \frac{y_m(T_n) - y_m(T_{n-1})}{\Delta T_n}. \quad (6.28)$$

Comparing with Fig. 6.8, the velocity of filaments are fluctuating.

6.3.3 Beam induced filaments velocity in magnetic field

6.3.3.1 *filaments velocity with 14 GeV beam in magnetic field*

Fig. 6.10 (a) shows the filament velocity as a function of 14 GeV beam intensity and magnetic field corresponding to the observed onset time of filaments shown in Fig. 6.10 (b). The filament velocity increases with the beam intensity. However, the magnetic field suppresses the filament velocity. At relatively low magnetic field of 5 T, the jet flow and/or the charged beam may be fluctuating depending on the initial conditions at experiment. Thus, there are scattering distributions over the resulting data points. The slope of the data points at higher magnetic fields are less than that associated with lower magnetic field. All velocities are less than 30 m/s regardless of the magnetic field. The filament velocity at 14 GeV, 20 T, 10 T is ~ 13 m/s.

6.3.3.2 *filaments velocity with 24 GeV beam in magnetic field*

Fig. 6.11 (a) shows the filament velocity as a function of 24 GeV beam intensity and magnetic field corresponding to the observed onset time of filaments shown in Fig. 6.11 (b). The filament velocity increases with the beam

intensity. The slope of the increase is $\sim 4 \times$ larger than that for the 14 GeV case, which indicates that parameters such as beam spot size may be affecting the energy deposition density since the ratio of peak energy deposition is ~ 1.5 at 0 T assuming the beam spot sizes for 14 GeV and 24 GeV are ~ 1.6 mm RMS. However, the magnetic field suppresses the filament velocity. At relatively low magnetic field up to 5 T as in the 14 GeV case, the jet flow and/or the charged beam is unstably fluctuating depending on the event conditions at experiment. Thus, there are distributions of the resulting data points. All velocities are less than 130 m/s regardless of the magnetic field, and the filament velocity for the 24 GeV, 20 Tp, 10 T case is ~ 70 m/s.

Table 6.1: Parameterized coefficients, its error, and statistics summary of fit function in figures.

Figure	1	2	3	4	5	6	7	8	9	10
6.5a	128	0.93517	43.57	4.44411	-	-	-	-	-0.26374	0.00392
6.5b(black)	112.1	-	-	-	-	-	-	-	-0.52	-
6.5b(blue)	122	0	0	0	-	-	-	-	-0.5865	0.01587
6.5b(red)	122	0	50	0	-	-	-	-	-0.81911	0.10777
6.13	1.5908	1.00492	16.2263	0	0.39275	0	1.39594	0	1.07591	0.33731
Figure	11	12	13	14	15	16	17	18	19	
6.5a	-	-	-	-	15	12	1.74908	0.99773	0.0505	
6.5b(black)	-	-	-	-	2	0	0	0	0	
6.5b(blue)	-	-	-	-	3	2	12.31396	0.99622	0	
6.5b(red)	-	-	-	-	3	2	281.74259	0.91351	0	
6.13	-0.01575	0.01702	0	0	25	22	2.15282	0.1527	0.0013	

1 : A1 value, **2** : A1 standard deviation,

3 : B1 value, **4** : B1 standard deviation, **5** : B2 value, **6** : B2 standard deviation,

7 : B3 value, **8** : B3 standard deviation , **9** : C1 value, **10** : C1 standard deviation,

11 : C2 value, **12** : C2 standard deviation, **13** : C3 value, **14** : C3 standard deviation,

15 : Number of points, **16** : Degrees of freedom, **17** : Reduced χ^2 , **18** : Adjusted \mathbf{R}^2 , **19** : χ^2 probability.

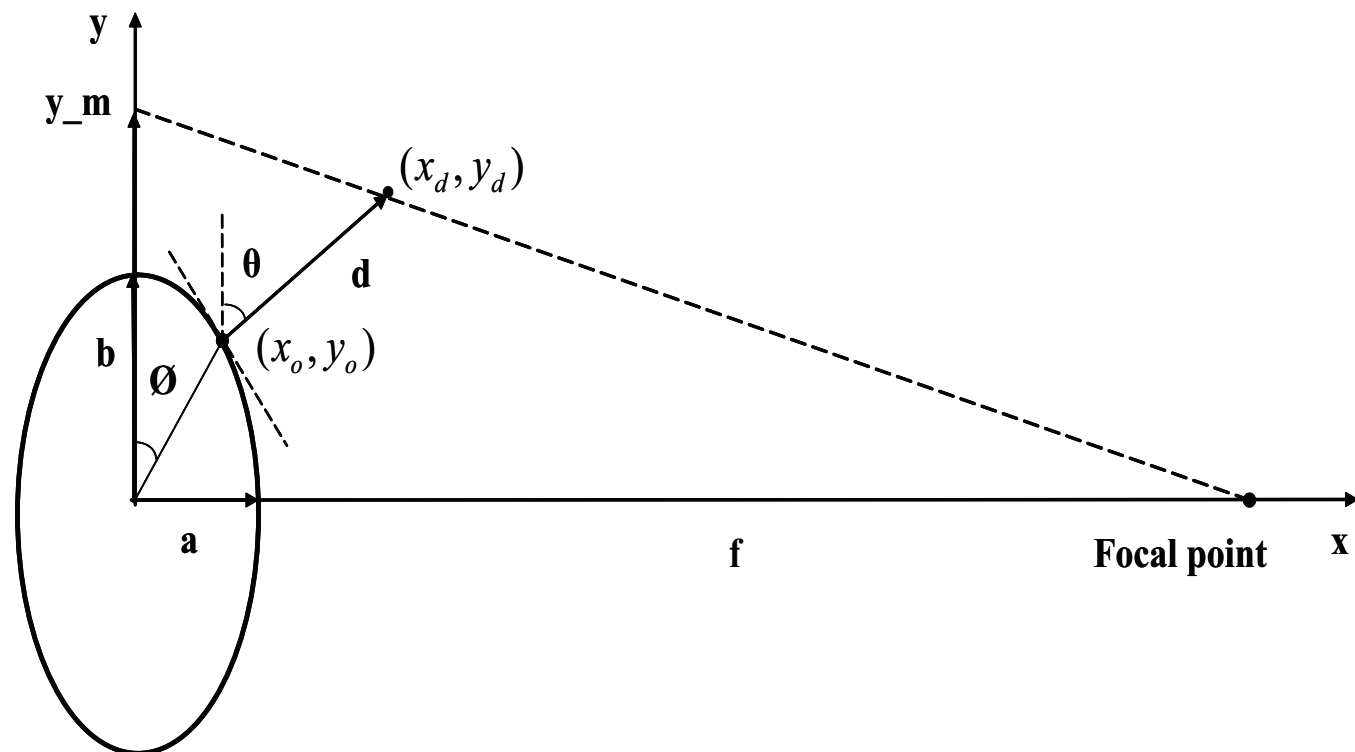
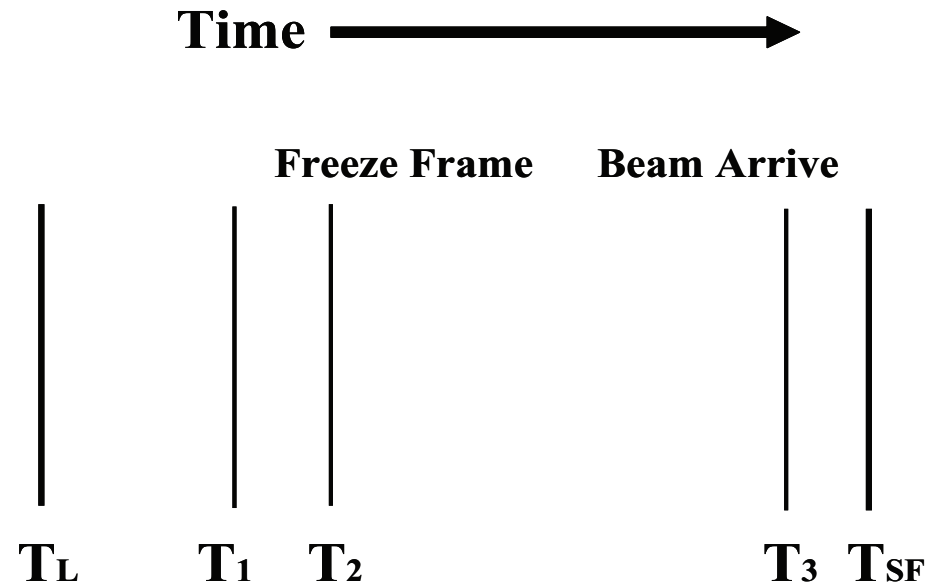


Figure 6.1: Schematic geometry of viewing mercury filaments.



T_L : Laser Enable

T_1 : Time of Delay to Peak Laser Pulse, 250 ns

T_2 : Time of Flight to Primary Vessel, 60 ns

T_3 : Time of Flight from Primary, 60ns

T_{SF} : Scintillating Fiber Signal

Figure 6.2: Time structures between light source enabling and proton beam arrival.

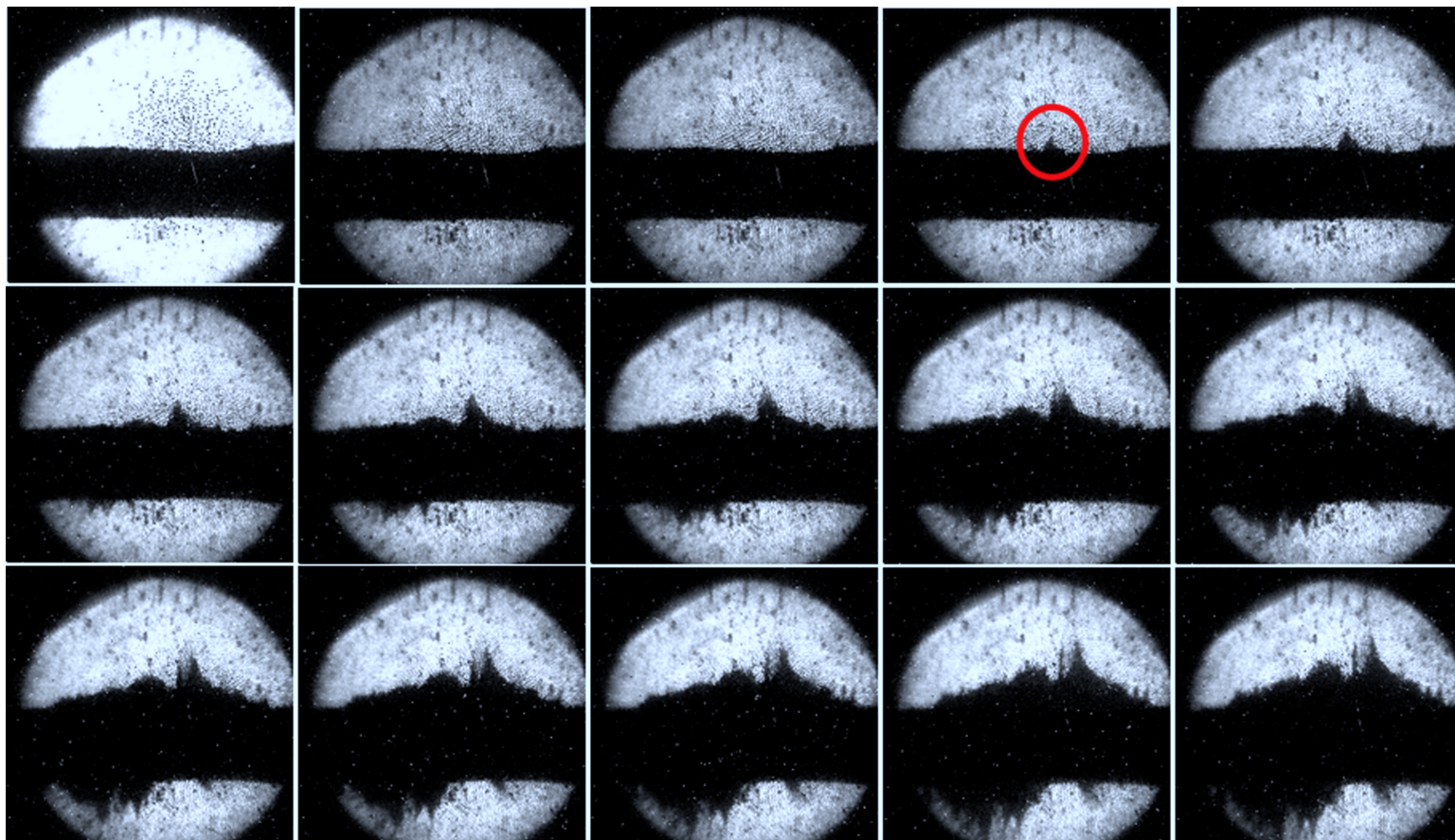


Figure 6.3: Photographs of filament evolution on the Hg jet surface as a function of time at $25 \mu\text{s}$ frame rate. The beam is 10 Tp, 24 GeV. The magnetic field is 10 T. The red circle on the 4th image of the top row points the filament that is used for velocity measurement in Fig. 6.8 (b) and Fig. 6.9 (b).

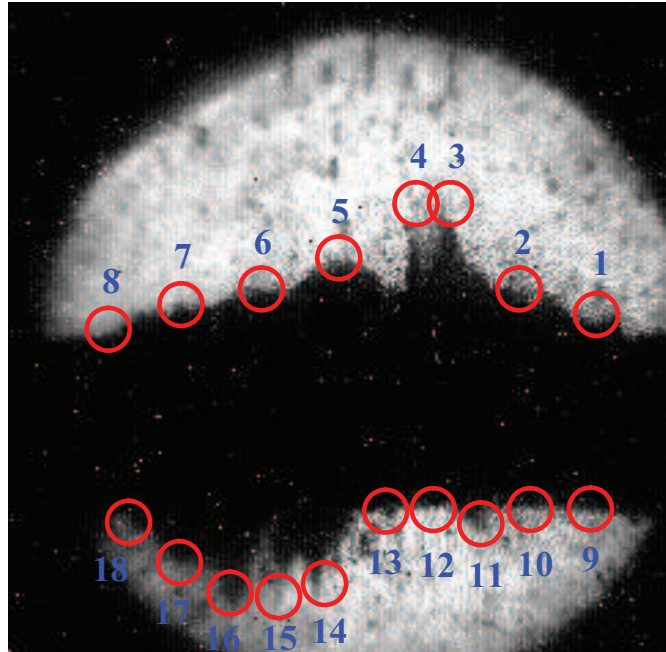


Figure 6.4: Location on the Hg jet surface for velocity measurement of 14 points of filament. The shot condition same with Fig. 6.3. The numbers above red circles points the filament that is used for velocity approximation in Fig. 6.6 and Fig. 6.7.

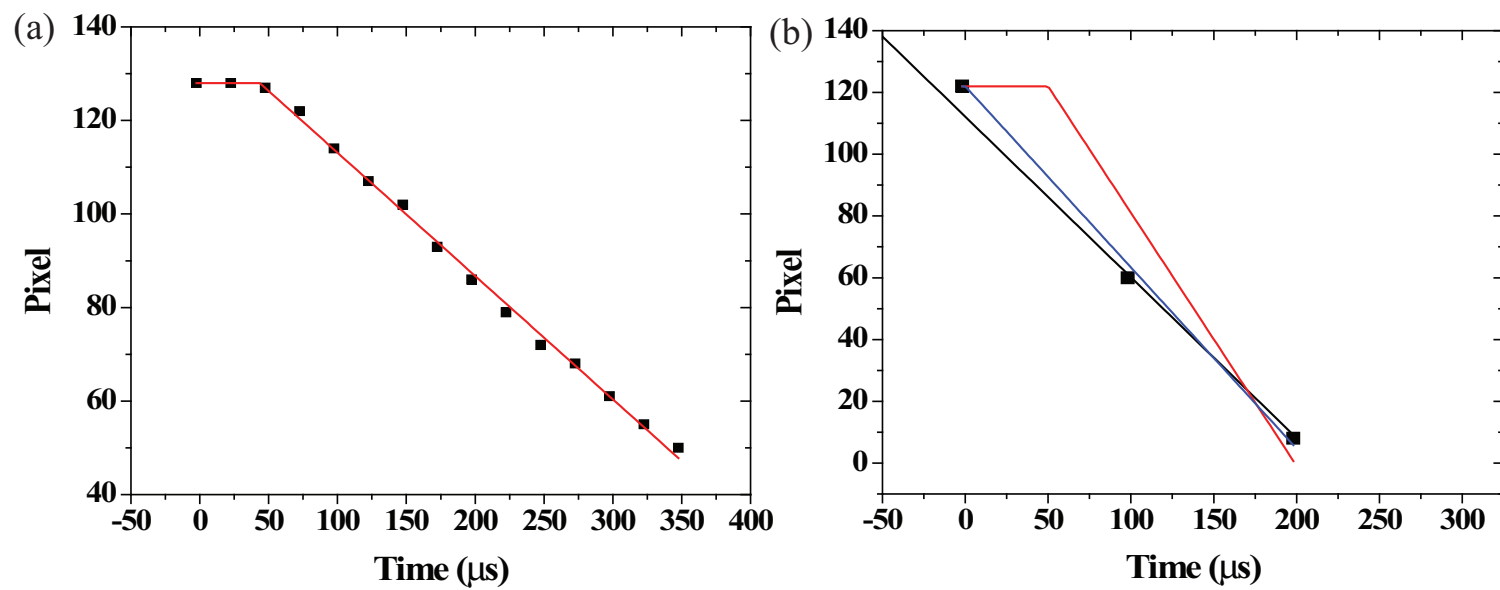


Figure 6.5: Illustration of curve fit for parameters estimation. a.) Multiple data points. b.) 3 data points.

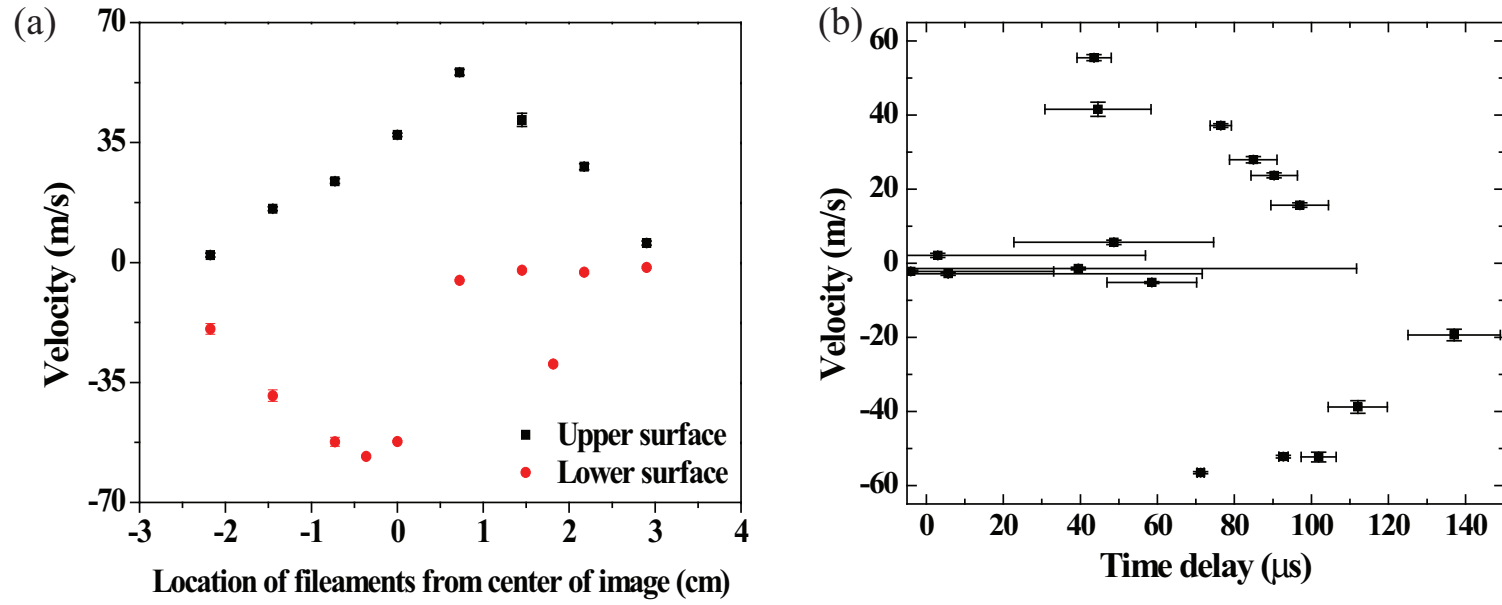


Figure 6.6: Approximation of velocity and onset time of filaments shown in Fig. 6.3. The beam is 10 Tp, 24 GeV. The magnetic field strength is 10 T. a.) Approximation of velocity of filaments. b.) Approximation of onset time of filaments.

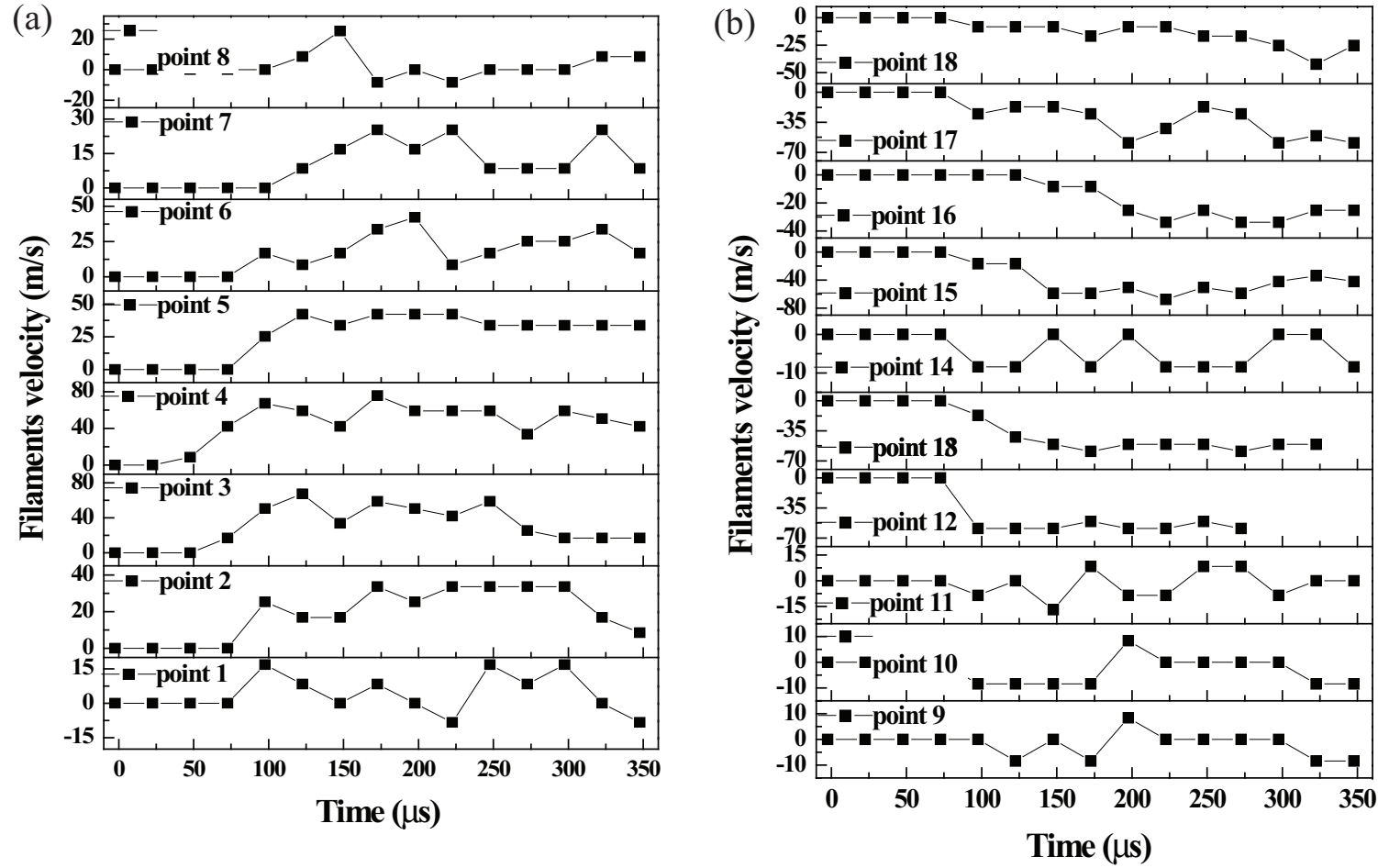


Figure 6.7: Time response of instantaneous filament velocity at jet surface in Fig. 6.3 as a function of distance from magnet center. The beam is 10 Tp, 24 GeV. The magnetic field is 10 T. a.) Upper surface. b.) Lower surface.

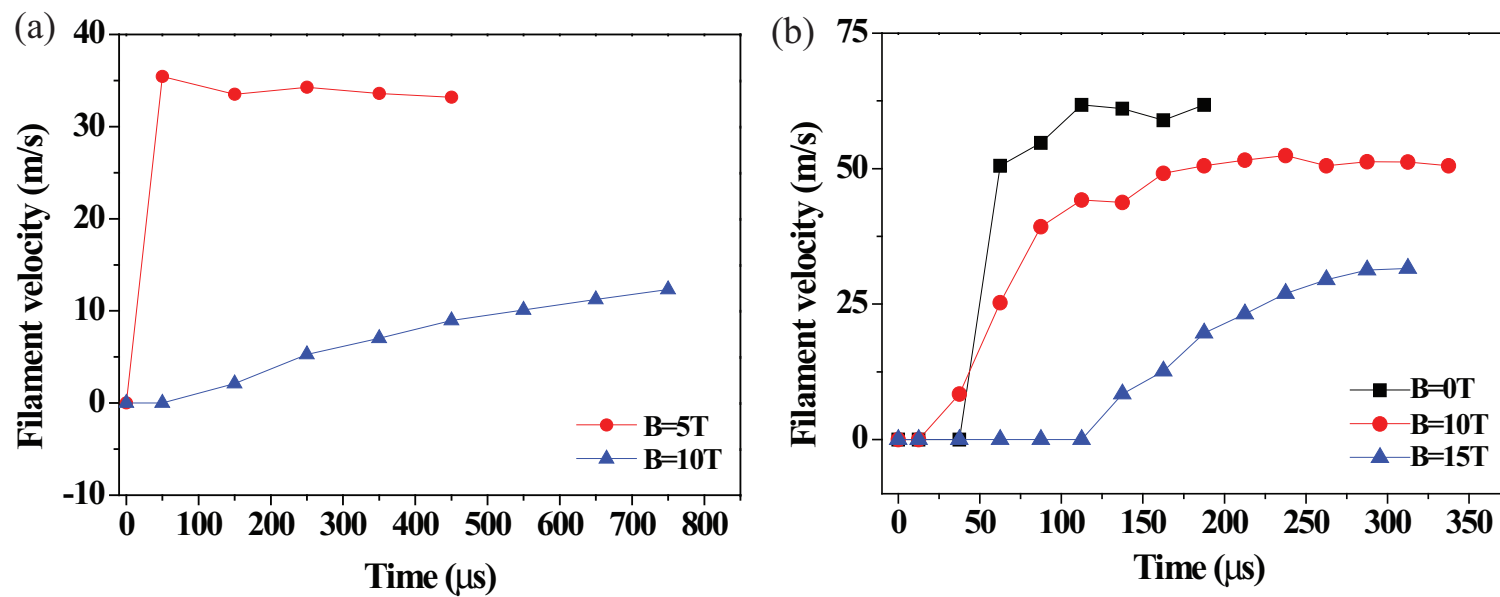


Figure 6.8: Time response of averaged filament velocity as a function of magnetic field. a.) 14 GeV, 20 Tp beam. b.) 24 GeV, 10 Tp beam.

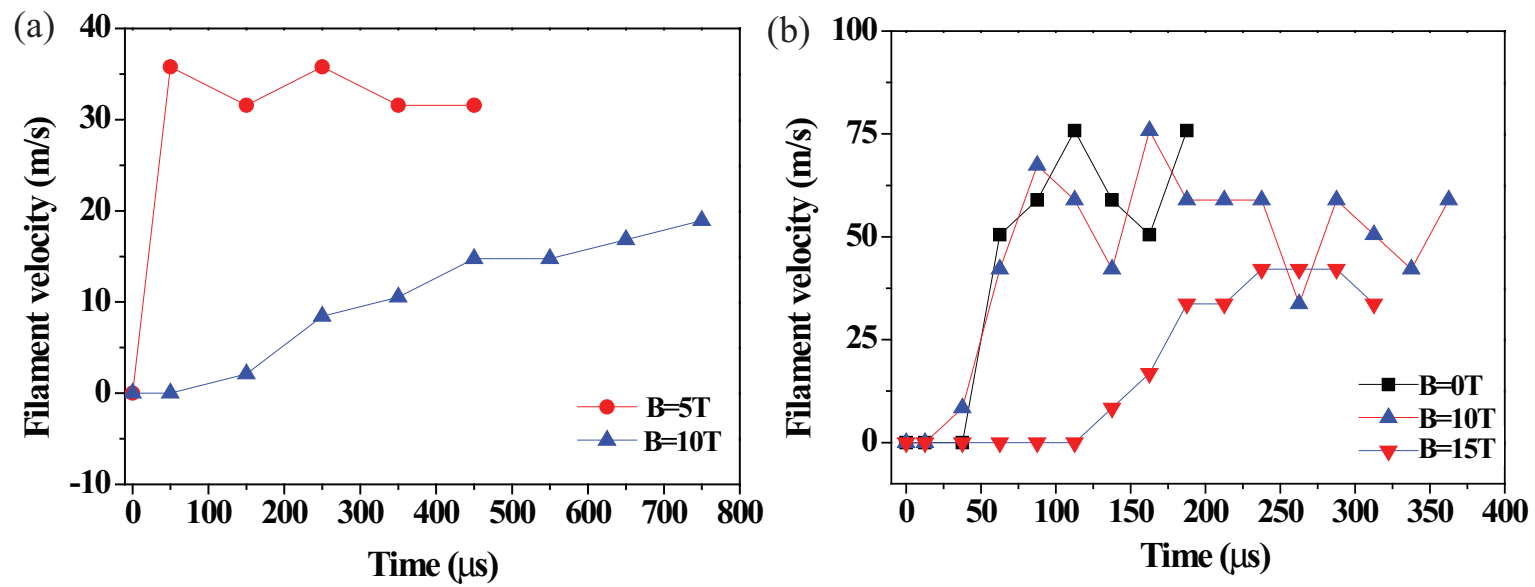


Figure 6.9: Time response of instantaneous filament velocity as a function of magnetic field. a.) 14 GeV, 20 Tp beam. b.) 24 GeV, 10 Tp beam.

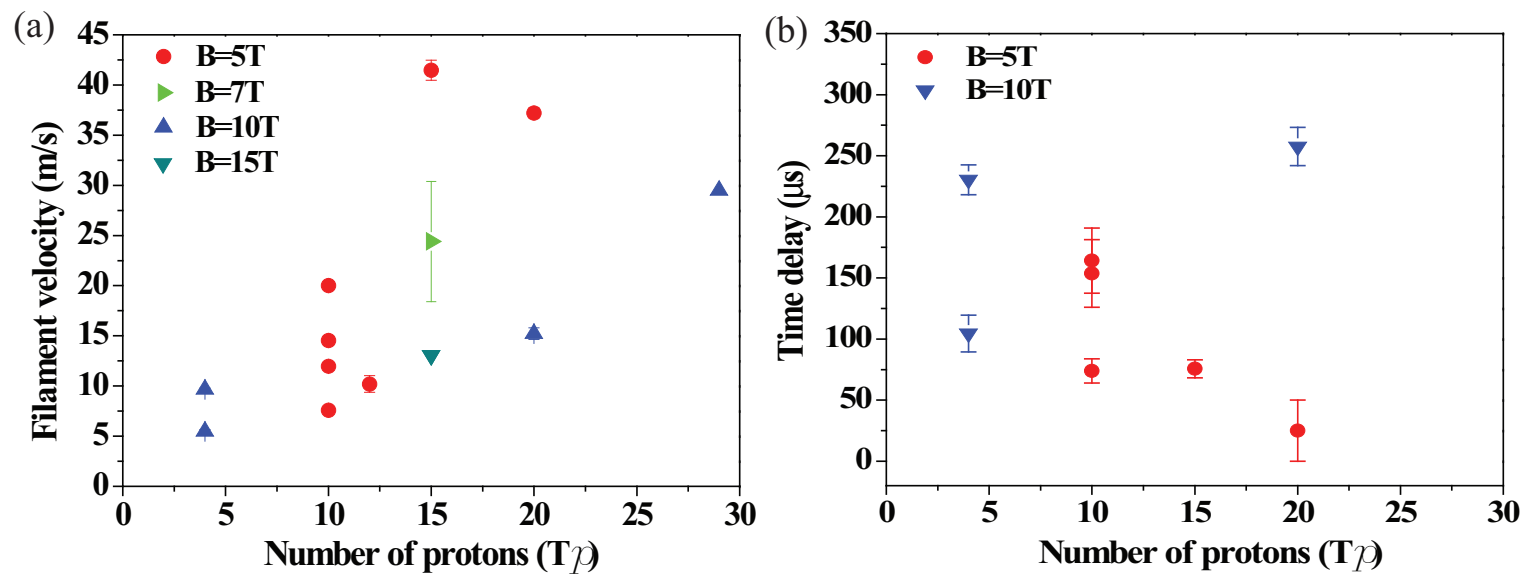


Figure 6.10: Filament velocity as a function of 14 GeV beam intensity and magnetic field. a.) Apparent filament velocity. b.) Onset time of filament.

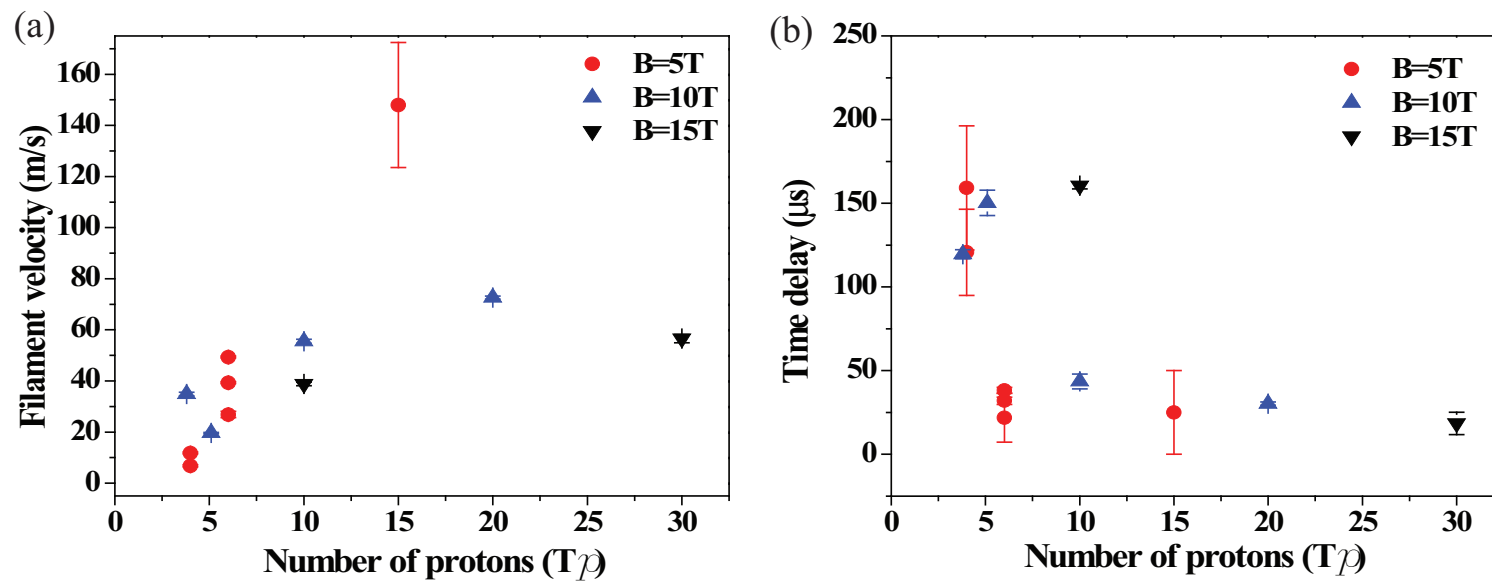


Figure 6.11: Filament velocity as a function of 24 GeV beam intensity and magnetic field. a.) Apparent filament velocity. b.) Onset time of filament.

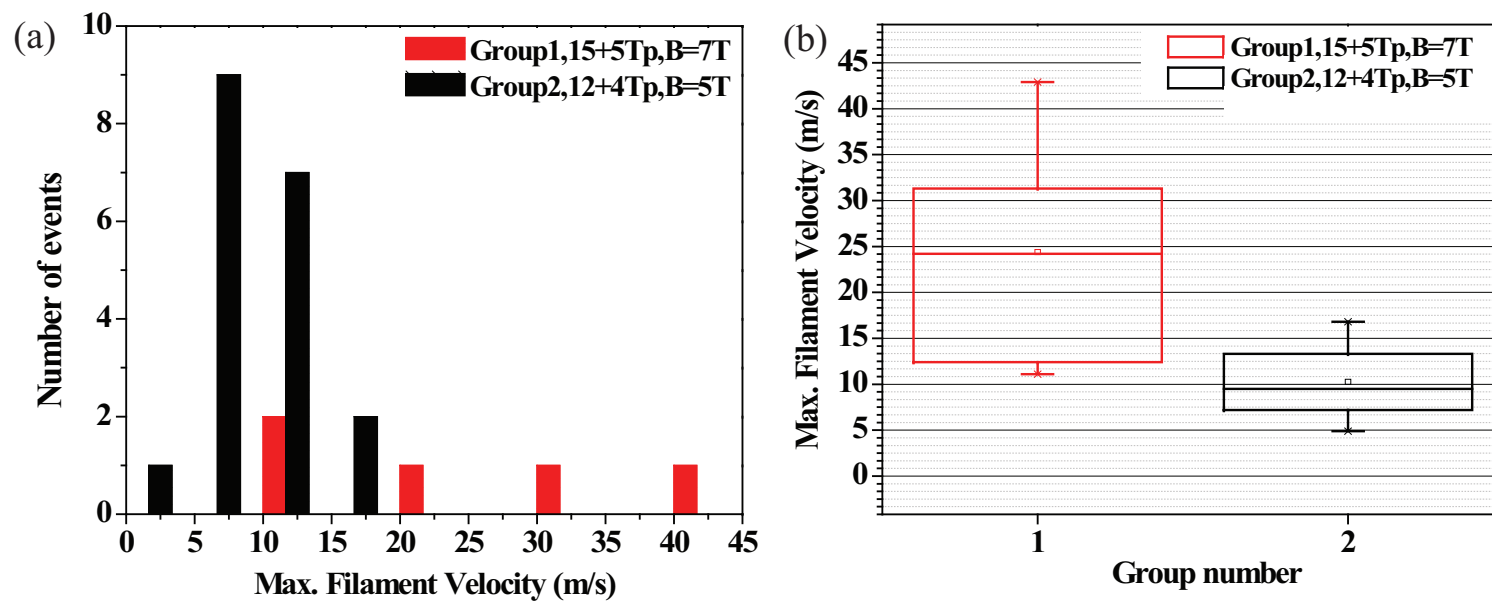


Figure 6.12: Filament velocity distribution measurement in a same condition. Pump probe conditions with harmonic 8 and 16 bunches are used.

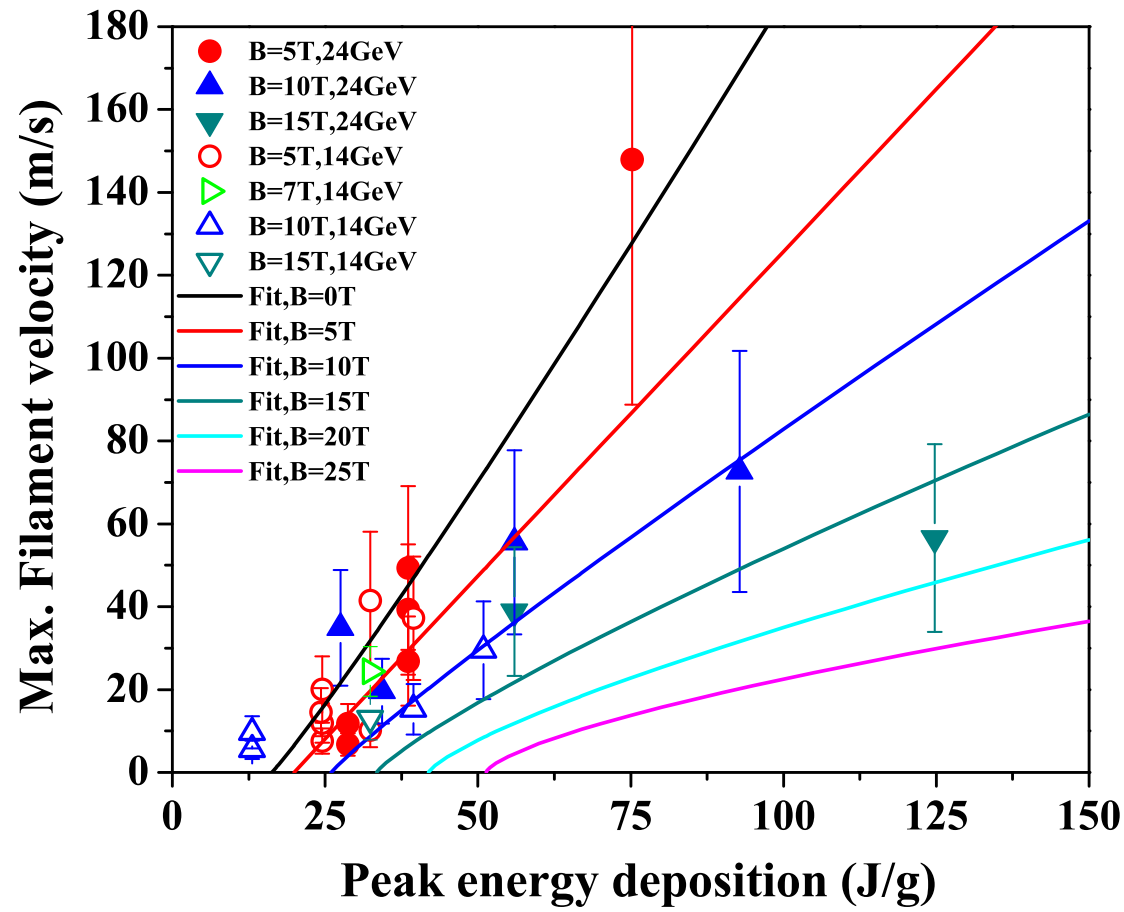


Figure 6.13: Filament velocity in magnetic fields ejected from jet surface as a function of peak energy deposition and its extrapolation.

Chapter 7

Conclusions

The experiment is a proof-of-principle test for a target system capable of accepting a high-intensity 4 MW proton beam. The system allows for the production of copious pions which subsequently decay into muons. These muons are magnetically captured, accelerated and inserted into storage rings. An experiment at the CERN Proton Synchrotron that combines a free mercury jet target with a 15 T solenoid magnet and 14 GeV and 24 GeV proton beam was performed. It validates the target concept for producing an intense secondary source of muons. When combined with a beam bunch of 30×10^{12} protons on the mercury target, this will generate a peak energy deposition of ~ 100 J/g. For this experiment, a pulsed solenoid was designed, which is capable of delivering a peak field of 15 T. The Hg jet loop system generates a mercury jet from 1 cm diameter nozzle with velocities up to 15 m/s. An optical diagnostic system based on back-illuminated laser shadow photography is employed to investigate the mercury jet flow. Synchronized short laser light pulses are used to illuminate the target and freeze the motion of the jet. A total of four optical imaging heads for each Viewport are mounted on the exterior of the

primary containment vessel. Three high speed cameras are used to simultaneously collect images on three Viewports. Integrated all-in-one compact optical heads, consisting of ball lens, illumination fiber, objective lens, and imaging fiber bundle, are placed at the radius of curvature of a retro-reflector allowing for the illumination and imaging collection on one side of the mercury primary containment vessel. Due to the short time of frame rate, the time delay from the light source to the image arrival at the camera CCD is adjusted considering the delay from the electronics as well as the fiber-optics. The optimum timing delay is judged by the uniformity of consecutive collected image brightness as well as the triggering signal pulse on the oscilloscope for each component of device. The trigger timing is adjusted using the response of the scintillating fiber on the oscilloscope with respect to the beam triggering timing. The motions of mercury jet for 0.4 s at Viewport 1, 3, and 4 and for 1.6 ms at Viewport 2 are collected, respectively, which enables us to give both the overall jet condition at upstream (downstream) and the accurate motion of jet at midstream, where the magnetic induction field is maximum and the center of beam-jet interaction is positioned. Image processing provides some information on the mercury jet thickness at various magnetic induction field strengths and velocities, i.e., the optical diagnostic observation shows the effects of the magnetic force on the cross-sectional distortion of mercury jet caused by the Lorentz force. In addition, the image analysis reveals the jet instability which might be caused by the strong induced axial magnetic induction field, which is possibly the onset of a quadrupole effect. Nevertheless, the experimental

3108 results clearly show that the magnetic induction field stabilizes the mercury jet
3109 by smoothing out the edges of the otherwise turbulent mercury flow, as pre-
3110 viously reported in the literatures (Shercliff 1956, Gold 1962, Kozyrev 1981,
3111 Bernshtam 1982). The comprehensive optical diagnostic method allows us to
3112 have a better understanding of the behavior of a conducting jet moving in a
3113 high magnetic induction field environment. It plays a key role as a primary
3114 diagnostic of free mercury jet interacting with an intense proton beam under
3115 high-magnetic induction field. The optical diagnostics will allow us to inter-
3116 pret the beam-jet interaction length caused by the energy deposition from the
3117 proton beam as well as the splash velocity on the mercury jet surface with the
3118 aid of the high speed camera.

3119 In order to achieve an understanding of liquid metal flow in a magnetic
3120 field, magnetohydrodynamic equations considering Lorentz force effect based
3121 on the Navier-Stokes equations as well as Maxwell equations are presented.
3122 The jet height is measured as a function of the magnetic field strength. The
3123 suppression of vorticity by the perpendicular magnetic field is introduced and
3124 the Stuart number gives the magnetic field effect.

3125 Such a reducing effect in rotational motion on the jet surface is observed
3126 qualitatively. As a result, the rotational motion of jet on the surface becomes
3127 more two dimensional motion of flow and thus the jet surface is more stabilized.

3128 For magnetohydrodynamic flow investigation, the mercury jet behavior is
3129 observed for various magnetic field strengths and then the jet deformation is
3130 measured. The fluctuation on the jet surface decreases as the magnetic field

3131 increases and the jet height increases slightly with magnetic field assuming the
3132 major and minor axis of Hg jet is reversed. Gravity affects the jet trajectory
3133 so that the jet bends down as it goes downstream. But this deflection of the
3134 jet by gravity is reduced at higher magnetic field. The jet axis becomes more
3135 straight toward the direction of magnetic field line.

3136 The stabilizing effect of the magnetic field on a turbulent jet is observed.
3137 It is well known that the turbulent fluctuation is suppressed by magnetic field
3138 and we could observe that the wave length on the jet surface increases. Thus,
3139 the jet surface is getting flattened as the magnetic field increases. Also, the
3140 critical Reynolds number increases due to the magnetic field. Therefore, the
3141 jet is getting more stabilized. The measured intermittency shows the fluctuat-
3142 ing surface of jet is getting more flattened as the magnetic field increases. The
3143 transverse magnetic field is more dominant to the jet stabilization though the
3144 longitudinal magnetic field is also influential. However, the jet has a different
3145 type of instability at magnetic fields larger than 10 T. The jet height becomes
3146 larger at larger magnetic field than 10 T. This is induced by the longitudinal
3147 current due to the tilted jet axis with respect to the magnet axis. Thus, the
3148 induced current generates a Lorentz force. As a result, additional anisotropic
3149 magnetic force is changing the jet height. As the magnetic field increase up to
3150 5 T, the jet fluctuation decreases and the jet is more elongating to the flow di-
3151 rection. Thus, the jet height decreases from 0 T to 5 T. However, the magnetic
3152 pressure is influencing at larger than 5 T. Since the optical diagnostics depends
3153 on the side view of jet flow, it is hard to tell in which direction the jet deflects

3154 since the jet and the magnetic field line is axially symmetric. However, the jet
3155 height clearly increases at 15 T, which indicates that the magnetic pressure
3156 apparently affects the jet height at 15 T.

3157 The longitudinal jet velocity is not varied. Again, the jet elongation to the
3158 field direction by the magnetic field is indicated from this result. The longi-
3159 tudinal magnetic field does not influence the jet flow velocity. The transverse
3160 magnetic field will change the jet velocity. This is known as the Hartmann
3161 flow. The longitudinal magnetic field does not influence the longitudinal jet
3162 flow as it is shown in the governing MHD equation.

3163 The pipe pressure driven by the syringe piston was measured. It shows that
3164 the Hg driving pressure is the same regardless of the magnetic field variation.
3165 The driving pressure at the Hg pipe inlet is independent of the magnetic field
3166 strength. Therefore, the mercury delivery is not influenced by the longitudinal
3167 magnetic field. However, there may be some pressure loss or jet velocity pro-
3168 file change due to the pipe bend. According to the velocity measurement at
3169 upstream, mid-stream, and downstream, it is not significantly different but it
3170 is same comparing with the flow velocity at 0 T. Therefore, the field effect at
3171 the pipe bend is expected to be somewhat negligible. To support this result,
3172 the pipe loss due to the geometry and friction is estimated.

3173 The most interesting result is the observation of the interaction of the pro-
3174 ton beam with the jet, for provides clue to validate the performance of high
3175 power target for future accelerator. The disruption as manifested by the jet
3176 break up is caused by the energy deposition of proton beam. The filaments

3177 begins on the bottom surface of Hg jet where the proton beam enters. The
3178 filaments ends on the top surface of Hg jet where the proton beam leaves. The
3179 jet breakup is occurring at the center of jet where the maximum energy is
3180 deposited. This phenomenon is consistent with the beam trajectory across the
3181 jet as well as the results of energy deposition by the proton beam. However,
3182 Hg jet breakup is influenced by the magnetic field. In order to validate the
3183 measured disruption length, circular jet shape with reduced mass density and
3184 elliptic jet shape are modeled in MARS code for calculation of energy depo-
3185 sition. Deposition of peak energy density to Hg jet according to the beam
3186 intensities and magnetic field strengths are analyzed. Based on the hypothe-
3187 sis of threshold of beam intensity causing the disruption of Hg jet at various
3188 magnetic field strength, the disruption length is estimated, which gives good
3189 agreement with experimentally measured disruption length.

3190 The filamentation velocity increases as the beam intensity increases due
3191 to the increased energy deposition but the magnetic field reduces the filamen-
3192 tation velocity. The disruption length increases with both beam energy and
3193 intensity because the energy deposition to Hg jet increases as the beam en-
3194 ergies and the beam intensities increase. However, the disruption length is
3195 also suppressed by the magnetic field because of the magnetic damping. As a
3196 result, the intensity threshold for breakup is lower at higher energy. The time
3197 scale of magnetic damping indicates the rate of decay of global kinetic energy
3198 due to the magnetic field strength. Thus, the energy decreases faster as the
3199 magnetic field increases. Therefore, the rising time to the maximum velocity

3200 increases as the magnetic field increases. It indicates that the magnetic damp-
3201 ing is getting larger by the magnetic field in terms of the transient response
3202 time.

3203 Finally, the performance and feasibility of utilizing liquid metal jet as a
3204 target for an intense proton beam is explored. The liquid jet target concept
3205 is based on the target being recycled after each pulse. Therefore, the power
3206 of the target has to be evaluated in terms of the replacing capability. The
3207 optimal interaction length for the 24 GeV beam energy is in the region of 30
3208 cm which corresponds to approximately 2 interaction length for mercury (Kirk
3209 *et al*, 2008). For a 20 m/s jet velocity, replacing two interaction lengths will
3210 be taken in 14 ms thus allowing for operations with a repetition rate of up to
3211 70 Hz. The beam energy per pulse is 115 kJ for a beam of 30×10^{12} protons
3212 with 24 GeV beam energy. The disruption length at 30×10^{12} protons with
3213 24 GeV beam energy in a magnetic field of 15 T is less than 20 cm at 24 GeV
3214 beam energy, thus preserving the 70 Hz beam repetition rate option, which
3215 corresponds to a beam power of 8 MW. It is validated that a target system
3216 capable of supporting proton beams with powers of up to 8 MW (Kirk *et al*,
3217 2008).

Bibliography

- 3219 [1] J. Alessi *et al*, 1998, “A proposal for an *R&D* program for targetry and
3220 capture at a muon collider source,” *Approved as BNL E951*
- 3221 [2] M. M. Alsharoa *et al*, 2003, “Recent progress in neutrino factory and
3222 muon collider research within the muon collaboration,” *submitted to Phys.*
3223 *Rev. ST Accel. Beams.*, [http : //www.cap.bnl.gov/mumu/pubs/prstab –](http://www.cap.bnl.gov/mumu/pubs/prstab-030422/prstab.pdf)
3224 [030422/prstab.pdf](http://www.cap.bnl.gov/mumu/pubs/prstab-030422/prstab.pdf)
- 3225 [3] C. M. Ankenbrandt *et al*, 1999, “Status of muon collider research and
3226 development and future plans” *Phys. Rev. ST Accel. Beams* **2**, **081001**
- 3227 [4] Robert P. Benedict, 1980, *Fundamentals of pipe flow*, John Wiley & Sons,
3228 Inc.
- 3229 [5] V. A. Bernshtam, S. V. Kozyrev, A. I. Él’kin, 1982, “Stability of flow
3230 of films of a conducting viscous liquid in longitudinal magnetic field,”
3231 *Magnetohydrodynamics*, **18**, pp.132
- 3232 [6] Herman Branover, 1978, *Magnetohydrodynamic flow in ducts*, John Wiley
3233 & Sons, Inc.
- 3234 [7] Michael P. Brenner, 2002, “Single bubble sonoluminescence,” *Reviews of*
3235 *Modern Physics*, **74**, pp.425-440
- 3236 [8] G. A. Carlson, 1975, “Dynamic tensile strength of mercury,” *J. Appl.*
3237 *Phys.*, v.46, pp.4069-4070
- 3238 [9] Donald Chang, Thomas Lundgren, 1961, “Duct flow in magnetohydrody-
3239 namics,” *Z. angew. Math. Phys.*, **12**, pp.100-114

- 3240 [10] I. G. Currie, 1993, *Fundamental Mechanics of Fluids*, Marcel Dekker, Inc.
- 3241 [11] P. A. Davidson, 1999, "Magnetohydrodynamics in materials processing,"
3242 *Annu. Rev. Fluid Mech.*, **31**, pp.273-300
- 3243 [12] G. F. D. Duff, D. Naylor, 1966, *Differential equations of applied mathe-*
3244 *matics*, John Wiley & Sons, Inc.
- 3245 [13] I. Efthymiopoulos, A. Fabich, J. Lettry, 2005, "CERN installation,"
3246 <http://cern.ch/proj-hiptarget>
- 3247 [14] I. Efthymiopoulos, 2008, "The MERIT ex-
3248 periment (nToF11)," *MUTAC review*, [http](http://www.hep.princeton.edu/mcdonald/mumu/target/Ilias/ie080408.pdf) :
3249 [//www.hep.princeton.edu/mcdonald/mumu/target/Ilias/ie080408.pdf](http://www.hep.princeton.edu/mcdonald/mumu/target/Ilias/ie080408.pdf)
- 3250 [15] A. Fabich, 2005, "nToF11: Multi-MW target experiment in TT2A,"
3251 <http://cern.ch/proj-hiptarget>
- 3252 [16] A. G. Fedin, 1973, "Use of optical methods in investigating MHD pro-
3253 cesses" *Magnetohydrodynamics (English translation of Magnitaya Gidro-*
3254 *dinamika)*, **9**, pp.301-308
- 3255 [17] T. A. Gabriel *et al*, 2001, "Targets for high-intensity particle production,"
3256 *Part. Accel. Conf.*, Chicago, pp.737
- 3257 [18] T.A. Gabriel, J.R. Haines, T. J. McManamy, P. Spampinato, B. W.
3258 Riemer, 2001, "Targets for high intensity particle production," *Part. Ac-*
3259 *cel. Conf.*, Chicago, pp737-741
- 3260 [19] J. Gallardo *et al*, 2001, "Calculation for a mercury jet target in a solenoid
3261 magnet capture system," *Part. Accel. Conf.*, Chicago, pp627-629
- 3262 [20] J. Gallardo *et al*, 2002, "First order perturbative calculations for a con-
3263 ducting liquid jet in a solenoid," *MUC-NOTE-TARGET-242, MU-047*
- 3264 [21] D. Gao, N. B. Morley, 2002, "Equilibrium and initial linear stability anal-
3265 ysis of liquid metal falling film flows in a varying spanwise magnetic field,"
3266 *Magnetohydrodynamics*, **38**, No.4, pp. 359-375

- 3267 [22] A. K. Geim, M. D. Simon, M. I. Boamfa, M. J. Lighthill, 1999, "Magnetic
3268 levitation at your finger tips," *Nature*, **400**, pp. 323
- 3269 [23] M. B. Glanert, M. J. Lighthill, 1955, "The axissymmetric boundary layer
3270 on a long thin cylinder," *Proc. Roy. Soc. Ser.*, **A 230**, pp. 188
- 3271 [24] Richard R. Gold., 1962, "Magnetohydrodynamic pipe flow: Part 1.," *J.*
3272 *Fluid Mech.*, **13**, pp.505-512
- 3273 [25] R. J. Goldstein, 1991, *Optical systems for flow measurement*, McGraw-
3274 Hill, Inc.
- 3275 [26] Andrew Gray and G. B. Mathews, 1966, *A treatise on Bessel functions*
3276 *and their applications to physics*, Dover, Inc.
- 3277 [27] V. Graves, 2007, "MIT testing results" *MUTAC review*, *http* :
3278 *//www.hep.princeton.edu/mcdonald/mumu/target/graves/VGraves-*
3279 *070418.pdf*
- 3280 [28] J. Hartmann, 1937, "Hg dynamics I," *Kgl. Danske Videnskab Selskabs*
3281 *Math. Fys.*, Medd. 15, No.6
- 3282 [29] A. Hassanein, I. Konkashbaev, 2001, "Dynamics of liquid metal jets pene-
3283 trating a strong magnetic field in high power colliders," *Part. Accel. Conf.*,
3284 Chicago, pp624-626
- 3285 [30] H. Ito, 1960, "Pressure losses in smooth pipe bends," *Trans. ASME., J.*
3286 *Basic Eng.*, **82**, pp.131
- 3287 [31] Uhlenbusch J., Fishcer E., 1961, "Hydromagnetische strömung im
3288 kreiszylindrischen rohr," *Z. Phys.*, **165**, pp.190-198
- 3289 [32] Colin Johnson, 2002, "A self focusing mercury jet target," *CERN-*
3290 *NUFACT-113*
- 3291 [33] T. Kakuta, T. Shikama, M. Marui, 1999, "Optical fibers and their appli-
3292 cations for radiation measurement," *Seventh Int. Conf. on Nuclear Engi-*
3293 *neering*, Tokyo, Japan, pp.19
- 3294 [34] H. G. Kirk *et al*, 2001, "Target studies with BNL E951 at the AGS,"
3295 *Part. Accel. Conf.*, Chicago, pp.1531-1537

- 3296 [35] H. G. Kirk *et al*, 2008, "The MERIT high power target experiments at
3297 the CERN PS," *European Part. Accel. Conf.*, Genoa, Italy, *WEPP169*
- 3298 [36] B. A. Kolovandin, 1965, "Stability of flow of conducting liquid with free
3299 surface in the presence of magnetic and electric fields," *Prikl. Mekh.*, **1**,
3300 No. 11, pp.95
- 3301 [37] S. V. Kozyrev, A. I. Él'kin, 1981, "Stability of flow of thin films of elec-
3302 trically conducting liquid in crossed magnetic and electric fields," *Mag-
3303 netohydrodynamics*, **17**, No. 4, pp.353
- 3304 [38] H. C. Lee, 1977, "Boundary layer around a liquid jet," *IBM J. Res. De-
3305 velop.*, pp.48
- 3306 [39] J. Lettry *et al*, 2003, "Thermal shocks and magnetohydrodynamics in
3307 high power mercury targets," *J. Phys. G: Nucl. and Part. Phys.*, **29**,
3308 pp.1621
- 3309 [40] Junwoo Lim *et al*, 1998, "Control of streamwise vortices with uniform
3310 magnetic fluxes," *Physics of Fluids*, **10**, 8, pp.1997
- 3311 [41] S. P. Lin, D. J. Kang, 1987, "Atomization of a liquid jet," *Physics of
3312 Fluids*, **30**, pp.2000-2006
- 3313 [42] K. T. McDonald *et al.*, 2001, "The primary target facility for a neutrino
3314 factory based on muon beams," *Proc. Part. Accel. Conf.*, Chicago, IL,
3315 pp.1583
- 3316 [43] K. T. McDonald, 2000, "Cooling of a target by helium gas," *Princeton
3317 /μ/μ/00-25*
- 3318 [44] K. T. McDonald, 2000, "Damping of radial pinch effects," *Princeton
3319 /μ/μ/00-26*
- 3320 [45] K. T. McDonald, 2000, "Magnetohydrodynamics of a continuous mercury
3321 jet coaxially entering a solenoid," *Princeton /μ/μ/00-29*
- 3322 [46] K. T. McDonald, 2000, "Magnetohydrodynamics of a pulsed mercury jet
3323 entering a solenoid at an angle," *Princeton /μ/μ/00-30*

- 3324 [47] K. T. McDonald, 2000, "Optics for E951 target tests in the A3 beamline,"
3325 *Princeton / $\mu/\mu/00-28$*
- 3326 [48] K. T. McDonald, 2009, *Private communication*
- 3327 [49] N. V. Mokhov, 2001, "Particle production for a muon storage ring: I.
3328 Targetry and π/μ yield" *Nucl. Inst. Methods in Phy. Res.*, **A 472**, pp.546-
3329 551
- 3330 [50] N. V. Mokhov, O. E. Krivosheev, 2000, "MARS code status,"
3331 *FERMILAB-Conf-00/181*
- 3332 [51] Neil B. Morley *et al*, 2000, "Liquid magnetohydrodynamics - recent
3333 progress and future directions for fusion," *Fusion Engineering and De-*
3334 *sign*, **51**, pp.701-713
- 3335 [52] Neil B. Morley, Sergey Smolentsev, Donghong Gao, 2002, "Modeling infi-
3336 nite/axisymmetric liquid metal magnetohydrodynamic free surface flows,"
3337 *Fusion Engineering and Design*, **63**, pp. 343-351
- 3338 [53] S. Ozaki, R. Palmer, M. Zisman, J. Gallardo, 2001, "Neu-
3339 trino factory feasibility study 2," *BNL-52623*, Ch.3, *http* :
3340 *//www.cap.bnl.gov/mumu/studii/FS2-report.html*
- 3341 [54] N. Otsu, 1979, "A threshold selection method from gray-level his-
3342 tograms," *IEEE Trans. Sys., Man., Cyber.*, **9**, pp. 62-66
- 3343 [55] Shuzo Oshima, Ryuichiro Yamane, Yoshihiro Mochimaru, Toshihiro Mat-
3344 suoka, 1987, "The shape of a liquid metal jet under a non-uniform mag-
3345 netic field," *JSME International Journal*, **30**, No.261, pp.437-448
- 3346 [56] R. B. Palmer, 1998, "Muon collider design," *Report BNL-65242, CAP-*
3347 *200-MUON-982C*
- 3348 [57] Mark A. Pinsky, 1991, *Partial differential equations and boundary value*
3349 *problems with applications*, McGraw-Hill, Inc.
- 3350 [58] R. D. Reitz, F. V. Bracco, 1982, "Mechanism of atomization of a liquid
3351 jet," *Physics of Fluids*, **25**, pp.1730-1742

- 3352 [59] Uflyand Y. S., 1960, "Hartmann problem for a circular tube," *Soviet*
3353 *Phys.*, **5**, pp.1194-1196
- 3354 [60] Roman Samulyak, 2006, "Target simulations," *MUTAC Review*, *http* :
3355 *//www.hep.princeton.edu/mcdonald/mumu/target/samulyak/*
3356 *mutac06_samulyak_targetsimulations.pdf*
- 3357 [61] SAE, 1960, "Aero-space thermodynamics manual," pp. A18-A20
- 3358 [62] R. Samulyak, 2006, "Target simulations" *MUTAC review*, *http* :
3359 *//www.hep.princeton.edu/mcdonald/mumu/target/samulyak/*
3360 *mutac06_samulyak_targetsimulations.pdf*
- 3361 [63] R. Samulyak, J. Du, J. Glimm, Z. Xu, 2007, "A numerical algorithm for
3362 MHD of free surface flows at low magnetic Reynolds numbers," *Jorunal*
3363 *of Computational Physics*, **226**, pp.1532-1549
- 3364 [64] J. A. Shercliff, 1953, "Steady motion of conducting fluids in pipes under
3365 transverse magnetic fields," *Proc. Camb. Phil. Soc.*, **49**, pp.136-144
- 3366 [65] J. A. Shercliff, 1956, "The flow of conducting flows in circular pipes under
3367 transverse magnetic fields," *J. Fluid Mech.*, **13**, pp.644-666
- 3368 [66] J. A. Shercliff, 1962, "Magnetohydrodynamic pipe flow: Part 2 High Hart-
3369 mann number," *J. Fluid Mech.*, **13**, pp.513-518
- 3370 [67] J. A. Shercliff, 1965, *A textbook of magnetohydrodynamics*, Pergamon
3371 Press
- 3372 [68] N. Simos, 2005, "MERIT experiment window study," *BNL Review*, *http* :
3373 *//www.hep.princeton.edu/mcdonald/mumu/target/simos/*
3374 *Simos_121205.pdf*
- 3375 [69] P. Sievers, P. Pugnati, 2000, "Response of solid and liquid targets to high
3376 power proton beams for neutrino factories," *Report CERN LHC/2000-4,*
3377 *CERN-NuFACT Note 035*
- 3378 [70] G. Skoro, 2008, "MERIT beam spot size : satura-
3379 tions and projections," *MERIT collaboration review*, *http* :
3380 *//www.hep.princeton.edu/mcdonald/mumu/target/Skoro/Saturation_profiles.pdf*

- 3381 [71] K. Stewartson, 1955, "The asymptotic boundary layer on a circular cylinder
3382 in axial incompressible flow," *Q. Appl. Math.*, **13**, pp. 113
- 3383 [72] P. T. Spampinato *et al*, 2005, "A free jet mercury system for use in a high
3384 power target experiment," *Part. Accel. Conf.*, Knoxville, TN, pp.1637
- 3385 [73] S. Striganov, 2009, Private communication
- 3386 [74] P. Thieberger, H. G. Kirk, R. J. Weggel, K. T. MacDonald, 2003, "Moving
3387 solid metallic targets for pion production in the muon collider/neutrino
3388 factory project," *Proc. Part. Accel. Conf.*, Portland, OR, pp.1634
- 3389 [75] N. Tsoupas *et al*, 2003, "Injection acceleration and extraction of high
3390 intensity proton beam for the neutrino facility project at BNL," *Part.*
3391 *Accel. Conf.*, Portland, OR, pp.1637
- 3392 [76] C. D. West, 2000, "Cavitation in a mercury target," *ORNL/TM-2000-*
3393 */263*
- 3394 [77] H. Q. Yang, 1992, "Asymmetric instability of a liquid jet," *Physics of*
3395 *Fluids*, **30**, pp.681-689
- 3396 [78] K. T. Yen, 1967, "Role of intermittency in free turbulent flows," *American*
3397 *Institute of Aeronautics and Astronautics*, **5**, No. 12 pp.2187-2192
- 3398 [79] W. M. Yao *et al*, 2006, "Accelerator physics of colliders" *Journal of*
3399 *Physics*, **33**, No.1, pp.35-62

Appendix A

Tabular Data for Chapter 3, Chapter 5, and Chapter 6

A.1 Specifications of Optics

Table A.1: Specifications of optical components in optical diagnostics.

Item	Value
Right angle prism mirror	Gold coated, 25 × 25 × 35.4, Surface flatness $\lambda/10$
Gradient index lens	
Size	d=1.0 mm, L=2.48 mm
Numerical aperture	0.5
Working distance	Infinity
Coating	AR coated at 800 ~ 960 nm
Sapphire ball lens	D=0.5 mm, Al_2O_3 , Index of refraction=1.77
Retro-reflecting Parabolic mirror	
Diameter	76.2 mm
Thickness	12.7 mm
Focal length	444 mm
Coating	Gold
Microscope objective	
Magnification	40 ×

Continued on next page

Table A.1: *Continued from previous page*

Item	Value
Numerical aperture	0.65
Working distance	0.6 mm
Clear aperture	5.0 mm
Power	160 mm (tube length) / f
Optical fiber	
Number of picture elements	30000
Jacketing diameter	800 μm
Picture elements area diameter	720 μm
Coating diameter	960 μm
Core material	GeO_2 containing Silica
Coating material	Silicone
Numerical aperture	0.35
Allowable bending radius	40 mm
Core diameter	200 μm

3407

A.2 Characteristic Response of 25 W Laser

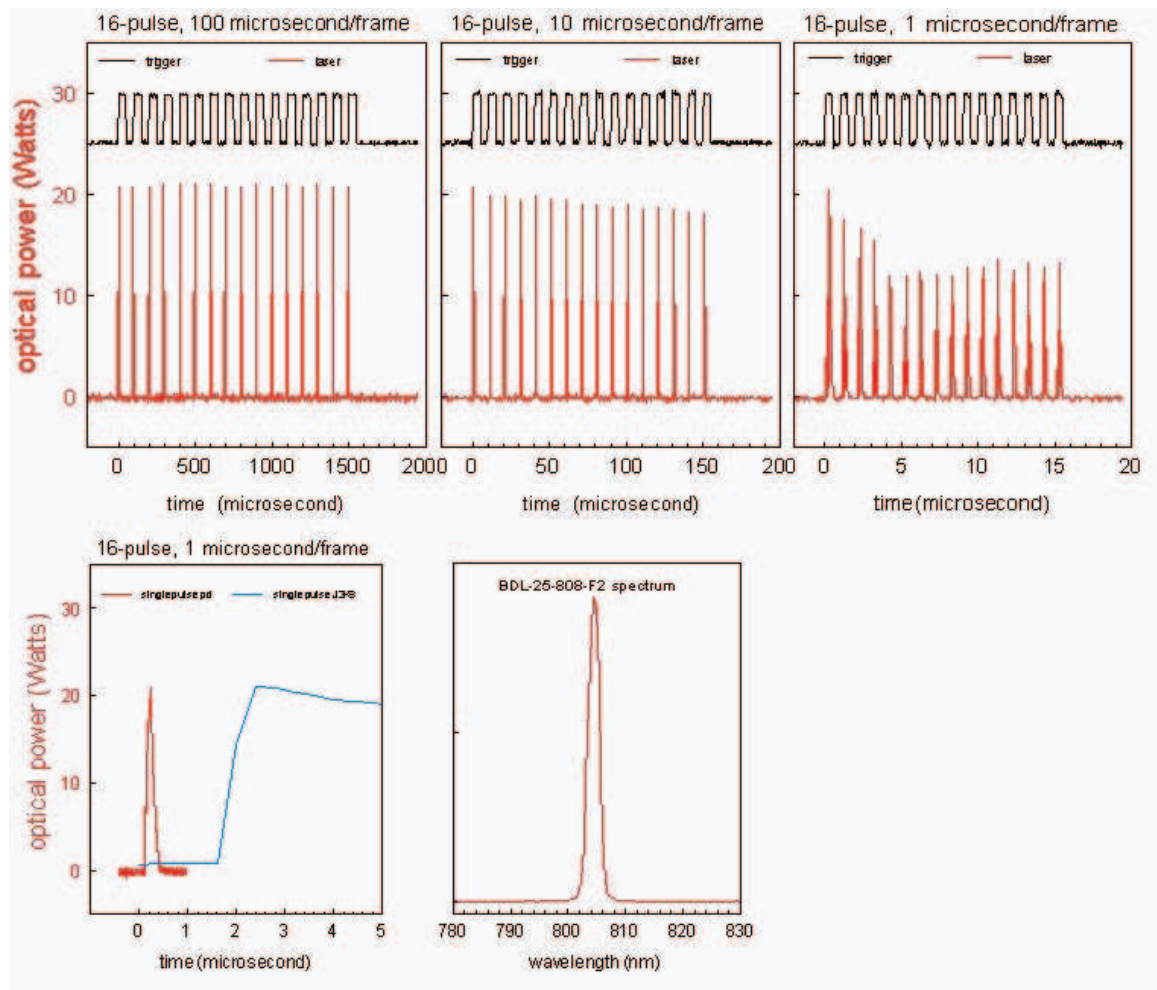


Figure A.1: Measurement of characteristic response of 25 laser used for high speed camera at Viewport 2 (Tsang, 2006).

A.3 Mercury Properties

Table A.2: Properties of mercury.

Property	Value	Unit
Atomic number	80	-
Atomic mass	200.59	-
Number of protons/electrons	80	-
Number of neutrons	121	-
Classification	Transition metal	-
Melting point	-38.87	°C
Boiling point	356.58	°C
Density	13.456 at 25 °C	g/cm^3
Naturally occurring isotopes	Hg-194 Hg-206	-
Group in periodic table	12	-
Period in periodic table	6	-
Electrical conductivity	1.06×10^6 at 25 °C	$\Omega^{-1}m^{-1}$
Thermal conductivity	8.34	$W m^{-1} K^{-1}$ at 27 °C
Specific heat	0.139	$J g^{-1} K^{-1}$
Heat of vaporization	59.229	kJ/mol
Heat of fusion	2.295	kJ/mol
Electrical resistivity	961 at 25 °C	$n\Omega \cdot m$
Speed of sound	1451.4 at 20 °C	m/s
Coefficient of thermal expansion	60×10^{-6} at 20 °C	K^{-1}
Bulk modulus	25	GPa
Dynamic viscosity	1.552×10^{-3}	$kg m^{-1} s^{-1}$
Kinematic viscosity	1.145×10^{-7}	$m^2 s^{-1}$
Dielectric constant	1.00074	-
Surface tension	485.5 (Hg-Air) at 25 °C	mN/m °C
Magnetic permeability	$4\pi \times 10^{-7}$	H/m

3411 **A.4 Measurement of Events with Pump Probe**
3412 **Condition**
3413

Table A.3: Measurement of disruption and filament velocity in pump probe condition with 8 and 16 harmonic bunches.

Condition		N ¹ , DL ²	A ³ , DL	S ⁴ , DL	N, V ⁵	A, V	S, V
Group 1	12+4 bunches 15+5 Tp 7 T	5	19.5	4.1	5	24.4	13.4
Group 2	6+2 bunches 12+4 Tp 5 T	30	19.8	6.1	19	10.2	3.6
Group 2, Spec. 1	700 μ s delay	12	19	5	6	12.4	3.7
Group 2, Spec. 2	350 μ s delay	11	22.2	7.2	7	8.4	1.9
Group 2, Spec. 3	40 μ s delay	7	17.3	5	6	10.2	4.1
Group 3	8 bunches 16 Tp 5 T	6	24.8	7.1	-	-	-
Group 4	8 bunches 6 Tp 5 T	6	5.9	3.8	-	-	-

¹ N represents number of events for measurement.

² DL (cm) represents disruption length of jet.

³ A represents average of measurement.

⁴ S represents standard deviation of measurement.

⁵ V (m/s) represents filament velocity on jet surface.

3414 **A.5 Beam Program List and Disruption Length**
3415 **Measurements**

- 3416
3417 1. Shot number
3418 2. Number of bunches
3419 3. Number of protons (Tp)
3420 4. Magnetic field (T)
3421 5. Jet velocity (m/s)
3422 6. Disruption length (m)
3423 7. Error (\pm cm)

Table A.4: Measured disruption length and beam shot program.

1	2	3	4	5	6	7
2002	1	0.25	0	0	-	-
2003	1	0.25	0	0	-	-
2004	1	0.25	0	0	-	-
2005	1	0.25	0	0	-	-
2006	1	0.25	0	0	-	-
2007	1	0.25	0	0	-	-
2008	1	0.25	0	0	-	-
2009	1	0.25	0	0	-	-
2011	1	0.25	0	0	-	-
2012	1	0.25	0	0	-	-
2013	1	0.25	0	0	-	-
2014	1	0.25	0	0	-	-
2015	1	0.25	0	0	-	-
2016	1	0.25	0	0	-	-
2017	1	0.25	0	0	-	-
2018	1	0.25	0	0	-	-
2019	1	0.25	0	0	-	-
2020	1	0.25	0	0	-	-
2021	1	0.25	0	0	-	-
2022	1	0.25	0	0	-	-

Continued on Next Page...

Table A.4 – Continued

1	2	3	4	5	6	7
2023	1	0.25	0	0	-	-
2026	1+1	0.50	0	15	0.085	4.0
3003	1+1	0.50	0	0	-	-
3005	1+1	0.50	0	0	-	-
3006	12+4	4.00	0	0	-	-
3007	12+4	4.00	0	0	-	-
3008	12+4	4.00	0	0	-	-
3011	12+4	4.00	0	0	-	-
3012	12+4	4.00	0	0	-	-
3014	1	0.25	0	0	-	-
3015	1	0.25	0	0	-	-
3016	1	0.25	0	15	No image	-
3017	1	0.25	0	15	0	0.0
3018	1	0.25	0	15	0	0.0
3019	1	0.25	0	15	0.013	0.7
3020	1	0.25	0	15	0	0.0
3021	1	0.25	0	15	0.005	0.5
3022	1	0.25	0	15	0.029	2.4
3023	1	0.25	0	15	0	0
3024	1	0.25	0	15	No image	-
3025	1	0.25	5	15	0	0
4001	1	0.25	0	15	0.018	1.5
4002	1	0.25	5	15	0	0
4003	1	0.25	5	15	0	0
4004	1	0.25	5	15	0	0
4005	1	0.25	5	15	0.054	3.4
4006	1	0.25	5	15	0.019	1.6
4007	1	0.25	5	15	0	0
4008	1	0.25	5	15	0	0
4009	1	0.25	5	15	No image	-
4010	1	0.00	5	0	-	-
4011	1	0.30	0	0	-	-
4012	1	0.30	5	0	-	-
4013	1	0.30	0	0	-	-
4014	1	0.30	5	15	0.007	0.7
4015	16	10.00	5	15	0.031	2.5

Continued on Next Page...

Table A.4 – Continued

1	2	3	4	5	6	7
4016	16	10.00	5	0	-	-
4017	16	10.00	0	15	0.038	2.9
4019	16	10.00	0	15	0.062	3.6
4020	2	0.50	0	0	-	-
4021	2	0.50	0	0	-	-
4023	2	0.50	0	0	-	-
4024	2	0.50	0	0	-	-
4025	2	0.50	0	0	-	-
4026	2	0.50	0	0	-	-
4028	16	10.00	0	0	-	-
4030	16	10.00	0	15	0.143	4.5
4031	16	10.00	5	15	0.080	3.9
5003	4	1.00	5	15	0	0
5004	16	10.00	5	15	0.111	4.3
5005	16	10.00	5	15	No image	-
5006	16	10.00	5	15	No image	-
5007	16	10.00	5	15	0.024	2.1
5008	16	10.00	5	15	0.031	2.5
5009	8	5.00	5	15	0.033	2.6
5010	8	5.00	5	15	0.022	1.9
5011	8	5.00	0	15	0.084	4.0
5012	16	10.00	5	15	No image	-
5014	16	15.00	0	15	No image	-
5015	16	15.00	5	15	0.189	4.8
5016	16	15.00	5	15	0.180	4.7
5017	16	20.00	5	15	0.303	5.1
5018	16	20.00	5	15	0.283	5.1
5019	16	20.00	5	15	0.204	4.8
5020	16	20.00	10	15	0.184	4.7
6001	16	4.00	0	15	0	0
6002	16	4.00	0	15	0.027	2.3
6003	16	10.00	5	15	0.105	4.2
6004	16	10.00	5	15	0.105	4.2
6005	16	10.00	5	15	0.035	2.7
6006	16	10.00	5	15	0.173	4.7
6007	16	10.00	5	15	0.028	2.3

Continued on Next Page...

Table A.4 – Continued

1	2	3	4	5	6	7
6008	16	10.00	5	15	0.052	3.3
6009	16	10.00	5	15	0.079	3.9
6010	16	10.00	5	15	0.074	3.8
6011	16	10.00	5	0	-	-
6012	1	0.25	0	0	-	-
6013	1	0.25	0	0	-	-
6014	1	0.25	0	0	-	-
6015	1	0.25	0	0	-	-
6016	1	0.30	0	0	-	-
6017	1	0.30	0	0	-	-
6018	1	0.30	0	0	-	-
6019	1	0.30	0	0	-	-
6020	1	0.30	0	0	-	-
6021	1	0.30	0	0	-	-
6022	1	0.30	0	0	-	-
6023	1	0.30	0	0	-	-
6024	16	4.00	0	0	-	-
6025	16	4.00	0	0	0.092	4.1
6026	16	4.00	0	15	0.101	4.2
6027	16	4.00	0	15	0.095	4.1
6028	16	4.00	5	15	0.005	0.5
6029	16	4.00	5	15	0.038	2.9
6030	16	4.00	10	15	0.044	3.1
6031	16	4.00	10	15	0.058	3.5
7001	16	4.00	0	0	-	-
7002	16	4.00	5	0	-	-
7003	16	4.00	10	0	-	-
7004	16	4.00	0	15	0.019	1.5
7005	16	4.00	0	15	0.036	2.8
7006	16	4.00	10	15	0.014	0.8
7008	16	4.00	0	0	-	-
7009	16	4.00	0	0	-	-
7010	16	4.00	0	0	-	-
7011	16	4.00	0	0	-	-
7012	16	4.00	0	0	-	-
7013	16	4.00	0	0	-	-

Continued on Next Page...

Table A.4 – Continued

1	2	3	4	5	6	7
7014	16	4.00	0	0	-	-
7015	16	4.00	0	0	-	-
7016	16	4.00	10	15	0	0
7017	16	4.00	10	0	-	-
7021	16	4.00	0	0	-	-
7022	16	4.00	0	0	-	-
7023	16	4.00	10	15	0.082	3.9
7024	16	4.00	10	0	-	-
7025	16	4.00	10	0	-	-
8001	16	4.00	0	0	-	-
8002	16	4.00	0	15	0.016	1.1
8003	16	4.00	0	15	0.024	2.1
8004	16	4.00	0	0	-	-
8005	16	4.00	0	15	0.051	3.3
8006	16	4.00	0	0	-	-
8007	16	4.00	0	15	0.147	4.6
8008	16	4.00	0	0	-	-
8009	16	4.00	0	15	0.132	4.5
8010	16	4.00	0	15	0.419	5.3
8011	16	4.00	0	0	-	-
8012	16	4.00	0	15	0.041	3.0
8013	16	4.00	0	0	-	-
8014	16	4.00	0	15	0.107	4.2
8015	16	4.00	0	0	-	-
8016	16	4.00	5	15	0	0.0
8017	16	4.00	5	0	-	-
8018	16	4.00	5	15	0.027	2.2
8019	16	4.00	5	0	-	-
8020		0.00	5	15	0	0
8021	16	4.00	5	15	0	0
8022	16	4.00	5	0	-	-
8029	16	4.00	7	15	No image	-
8030	16	4.00	7	15	0	0
8031	16	4.00	7	0	-	-
8032	16	4.00	7	15	0	0
8033	16	4.00	7	0	-	-

Continued on Next Page...

Table A.4 – Continued

1	2	3	4	5	6	7
8034	12+4	15+5	7	15	0.208	4.8
8035	12+4	15+5	7	15	0.152	4.6
8036	12+4	15+5	0	0	-	-
8037	12+4	15+5	7	15	0.160	4.6
8038	0	0.00	7	0	-	-
8039	-	-	0	0	-	-
8040	-	-	0	0	-	-
8041	12+4	15+5	7	15	0.203	4.8
8042	12+4	15+5	7	0	-	-
8043	12+4	15+5	7	0	-	-
8044	12+4	15+5	7	15	0.253	5.0
8045	12+4	15+5	7	15	0.165	4.7
8046	12+4	15+5	0	0	-	-
8047	12+4	15+5	7	0	-	-
9003	1	0.25	5	15	0	0
9004	16	4.00	5	15	0.064	3.6
9005	16	4.00	5	15	0.082	3.9
9006	16	4.00	5	15	0.215	4.9
9008	16	4.00	5	15	0.080	3.9
9009	12	3.00	5	15	0.108	4.2
9010	8	2.00	5	15	0	0
9011	-	-	-	-	0.068	3.7
9012	10	2.50	5	15	0.040	2.9
9013	-	-	-	-	0.040	3.0
9014	12	3.00	5	15	0.078	3.9
9015	16	6.00	7	15	0.162	4.6
9016	16	4.00	7	15	0.109	4.3
9017	12	3.32	7	15	0.005	0.5
9018	12	3.64	7	15	0	0
9019	12	3.78	7	15	0.040	3.0
9020	12	5.10	10	15	0.079	3.9
10001	16	4.00	0	0	No image	-
10002	16	4.00	0	0	No image	-
10003	16	4.00	0	15	0.188	4.8
10004	16	4.00	5	15	0.202	4.8
10005	16	4.00	5	15	0.128	4.4

Continued on Next Page...

Table A.4 – Continued

1	2	3	4	5	6	7
10006	18	4.00	10	15	0.038	2.9
10007	16	10.00	5	15	0.258	5.0
10008	16	15.00	5	15	0.291	5.1
10009	4	6.00	5	15	0.154	4.6
10010	2+2	6.00	5	15	0.184	4.7
10011	2+2	6.00	5	15	0.294	5.1
10012	4	6.00	5	15	0.228	4.9
10013	4	6.00	5	15	0.182	4.7
10014	4	6.00	5	0	-	-
10015	2+2	6.00	5	15	No image	-
10016	8	6.00	5	15	0.155	4.6
10017	8	6.00	5	0	-	-
10018	4+4	6.00	5	15	0.250	5.0
10019	4+4	6.00	5	0	-	-
11001	4	1.0	0	15	0.029	2.4
11002	16	6.0	5	15	0.202	4.8
11004	4	6.0	5	15	0.260	5.0
11005	4	6.0	5	15	0.246	5.0
11006	4	6.0	5	15	0.239	5.0
11007	4	6.0	5	15	0.174	4.7
11008	4	6.0	5	15	0.122	4.4
11010	4	6.0	5	15	0.194	4.8
11019	16	10.0	10	15	0.167	4.7
11020	16	3.5	10	15	0	0
11021	16	3.8	10	15	0.062	3.6
11022	16	15.0	10	15	0.158	4.6
11032	16	20.0	10	15	0.218	4.9
11033	16	30.0	10	15	0.214	4.9
11034	16	30.0	15	15	0.164	4.7
12001	4	5.0	0	15	0.201	4.8
12003	4	5.0	0	15	0.238	5.0
12004	4	5.0	0	15	0.273	5.1
12005	4	5.0	0	15	0.245	5.0
12007	-	-	0	15	0.039	2.9
12006	4	4.0	0	15	0.149	4.6
12008	4	4.0	0	15	0.252	5.0

Continued on Next Page...

Table A.4 – Continued

1	2	3	4	5	6	7
12009	4	4.0	5	0	-	-
12010	4	4.0	5	15	0.103	4.2
12011	4	4.0	5	15	0.079	3.9
12012	4	4.0	5	15	0	0
12013	4	4.0	5	0	-	-
12014	4	4.0	0	0	-	-
12015	4	4.0	5	15	0.105	4.2
12016	4	4.0	5	0	-	-
12029	8	15.0	15	15	0.046	3.2
12031	8	10.0	0	15	0.368	5.3
12032	8	10.0	15	15	0.149	4.6
12033	16	30.0	15	20	0.170	4.7
13001	2	2.5	0	15	0.042	3.0
13002	4	5.0	0	15	0.129	4.4
13003	4	5.0	0	15	0.138	4.5
13004	4	8.0	0	15	0.156	4.6
13007	6+2	16.0	5	15	0.157	4.6
13008	6+2	16.0	5	15	0.202	4.8
13009	6+2	16.0	5	15	0.196	4.8
13010	6+2	16.0	5	15	0.157	4.6
13011	6+2	16.0	5	15	0.170	4.7
13012	6+2	16.0	5	0	-	-
13013	6+2	16.0	5	15	0.221	4.9
13014	6+2	16.0	5	0	-	-
13015	6+2	16.0	5	15	0.167	4.7
13016	6+2	16.0	5	0	-	-
14008	6	6.0	5	15	0.061	3.6
14009	6	6.0	5	15	0.103	4.2
14010	6	6.0	5	15	0	0
14011	6	10.0	5	15	0.174	4.7
14012	6	10.0	5	0	-	-
14013	6	10.0	5	0	-	-
14014	6	10.0	5	15	0.151	4.6
14015	6	10.0	5	15	0.261	5.0
14017	6+2	16.0	5	15	0.290	5.1
14018	6+2	16.0	5	15	0.239	5.0

Continued on Next Page...

Table A.4 – Continued

1	2	3	4	5	6	7
14019	6+2	0.0	5	15	0.127	4.4
14020	6+2	16.0	5	0	-	-
14021	6+2	16.0	5	0	-	-
14022	6+2	16.0	5	15	0.233	4.9
14023	6+2	16.0	5	0	-	-
14024	6+2	16.0	5	15	0.119	4.3
14025	6+2	16.0	5	0	-	-
14026	6+2	16.0	5	15	0.215	4.9
14027	6+2	16.0	0	0	-	-
14028	6+2	16.0	5	15	0.186	4.8
14029	6+2	16.0	5	15	0.283	5.1
14030	6+2	16.0	5	0	-	-
14031	6+2	16.0	5	15	0.138	4.5
14032	6+2	16.0	5	0	-	-
14033	6+2	16.0	5	15	0.189	4.8
14034	6+2	16.0	5	15	0.383	5.3
14035	6+2	16.0	5	0	-	-
14036	6+2	4.0	5	15	0.032	2.6
14037	8	4.0	5	15	0	0
15001	8	4.0	5	15	0.014	0.8
15002	6+2	16.0	5	15	0.228	4.9
15003	6+2	16.0	5	15	0.117	4.3
15004	6+2	16.0	5	15	0.259	5.0
15005	6+2	16.0	5	0	-	-
15006	6+2	16.0	5	15	0.245	5.0
15007	6+2	16.0	5	0	-	-
15008	6+2	16.0	5	15	0.200	4.8
15009	6+2	16.0	5	0	-	-
15010	6+2	16.0	5	15	0.103	4.2
15011	6+2	16.0	5	15	0.188	4.8
15012	6+2	16.0	5	15	0.260	5.0
15013	6+2	16.0	5	0	-	-
15014	6+2	16.0	5	15	0.195	4.8
15015	6+2	16.0	5	0	-	-
15016	6+2	16.0	5	15	0.173	4.7
15017	6+2	16.0	5	0	-	-

Continued on Next Page...

Table A.4 – Continued

1	2	3	4	5	6	7
15018	6+2	16.0	5	15	0.157	4.6
15019	6+2	16.0	5	15	0.132	4.4
15020	8	16.0	5	15	0.341	5.2
15021	8	16.0	5	15	0.165	4.7
15022	8	16.0	5	15	0.236	4.9
15023	8	16.0	5	15	0.260	5.0
15024	8	16.0	5	0	-	-
15025	8	16.0	5	15	0.175	4.7
15026	8	16.0	5	0	-	-
15027	8	16.0	5	15	0.313	5.2
15028	8	16.0	5	15	-	-
15029	8	6.0	5	15	0.066	3.7
15030	8	6.0	5	0	-	-
15031	8	6.0	5	15	0.068	3.7
15032	8	6.0	5	0	-	-
15033	8	6.0	5	15	0.026	2.2
15034	8	6.0	5	0	-	-
15035	8	6.0	5	15	0.021	1.8
15036	8	6.0	5	0	-	-
15037	8	6.0	5	15	0.115	4.3
15038	8	10.0	5	15	0.080	3.9
15039	8	8.0	5	15	0.053	3.4
15040	8	8.0	5	15	0.054	3.4
15041	8	6.0	5	15	0.008	0.8
15042	8	6.0	5	15	0.007	0.7
15043	16	6.0	5	15	0.027	2.3
15044	4	12.0	5	15	0.043	3.1
15045	4	12.0	5	15	0.027	2.3
16001	4	2.0	0	15	0.082	3.9
16002	4	10.0	4.1	15	0.068	3.7
16003	4	12.0	4.1	15	0.205	4.8
16004	4	14.0	6	15	0.222	4.9
16005	8	12.0	5	15	0.136	4.5
16006	8	12.0	5	15	0.208	4.9
16007	8	12.0	5	15	0.189	4.8
16008	4+4	6+6	5	15	0.212	4.9

Continued on Next Page...

Table A.4 – Continued

1	2	3	4	5	6	7
16009	4+4	6+6	5	15	0.071	3.8
16010	4+4	6+6	5	15	0.164	4.7
16011	4+4	6+6	5	15	0.215	4.9
16012	4	14.0	5	15	0.229	4.9
16013	4	14.0	10	15	0.188	4.8
16014	4	12.0	10	15	0.172	4.7
16015	4	12.0	15	15	0.144	4.5
16016	4	10.0	5	15	0.131	4.4
17001	16	6.0	5	15	0.015	1.0
17002	16	8.0	5	15	0.125	4.4
17003	16	6.0	5	15	0.037	2.8
17004	16	6.3	5	15	0.048	3.2
17005	16	6.0	5	15	0.013	0.7
17006	16	6.0	7	15	0.093	4.1
17007	16	4.2	7	15	0	0
17008	16	8.0	7	15	0.101	4.2
17009	8+8	8.0	7	15	0.074	3.8
17010	8+8	8.0	7	15	0.062	3.6
17011	8+8	8.0	7	15	0.155	4.6
17012	8+8	8.0	7	15	-	-
17013	8+8	8.0	7	15	0.047	3.2
17014	8+8	8.0	7	15	0	0
17015	8+8	7.5	7	15	0.016	1.2
17016	8+8	7.4	7	15	0.086	4.0
17017	8+8	8.4	7	15	0.111	4.3
17018	8+8	6.0	7	15	0.057	3.5
17019	8+0	4.0	7	15	0.007	0.7
17020	8+0	6.0	7	15	0.059	3.5
17021	16	15.0	10	15	0.174	4.7
17022	16	15.0	15	15	0.148	4.6
17023	16	29.0	15	15	0.180	4.7
17024	16	29.0	10	20	0.230	4.9

Appendix B

Image Data for Chapter 6

B.1 Images for filament velocity measurement at Viewport 2

1. Shot number
2. Camera frame rate (μ s)
3. Beam energy (GeV)
4. Number of bunches
5. Number of protons (Tp)
6. Magnetic field (T)
7. Jet velocity (m/s)
8. Lag time between peak laser emittance and proton beam arrival (μ s)

Table B.1: Properties of shots used for filaments velocity analysis.

1	2	3	4	5	6	7	8
11004	25	24	4	6	5	15	-4.03
11007	25	24	4	6	5	15	-3.97
11010	25	24	4	6	5	15	-3.99
11019	25	24	16	10	10	15	-2.43
11021	25	24	16	3.8	10	15	-2.43
11032	25	24	16	20	10	15	-2.03
12031	25	24	8	10	0	15	-1.93
12032	25	24	8	10	15	15	-1.83
12033	25	24	16	30	15	20	-1.85

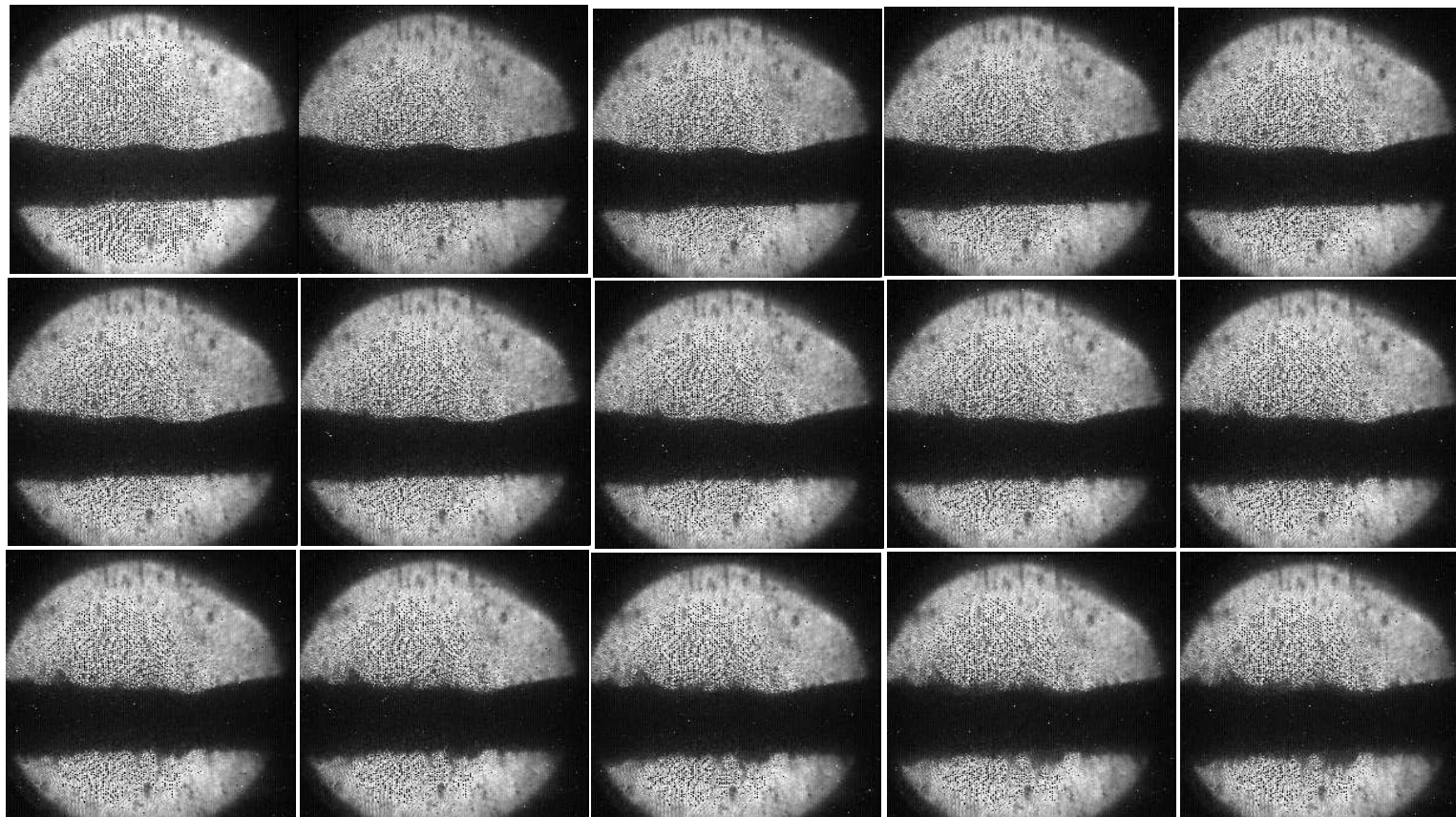


Figure B.1: Photo of continuous 15 frames of captured image. The timing for the 1st image is given in Table B.1. Shot number is 11004.

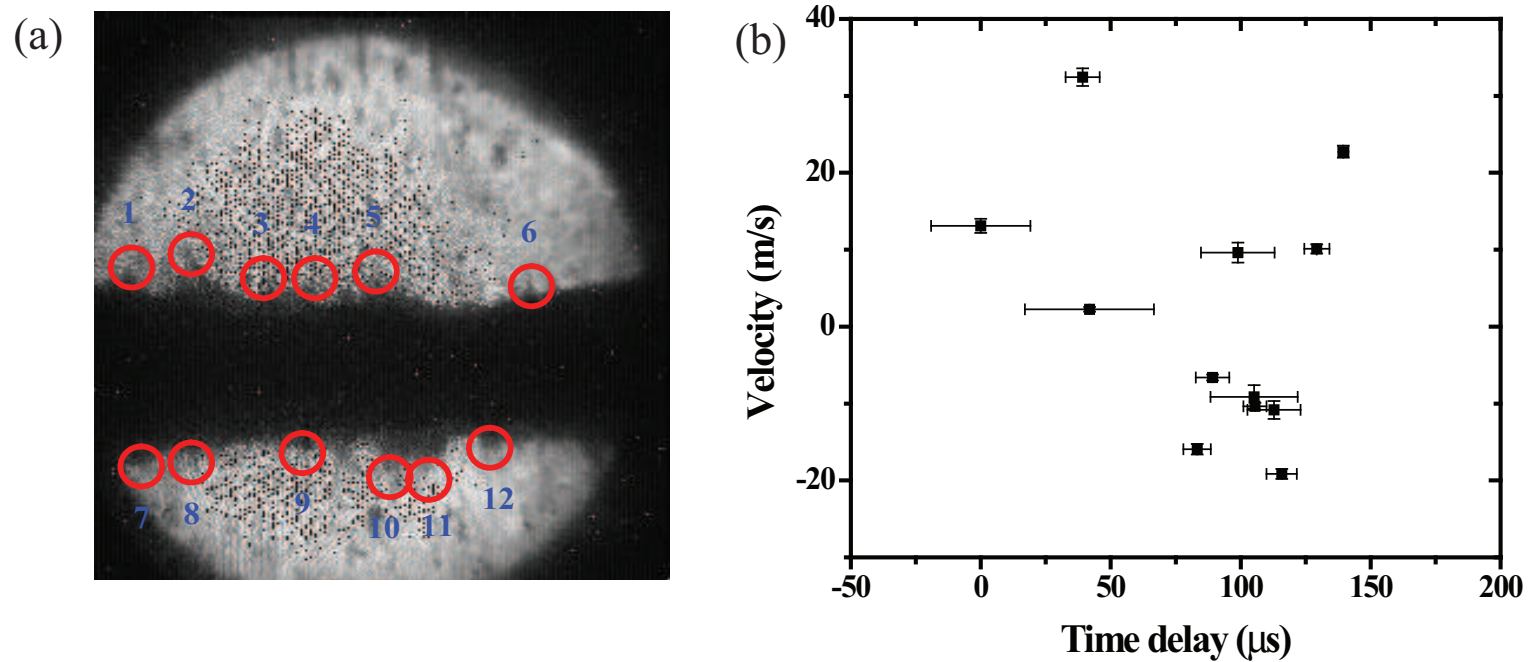


Figure B.2: Location on the Hg jet surface for velocity measurement of filaments. The numbers above red circles points the number of filaments that is used for velocity approximation. Shot number is 11004. a.) Illustration of measured filaments. b.) Velocity of filaments with it's onset time.

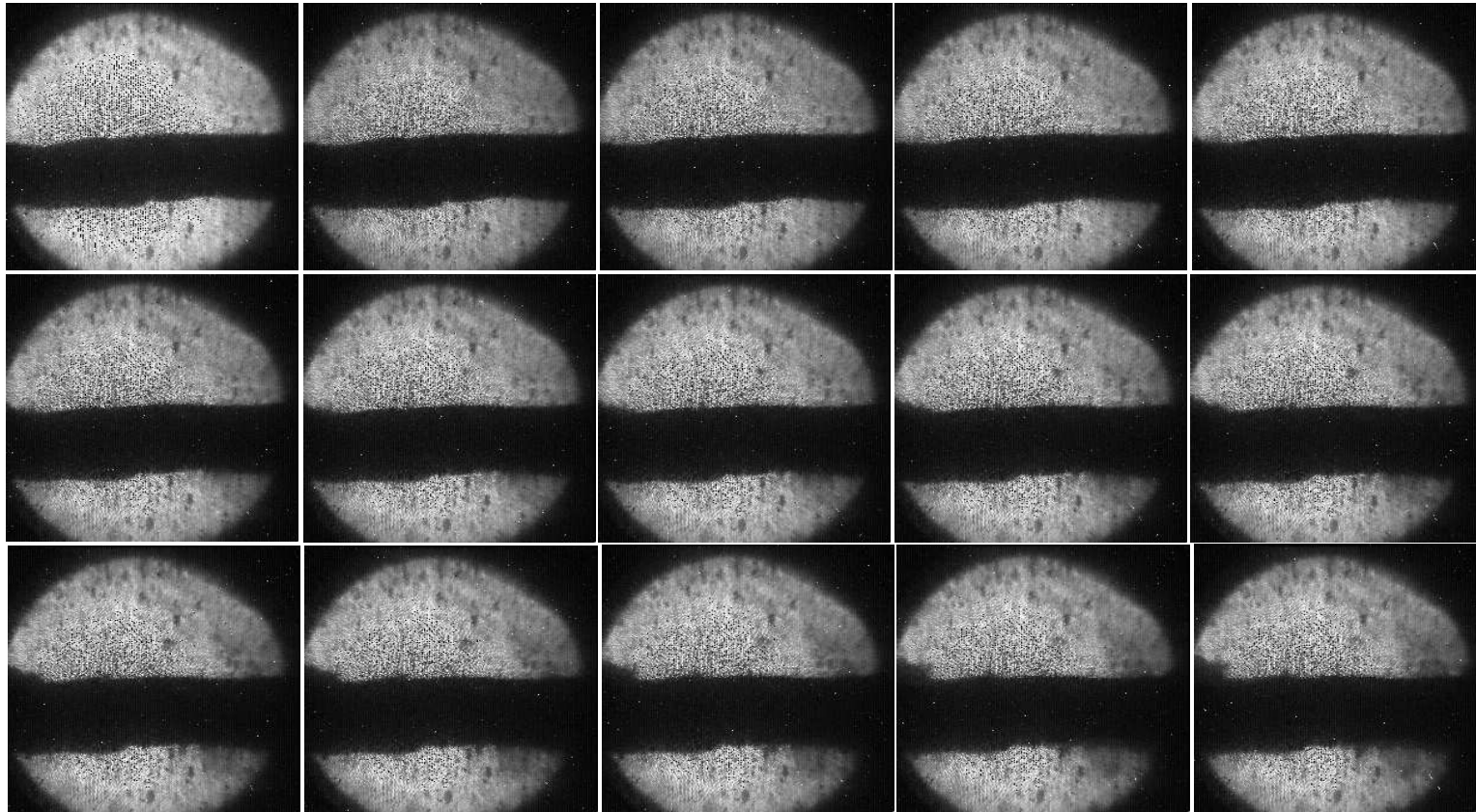


Figure B.3: Photo of continuous 15 frames of captured image. The timing for the 1st image is given in Table B.1. Shot number is 11007.

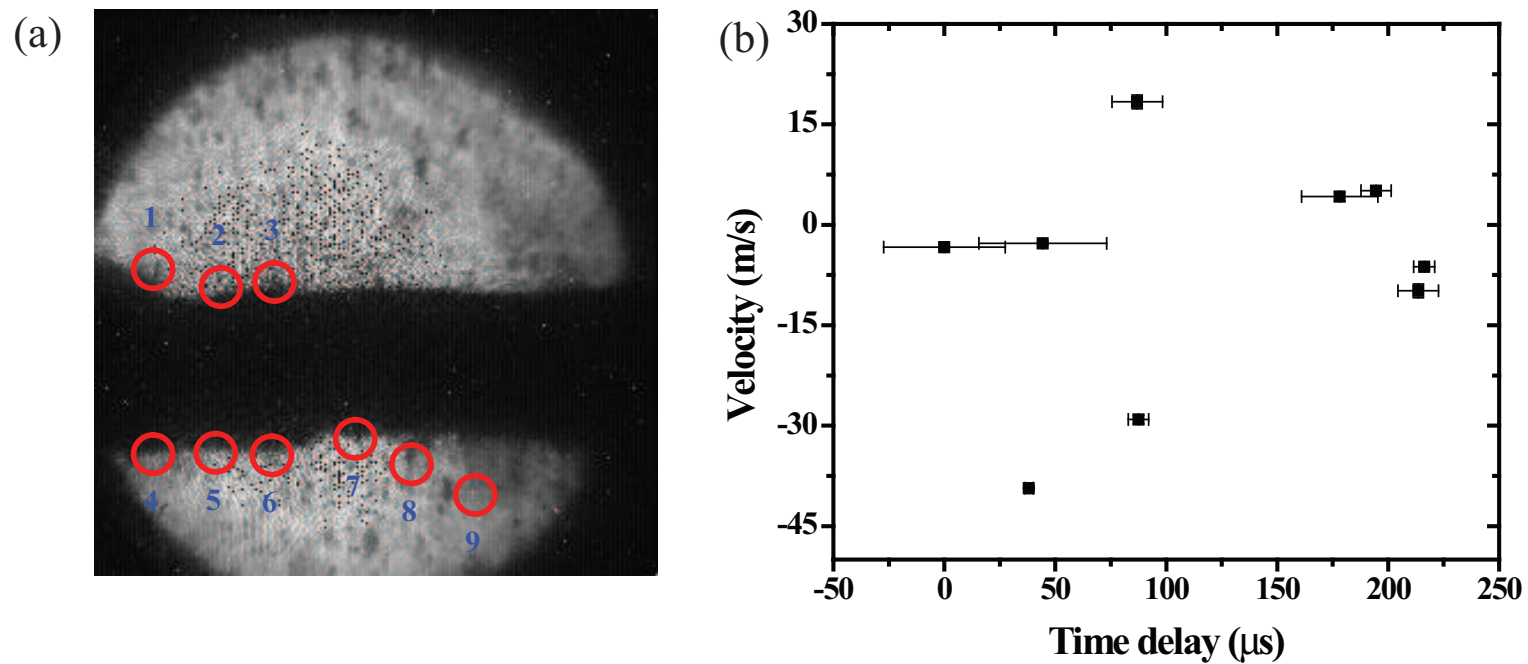


Figure B.4: Location on the Hg jet surface for velocity measurement of filaments. The numbers above red circles points the number of filaments that is used for velocity approximation. Shot number is 11007. a.) Illustration of measured filaments. b.) Velocity of filaments with it's onset time.

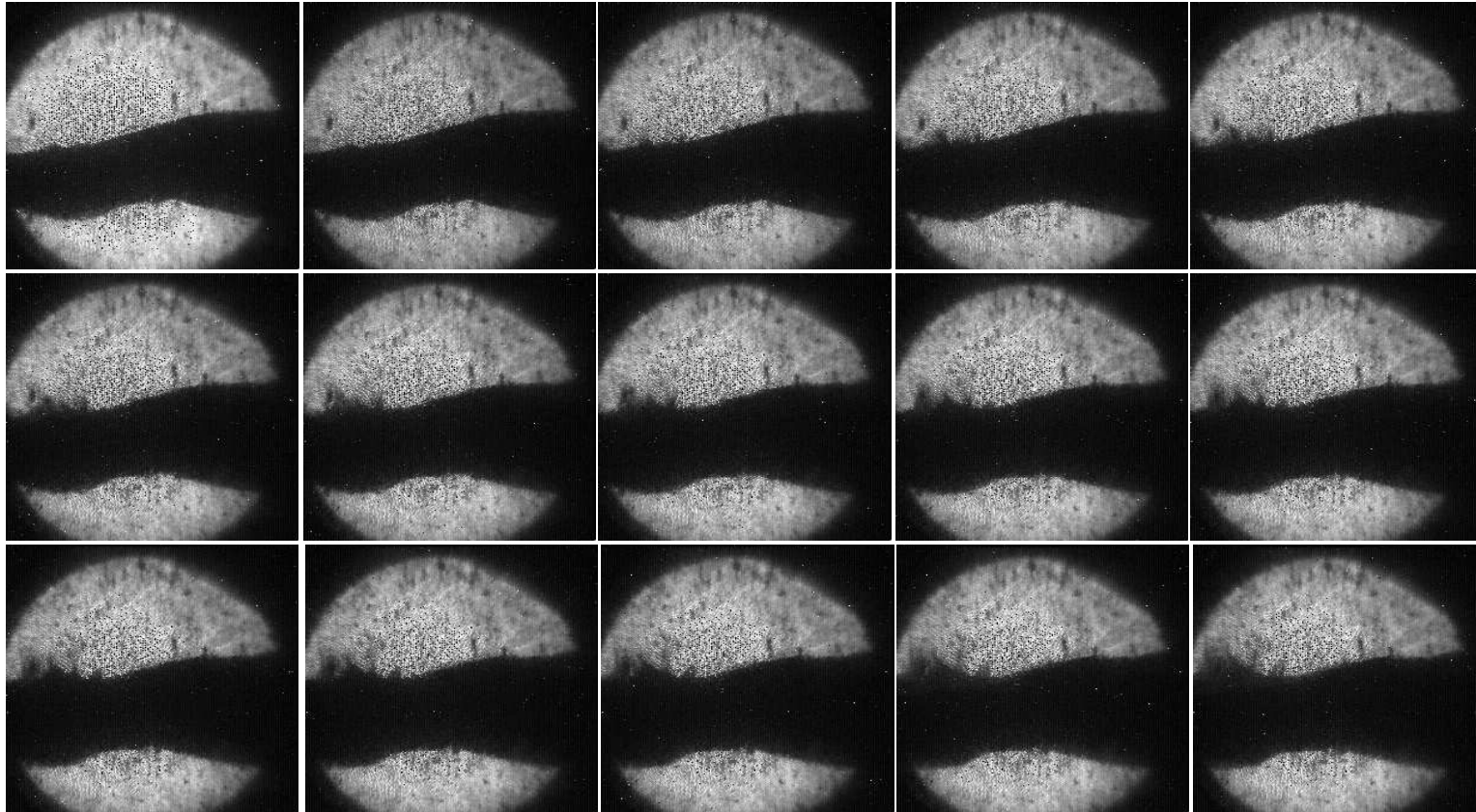


Figure B.5: Photo of continuous 15 frames of captured image. The timing for the 1st image is given in Table B.1. Shot number is 11010.

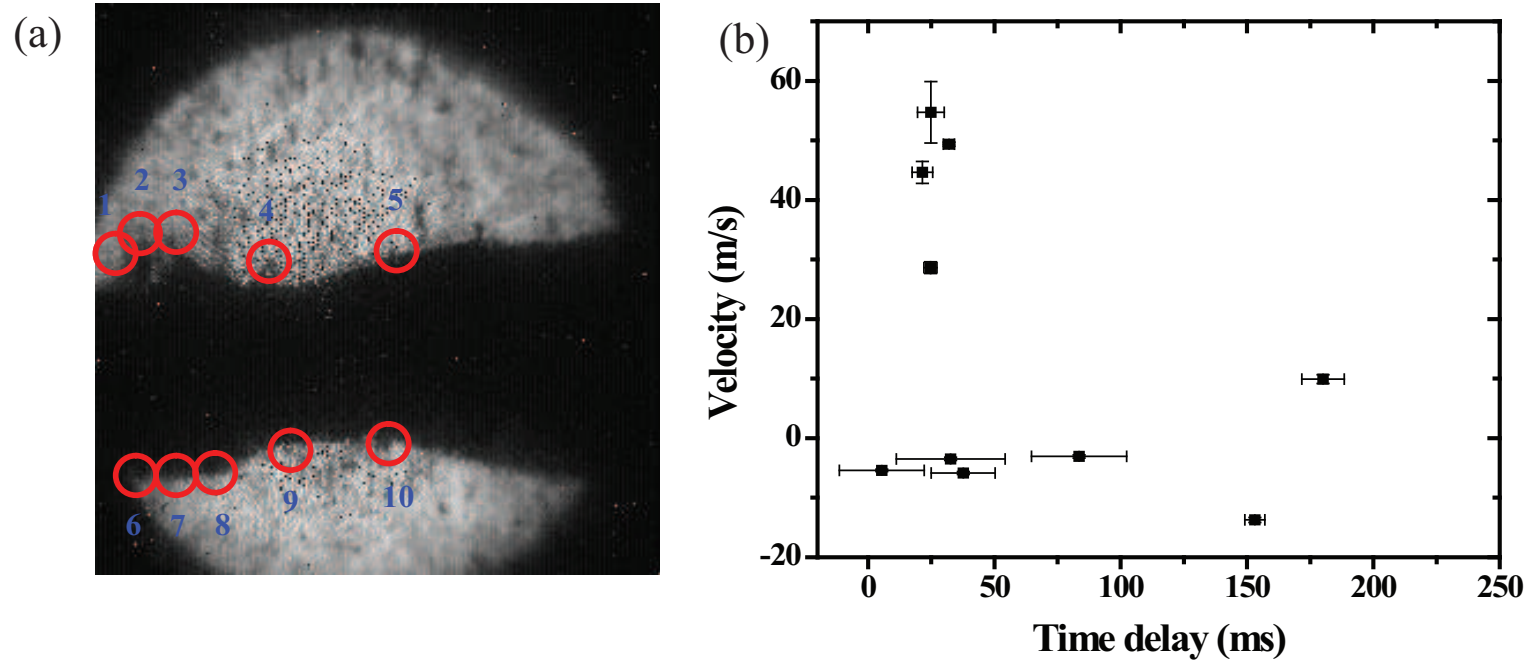


Figure B.6: Location on the Hg jet surface for velocity measurement of filaments. The numbers above red circles points the number of filaments that is used for velocity approximation. Shot number is 11010. a.) Illustration of measured filaments. b.) Velocity of filaments with it's onset time.

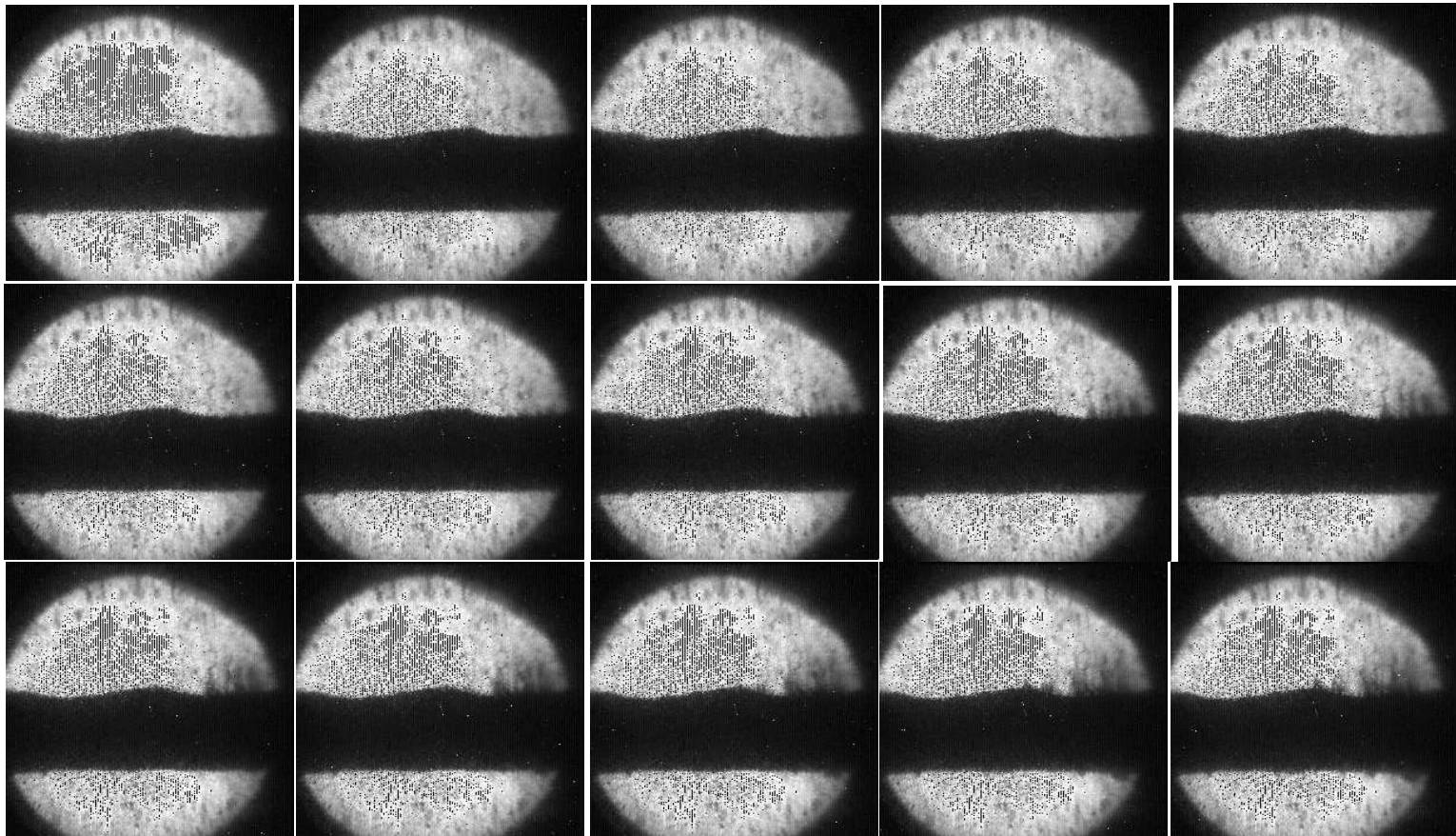


Figure B.7: Photo of continuous 15 frames of captured image. The timing for the 1st image is given in Table B.1. Shot number is 11021.

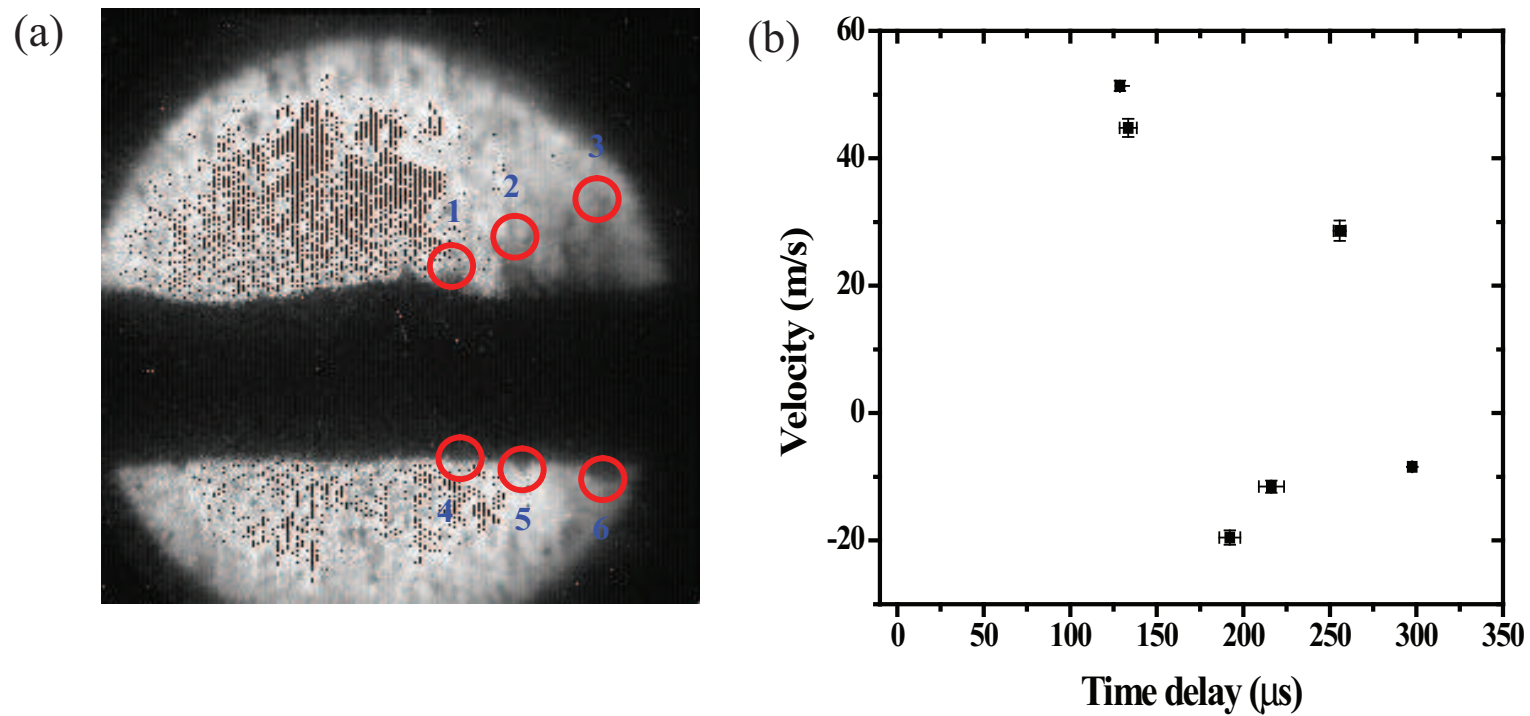


Figure B.8: Location on the Hg jet surface for velocity measurement of filaments. The numbers above red circles points the number of filaments that is used for velocity approximation. Shot number is 11021. a.) Illustration of measured filaments. b.) Velocity of filaments with it's onset time.

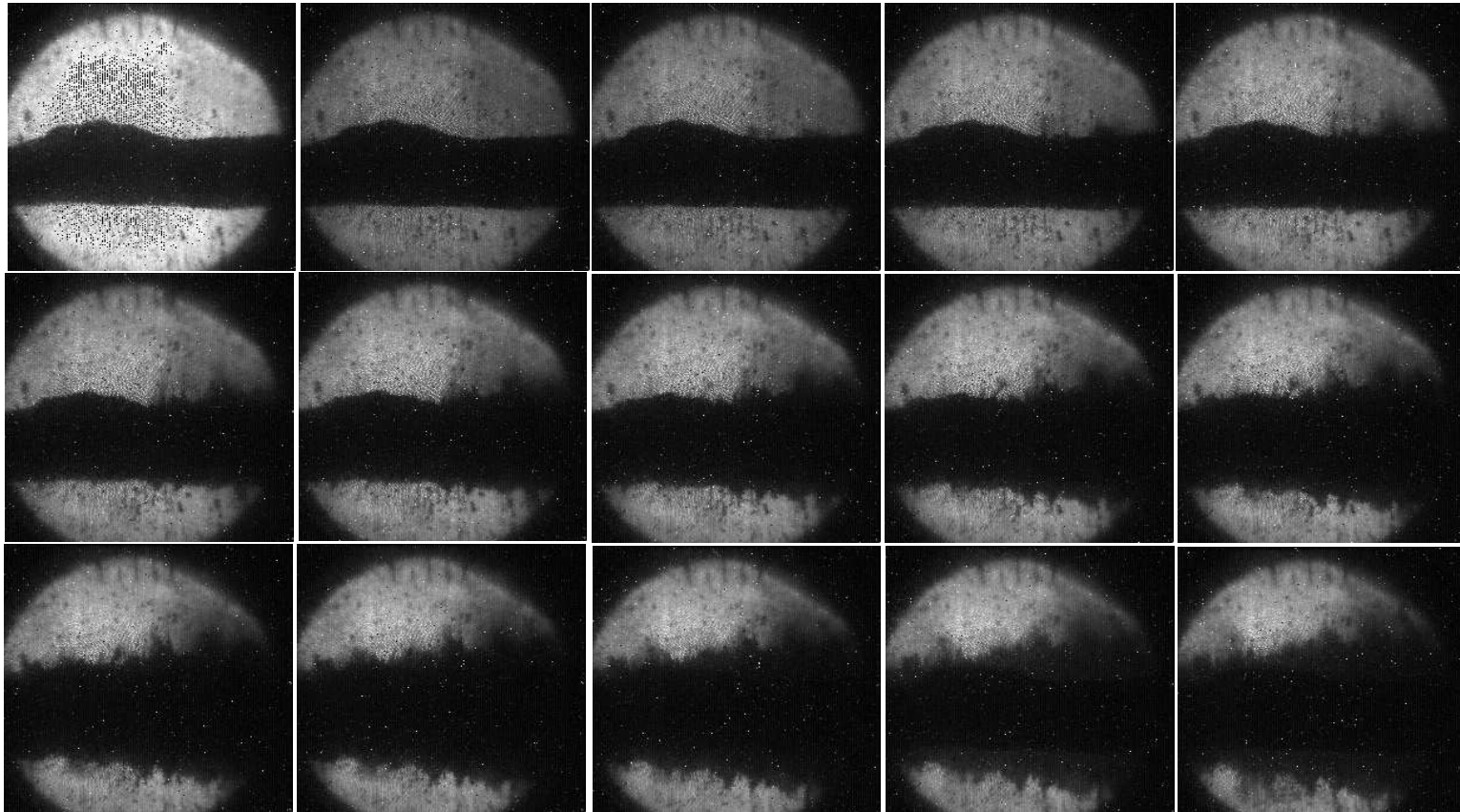


Figure B.9: Photo of continuous 15 frames of captured image. The timing for the 1st image is given in Table B.1. Shot number is 11032.

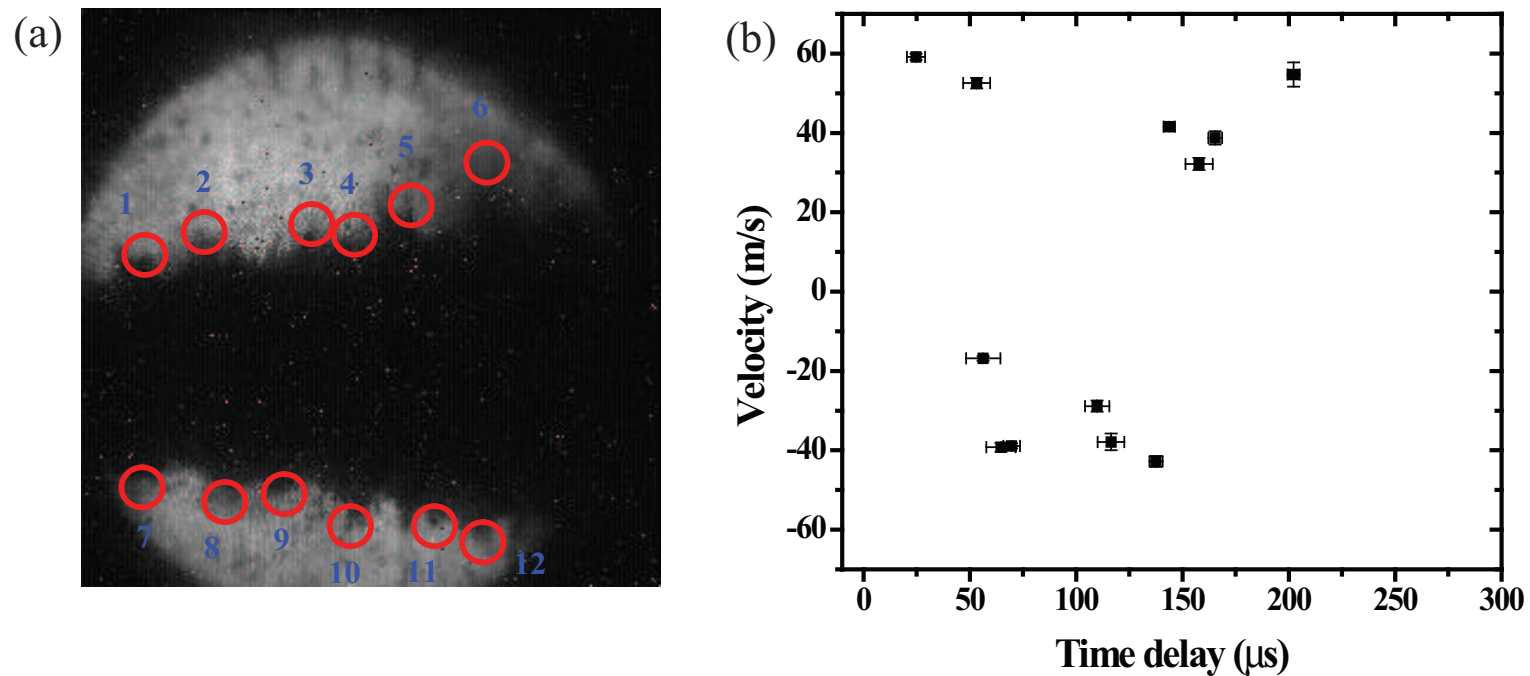


Figure B.10: Location on the Hg jet surface for velocity measurement of filaments. The numbers above red circles points the number of filaments that is used for velocity approximation. Shot number is 11032. a.) Illustration of measured filaments. b.) Velocity of filaments with it's onset time.

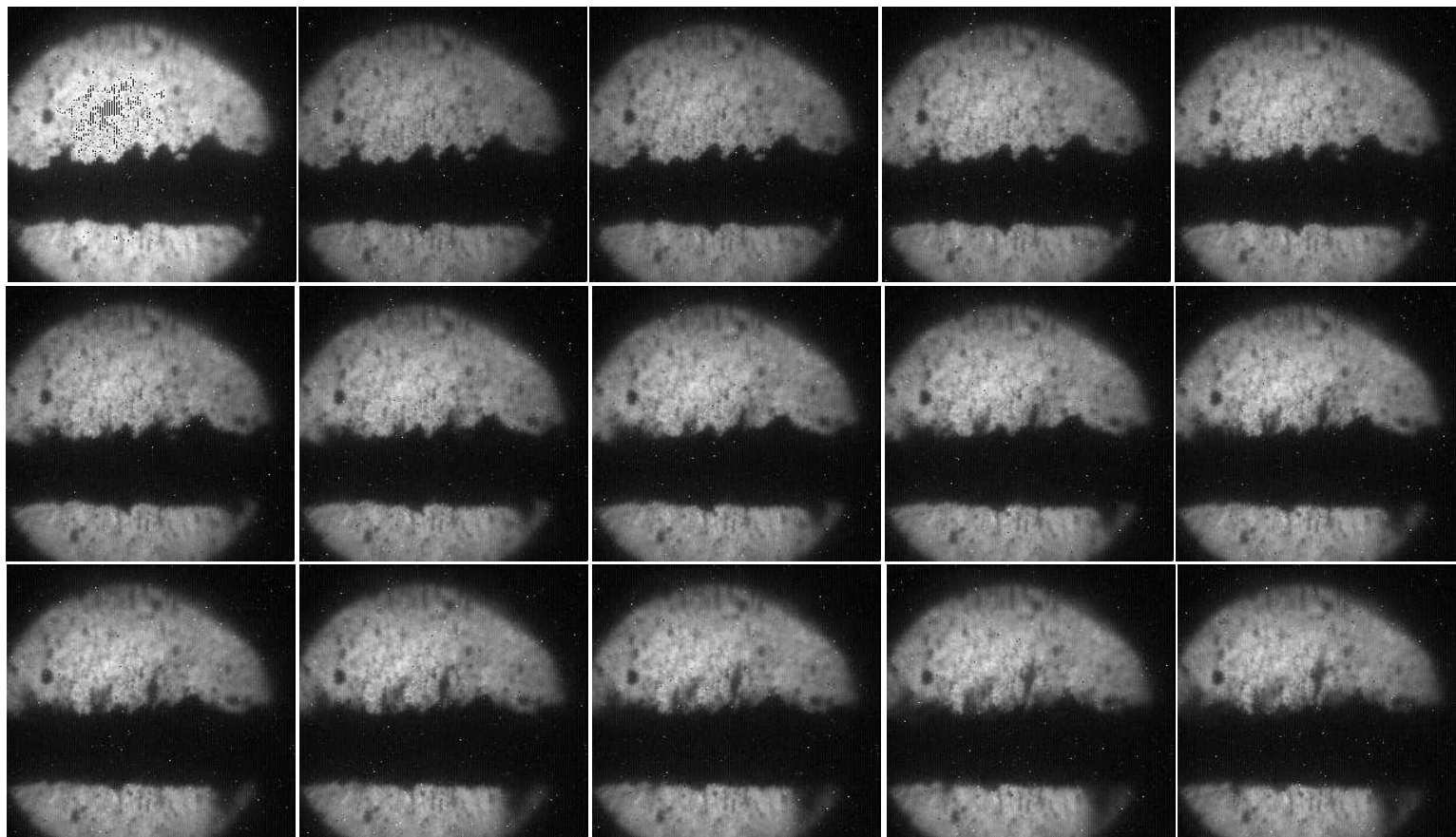


Figure B.11: Photo of continuous 15 frames of captured image. The timing for the 1st image is given in Table B.1. Shot number is 12031.

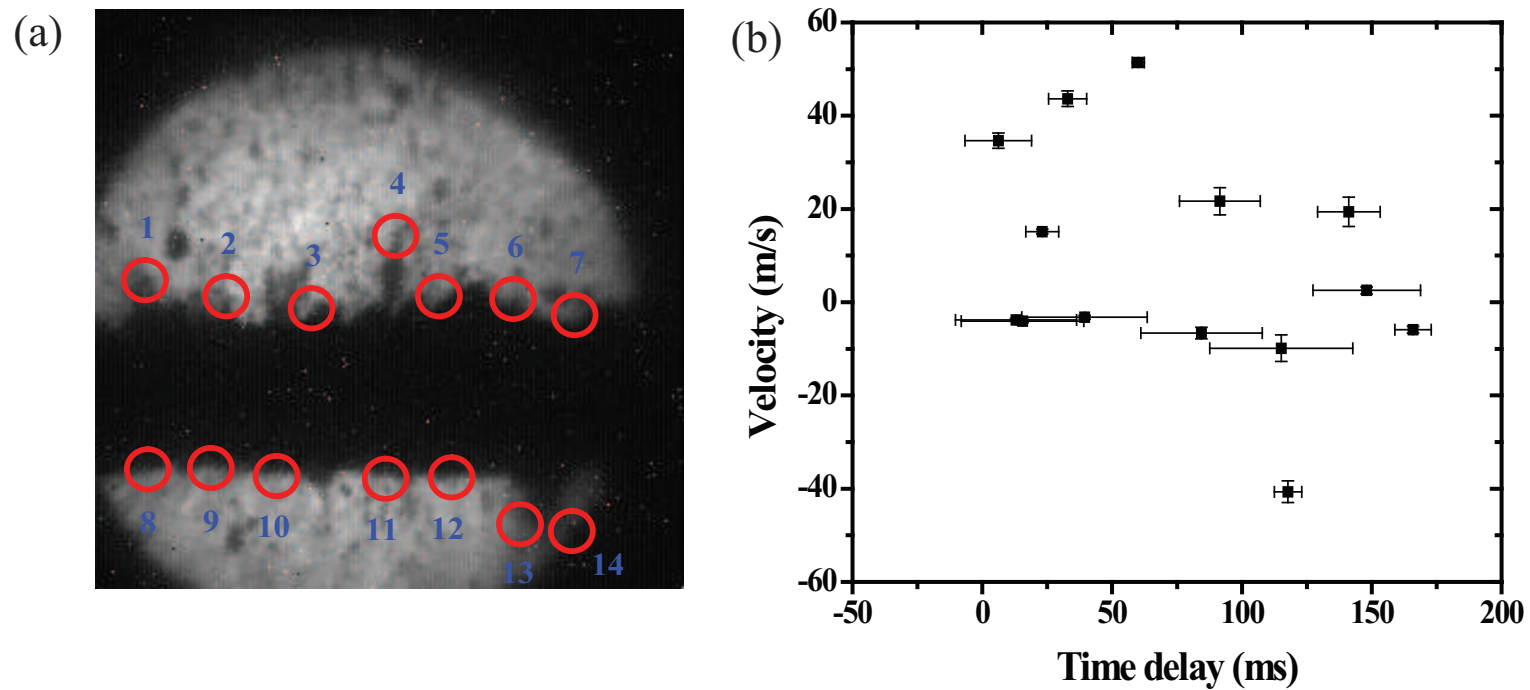


Figure B.12: Location on the Hg jet surface for velocity measurement of filaments. The numbers above red circles points the number of filaments that is used for velocity approximation. Shot number is 12031. a.) Illustration of measured filaments. b.) Velocity of filaments with it's onset time.

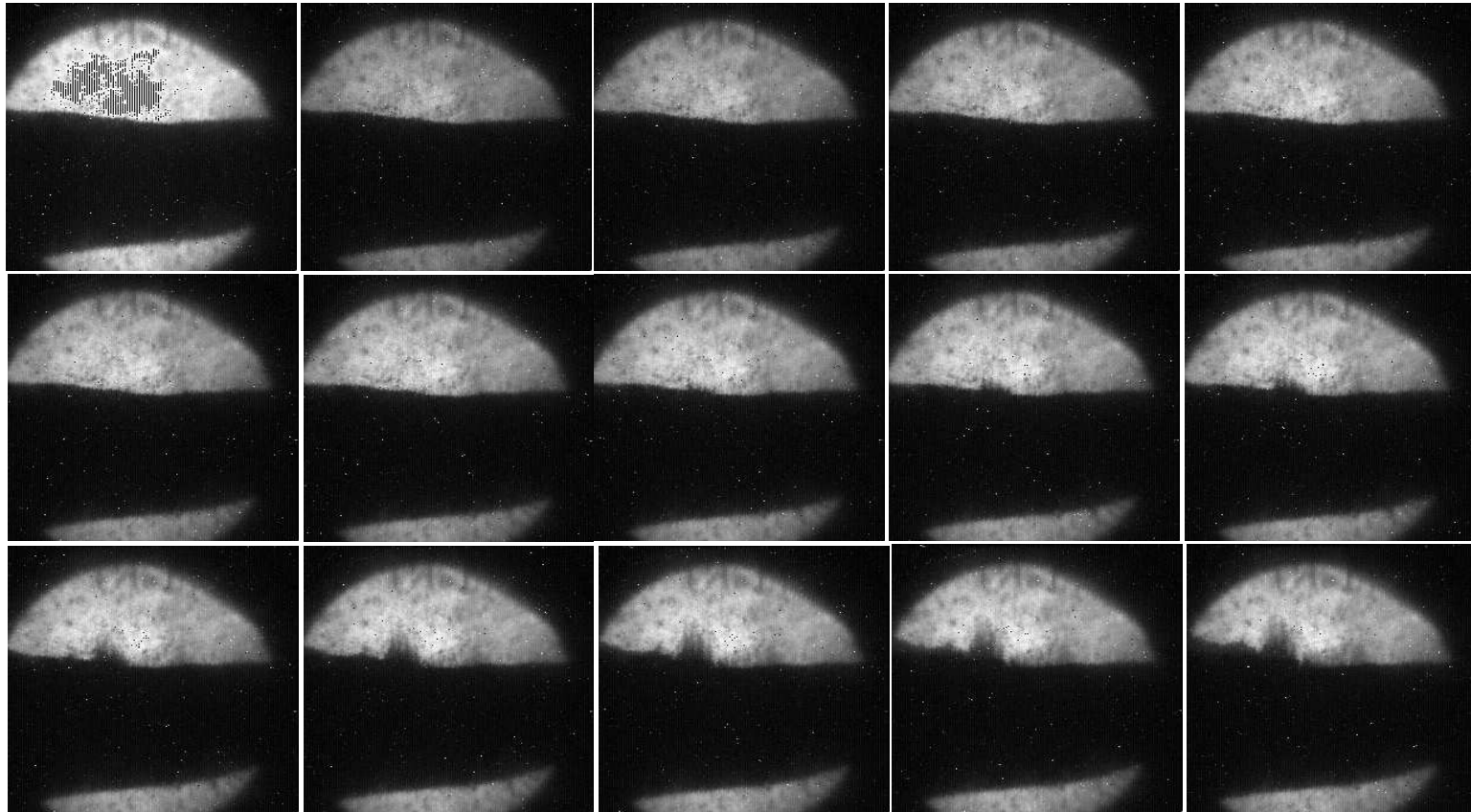


Figure B.13: Photo of continuous 15 frames of captured image. The timing for the 1st image is given in Table B.1. Shot number is 12032.

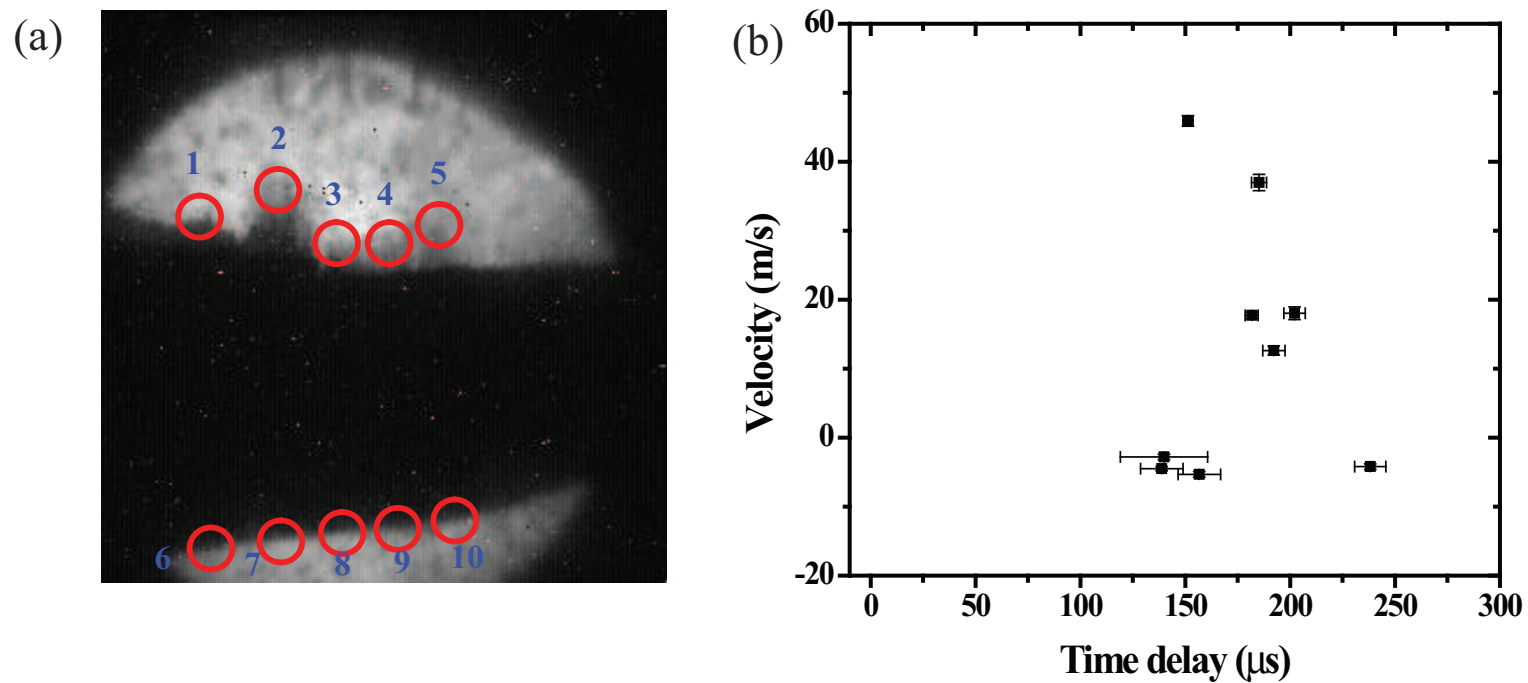


Figure B.14: Location on the Hg jet surface for velocity measurement of filaments. The numbers above red circles points the number of filaments that is used for velocity approximation. Shot number is 12032. a.) Illustration of measured filaments. b.) Velocity of filaments with it's onset time.

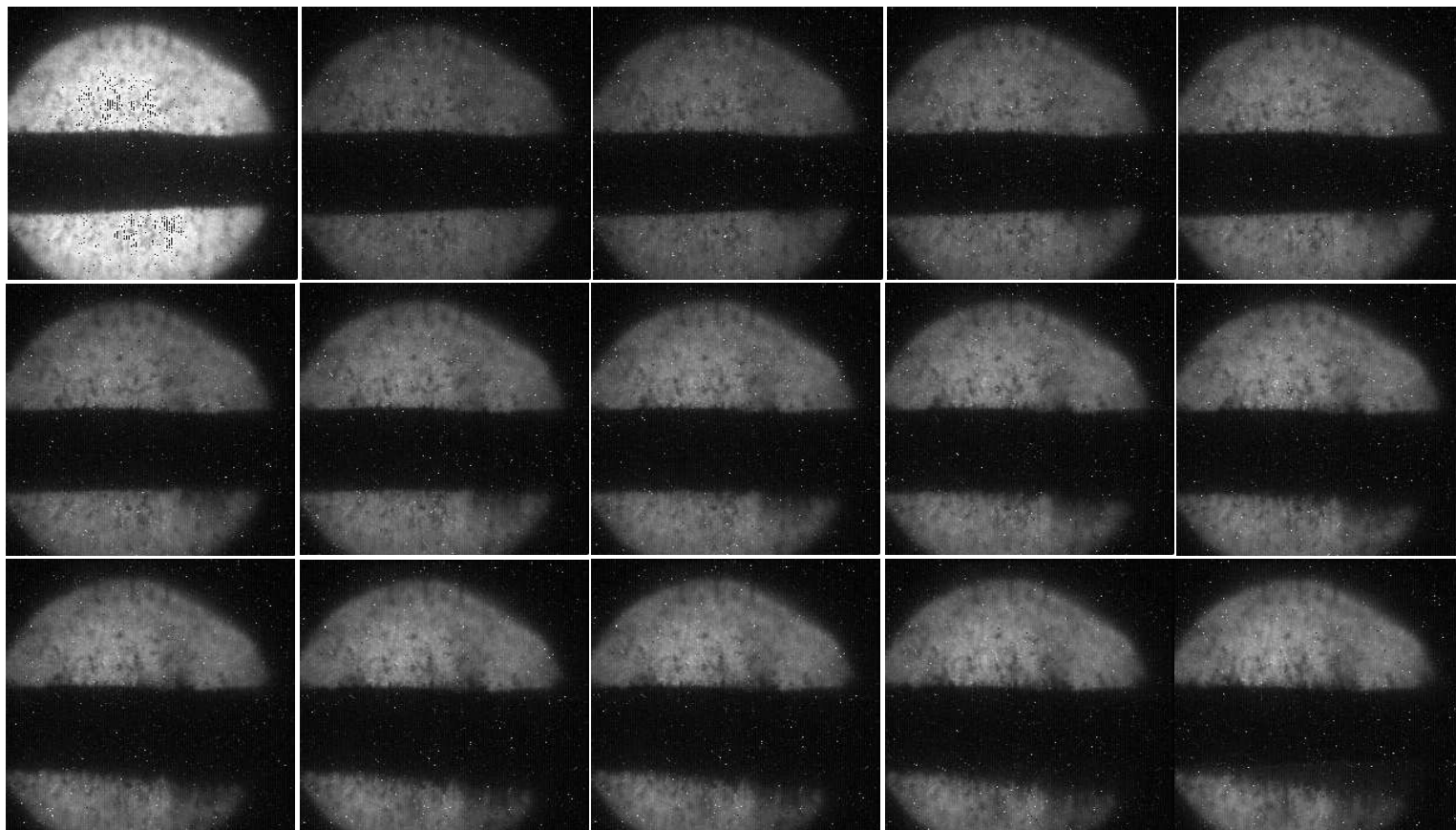


Figure B.15: Photo of continuous 15 frames of captured image. The timing for the 1st image is given in Table B.1. Shot number is 12033.

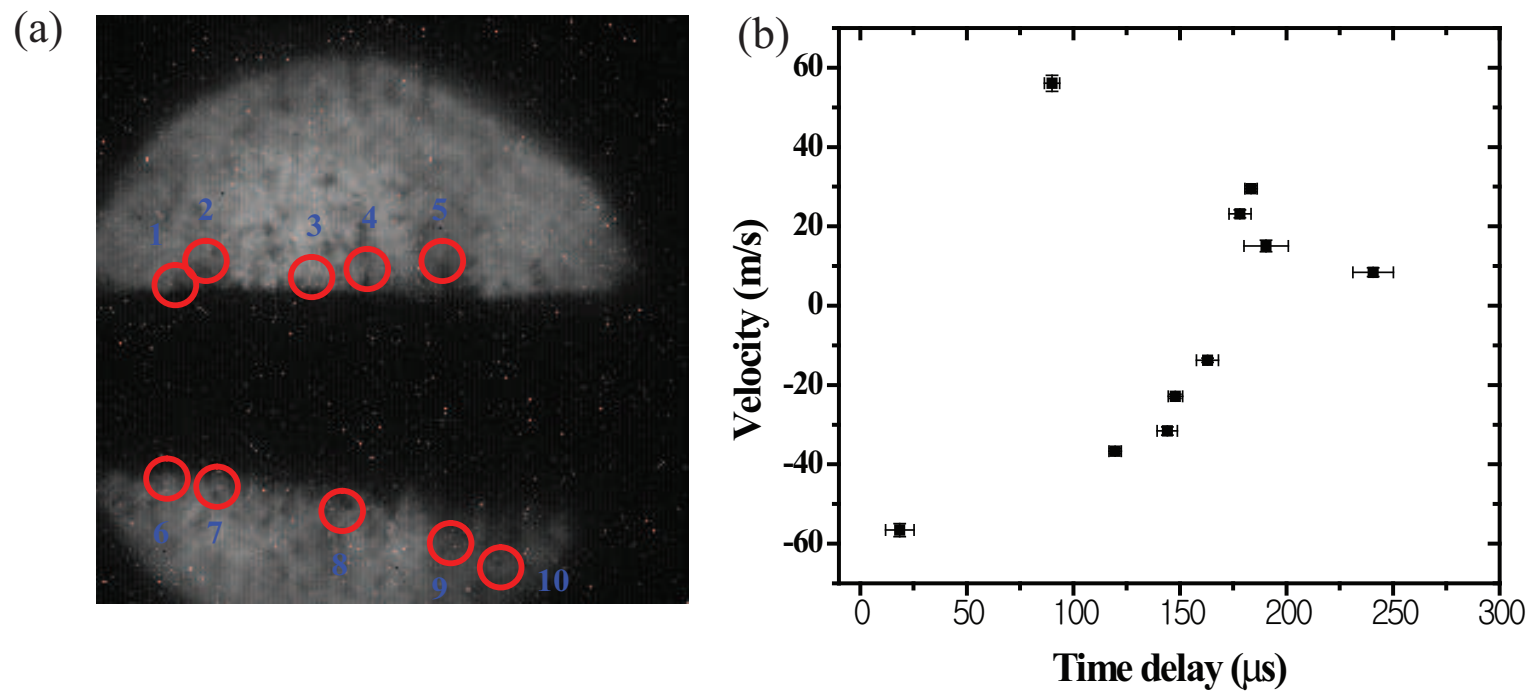


Figure B.16: Location on the Hg jet surface for velocity measurement of filaments. The numbers above red circles points the number of filaments that is used for velocity approximation. Shot number is 12033. a.) Illustration of measured filaments. b.) Velocity of filaments with it's onset time.

Appendix C

Mathematical Derivation for Chapter 2

C.1 The governing equations for MHD in cylindrical coordinates

The momentum equations in the (r, θ, z) coordinates in Fig. 2.2 can be written as follows:

$$\begin{aligned} & -\rho(v_r \frac{\partial v_r}{\partial r} + \frac{v_\theta}{r} \frac{\partial v_r}{\partial \theta} + v_z \frac{\partial v_r}{\partial z}) - \frac{\partial p_t}{\partial r} - \rho g \cos \theta + \eta(\frac{\partial^2 v_r}{\partial r^2} + \frac{1}{r} \frac{\partial v_r}{\partial r} + \frac{1}{r^2} \frac{\partial^2 v_r}{\partial \theta^2} + \frac{\partial^2 v_r}{\partial z^2}) \\ & + \frac{1}{\mu}(B_r \frac{\partial B_r}{\partial r} + \frac{B_\theta}{r} \frac{\partial B_r}{\partial \theta} + B_z \frac{\partial B_r}{\partial z}) = \rho \frac{\partial v_r}{\partial t} , \end{aligned} \tag{C.1}$$

$$\begin{aligned} & -\rho(v_r \frac{\partial v_\theta}{\partial r} + \frac{v_\theta}{r} \frac{\partial v_\theta}{\partial \theta} + v_z \frac{\partial v_\theta}{\partial z}) - \frac{1}{r} \frac{\partial p_t}{\partial \theta} + \rho g \sin \theta + \eta(\frac{\partial^2 v_\theta}{\partial r^2} + \frac{1}{r} \frac{\partial v_\theta}{\partial r} + \frac{1}{r^2} \frac{\partial^2 v_\theta}{\partial \theta^2} + \frac{\partial^2 v_\theta}{\partial z^2}) \\ & + \frac{1}{\mu}(B_r \frac{\partial B_\theta}{\partial r} + \frac{B_\theta}{r} \frac{\partial B_\theta}{\partial \theta} + B_z \frac{\partial B_\theta}{\partial z}) = \rho \frac{\partial v_\theta}{\partial t} , \end{aligned} \tag{C.2}$$

3452

$$\begin{aligned}
& -\rho\left(v_r\frac{\partial v_z}{\partial r} + \frac{v_\theta}{r}\frac{\partial v_z}{\partial\theta} + v_z\frac{\partial v_z}{\partial z}\right) - \frac{\partial p_t}{\partial z} + \eta\left(\frac{\partial^2 v_z}{\partial r^2} + \frac{1}{r}\frac{\partial v_z}{\partial r} + \frac{1}{r^2}\frac{\partial^2 v_z}{\partial\theta^2} + \frac{\partial^2 v_z}{\partial z^2}\right) \\
& + \frac{1}{\mu}\left(B_r\frac{\partial B_z}{\partial r} + \frac{B_\theta}{r}\frac{\partial B_z}{\partial\theta} + B_z\frac{\partial B_z}{\partial z}\right) = \rho\frac{\partial v_z}{\partial t} ,
\end{aligned}$$

3453

(C.3)

3454

where $p_t = p + \frac{\mathbf{B}^2}{2\mu}$. The magnetic induction equation in the (r, θ, z) coordinate directions can be written as follows:

3455

3456

$$\begin{aligned}
& \frac{1}{\mu\sigma}\left[\frac{\partial^2 B_r}{\partial r^2} + \frac{1}{r}\frac{\partial B_r}{\partial r} + \frac{1}{r^2}\frac{\partial^2 B_r}{\partial\theta^2} + \frac{\partial^2 B_r}{\partial z^2}\right] + \frac{1}{r}B_r\left(r\frac{\partial v_r}{\partial r}\right) + \frac{1}{r}B_\theta\frac{\partial v_r}{\partial\theta} + B_z\frac{\partial v_r}{\partial z} \\
& - \frac{1}{r}v_r\left(r\frac{\partial B_r}{\partial r}\right) - \frac{1}{r}v_\theta\frac{\partial B_r}{\partial\theta} - v_z\frac{\partial B_r}{\partial z} = \frac{\partial B_r}{\partial t} ,
\end{aligned}$$

3457

(C.4)

3458

$$\begin{aligned}
& \frac{1}{\mu\sigma}\left[\frac{\partial^2 B_\theta}{\partial r^2} + \frac{1}{r}\frac{\partial B_\theta}{\partial r} + \frac{1}{r^2}\frac{\partial^2 B_\theta}{\partial\theta^2} + \frac{\partial^2 B_\theta}{\partial z^2}\right] + \frac{1}{r}B_r\left(r\frac{\partial v_\theta}{\partial r}\right) + \frac{1}{r}B_\theta\frac{\partial v_\theta}{\partial\theta} + B_z\frac{\partial v_\theta}{\partial z} \\
& - \frac{1}{r}v_r\left(r\frac{\partial B_\theta}{\partial r}\right) - \frac{1}{r}v_\theta\frac{\partial B_\theta}{\partial\theta} - v_z\frac{\partial B_\theta}{\partial z} = \frac{\partial B_\theta}{\partial t} ,
\end{aligned}$$

3459

(C.5)

3460

$$\begin{aligned}
& \frac{1}{\mu\sigma}\left[\frac{\partial^2 B_z}{\partial r^2} + \frac{1}{r}\frac{\partial B_z}{\partial r} + \frac{1}{r^2}\frac{\partial^2 B_z}{\partial\theta^2} + \frac{\partial^2 B_z}{\partial z^2}\right] + \frac{1}{r}B_r\left(r\frac{\partial v_z}{\partial r}\right) + \frac{1}{r}B_\theta\frac{\partial v_z}{\partial\theta} + B_z\frac{\partial v_z}{\partial z} \\
& - \frac{1}{r}v_r\left(r\frac{\partial B_z}{\partial r}\right) - \frac{1}{r}v_\theta\frac{\partial B_z}{\partial\theta} - v_z\frac{\partial B_z}{\partial z} = \frac{\partial B_z}{\partial t} .
\end{aligned}$$

3461

(C.6)

3462

3463

The Ampère's law can be written as

$$\begin{aligned}
j_r &= \frac{1}{\mu}\left(\frac{1}{r}\frac{\partial B_z}{\partial\theta} - \frac{\partial B_\theta}{\partial z}\right) , \\
j_\theta &= \frac{1}{\mu}\left(-\frac{\partial B_z}{\partial r} + \frac{\partial B_r}{\partial z}\right) , \\
j_z &= \frac{1}{\mu}\left(\frac{\partial B_\theta}{\partial r} - \frac{1}{r}\frac{\partial B_r}{\partial\theta}\right) ,
\end{aligned}$$

3464

(C.7)

and the equation of continuity and the solenoidal condition for the magnetic field are

$$\frac{1}{r} \frac{\partial}{\partial r}(rv_r) + \frac{1}{r} \frac{\partial v_\theta}{\partial \theta} + \frac{\partial v_z}{\partial z} = 0 , \quad (\text{C.8})$$

$$\frac{1}{r} \frac{\partial}{\partial r}(rB_r) + \frac{1}{r} \frac{\partial B_\theta}{\partial \theta} + \frac{\partial B_z}{\partial z} = 0 . \quad (\text{C.9})$$

C.2 Derivation of Rayleigh's instability at an interface separating two flows in magnetic field

C.2.1 *kinematic boundary condition at interface*

We consider the (x, y, z) coordinate system in Fig. 2.1. A particle of fluid that is at some time on the free surface will always remain on the free surface. Then, since the equation of the free surface is $y - (\xi + a) = 0$, it follows that

$$\frac{D}{Dt}(y - (\xi + a)) = 0 . \quad (\text{C.10})$$

Neglecting quadratically small terms, Eqn. (C.10) yields at the interface($y = \pm a$),

$$\frac{\partial \xi}{\partial t} + U_i \frac{\partial \xi}{\partial x} = \frac{\partial \phi_i}{\partial y} \quad (\text{C.11})$$

In the region $(-a < y < a)$, the velocity potential ϕ_i must satisfy $\frac{\partial^2 \phi_1}{\partial x^2} + \frac{\partial^2 \phi_1}{\partial y^2} = 0$, $|\nabla \phi_1| = \text{finite}$. In the region $y > a$, $y < -a$, the velocity potential must satisfy $\frac{\partial^2 \phi_2}{\partial x^2} + \frac{\partial^2 \phi_2}{\partial y^2} = 0$, $|\nabla \phi_2| = \text{finite}$. In view of the shape of the interface, the solutions should be trigonometric in x , then the y dependence will be exponential. In view of the finite conditions of velocity potentials, the negative

3489 exponential should be rejected for ϕ_1 and the positive exponential should be
 3490 rejected for ϕ_2 . Therefore, the general solutions are
 3491

$$\begin{aligned} \phi_1(x, y, t) &= A_1 e^{(2\pi/\lambda)y} e^{i(2\pi/\lambda)(x-ct)} , \\ \phi_2(x, y, t) &= A_2 e^{-(2\pi/\lambda)y} e^{i(2\pi/\lambda)(x-ct)} \end{aligned} \quad (\text{C.12})$$

3493 Imposing the kinematic conditions on these solutions, the coefficients are
 3494 determined at $y = a$ and $y = -a$ respectively.
 3495

$$\begin{aligned} \phi_1(x, y, t) &= -i\epsilon(c - U_1) e^{i(2\pi/\lambda)(x-ct)} , \\ \phi_2(x, y, t) &= i\epsilon(c - U_2) e^{i(2\pi/\lambda)(x-ct)} \end{aligned} \quad (\text{C.13})$$

3497 ,where $U_1 = U_1(a)$, $U_2 = U_2(a)$.
 3498

$$\begin{aligned} \phi_1(x, y, t) &= i\epsilon(c - U_1) e^{i(2\pi/\lambda)(x-ct)} \\ \phi_2(x, y, t) &= -i\epsilon(c - U_2) e^{i(2\pi/\lambda)(x-ct)} \end{aligned} \quad (\text{C.14})$$

3500 ,where $U_1 = U_1(-a)$, $U_2 = U_2(-a)$.

3501 Since the perturbed surface at $y = a$ and $y = -a$ are supposed to be
 3502 symmetric, half of the jet section for the surface stability is considered in the
 3503 following work.

3504 **C.2.2 hydrodynamic stability in magnetic field**

3505 Substituting the perturbed expressions into the equations of motion, ne-
 3506 glecting second order terms in the perturbed quantities, and making use of the
 3507 fact that U, P satisfy the flow equations and the current density in Lorentz
 3508 force term can be represented using Ohm's law, we have the linearized equa-
 3509 tions governing the motion of disturbance.
 3510

$$\begin{aligned} &\frac{\partial v'_{xi}}{\partial t} + U_i \frac{\partial v'_{xi}}{\partial x} + v'_{xi} \frac{dU_i}{dy} \\ &= -\frac{1}{\rho_i} \frac{\partial p'_i}{\partial x} - \frac{\sigma_i}{\rho_i} B_y^2 v'_{xi} + \frac{\sigma_i}{\rho_i} B_x B_y v'_{yi} \end{aligned} \quad (\text{C.15})$$

3512

$$\begin{aligned} & \frac{\partial v'_{yi}}{\partial t} + U_i \frac{\partial v'_{yi}}{\partial x} \\ & = -\frac{1}{\rho_i} \frac{\partial p'_i}{\partial y} - \frac{\sigma_i}{\rho_i} B_x^2 v'_{yi} + \frac{\sigma_i}{\rho_i} B_x B_y v'_{xi} \end{aligned} \quad (\text{C.16})$$

3513

3514 ,where $p'_i = f_i(c, \lambda, y)e^{i(2\pi/\lambda)(x-ct)}$.

3515 The perturbed velocity v'_x, v'_y are given

3516

$$\begin{aligned} v'_x &= \frac{\partial \phi_1}{\partial x} = i\left(\frac{2\pi}{\lambda}\right) A_1 e^{(2\pi/\lambda)y} e^{i(2\pi/\lambda)(x-ct)} \\ v'_y &= \frac{\partial \phi_1}{\partial y} = \left(\frac{2\pi}{\lambda}\right) A_1 e^{(2\pi/\lambda)y} e^{i(2\pi/\lambda)(x-ct)} \end{aligned} \quad (\text{C.17})$$

3517

3518 Putting Eqn. (C.17) into Eqn. (C.15) and Eqn. (C.16), equate the hydrody-
3519 namic pressures since it is isotropic, which leads to Rayleigh's stability equa-
3520 tion for the flow in magnetic field.

3521

$$\sigma_1 B_x B_y + i\sigma_1 B_x^2 = \sigma_1 B_y^2 i - \sigma_1 B_x B_y + \rho_1 \left(\frac{\lambda}{2\pi}\right) \frac{d^2 U_1}{dy^2} \quad (\text{C.18})$$

3522

3523 ,where $U_1 = U_1(y)$.

3524 In the same manner, the Rayleigh's stability equation for the upper flow
3525 in magnetic field is be derived.

3526

$$\sigma_2 B_x^2 + \sigma_2 B_x B_y i = \sigma_2 B_y^2 - i\sigma_2 B_x B_y - \rho_2 i \left(\frac{\lambda}{2\pi}\right) \frac{d^2 U_2}{dy^2} \quad (\text{C.19})$$

3527

3528 ,where $U_2 = U_2(y)$.

3529 **C.2.3 dynamic boundary condition at interface**

3530 The difference of the normal stresses must be balanced by the normal stress
3531 induced by surface tension at the interface.

3532

$$(P_1 + \frac{\partial P_1}{\partial y} \xi + \frac{\partial^2 P_1}{\partial y^2} \xi + \dots + p'_1) - (P_2 + \frac{\partial P_2}{\partial y} \xi + \frac{\partial^2 P_2}{\partial y^2} \xi + \dots + p'_2) + \Gamma \frac{\partial^2 \xi}{\partial x^2} = 0 \quad (\text{C.20})$$

3533

3534 , where Γ is surface tension.

3535 Considering the gravity force in the free surface waves, Eqn. (C.20) can be
 3536 rewritten as follows.
 3537

$$\begin{aligned}
 & (\rho_2 - \rho_1)g \cos \theta + \rho_1(c - U_1)^2\left(\frac{2\pi}{\lambda}\right) + \rho_2(c - U_2)^2\left(\frac{2\pi}{\lambda}\right) \\
 & + \rho_1(c - U_1)\frac{dU_1}{dy} - \rho_2(c - U_2)\frac{dU_2}{dy} + iB_y^2(\sigma_1(c - U_1) + \sigma_2(c - U_2)) \\
 3538 & + B_x B_y(\sigma_2(c - U_2) - \sigma_1(c - U_1)) - \Gamma\left(\frac{2\pi}{\lambda}\right)^2 = 0 \tag{C.21}
 \end{aligned}$$

3539 ,where $U_1 = U_1(a)$, $U_2 = U_2(a)$.

3540 Consider the case that $U_2 = 0$, $\frac{dU_2}{dy} = 0$, $\rho_2 = 0$, $\sigma_2 = 0$. This would corre-
 3541 spond to the stationary fluid on the upper and the density and conductivity
 3542 of the upper fluid are very small compared with these of the lower fluid. The
 3543 wave velocity is represented as follow.
 3544

$$\begin{aligned}
 c = [& -\rho_1 \frac{dU_1}{dy} + B_x B_y \sigma_1 - iB_y^2 \sigma_1 + 2\left(\frac{2\pi}{\lambda}\right) \rho_1 U_1 \\
 & \pm \sqrt{\rho_1^2 \left(\frac{dU_1}{dy}\right)^2 + 4\left(\frac{2\pi}{\lambda}\right) \cos \theta g \rho_1^2 - 2B_x B_y \rho_1 \sigma_1 \frac{dU_1}{dy} + 2iB_y^2 \rho_1 \sigma_1 \frac{dU_1}{dy}} \\
 & \pm \sqrt{B_x^2 B_y^2 \sigma_1^2 - 2iB_x B_y^3 \sigma_1^2 - B_y^4 \sigma_1^2 + 4\left(\frac{2\pi}{\lambda}\right)^3 \rho_1 \Gamma} \quad] \times \frac{1}{2\left(\frac{2\pi}{\lambda}\right) \rho_1} \tag{C.22}
 \end{aligned}$$

3545